

Towards Single Photon Detection with Amorphous Silicon Based Microchannel Plates

Présentée le 4 mai 2021

Faculté des sciences et techniques de l'ingénieur
Laboratoire de photovoltaïque et couches minces électroniques
Programme doctoral en photonique

pour l'obtention du grade de Docteur ès Sciences

par

Janina Christine Isabelle LÖFFLER

Acceptée sur proposition du jury

Prof. A. Kis, président du jury
Prof. C. Ballif, Dr N. Wyrsh, directeurs de thèse
Dr W. Lustermann, rapporteur
Dr A. Tremsin, rapporteur
Prof. J.-M. Sallèse, rapporteur

To my parents.

Abstract

An exciting new approach for microchannel plate (MCP) detectors could help make them suitable for single photon detection. State-of-the-art clean room technology allows amorphous silicon based microchannel plates (AMCPs) to take a variety of shapes. This versatility together with a new form of on-chip integration enables detector configurations that can be manufactured to meet the exact requirements of the application. The collection efficiency can be increased to 100% while maintaining a maximum gain. With channel lengths of $60\text{ }\mu\text{m}$ and diameters below $3\text{ }\mu\text{m}$, the detector gains are now in a range where low level signals can be amplified. In this thesis, we extend the fabrication possibilities of MCP detectors towards structures with diameters in the sub micrometer range, where we expect high gains and excellent timing. We found the minimum channel length of AMCPs with high gain to be $30\text{ }\mu\text{m}$. We show that the timing of such narrow channels is one of the fastest signal amplifications compared to other technologies. Their fast timing together with their high spatial resolution make them a valuable solution for applications where sub millimeter precision is crucial, for example in medical imaging. The results of the thesis alleviate the fabrication process of AMCPs, as the deposition of thick amorphous silicon layers has been identified as the current bottleneck of the fabrication. Through the detailed analysis of secondary emission properties and the implementation in a Monte-Carlo model we can now confidently predict the response of AMCPs with various shapes to a single incident electron. This now provides a quick path to adapt the AMCP configuration directly to the application and makes them a viable alternative to other single photon detectors.

Zusammenfassung

Einzelne Photonen zu detektieren ist ein Hot-topic in vielen Bereichen. Hier präsentieren wir einen innovativen Ansatz für Mikrokanalplatten-Detektoren, mit dem wir diesem Ziel näher kommen. Modernste Reinraumtechnologie ermöglicht es Mikrokanalplatten auf der Basis von amorphem Silizium herzustellen - Dies in einer Vielzahl von Formen, die nicht mehr an die konventionelle Zylinderform gebunden sind. Diese Vielseitigkeit und eine neue Form der On-Chip-Integration erlauben die Herstellung von Detektoren, die genau auf die Anforderungen der Anwendung zugeschnitten werden können. Die Sammeleffizienz kann unter Beibehaltung der maximalen Verstärkung bis zu 100% betragen. Bei Kanallängen von $60\text{ }\mu\text{m}$ und Durchmessern unter $3\text{ }\mu\text{m}$ liegt der Detektor Gain jetzt in einem Bereich, in dem auch sehr schwache Signale verstärkt werden können. In dieser Arbeit erweitern wir die Herstellungsmöglichkeiten von MCP-Detektoren auf Strukturen mit Durchmessern im Submikrometerbereich, wo wir hohe Verstärkungen und ein aussergewöhnlich gutes Timing erwarten. Wir haben festgestellt, dass die minimale Kanallänge von AMCPs mit hoher Verstärkung $30\text{ }\mu\text{m}$ beträgt. Wir zeigen, dass das Timing solch schmaler Kanäle im Vergleich zu anderen Technologien eine der schnellsten Signalverstärkungen ist. Ihr exzellentes Timing zusammen mit ihrer hohen räumlichen Auflösung machen sie zu einer wertvollen Lösung für Anwendungen, bei denen es auf jeden Millimeter ankommt, zum Beispiel bei medizinischen Scans. Die Ergebnisse dieser Arbeit erleichtern den Herstellungsprozess von AMCPs, da die Abscheidung dicker amorpher Siliziumschichten als aktueller Engpass bei der Herstellung identifiziert wurde. Durch die detaillierte Analyse der sekundären Emissionseigenschaften und die Umsetzung in ein Monte-Carlo-Modell können wir erstmals die Antwort von AMCPs mit verschiedenen Formen auf ein einzelnes einfallendes Elektron sicher vorhersagen. Hiermit existiert nun ein schneller Weg, die AMCP-Konfiguration direkt an die Anwendung anzupassen, und macht sie zu einer attraktiven Alternative zu anderen Einzelphotonendetektoren.

Résumé

La détection de photons individuels est un sujet brûlant dans de nombreux domaines. Nous présentons ici une approche innovante pour les détecteurs à plaques à microcanaux, qui nous rapproche de cet objectif. La technologie de pointe des salles blanches nous permet de produire des plaques à microcanaux à base de silicium amorphe dans une variété de formes qui ne sont plus liées à la forme cylindrique conventionnelle. Cette polyvalence, associée à une nouvelle forme d'intégration sur puce, permet de produire des détecteurs qui peuvent être adaptés exactement aux exigences de l'application. L'efficacité de la collecte peut atteindre 100% tout en maintenant le gain maximum. Avec des longueurs de canal de $60\mu\text{m}$ et des diamètres plus petit que $3\mu\text{m}$, les gains du détecteur sont maintenant dans une plage où même les signaux très faibles peuvent être amplifiés. Dans cette thèse, nous étendons les possibilités de fabrication des détecteurs MCP vers des structures dont le diamètre est inférieur au micromètre, où nous attendons des gains élevés et un excellent timing. Nous avons trouvé que la longueur minimale de canal des AMCP à haut gain est de $30\mu\text{m}$. Nous montrons que la multiplication dans ces canaux étroits est l'une des façons de génération de signal les plus rapides par rapport aux autres technologies. Leur rapidité et leur haute résolution spatiale font des détecteurs présents une solution précieuse pour les applications où chaque millimètre compte, par exemple dans la tomographie médicale. Les résultats de la thèse atténuent le processus de fabrication des AMCP, car le dépôt d'épaisses couches de silicium amorphe a été identifié comme le goulot d'étranglement actuel de la fabrication. Grâce à l'analyse détaillée des propriétés d'émission secondaire et à la mise en œuvre dans un modèle de Monte-Carlo, nous pouvons maintenant prédire avec confiance la réponse des AMCP de formes diverses à un seul électron incident. Cela permet maintenant d'adapter rapidement la configuration des AMCP directement à l'application et en fait une alternative viable aux autres détecteurs de photons individuels.

Contents

Abstract (English/Deutsch/Français)	i
List of figures	viii
List of tables	xviii
1 Introduction	1
1.1 Motivation and objective of this work	1
1.2 Structure of the thesis	2
1.3 Contribution to the research field	3
2 Microchannel plate and single photon detectors	5
2.1 Microchannel plate	5
2.2 Single photon detectors	8
3 Amorphous silicon based microchannel plate	11
3.1 Why 'amorphous silicon based' MCPs?	11
3.2 Hydrogenated Amorphous Silicon	12
3.3 Deep Reactive Ion Etching	14
3.4 State-of-the-art amorphous silicon based microchannel plate	15
4 AMCPs with high aspect ratio	19
4.1 Modifications of the AMCP fabrication process for high aspect ratio	19
4.2 Fabrication of the bottom layers	20
4.3 Fabrication of the multiplication layer	23
4.4 Deep reactive ion etching of AMCP microchannels	27
4.5 AMCP channel surface roughness	32
4.6 Characterization	35
5 (A)MCP operating principle	43
5.1 Secondary electron emission at low energies	43
5.2 Electron scattering simulators	46
5.3 Probabilistic model for electron emission	48
5.4 Secondary electron emission yield modeling	51
5.5 Microchannel plate modeling	56
	vii

Contents

6	Electron emission in AMCPs	65
6.1	Experimental setup to characterize electron emission	66
6.2	Energy distribution of emitted electrons	67
6.3	Backscattering probability	75
6.4	Electron emission yield	80
6.5	Backscattering and secondary yield parametrizations	84
6.6	Summary and parameter lookup table	90
7	Single channel model for AMCPs	95
7.1	General setup of the Monte-Carlo model for a single channel	95
7.2	3D cinematic model	96
7.2.1	Model setup	99
7.2.2	Calibration of the secondary yield curves with AMCP measurement data	100
7.2.3	Results	103
7.3	Simplified gain model evaluated for high aspect ratio	112
7.4	Summary	114
8	Simulations of AMCPs with non-cylindrical channel shapes	115
8.1	General model setup	115
8.2	Funnel shaped channels	118
8.3	3D electron trajectories in funnel shaped channels	121
9	Conclusion and optimization path for single photon detection	125
9.1	Summary of the key results	125
9.2	Perspectives	126
9.2.1	Future developments	126
9.2.2	AMCP applications	127
	Bibliography	129
	Acknowledgements	141
	Curriculum Vitae	145

List of Figures

2.1	(a) Image of a microchannel plate in various magnifications [Mazuritskiy 2019] and (b) schematic of electron multiplication mechanism in one of the channels.	6
2.2	(a) Various stages of the MCP fabrication process are shown. Glass fibers are assembled, drawn and etched in several steps, (b) Schematic drawing of a typical microchannel plate assembly. An electron from the photocathode is multiplied in the MCPs and creates a charge cloud that can be detected by the electronics. Image taken from [Siegmond 2013].	7
2.3	(a) Operation regimes for single photon photodiode detectors, linear mode for low reverse bias, avalanche mode biased around the breakdown voltage V_{BD} and Geiger mode with bias higher than the breakdown voltage. (b) Photon counting spectrum recorded with a SiPM [Vacheret 2011]. Each peak represents a number of photons, starting with 0 at the pedestal peak.	10
3.1	Reaction chamber for plasma enhanced chemical vapor deposition, PECVD. Between the two electrodes a plasma is ignited, which is driven by the radio frequency. Dissociated molecules from the plasma react at the surface of the substrate and grow films.	13
3.2	How localized states influence the charge transport in a-Si:H: (a) Position of the three contributing transport mechanisms and representation of their density of states, (b) Dynamics of charge transport in their respective energetic levels. ① Defect states around E_F contribute to charge transport at low temperature. ② Hindered transport via hopping with nearest neighbor in the band tail states at higher temperatures and ③ dispersive charge transport in conduction band through trapping in localizes band tail states. Drawing taken from [Despeisse 2006].	14
3.3	Illustration of deep reactive ion etching with a standard Bosch process. The cyclic process consists of two alternating steps, passivation of the sidewalls and the main isotropic etching. Deep isotropic etching creates a scalloping sidewall structure.	14

List of Figures

3.4	AMCP architecture of 3rd generation devices as developed by [Franco 2014b]. Micro channels in a thick amorphous silicon layer act as electron amplifiers. A decoupling layer separates the multiplication layer from the electronic readout. The leakage current I_L (yellow) is evacuated and the electron cloud signal (red) impinges on the readout pad.	15
3.5	(a) Leakage current measured on intermediate electrode compared to the anode current, (b) gain measurements for AMCPs with different aspect ratios. Reproduced from [Franco 2014a]	17
4.1	Structure and SEM images of 4 th generation of AMCPs. Compared to the structure of the previous generation (figure 3.4) the size of the c-Si wafer was increased to 6" in order to use a state-of-the-art DRIE system. The top electrode was replaced by a metallic layer, that was used to fabricate channels with diameters down to 2.7 μm	20
4.2	Process flow for the fabrication of AMCPs: 1. Si wafer with 1.5 μm SiO_2 and a 100 nm Cr layer , 2. Patterning of the Cr anode after first lithography, 3. PECVD of a 80 nm SiO_x adhesion layer, a 2 μm a-Si:H and a 200 nm n-doped $\mu\text{c-Si:H}$ layers, 4. Evaporation of the 50 nm intermediate electrode Cr pads, PECVD of a 80 nm SiO_x adhesion layer and of about 80 μm a-Si:H layers, 5.-8. Evaporation of a 20 nm Cr top electrode, patterning with lithography with a very thin photoresist layer of 1 μm and micro channel etching through the whole layer stack with DRIE, these steps are new compared to previous generations' fabrication, 9. After removal of residual resist, the AMCP is finished.	21
4.3	(a) Image of the bottom electrode structure of AMCPs on a 6" wafer. (b) Placement of AMCP test structures (white squares) and SEM test structures on 6" wafer. SEM1-9 test structures are used to determine layer thickness and channel etch parameters by examining their cross-sections. (c) Schematic drawing of one AMCP test structure. The active area is numbered and each of the numbered squares except number 1 represent an AMCP pad that can be measured independently. The top electrode and intermediate electrode are shared for all pads of one test structure. (b) Microscope image of the intermediate contact on the $\mu\text{c-Si}$ layer at pad number 1	22
4.4	Microscope images of the surface of a 95 μm layer and 82 μm layer of a-Si:H, that were deposited on a 4" (a) and on a 6" (b) wafer respectively, using the same deposition recipe.	24
4.5	SEM images of defects in 80 μm thick amorphous silicon layers in an AMCP stack on 6" wafers. Defects run through the whole depth of the a-Si:H layer and delaminate at the adhesion layer.	25
4.6	SEM image of about 80 μm of a-Si:H deposited on a 6" wafer, after optimization of the deposition temperature.	25

4.7	a-Si:H layer thickness variation (a,c,e) and their respective deposition temperature profile (b,d,f). The thickness was measured from cross sections of SEM1-9, located on the wafer as shown in figure 4.3a. The deposition temperature was optimized to reduce defects in the a-Si:H layer. At the same time, due to higher temperatures, the deposition rate was reduced and the homogeneity improved. The total thickness after optimization varies up to 16 μm over the 6" area. The red circle shows a 4" inlet.	26
4.8	(a) SEM cross section of DRIE etched super straight micro channels in a Si wafer with 5.6 μm diameter and excellent verticality. (b) On the same wafer, channels with diameters down to 2-3 μm have been etched.	28
4.9	(a) SEM image of AMCP channels cross section showing typical etching difficulties during DRIE due to wafer bending, thickness variation and channel diameter variation. (b) Top view of overetched channels.	28
4.10	(a) Cross section showing the etch depth of narrow channels, that are not completely etched to the bottom electrode of the AMCP due to the thickness variations of the a-Si:H layer. (b) SEM image of the channel bottom of a completely etched narrow channel, showing the reduced diameter at greater etch depth. A rough surface structure of the channel is visible, which might have an effect on the secondary yield.	29
4.11	Etch depth of microchannels where (a) at the outer parts of the wafer (SEM1-9) thin channels are not completely etched and (b) in the middle of the wafer (SEM5) with an average thickness of about 55 μm channels with diameters down to 2.9 μm have been etched completely	30
4.12	SEM images of AMCPs with channels etched in about 60 μm a-Si:H layers. The minimal channel diameter was 2.7 μm	31
4.13	(a) SEM of a rough channel structure and channel diameter of about 2.5 μm . (b) SEM image of the spatial resolution of tens of nm of the photolithography systems used. For a roughly circular geometry channel diameters down to 500 nm could potentially be fabricated using this lithography process.	31
4.14	Reconstructed 3D surface of a of a 3 rd generation AMCP microchannel.	33
4.15	Roughness values of the channel surface shown in 4.14	33
4.16	Reconstructed 3D surface of a of a 5 th generation AMCP microchannel.	34
4.17	Roughness values of the channel surface shown in 4.16	34
4.18	Line profiles of the characterized surfaces. A periodicity in surface rugosity can be seen at the top of the channel in (b) and disappears at the end of the channel in (a). See the color scale of the respective images for height values of the colored areas.	35
4.19	Setup for transient characterization of AMCPs. The UV laser pulse from with 7 ns FWHM and tunable frequency between 1 kHz and 4.7 kHz is guided through a filter into the vacuum chamber. Inside the chamber, UV photons are hitting a photocathode and release photoelectrons. The photoelectrons are impinging on the AMCP through an electron screen.	36

List of Figures

4.20	(a) Schematic drawing of the geometrical arrangement of photocathode and the AMCP test structure. (b) Electric potential (V) between the photocathode and the AMCP.	37
4.21	(a) Picture of an AMCP mounted on the PCB. For all the contacts, gold pads are glued on the electrodes using a silver glue and then the pads are wire bonded to the PCB. (b) Vacuum chamber after a first revision with shielded cables.	38
4.22	(a) Oscilloscope output showing an AMCP response to a 266 nm laser pulse, using the setup described figure 4.19. The AMCP area was 3.6 mm^2 and the aspect ratio was 13.6. The AMCP signal was triggered on the photo diode output. We used an external amplifier that was connected to the AMCP output outside the vacuum chamber. (b) Current and charge calculated from the signal in (a). No reference signal could be measured due to the very low incident number of electrons. As a conclusion, a further system upgrade was decided to improve transient measurements.	39
4.23	Electrical circuit between the intermediate electrode and the bottom pad. We calculate the RC constant to evaluate potential leakage currents towards the intermediate electrode in transient mode. C_{SiO_x} and R_{SiO_x} are the capacitance and resistance of the SiO_x layer, C_{aSi} and R_{bulk} are the capacitance and resistance of the a-Si:H decoupling layer and R_{surface} is the resistance of the channel surface.	40
4.24	(a) Top and (b) bottom side of the newly designed PCB for transient measurements with an integrated charge sensitive amplifier, CR-110, that can be mounted from the bottom side of the PCB along with all the electronics parts. The AMCP is mounted on top and wire bonded to the gold pads around the open space in the middle.	40
5.1	(a) Elastic backscattering of an incident electron. (b) Inelastic backscattering of an incident electron (c) Scattering of an incident electron inside the material and secondary electron creation. (d) Secondary electron scattering inside the material and emission to the vacuum.	44
5.2	(a) Interface currents. A probabilistic model for electron emission is developed based on measurements of the interface currents, which are the incident current I_0 , the elastically reflected electron current I_e , rediffused electron current I_r and the secondary electron current I_{ts} . (b) Electron emission energy spectrum. According to their respective energies, the electron peaks are attributed to the nature of emission. The peak at low energies are secondary electrons, and the peak around the incident energy are backscattered electrons. Electrons with energies in between are inelastically backscattered. Images taken from [Furman 2002].	48

5.3	(a) Secondary electron emission angle θ_{SE} distribution calculated for Au and Si for normalized angles from -1 to 1, corresponding to -90° to 90° . For high incident electron energies, the angular distribution inside the material can be assumed to be isotropic. From the most probably emission energy (MPE), the angular distribution of emission can be calculated using the law of refraction at the interface. The emission angle distribution varies with the MPE. (b) Emission energy spectrum of Si. Both taken from [Cazaux 2010b]	51
5.4	(a) Effect of charging in an insulator on the emission yield spectrum at different energies. Positive charging accumulates in areas where the total emission yield is above 1. Negative charging in areas that have a yield below 1 at high incident electron energies. (b) Modification of total emission yield curve due to charging under an incident electron fluence $I_0\tau/S$ where τ is the time interval and S the illuminated area. From [Cazaux 2006]	53
5.5	(a) Potential barrier for secondary electrons and (b) its effect on the secondary yield of KCl. Both taken from [Cazaux 2010a]	53
5.6	(a) Comparison of different empirical models for the incident electron energy dependence of the secondary yield used for MCP simulations [Insepov 2010]. For comparison the yield is plotted relative to the maximum yield and with the maximum yield at a fixed energy. (b) Angular dependence of secondary electron yield in glass MCPs according to [Kruschwitz 2011]. Experimental results from MCP gain measurements were fitted to the SEY model of [Vaughan 1989].	54
5.7	Exceptional angular dependence of the total electron emission yield measured for (a) a rough Cr sample [Balcon 2012] and measured for (b) a CVD diamond surface [Lapington 2009].	56
5.8	(a) Simple representation of a discrete dynode with a fixed number of stages for electron multiplication. This simplification was used in the first MCP models. (b) Electrical network describing an element between two stages of the MCP channel in the time dependent transmission line model, taken from [Giudicotti 2011].	57
6.1	AFM images of sample surfaces used for the measurements. (a) Surface of a rough sample used for measuring the electron emission spectrum. Samples with this kind of roughness were used to measured the emission spectra of a-Si:H and AlO_x . The total emission yield was measured as well. (b) As the electron emission yield varies greatly with the incident angle, samples with a flat surface have been used for complementary electron yield measurements at a various incident angles.	66

List of Figures

- 6.2 (a) Setup for energy emission spectra measurements. An incident monochromatic electron beam creates electron emission at various emission energies E_a , that are analysed using a hemispherical electron energy analyser, positioned at an angle of 45° relative to the incident electron beam. Image taken from [Villemant 2017]. (b) Kelvin probe based setup for total electron yield measurements developed for measurements of thin insulating layers. The emission yield is measured indirectly, by measuring the charge induced by electron emission inside the sample. Image taken from [Belhaj 2009] 67
- 6.3 Electron emission energy spectra measured using the setup shown in figure 6.2a with the hemispherical electron analyzer. The energy spectrum in (a) has been measured for the rough a-Si:H layer of 12 nm without an additional coating. The normalized data are shown in (c). The emission spectrum of the rough a-Si:H layer of 12 nm with an ALD coating of 5 nm AlO_x is shown in (b) and the normalized data are shown in (d). 68
- 6.4 Transfer function to correct the measured emission energy data according to [Villemant 2017] 69
- 6.5 Emission energy spectra after correction. (a) Emission spectra of a-Si:H for the corrected incident energies. (b) The low energy spectra, with the secondary electron emission peak overlapping for the different incident energies. (c) Emission spectra of AlO_x for the corrected incident energies and (d) low energy part of the AlO_x emission spectra, where the secondary electron energy distribution overlaps for incident energies of 13.5 eV and above. 71
- 6.6 Secondary electron emission energy distribution after correction shown for 0 to 10 eV. (a) a-Si:H spectra compared to measured literature values of Si from [Cazaux 2010b] and the calculated curve for Si and a-Si:H and the general curve fits of equation 5.51 [Yakobson 1966], equation 5.40 [Price 2001], and equation 5.42 [Kruschwitz 2011]. The literature values of table 6.1 and the average emission energy values of table 6.2 have been used to calculate the curves. (b) The AlO_x spectrum fits well to the calculated curve of Al_2O_3 using the theoretical formula of [Cazaux 2010b] and the values of table 6.1 72
- 6.7 Secondary electron emission spectra probability density function (PDF) and resulting cumulative distribution function (CDF). For a-Si:H the measured curves are compared to the fit of [Kruschwitz 2011]. (a) In the low energy range the measured curve cannot be represented by the model, thus we use a fit for incident energies below 25 eV. (b) For higher energies the modeled curve fits well. For AlO_x we use the model of Cazaux [Cazaux 2010a]. (c) As for a-Si:H, in the low energy range, data are better represented by a fit. (d) For energies above 25 eV the model fits well to the measurement. 73

6.8	a-Si:H emission energy spectra after correction. The blue part of the total area corresponds to the elastic backscattering probability (BS), the green part to inelastic scattering (IBS) and the red part to the secondary emission probability (SE). In this low energy range, the relative probability of backscattering decreases for increasing incident energies.	76
6.9	AlO _x emission energy spectra after correction. The blue part of the total area corresponds to the backscattering probability (BS), the green part to inelastically backscattered electrons (IBS) and the red part to the secondary emission probability (SE). As for a-Si:H the relative proportion of backscattering decreases and the proportion of secondary emission increases with increasing incident energy.	77
6.10	(a) Relative probability for elastic backscattering (BS) fits for a-Si:H and AlO _x . The data point at 3.5 eV for AlO _x has been ignored for the fit, as there is no equivalent point for a-Si:H. (b) Probability for electrons to be inelastically backscattered (IBS) and linear fits for a-Si:H and AlO _x on two IBS measurement points. Inelastic backscattering was extracted from the measured spectra at two points above 50 eV. In this energy range it is the major backscattering mechanism. The fits together with total yield curves are used to quantify elastic and inelastic backscattering events for AMCP calculations.	78
6.11	Backscattering probability $P_{(I)BS} = P_{BS} + P_{IBS}$ calculated from literature values and MC models for Si and our experimental data for a-Si:H. (a) At energies below 50 eV we see that the our calculated backscattering probability fits very well to literature values. Only the simulations done with CASINO differ. (b) At energies above 50 eV: The backscattering probability lies in a wide interval between 0.07 according to our measurements up to about 0.4 according to our MC simulations. Literature values are in between these values.	78
6.12	Backscattering probability, $P_{IBS} + P_{BS}$ of Al ₂ O ₃ from simulations and measurements. (a) At low energies we can only compare our measurements to the curves calculated with CASINO. (b) At high energies: As for Si, the backscattering probability lies in a wide interval between 0.05 according to our measurements up to about 0.4 according to our MC simulations. We assume this is mostly due to inelastic backscattering.	79
6.13	(a) The mean emission energy of emitted electrons depending on the incident energy. The emission energies are generally higher in a-Si:H, while the emission yield of a-Si:H is lower. Inelastically backscattered electrons should be taken into account for AMCP simulations, as their energetic contribution is very high. (b) The energy efficiency has been calculated from the total emission yield and the emission spectra. The efficiency is similar for the two materials and generally higher at low energies where a bigger part of the electrons are backscattered.	80
6.14	(a) Total emission yield (TEY) measurements of rough and flat a-Si:H, AlO _x on rough a-Si:H, and flat ALD deposited AlO _x and MgO measured at various degrees of incidence in the energy range between 0 and 1000 eV. (b) TEY of the low energy region from 0 to 100 eV.	81

6.15 (a) Total emission yield measurements of a flat a-Si:H layer at 0° to 75° incidence and a rough a-Si:H layer at 0 ° incidence. The yield of the rough sample behaves like a mixture of the yields of the flat sample at different angles. (b) TEY enhancement through AlO _x layer on a-Si:H. (c) TEY measurements of ALD deposited AlO _x layers. The yield is comparable to literature values of [Jokela 2012] and [van der Graaf 2017], taking into account the thickness of 5 nm. (d) TEY of ALD deposited MgO coating and comparison to [Jokela 2012]. The MgO coating needs to be improved.	82
6.16 Total emission yield of Si at normal incidence from simulations and measurements compared to measurements of a-Si:H, of a flat and a rough surface and Monte-Carlo simulations of the total yield of Si using the electron scattering code of TU Delft.	83
6.17 Total emission yield of Al ₂ O ₃ at normal incidence and a high incident angle of 80° from simulations and of 75° from measurements compared to literature values. Measurements of different authors agree well with out measurements. The simulated curves are very different for Al ₂ O ₃ . This may be because electron scattering simulations are mostly used and developed for Si and metals.	83
6.18 Total emission yield of (a) a-Si:H and (b) AlO _x after adding TEY(0 eV)=1 and deriving the TEY at 45°.	85
6.19 Backscattering yield of a-Si:H, for incident energies between 0 and 100 eV in (a), shown for higher incident energies in (b). The yield is calculated using the relative probability P_{BS} and the TEY. The backscattering yield does not vary much with the incident angle, as we calculated P_{BS} only for 45°. The fit curve of [Kruschwitz 2011], equation 5.43 and the formula of [Cazaux 2012] can both be used to describe the yield.	86
6.20 Backscattering yield of AlO _x , for incident energies between 0 and 100 eV in (a) and for energies between 100 eV and 1000 eV in (b). The backscattering yield does not vary much with the incident angle for AlO _x either. The fit curve of [Kruschwitz 2011], equation 5.43 and the formula of [Cazaux 2012] can both be used to describe the yield.	86
6.21 Inelastic backscattering yield curves and fits with $a(\theta) \cdot \exp(b(\theta) \cdot E_{in}) + c(\theta) \cdot \exp(d(\theta) \cdot E_{in})$. Inelastic backscattering is the main backscattering mechanism at high incident energies, whereas at low energies elastic backscattering is predominant.	87
6.22 Secondary yield and backscattering yield of Si from literature values compared to our MC calculations and the yields calculated from our experimental TEY curve of a-Si:H	88
6.23 Secondary yield of a-Si:H and AlO _x without (blue) and with (red) correction term for mutual exclusivity of elastic backscattering and secondary emission in Monte Carlo simulations. This correction is most important at energies below 50 eV.	89

6.24	Secondary yield of a-Si:H fitted to the curve of [Bundaleski 2015] in (a) and (b) and fitted to the curve of [Vaughan 1989] in (c) and (d). The Vaughan fit is used for AMCP simulations and the fit* curves were fitted to the experimental gain of AMCPs.	91
7.1	Schematic drawing of the 3D channel geometry used for the simulations shown in this chapter. The channel length is l and its diameter is d . The electron is assumed to hit the channel at a random height in the upper part between l and a height $l - \tan(\theta)/d$, depending on the incident angle θ of the beam. The AMCP bias voltage is always negative with respect to the ground (GND), even when not explicitly mentioned in the text.	97
7.2	Definition of angles and distances in the cinematic AMCP model and its coordinate system.	98
7.3	AMCP gain measurements that are used to calibrate the secondary yield parameter δ_m of a-Si:H and AlO_x for AMCP modeling. Measurements done with the same flux (see table 7.1) are illustrated with the same line style. The gain data are displayed in logarithmic scale in (b).	101
7.4	AMCP gain dependence on the applied electric field (a), displayed with logarithmic scale in (b)	102
7.5	(a) Gain calculated with the AMCP single channel model before and after calibration of the maximum secondary yield at normal incidence δ_m of a-Si:H for all measured aspect ratios at the maximum electric field they were measured respectively. (b) Gain depending on the bias voltage calculated for AlO_x before and after calibration and compared to the experimental values.	102
7.6	Sensitivity of AMCP gain and rise time for an AMCP sample with aspect ratio 13.6 and expected gain of about 100 on the secondary yield curve shaping parameters s and k shown in (a) and (b), and on the maximum secondary yield δ_m and the additional inelastic backscattering probability IBS shown in (c) and (d).	104
7.7	Results for an AMCP with aspect ratio 30 and without an additional coating. . .	106
7.8	a) Current signals for an AMCP with aspect ratio 30 and without an additional coating calculated for 1000 events. One event is one incident electron at the top of the channel according to the incident angle of 30° , see figure 7.1. b) Definition of the current rise time, amplitude and threshold timing for each current pulse. c) Distribution of the current rise times. d) Current amplitude distribution. e) Timing distribution for a constant threshold. The timing jitter is 5.8 ps. f) The timing jitter is reduced to 2.7 ps, when a constant fraction discriminator is used.	107
7.9	Results for an AMCP with aspect ratio 30 with no additional coating inside the channel and a coating on top of the channel with an average SEY of 5.	108

List of Figures

7.10	Variation of the average gain and rise time with the incident angle of the first electron and thereby the range of the impact height (see figure 7.1) for AMCP channels with a length of $60\mu\text{m}$ and diameters between $2\mu\text{m}$ and $4\mu\text{m}$. The standard variation of the gain varies in the same manner as the gain. Variations in the gain are not due to the incident angle, but due to the Poisson distribution of the secondary electron emission. The rise time decreases for lower incident angles, as electrons travel a smaller part of the channel.	110
7.11	Overview of expected gain and rise time for AMCPs with a channel length of $60\mu\text{m}$ for different channel diameters and a bias voltage between 200 V and 600 V. 600 V correspond to half of the maximum electric field a-Si:H can sustain. . . .	111
7.12	Expected gain and rise time when miniaturizing AMCPs. The results are shown for the maximum electric field of $2 \cdot 10^7 \text{ V/m}$. The channel length was varied between $10\mu\text{m}$ - $30\mu\text{m}$ and the diameter was varied between $0.5\mu\text{m}$ - $1\mu\text{m}$. . .	112
7.13	Limits of reducing the diameter for high gain in AMCPs. (a) Linear secondary yield fitted to AMCP gain measurements with different aspect ratios (ARs) result in slightly different curves. Overall, diameters below $1\mu\text{m}$ result in a rapid decrease in gain. (b) Assuming an upper limit for the electric field, an increase in channel length leads to an increase of the expected gain without changing the ideal diameter.	113
8.1	Single channel model geometry with the cylindrical channel and a photocathode above the channel entrance. (a) The blue parts represent air (vacuum). (b) Bias voltage is set at the blue layers. From top to bottom the layers represent the photocathode, the AMCP top electrode and the AMCP bottom electrode.	116
8.2	The electric field distribution is shown for an AMCP channel bias of -500 V and a photocathode bias of -520 V, to take into account the reduced distance here with respect to the experiments.	116
8.3	Results of the single channel FEM model.	117
8.4	Distance parameters of funnels that were varied in this study of the electric field distribution.	119
8.5	Electric field lines (red) and electric potential lines (blue) simulated in 2D for AMCP channels with different funnel widths in (a) and (c), and different funnel depths in (b) and (c), while all other parameters are constant.	119
8.6	Electric field lines (red) and electric potential lines (blue) simulated in 2D for AMCP channels with funnel opening. From (a) to (d) we show different funnel shapes, keeping the same funnel depth and funnel opening for all examples . .	120
8.7	(a) Electric field distribution in the AMCP assembly with a photocathode bias of -1000 V and a channel bias of -500 V. (b) Particle trajectories upon one event, the emission of one electron from the photocathode. The unit of the colorbar is eV.	121
8.8	Results of the FEM model for funnel shaped channels.	122

List of Tables

6.1	Material constants and normalization factor used to calculate the secondary electron emission energy spectra in figure 6.6 and the resulting most probable emission energy (MPE) of the distribution.	70
6.2	Most probable emission energy of secondary electrons and the average energy of secondary electrons for the measured a-Si:H and AlO_x surfaces	71
6.3	Derived fit constants for the relative elastic (BS) and inelastic (IBS) backscattering probabilities of a-Si:H and AlO_x	76
6.4	Fit parameter values for the elastic backscattering yield and the secondary emission yield of a-Si:H, AlO_x and MgO. The inelastic backscattering yield was approximated to be 0.2 for incident energies above 50 eV. Fit* values were fitted to the experimental AMCP gain. The values for MgO were fitted to the secondary yield measured by [Jokela 2012] and the angular dependence simulated by [Ivanov 2018]. For conventional MCPs the values ** were derived by [Kruschwitz 2011] and those marked *** were derived by [Ivanov 2018].	93
7.1	Dimensions of all measured AMCPs and the flux used for gain measurements. * Samples of these dimensions have been fabricated with an AlO_x coating as well and measured with the same flux.	101

1 Introduction

Humans have tried to explain the world around them since they exist. Advances in instrumentation have made it possible to physically explain many phenomena happening not only in space, but also in the human body and, on a microscopic scale, in cells as well as in atoms. Some processes release characteristic radiation, which can be detected and information collected. In other cases, we use the interaction of radiation with matter to find answers. In medicine and biology for example, we collect a great deal of information from the interaction of radiation with tissue. Radiation detectors are not only used for fundamental research, but also for diagnostics in medicine. By improving the detector timing, the resolution of medical scans can be improved, which can be a huge relief for patients, as they need to spend less time in a scanner and the injected radiation dose can be reduced. And by improving the fabrication processes, we can make medical equipment more accessible.

1.1 Motivation and objective of this work

A radiation detector transforms information gathered from the surrounding into an electronic signal. Usually the measured quantity needs to overcome a certain threshold in order to be detected. The resolution of a detected signal can be increased either by increasing the collection time, which only works for stationary systems, or by amplifying the incoming flux. The minimal detectable signal with modern electronics is a number of several hundreds of electrons. In order to detect processes that release a very small number of particles, down to a single photon, an amplification scheme needs to be used. In microchannel plate (MCP) detectors an incident photon can release an electron and subsequently a multiplication process happens to produce this huge number of electrons from only one incident electron. The multiplication of that electron is confined to one channel with a typical diameter of few micrometers, retaining a spatial resolution that no other detector can easily provide. With additional benefits through on-chip integration, amorphous silicon based microchannel plates (AMCPs) could pave the way for new applications that the transient behavior of conventional MCPs does not allow for. Among others, AMCPs could represent an alternative to silicon photomultipliers in modern time-of-flight positron emission tomography (PET) scanners,

where a higher photon count rate, very high detection speed and spatial resolution are vital in order to lower the radiation dose on patients, while creating highly detailed tomographic scans [Vandenberghe 2016] [Iagaru 2015].

The objective of this work was to determine if amorphous silicon based microchannel plates (AMCPs) can be competitive in terms of multiplication gain to present a viable alternative to existing single photon detector technologies. The gain of AMCPs had formerly been limited to about 100, due to the limits in the minimal channel diameter that could be fabricated. As a first step, ways to improve the gain had to be identified and the limits of the AMCP gain had to be explored. The goal was to fabricate AMCPs with a high multiplication gain, so that the transient response of AMCPs in a low flux regime could be tested. Even more crucial was to understand electron multiplication in AMCPs, to analyze their transient behavior and the effect of various geometries on AMCP performance. Additionally, we needed to develop a tool to predict AMCP performance for the various shapes that can be realized with state-of-the-art cleanroom technologies.

1.2 Structure of the thesis

We introduce the topic and the main objectives of this work in chapter 1 of the thesis. In chapter 2, we then review the state-of-the art of microchannel plates and existing single photon detectors. We explain the different technologies and the challenges that still need to be overcome.

In chapter 3 we describe amorphous silicon based microchannel plates and explain why AMCPs present an interesting alternative to the existing technologies. We also present the state-of-the-art of AMCPs at the beginning of the thesis.

Chapter 4 is a detailed account of high aspect ratio AMCPs that were developed for the work of this thesis. We present their fabrication and a newly designed characterization setup for transient measurements of AMCPs.

We introduce electron emission processes, which are the core of AMCP detector operations, in chapter 5. We address the theory of secondary electron emission, probabilistic modeling of electron emission and secondary yield modeling. Finally, we present both main approaches for MCP models: transmission line models and Monte-Carlo models.

In order to develop an AMCP model, we characterized the electron emission properties of the materials used for AMCPs. In chapter 6, we present electron emission measurements and simulations of those materials, namely a-Si:H and atomic layer deposited AlO_x and MgO . Consequently, we deduced the parametrization of the electron emission in AMCPs. The results obtained in this chapter, served as a basis for Monte-Carlo simulations of electron trajectories in AMCPs, which were implemented in a cinematic model. The cinematic model is presented in chapter 7 along with an analytic AMCPs model for very high aspect ratios.

Furthermore, a Monte-Carlo model based on the finite element method was developed, which allows us to extend the simulations of electron trajectories beyond the classical cylinder shape. The model is introduced in chapter 8. Here, we present results of AMCP simulations for

geometries funnel shaped channels and analyze the effect of geometric variations on the output signal.

In the last chapter, we conclude the results of this work and elaborate future improvements of detection schemes with AMCPs.

1.3 Contribution to the research field

We uncovered the potential of AMCPs as single photon detectors in this thesis in two ways: First, by fabricating high aspect ratio AMCPs and second, by developing a modeling tool for AMCPs to accurately predict their expected gain and timing. In a first step, we identified ways to improve the fabrication by the means of state-of-the-art clean room technology. The aspect ratio of state-of-the-art AMCPs has been improved from 13 to 23 and the potential of aspect ratios up to 30-40 has been established. The expected gain at these aspect ratios is in the range of 10^3 and thus detectable with modern electronics. With additional highly emissive coatings, AMCPs now present a real alternative to conventional MCPs. The AMCP design was adapted for high frequency measurements, which now enables measurements in the transient regime. The electron emission parameters were investigated in depth. On the basis of these parameters, we implemented a probabilistic electron emission model into a finite element method tool. This brings together the possibility to generate any geometries and easily calculate the potential distribution with the Monte-Carlo model needed to calculate the response of AMCPs to an incident electron. On the basis of the model, AMCP geometries can now be optimized for the required performance in terms of gain, time resolution, active area and spatial resolution.

2 Microchannel plate and single photon detectors

In this chapter we introduce microchannel plates (MCPs), their working principle and applications. We address current developments in the field of MCPs, as various aspects from manufacturing technology to the electrical readout have been continuously improved in recent years. The remaining shortcomings of the technology are discussed as well. We then provide a brief overview of the state-of-the-art in single photon detectors.

2.1 Microchannel plate

Microchannel plates (MCPs) are an invention from the 1970s [Ladislav Wiza 1979] and are amongst the fastest radiation detectors, with a time constant in the sub nanosecond regime. A MCP converts an incoming particle, which can be an electron, ion, atom, neutron or a photon, into an electrical pulse. Figure 2.1 (a) shows an image of MCPs in various magnifications taken from [Mazuritskiy 2019] and (b) shows the working principle of MCPs, namely the electron multiplication in an MCP channel.

The active part of a microchannel plate that multiplies electrons are the channel walls. When ionizing radiation hits the surface of a channel, an electron avalanche is created by secondary electrons emitted from the channel surface in the following way: The secondary electrons are accelerated through vacuum to the anodes by a high electric field in the order of 10^7 V/m. Each of the secondary electrons creates additional secondary electrons each time it hits the channel walls. The initial electron number is multiplied by a factor of 10^3 - 10^4 in an MCP and by around 10^7 in modern microchannel plate assemblies, consisting of 2-3 stacked MCPs. The avalanche process happens on a time scale of picoseconds, giving the very fast time constant of MCPs. When an avalanche occurs in a channel, electrons are drawn from the bulk. The time it takes for the material to recover to its initial state is called charge replenishment time. This is the needed waiting time between the detection of two consecutive events. Incoming electrons, ions, UV radiation, X-rays and γ -rays can trigger an avalanche while photons in the visible range are usually detected using a photocathode mounted in front of the MCP with converts the incoming photons into electrons. A typical MCP assembly for photon detection

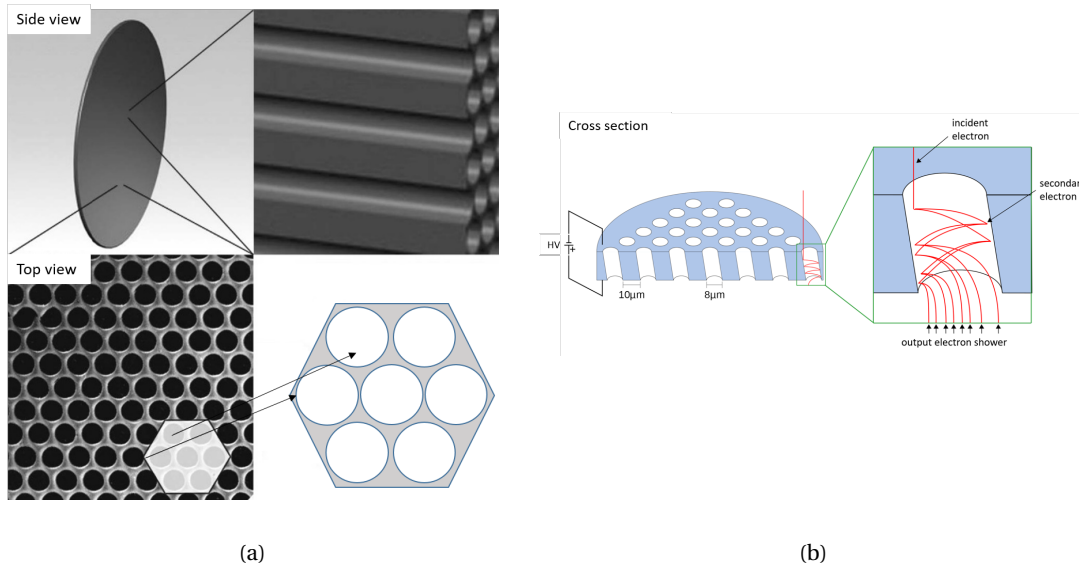


Figure 2.1 – (a) Image of a microchannel plate in various magnifications [Mazuritskiy 2019] and (b) schematic of electron multiplication mechanism in one of the channels.

is shown in figure 2.2b.

Channels in conventional MCPs are slightly tilted at an angle of about 7° with respect to the MCP surface normal. For one part, this assures that radiation impinges on the channel wall right at the channel entrance. Second, this minimizes ion feedback which is due to the following mechanism. The electron avalanche can ionize molecules adsorbed on the channel walls. Under the electrical field, the ions can then be accelerated towards the entrance of the MCP and the photocathode. This may produce a large electron avalanche from secondary electrons generated by accelerated ions. Additionally, this degrades the photocathode. In assemblies, MCPs are stacked as Chevron or z-stacks in order to minimize ion feedback. Bent channels are also used for that purpose. For a high collection efficiency MCPs are fabricated with funnel shaped openings reaching open area ratios of up to 90%.

Conventional MCPs are fabricated from Pb doped glass fibers by a cumbersome glass fiber drawing process shown in figure 2.2a. Lead glass assures the optimal compromise between conductivity and a moderate secondary emission yield. Due to the glass fiber drawing and core etching fabrication process, conventional Pb doped glass MCPs' area is limited to few cm^2 and their aspect ratio is limited to about 100:1.

The desire to develop the properties of MCPs stems from the need to track radiation with at the same time accurate timing and spatial precision. This is crucial in many fields of applications. To name a few examples, MCPs are used in biotechnology for time-resolved fluorescence [Michalet 2011], in astrophysics [Fraser 2001], in medical imaging for time-of-flight positron emission tomography (PET) and neutron radiography, and in high-energy physics for time-of-flight experiments [Va'vra 2008] and Cherenkov detectors [Siegmond 2011]. As a

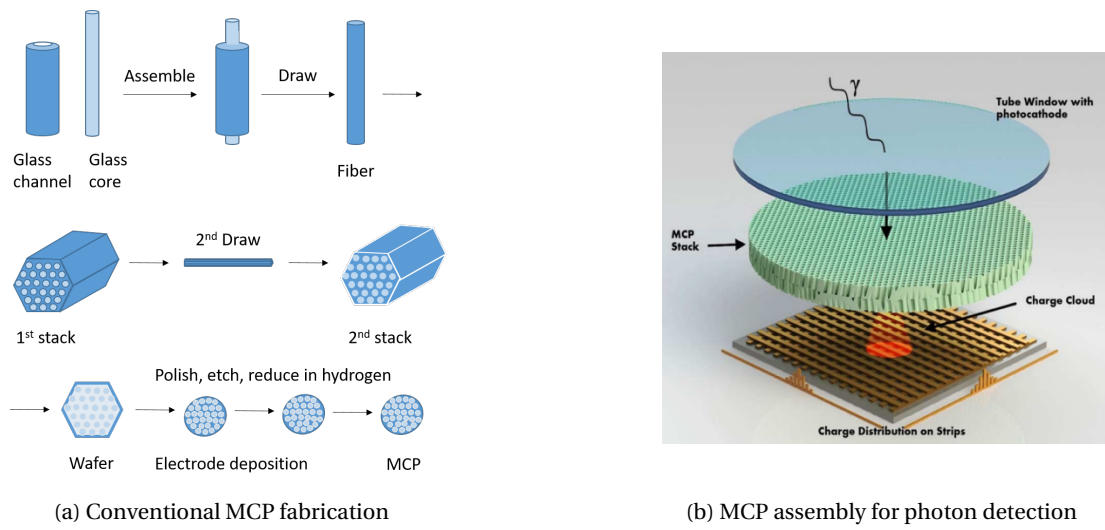


Figure 2.2 – (a) Various stages of the MCP fabrication process are shown. Glass fibers are assembled, drawn and etched in several steps, (b) Schematic drawing of a typical microchannel plate assembly. An electron from the photocathode is multiplied in the MCPs and creates a charge cloud that can be detected by the electronics. Image taken from [Siegmond 2013].

consequence, important research activities are pursued in time-resolved detection using MCPs [Lapington 2009] [Tremis 2020a].

One example for the application of MCPs is time-of-flight photoemission spectroscopy with femtosecond lasers [Anacker 1991], [Arrell 2014]. The energy of emitted electrons from ultra-fast electronic and vibrational excitations in molecules help to get a fundamental understanding of biochemical processes. The kinetic energy of photoelectrons is measured by their time of flight through an electric field. Thus, the arrival time of the electron has to be detected as accurately as technologically feasible. Fast timing resolution of MCPs make this possible. Customizations of microchannel plates have been realized for different radiation types. For the detection of X-rays, geometries of square channel assemblies have been studied [Price 2002]. Microsphere plates [Tremis 1996b], [Ghiringhelli 1999] have been proposed as an alternative to microchannel plates, enabling working pressures as high as 0.1 mbar. The drawback is an efficiency loss compared to MCPs.

The most important advantage of MCPs over other recent developments in detectors like silicon photomultipliers (SiPM), or single photon avalanche diodes (SPAD) lies in their high spatial resolution and low dark count rate which, depending on spontaneous emission of the photocathode influenced by the work function and temperature, can be below 1 Hz/cm² [Tremis 1996a] or between 10 Hz/cm² and 10 kHz/cm² [Lehmann 2017]. Additionally, there is no cross talk in MCPs. Exceptions to that, where cross talk has been observed were experiments with high count rates or when MCPs were used to detect hard X-rays. Minimal timing jitter of 10-20 ps of the electronic signal can be achieved with minimal MCP channel diameters and further improved with ultra flat MCP surfaces, where the thickness variation is below 10 μm. This is particularly important for applications measuring the time-of-flight. Addition-

ally, the electron detection efficiency of MCPs can be increased up to 100% by accelerating all secondary electrons from the top surface towards the interior of MCP channels. The detection efficiency for photons then solely depends on the conversion to photoelectrons [Blase 2018]. Since the advance of atomic layer depositions (ALD) in the recent years, novel MCPs are fabricated where the bulk material is independent of the MCP functionality [Beaulieu 2009]. Boron silicate glass is used to fabricate large area MCPs [O'Mahony 2016]. To functionalize the MCPs, ALD layers are added on the channel surface. The outer layer is highly secondary emissive, and the first deposited layer is usually a conductive material to assure charge replenishment for secondary emission. These novel MCPs reach areas of up to $20 \times 20 \text{ cm}^2$. Other alternative bulk materials including Si, aluminum oxide or polymer-based MCPs did not prove to be successful.

Extensive developments in microelectronics allowed to improve the MCP readout considerably. Nowadays, MCP detection system capabilities extend to GHz rates, they can detect multiple simultaneous events and have a spatial resolution in the range of the channel diameters of about $10 \text{ }\mu\text{m}$ and a timing resolution of tens of ps. An overview of state-of-the-art MCP performance depending on the chosen readout circuit is given in [Tremsin 2020b]. Novel low-noise amplifiers operate at electron charge input levels as low as 10^4 , and since the charge replenishment of a single pore depends on the gain provided, this leads to a reduced charge replenishment time and thus to higher local count rates in MCPs. Furthermore, this leads to a longer MCP lifetime, since the lifetime is proportional to the extracted charge per given MCP area.

Following the immense progress that has been made in recent years, the three major drawbacks of MCPs started to be addressed, namely their limited count rate capability [Gershman 2018], the limited lifetime of an MCP assembly due to ion feedback [Lehmann 2017] and their cumbersome manufacturing process [Popecki 2016]. Nevertheless, the fabrication of new types of borosilicate MCPs is still based on glass fiber drawing, which is a not easily scalable process. Batches of fibers are fused together to fabricate large area structures, which leaves imperfections in the pore arrangement. Additionally, the bulk properties of borosilicate glass are fixed, while a bulk material with an optimized conductivity might be needed to further improve the count rate capability. Furthermore, the traditional MCP setup with a vacuum gap between the MCP channel exit and the electronic readout leads to widening of the exiting charge cloud. This results in a loss of spatial resolution. The vacuum gap also leaves the charge cloud sensitive to influences such as magnetic fields, with resulting deflections of the electron trajectories further decreasing the spatial resolution. This can be significant for the development of novel medical imaging applications, for example for the integration of MR (magnetic resonance) and PET (positron emission tomography) scanners.

2.2 Single photon detectors

Detectors, in general, convert radiation into a detectable and quantifiable electronic signal. On the quest for single photon detection, their ability to produce a minimum number of

10^4 - 10^5 electrons from one event is crucial. At the same time, they should not amplify noise. The ideal detector would have a 100% conversion efficiency, no dark count rate, zero dead time, a spatial resolution in the order of nm and no timing jitter. Many different approaches for detector systems exist, all of them come with their strengths to approach one or more of these goals, failing in others. Photon interaction with matter produces free electrons if the photon energy is higher than the work function of a given surface. The interaction can be divided into three main contributing effects. First, the photoelectric effect used in photocathodes where the energy of the photon is ionizing an atom and releasing an electron. The second effect is the Compton effect, which is inelastic scattering of light. The energy lost by the photon frees an electron. The third effect is pair production, where an electron and a positron are created. Visible light photons, even if not energetic enough to create free electrons, also transfer their energy to electrons. They shift electrons to higher electronic states. In the case of semiconductors or materials with a partially empty band structure, the excited electrons can then contribute to an electric current.

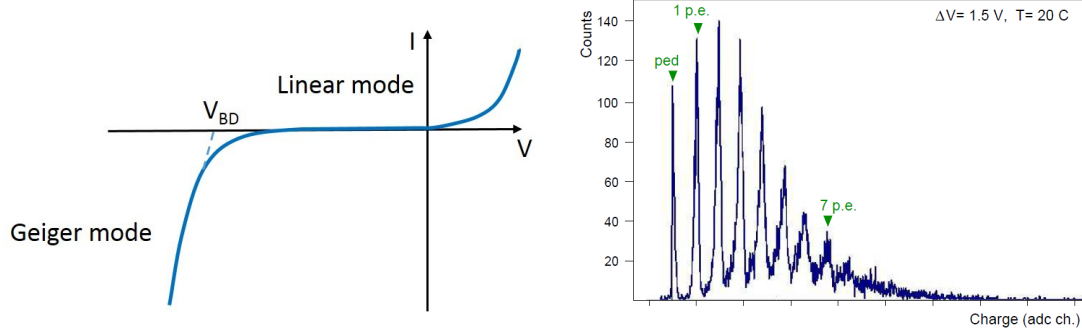
Most detectors are semiconductor devices that are sensitive to visible light. Often scintillators are used to convert high-energy radiation to visible light. For a high gain of 10^5 - 10^6 , avalanche photo diodes (APDs) are operated above their breakdown voltage in Geiger mode, see figure 2.3a. In this operation mode APDs become conductive and the avalanche has to be stopped by a quenching resistor.

Silicon photomultipliers (SiPMs) are an array of APDs working in Geiger mode. They are used for photon counting and enable the identification of single events. Their drawbacks are a high dark count rate, cross-talk between pixels of the detector and afterpulses, as avalanches can easily be triggered. Nevertheless, all of these effects can be identified in the spectra, and separated. The pixelated architecture of SiPMs does not lead to a spatially resolved detection, it makes it possible though to count the number of photons on the total area of a SiPM.

One example for an experimentally measured spectrum is shown in figure 2.3b. In SiPMs, the measured signal is always a convolution of the Poisson distribution of the measured number of photons with dark count, cross talk, afterpulses and electronic noise. This kind of multi-pixel photon counters have been extensively characterized [Vacheret 2011] and are further developed for low level light detection. As they are insensitive to magnetic fields, SiPMs are one of the competitive technologies that have been applied in the first PET time-of-flight (TOF) and combined PET/MR scanners.

A similar approach for single photon detection integrates avalanche photodiode arrays with their electronics directly on the detecting surface [Burri 2014] and allows for a spatially resolved detection scheme. This comes at the price of lowering the active area to a maximum of 30%.

A newly developed stack of transmission dynodes, so-called tynodes [van der Graaf 2017], can be integrated on top of a CMOS readout for fast time resolution and single photon detection. Tynodes have been tested and integrated on readout chips measuring time of arrival of photons (Timepix, developed at the European Laboratory for Particle Physics CERN). The tynode stack has a working principle similar to microchannel plates and amplifies electrons in



(a) Operation principle of APDs

(b) Single photon counting

Figure 2.3 – (a) Operation regimes for single photon photodiode detectors, linear mode for low reverse bias, avalanche mode biased around the breakdown voltage V_{BD} and Geiger mode with bias higher than the breakdown voltage. (b) Photon counting spectrum recorded with a SiPM [Vacheret 2011]. Each peak represents a number of photons, starting with 0 at the pedestal peak.

multiple stages. Both technologies, MCPs and integrated tynodes, are promising approaches for single photon counting while providing a high active area ratio, high spatial resolution and fast timing.

There exist many other innovative approaches to single photon counting. For example superconducting nanowire single-photon detectors [Gol'tsman 2001]. These detectors exhibit an excellent timing resolution as well, but the active area is very limited and typical detection efficiencies merely reach 20%. Additionally, this kind of detectors need a cryostatic environment. It is evident that new technologies need to catch up on the already well-understood photo-multipliers. Nevertheless, there is room for new inventions as some of the challenges, like high spatial resolution, short dead time between consecutive events and a high conversion efficiency for single photon detection are far from being overcome.

3 Amorphous silicon based microchannel plate

With their high spatial resolution and a short signal transit time amorphous silicon based microchannel plates (AMCPs) could overcome a number of challenges that arise for the detection of single photons. In this chapter we present AMCPs: First, the base material, amorphous silicon and its fabrication is introduced, then we explain the fabrication principle of micro channels via deep reactive ion etching. Finally, we review the state-of-the-art of amorphous silicon based microchannel plates as it was at the beginning of this thesis (3rd generation). AMCPs with aspect ratios up to 12.5 had been fabricated, showing gains up to 80 with a highly emissive AlO_x coating.

3.1 Why 'amorphous silicon based' MCPs?

Amorphous silicon based microchannel plates present an exciting new approach for MCPs in terms of their electronic properties and fabrication possibilities. AMCPs are fabricated by plasma enhanced chemical vapor deposition (PECVD) of a thick layer of hydrogenated amorphous silicon (a-Si:H) of up to $100\text{ }\mu\text{m}$ and deep reactive ion etching (DRIE) of the micro channels. While amorphous Si is widely used as thin film for displays, position sensors, medical imaging devices and solar cells [Street 2000], a thick amorphous layer of around $100\text{ }\mu\text{m}$ is a novelty and a technological challenge. With its semi-insulating nature and radiation hardness, a-Si:H has very useful properties that could help to overcome today's remaining MCP bottlenecks.

During the deposition of the a-Si:H layer, the layer resistivity can easily be varied by doping, and the vertical resistivity and thereby the electric field of the AMCP can be optimized. Shikahliev et al. [Shikahliev 1999] pointed out that saturation in MCPs could be alleviated or even eliminated by a nonlinear dynode resistance. With a change in resistivity along the channel, the electric field could be shaped in a way that counteracts saturation. The intrinsic dark conductivity σ of a-Si:H is 10^{-10} - $10^{-12}\text{ }\Omega^{-1}\text{cm}^{-1}$, which can be extended to $\sigma = 10^{-2}\text{ }\Omega^{-1}\text{cm}^{-1}$ by doping. Depending on the atomic composition the conductivity of silicate glass can be in the range of $\sigma = 10^{-9}$ - $10^{-3}\text{ }\Omega^{-1}\text{cm}^{-1}$ [Braunger 2012]. The conductivity of conventional MCPs depends on Pb doping of the silica glass. Hydrogen reduction is used to increase the conduc-

tivity. The typical sheet resistance at the surface of a treated MCP channel is 10^7 - 10^{13} Ω/sq [Gys 2015]. In modern borosilicate glass MCPs atomic layer deposited conductive layers are applied directly on the channel surface and their resistivity can be chosen according to the experimental requirements [Ertley 2017]. None of these processes though can access the MCP bulk material or form a well controlled nonlinear resistance along the length of the channels. Additionally, variations in the shape of AMCP microchannels have no limitations other than the maximum aspect ratio of DRIE. As a result of constant improvements in etching processes, this aspect ratio keeps increasing. The maximum area of patterning the channels with lithography is constantly increasing as well, nowadays the area is in the range of m^2 [Bläsi 2016]. The concept of AMCPs was first investigated and patented by Jarron et al. in 2014 [Jarron 2014] and developed to provide the proof of concept of the technology by Franco [Franco 2012]. The thick layer of amorphous silicon can be deposited directly on the ASIC's (Application Specific Integrated Circuit) readout. Integration of a sensing layer on top of the electronic readout has been successfully used for vision sensors [Schneider 1999]. Following that concept, the vertical integration of thin-film amorphous Si on top of CMOS readout electronics has been explored for the application as radiation detectors [Anelli 2004], [Wyrsh 2005]. The same integration scheme could be applied for AMCPs.

3.2 Hydrogenated Amorphous Silicon

The main feature distinguishing amorphous silicon from its crystalline form is the missing long-range order in the network of Si atoms [Brodsky 1970], [Street 1991]. In crystalline Si every atom is bound to four other atoms and forms a diamond cubic crystal structure. Whereas, in amorphous Si, while preserving the coordination number of four, the bond lengths and bond angles vary. Amorphous Si alone would be very defective. By introducing hydrogen to form a-Si:H, intrinsic defects, such as dangling bonds, are passivated and it forms a material with very useful optoelectronic properties. In fact, the flexible amorphous network allows for an easy incorporation of H atoms. In the following, the term 'amorphous silicon' also stands for the hydrogenated form, a-Si:H.

Amorphous silicon has been deposited from SiH_4 in a chemical vapor deposition since the 1960s [Sterling 1965], [Chittik 1969]. This process has been developed since to deposit a-Si:H thin films with excellent properties for thin-film transistors (TFTs), solar cells and detectors. The most widely used process to fabricate a-Si:H layers is to use a mixture of SiH_4 and H_2 gases in a plasma-enhanced chemical vapor deposition (PECVD). A radio frequency (RF) discharge between two capacitive coupled electrodes generates a plasma from the gas mixture in a vacuum chamber, see figure 3.1. The plasma precursors, dissociated SiH_4 and H_2 molecules, react at the surface of the substrate and form a film. The high temperature of excited particles in a plasma allows keeping the substrate and reaction chamber at relatively low temperatures around 200°C . The plasma frequency, substrate temperature, gas mixture, gas flow and chamber pressure determine the film composition and quality and have to be finely tuned.

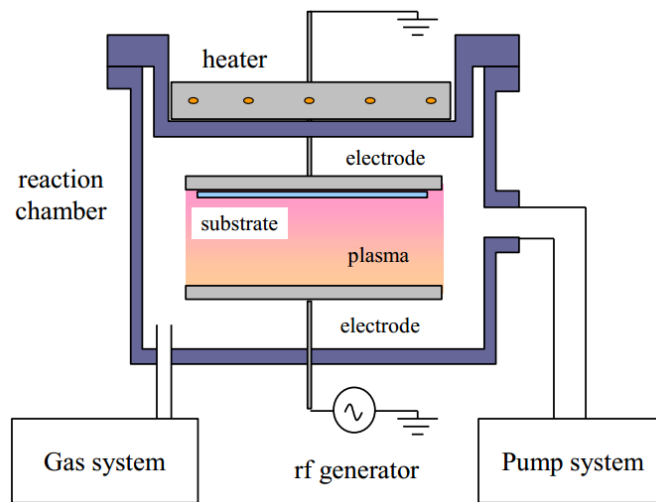


Figure 3.1 – Reaction chamber for plasma enhanced chemical vapor deposition, PECVD. Between the two electrodes a plasma is ignited, which is driven by the radio frequency. Dissociated molecules from the plasma react at the surface of the substrate and grow films.

Semiconductor theory is built on the premise of a periodic atomic network, thus amorphous semiconductors need to be described by their own theory. Albeit that, band diagrams are used to describe their electronic structure. In fact, starting from crystalline silicon, relaxing the bands in the band diagram and adding intermediate states can partly explain the band diagram of amorphous Si, because of the equivalent short-range order. From its band diagram and the fact that amorphous Si is metastable, some effects contributing to its electrical conductivity can be explained. Figure 3.2 shows a schematic overview of the band structure of amorphous Si and the related charge transport processes.

The band structure of a-Si:H is similar to that of a crystalline material, with the difference that the disorder creates a tail of localized band tail states. Additionally, there are localized defect states that are energetically located in the middle of the band gap. Defects in the amorphous material are created by deviations from the four-fold coordination of Si atoms. The defect states located around the Fermi energy contribute to the conduction mechanism at low temperature via variable range hopping as illustrated in figure 3.2 ①. At higher temperature charge hopping with the nearest neighbor occurs in localized band tail states ②. The main charge transport takes place in extended states in the conduction band. As localized bandtail states are located energetically close to them, multiple trapping in the band tail states influence the conductivity, and result in a dispersive charge transport ③.

At the surface of amorphous silicon, the network of four-coordinated Si atoms is disrupted creating additional dangling bonds and band tail states. Exposing the surface to ambient air leads to an oxidation of the surface. Gas molecules like oxygen and water vapor from air can be adsorbed [Tanielian 1982]. The additional atoms create a positive charge and bending of the bands. The conductivity can locally, in the vicinity of the surface, increase several orders of magnitude, especially in high quality material.

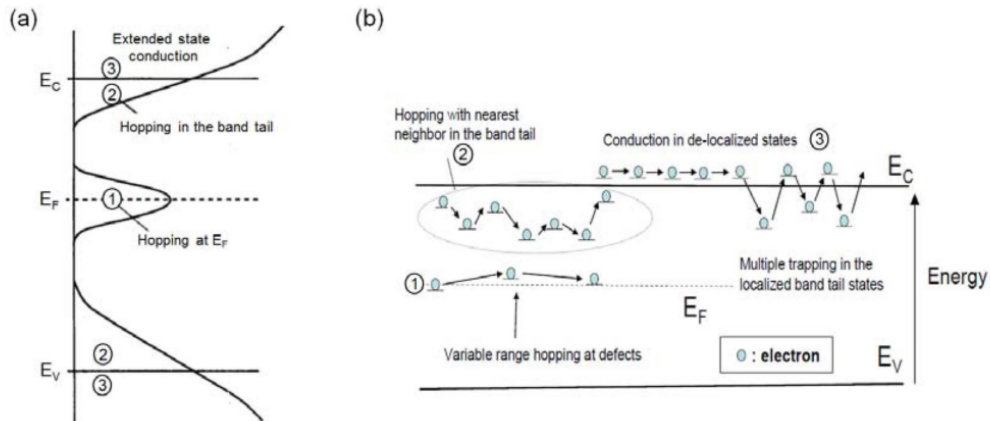


Figure 3.2 – How localized states influence the charge transport in a-Si:H: (a) Position of the three contributing transport mechanisms and representation of their density of states, (b) Dynamics of charge transport in their respective energetic levels. ① Defect states around E_F contribute to charge transport at low temperature. ② Hindered transport via hopping with nearest neighbor in the band tail states at higher temperatures and ③ dispersive charge transport in conduction band through trapping in localizes band tail states. Drawing taken from [Despeisse 2006].

Doping with phosphorous or boron in a-Si:H can modify the conductivity σ on a wide range, from $\sigma = 10^{-12} \Omega^{-1} \text{ cm}^{-1}$ to $\sigma = 10^{-2} \Omega^{-1} \text{ cm}^{-1}$ at room temperature. Actually, intrinsic a-Si:H is slightly n-doped due to the incorporation of impurities, especially oxygen. Slightly p-doped a-Si:H exhibits the lowest conductivity.

It has been shown that a-Si:H is a radiation hard material [Wyrsh 2006]. Annealing a-Si:H after irradiation with a high electron flux can completely recover the material properties [Schneider 1987], [Scholz 1993]. This can be explained by the fact that electron irradiation creates metastable defects that can be annealed out for a full recovery.

3.3 Deep Reactive Ion Etching

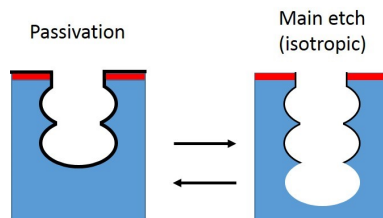


Figure 3.3 – Illustration of deep reactive ion etching with a standard Bosch process. The cyclic process consists of two alternating steps, passivation of the sidewalls and the main isotropic etching. Deep isotropic etching creates a scalloping sidewall structure.

Standard etching processes are usually isotropic. In order to realize a deep penetration depth

3.4. State-of-the-art amorphous silicon based microchannel plate

in the material for high aspect ratio structures, an anisotropic etching process has to be used. To accomplish this, dry etching with periodically alternating gases has been developed, the Bosch process [Laermer 1996], [Laermer 2010]. The Bosch process is a repeatedly executed two-step process. The first step is etching, typically with SF_6 , the second step is side wall passivation. For the second step, a Teflon®-like fluorocarbon polymer film is deposited on the silicon surface from C_4F_8 precursors. The isotropic etch step drives the passivation deeper in trenches of the sidewalls, as it removes the fluorocarbon polymer from the bottom surface. This way the passivation on the vertical structures is maintained, while channels can be etched deeper. DRIE (Deep Reactive Ion Etching) is a balancing act between etching and passivation with the polymer species. In the standard process, trenches create a scalloping structure of the sidewalls. A schematic representation is shown in figure 3.3. Alternative Bosch processes have been developed for a steep sidewall with isotropic etching [Gao 2014]. Microchannel plates have been fabricated from thin Si wafers using DRIE [Beetz 1999]. Although DRIE is very well suited for the fabrication, other issues like the high conductivity of Si and engineering problems prevented this technology from being further pursued.

3.4 State-of-the-art amorphous silicon based microchannel plate

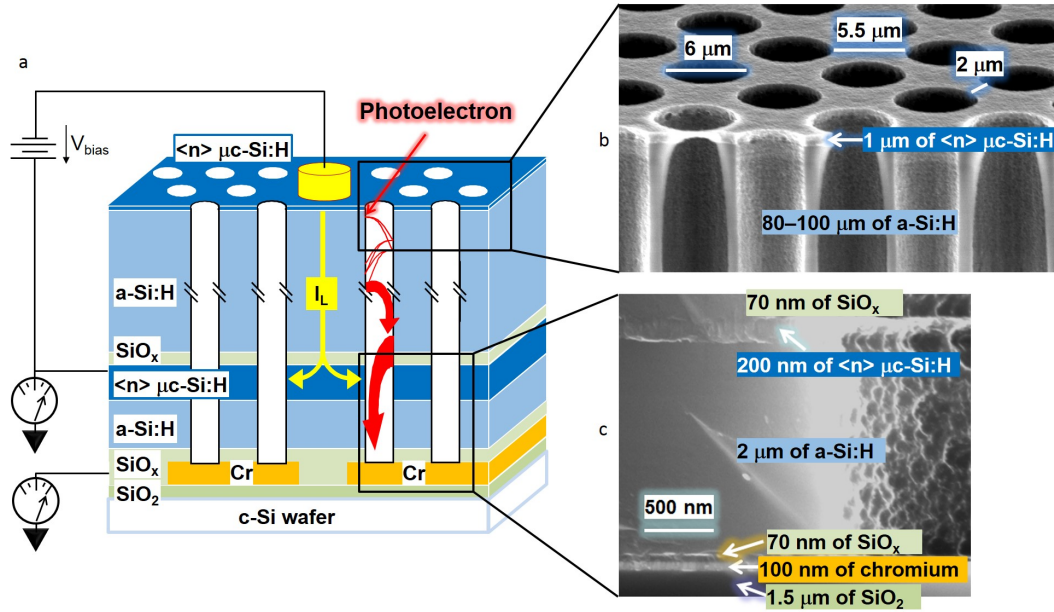


Figure 3.4 – AMCP architecture of 3rd generation devices as developed by [Franco 2014b]. Micro channels in a thick amorphous silicon layer act as electron amplifiers. A decoupling layer separates the multiplication layer from the electronic readout. The leakage current I_L (yellow) is evacuated and the electron cloud signal (red) impinges on the readout pad.

The state-of-the-art at the beginning of this thesis were 3rd generation AMCPs developed by Franco [Franco 2012], [Franco 2014a], [Franco 2014b]. A schematic drawing of the layer structure and SEM images of the microchannels and PECVD layers is shown in figure 3.4. The

3rd generation AMCP consists of a layered structure with a conductive intermediate electrode to evacuate the leakage current and a conductive top electrode to apply the bias voltage. The active layer of the AMCP is the multiplication layer. This multiplication layer consists of about 80-90 μm of amorphous silicon wrapped by the electrodes. The top electrode consists of a 100 nm n-doped $\mu\text{c-Si}$, where the AMCP bias voltage is applied. The grounded electrode beneath the multiplication layer is called intermediate electrode, as it is separating the anode from the multiplication AMCP stack. The intermediate electrode was introduced as a special layer in the 3rd generation of AMCPs to evacuate the leakage current. The decoupling layer (resistive separation layer) between intermediate electrode and anode is similar to the vacuum space between a standard MCP and its readout electronics. The effect of this decoupling layer can be seen in figure 3.5a, where the anode current is reduced compared to the intermediate electrode current by four orders of magnitude. This made it possible to measure the AMCP signal, separating it from much of the background noise originating from the high AMCP bias. The substrate of AMCPs is simulating the surface of an ASIC. For that purpose, a patterned chromium electrode is deposited on an oxidized c-Si wafer. This allows for electrical insulation between the Cr pads that collect the secondary electron cloud at the bottom of the micro channels. All the following layers are then deposited via PECVD. First, a thin SiO_2 layer is deposited to guarantee a good adhesion of the a-Si:H layer to the metal pads. On this, the 2 μm a-Si:H decoupling layer is deposited. The intermediate electrode is created by a 200 nm thick phosphorous doped (n-doped) $\mu\text{c-Si:H}$ layer, with a sheet resistance of about 1 $\text{k}\Omega/\text{sq}$. To contact the intermediate electrode, 50 nm thin Cr contacts are introduced locally outside of the active area. Then, a thin adhesion layer is deposited, prior to the thick amorphous Si layer which is the multiplying part of the AMCP. A SEM image of the layered structure around the decoupling layer is shown in figure 3.4c.

The deposition of thick films of around 90 μm a-Si:H is a technological challenge. Because of its amorphous structure, intrinsic stress accumulates in thick a-Si:H layers. This can lead to delamination of the layers. Because of the high hydrogen content in the material, molecular hydrogen can accumulate and form bubbles and craters in the layer. Even for thin amorphous silicon layers, intrinsic stress has been observed as a function of the hydrogen content [Paduschek 1983]. Additionally, the deposition of such a thick film can take several days. To tackle these challenges, a fast PECVD process for AMCP fabrication on 4" wafers has been developed by Franco [Franco 2014b]. On top of the a-Si:H layer, a n-doped $\mu\text{c-Si:H}$ layer was deposited as top electrode. The top electrode was contacted at one point with a gold pad, to apply the high voltage on the channels. Its sheet resistance was 500 Ω/sq for a 1 μm thick layer. At last, the micro channels were machined using DRIE.

AMCPs were fabricated in a modular configuration with bottom electrode pads of 0.25 mm^2 , 1 mm^2 and 4 mm^2 sizes. Keeping the pad size small lowers the probability of fabrication errors in the respective pads. In order to detect the signal on a bigger surface, one complete AMCP reticle can be connected to form a total active area of 24 mm^2 . On top of these pads, micro channels were etched into the whole layer stack from the top n-doped $\mu\text{c-Si}$ electrode to the bottom Cr pads. This last step of the process was done via deep reactive ion etching (DRIE) at

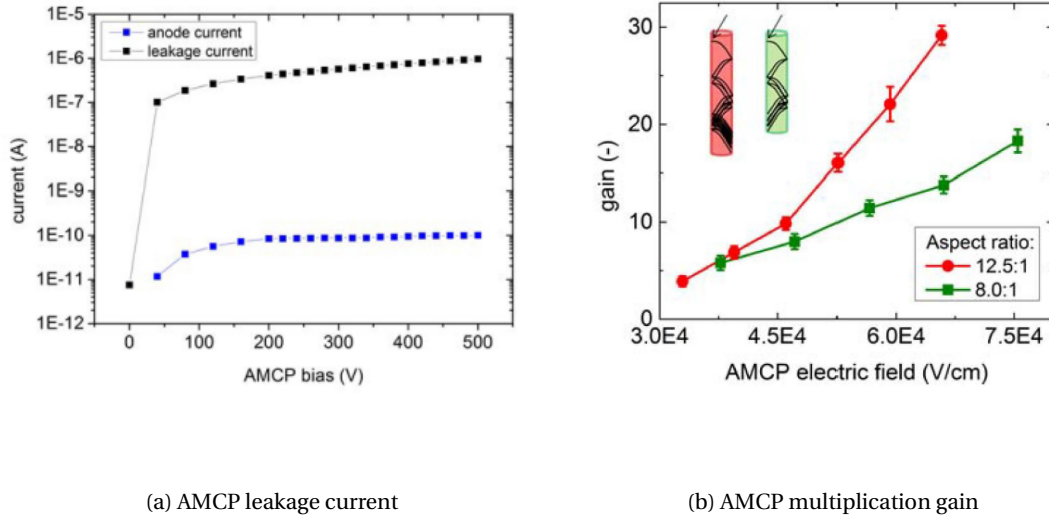


Figure 3.5 – (a) Leakage current measured on intermediate electrode compared to the anode current, (b) gain measurements for AMCPs with different aspect ratios. Reproduced from [Franco 2014a]

the Centre Suisse d'Electronique et de Microtechnique (CSEM). A SEM image of the channels is depicted in figure 3.4 b. Here, the typical channel diameters of the 3rd generation AMCP devices are displayed. The open area ratio for the structure is 0.2, which corresponds to the active area of the AMCP.

This 3rd generation AMCP structure has been characterized electrically and the gain has been measured with respect to the incoming electron flux [Franco 2014a]. The characterization was done with a UV lamp, a chopper and a gold photocathode to convert UV photons into electrons. With the chopper, the incoming electron stream could be synchronized with the readout electronics. With this setup, a gain of up to 30 was measured for an AMCP with aspect ratio 12.5:1 and an applied electric field of up to $7.5 \cdot 10^6$ V/m, see figure 3.5b. On another test structure, AMCP channels have been coated with a secondary electron emissive layer Al_2O_3 . Here a gain of up to 80 has been measured. Taking into account the limited aspect ratios of the 3rd generation AMCPs, the gain values are comparable to the ones of conventional MCPs. In order to reach the gains needed for a reliable detection system, the gain of AMCPs needed (and still needs) to be further increased. As the gain grows significantly with the aspect ratio, one of the main goals of this thesis was to increase the aspect ratio and explore the technological limits of dry reactive ion etching in a-Si:H. In the next chapter, we present the highlights of the fabrication of high aspect ratio AMCPs using an advanced DRIE system.

4 AMCPs with high aspect ratio

In this chapter we present AMCPs with high aspect ratio, the 4th generation of AMCPs, paving the way to AMCPs with higher gain. We illustrate the modified fabrication process with respect to the 3rd generation in its various steps - from the bottom electrode, to multiplication layer and deep reactive ion etching of the channels. The fundamental layer structure of AMCPs has not been modified for this 4th generation with respect to the 3rd generation. Nevertheless, we present the modifications that arose as a result of the fabrication of 4th generation AMCPs on 6" substrates, compared to the former 4" substrates. The use of 6" substrates allowed us to fabricate AMCPs with high aspect ratios via deep reactive ion etching with an advanced DRIE machine. As a result we show the fabricated AMCPs with channel diameters reduced by a factor of 2 and hence increased aspect ratios of up to 23. Finally we present the characterization of 4th generation AMCPs with transient signals in a low photon flux regime.

4.1 Modifications of the AMCP fabrication process for high aspect ratio

Using state-of-the-art deep reactive ion etching (DRIE), we fabricated high aspect ratio amorphous silicon based microchannel plates. Previously, the etching process of the channels had limited the aspect ratio of the 3rd generation AMCPs to a maximum of 13.6. For this 4th generation of AMCPs, channel aspect ratios of up to 23 have been realized. The structure of amorphous Si microchannel plates elaborated by A. Franco [Franco 2014b] serves as a basis for microchannel plates fabricated here. We use the SPTS RapierTM, which is an advanced DRIE system to etch high aspect ratios. Aspect ratios greater than 40 over 3 μm wide features and a fast etch rate over 20 $\mu\text{m}/\text{min}$ can be realized, according to technical reports of the system. Compared to the former process on 4" wafers, the advanced DRIE system requires working on 6" wafers. However this allows for etching of finer micro channels, thus the high aspect ratio.

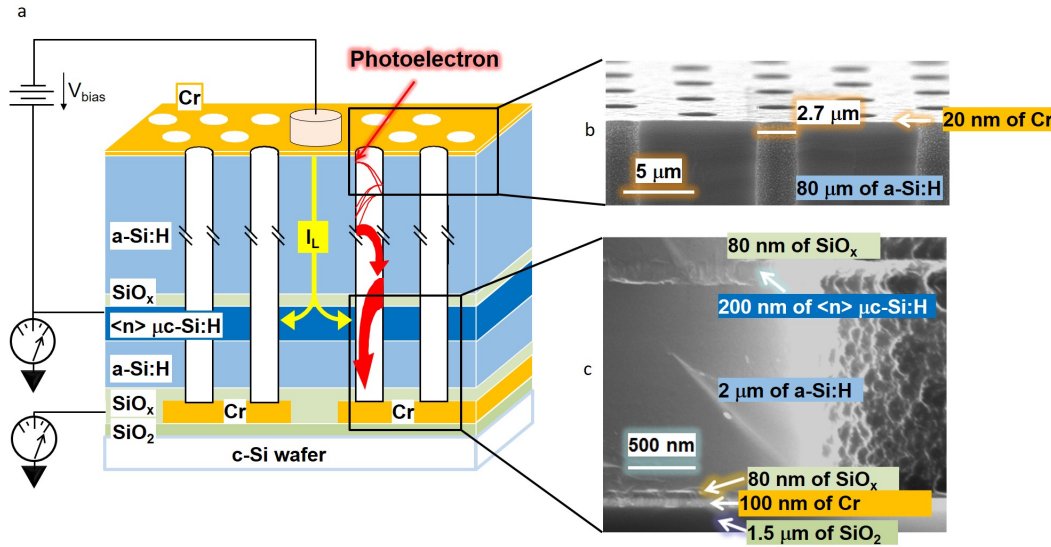


Figure 4.1 – Structure and SEM images of 4th generation of AMCPs. Compared to the structure of the previous generation (figure 3.4) the size of the c-Si wafer was increased to 6" in order to use a state-of-the-art DRIE system. The top electrode was replaced by a metallic layer, that was used to fabricate channels with diameters down to 2.7 μm

The former AMCP architecture shown in figure 3.4 has only been slightly modified for the new design shown in figure 4.1. Modifications, other than choice of the substrate, were in the choice of material for the top electrode. A 25 nm layer of Cr replaced the layer of 1-2 μm n-doped microcrystalline silicon ($\mu\text{c-Si}$) as top electrode. The thin Cr was used as an etching mask for deep reactive ion etching of a-Si:H. With its high conductivity, the Cr layer is an ideal top electrode to set the high voltage potential evenly over the test structure.

4.2 Fabrication of the bottom layers

The process flow for the fabrication of the 4th generation AMCPs is shown in figure 4.2. A 6" wafer coated with 1.5 μm thermal oxide was used as a substrate. The oxide coating provides electrical insulation between the electrode pads (anodes). The oxide on the back surface of the Si-wafer is not shown in the diagram, as it is not relevant in this context. The bottom electrode was fabricated with a standard lithographic process. A 100 nm Cr layer was evaporated, and a 2 μm layer of AZ1518 photoresist was used along with wet etching of Cr to fabricate the bottom electrode structure.

The test structures were designed as described in [Franco 2014b], however, the number of test structures per wafer was increased to cover the entire area of the 6" wafers. A picture of the fabricated bottom electrode with 52 AMCP test structures and 9 SEM test structures is shown in figure 4.3a. A schematic drawing in figure 4.3b shows the placement of AMCP test structures and SEM test structures on the wafer. One AMCP test structure, shown in figure 4.3c consists

4.2. Fabrication of the bottom layers

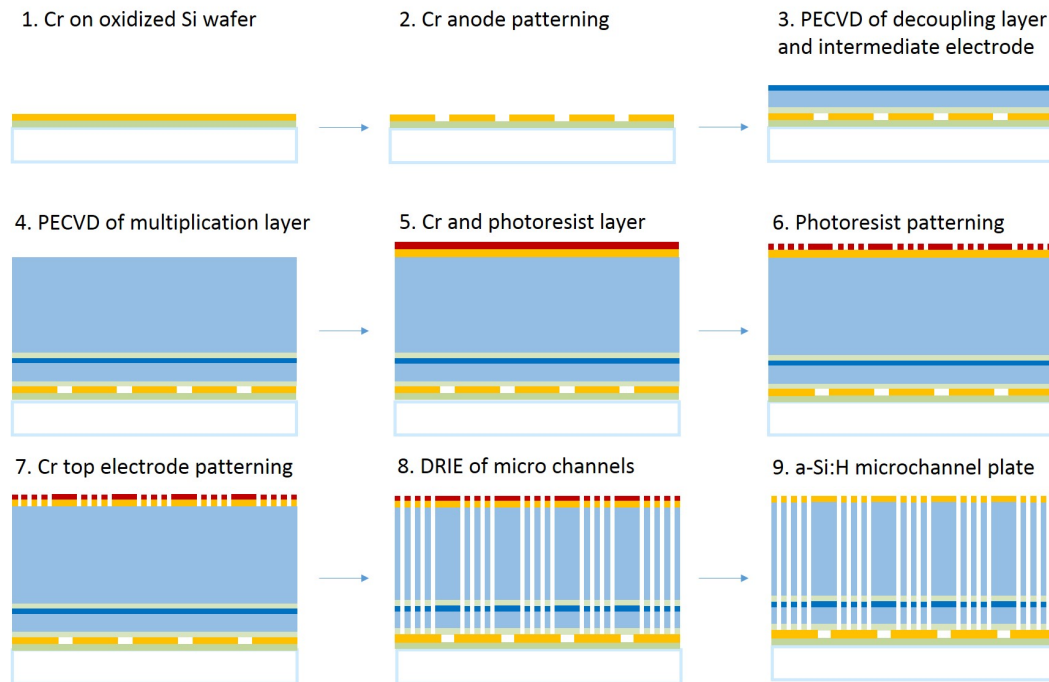


Figure 4.2 – Process flow for the fabrication of AMCPs: 1. Si wafer with $1.5\text{ }\mu\text{m}$ SiO_2 and a 100 nm Cr layer , 2. Patterning of the Cr anode after first lithography, 3. PECVD of a 80 nm SiO_x adhesion layer, a $2\text{ }\mu\text{m}$ a-Si:H and a 200 nm n-doped $\mu\text{c-Si:H}$ layers, 4. Evaporation of the 50 nm intermediate electrode Cr pads, PECVD of a 80 nm SiO_x adhesion layer and of about $80\text{ }\mu\text{m}$ a-Si:H layers, 5.-8. Evaporation of a 20 nm Cr top electrode, patterning with lithography with a very thin photoresist layer of $1\text{ }\mu\text{m}$ and micro channel etching through the whole layer stack with DRIE, these steps are new compared to previous generations' fabrication, 9. After removal of residual resist, the AMCP is finished.

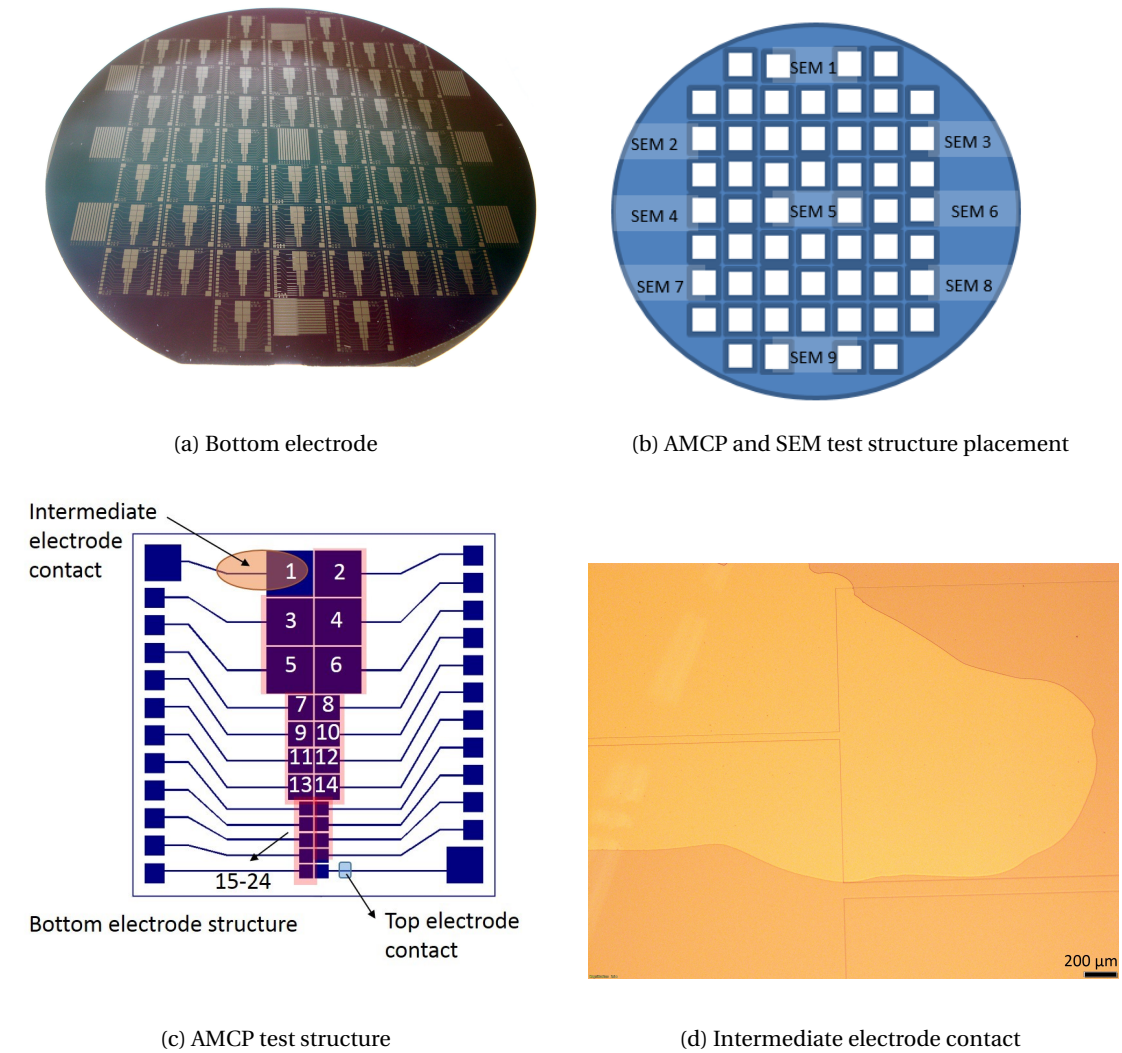


Figure 4.3 – (a) Image of the bottom electrode structure of AMCPs on a 6" wafer. (b) Placement of AMCP test structures (white squares) and SEM test structures on 6" wafer. SEM1-9 test structures are used to determine layer thickness and channel etch parameters by examining their cross-sections. (c) Schematic drawing of one AMCP test structure. The active area is numbered and each of the numbered squares except number 1 represent an AMCP pad that can be measured independently. The top electrode and intermediate electrode are shared for all pads of one test structure. (b) Microscope image of the intermediate contact on the $\mu\text{c-Si}$ layer at pad number 1

of 24 AMCP pads of three different sizes, 10 pads of $500 \times 500 \mu\text{m}^2$, 8 pads of $1000 \times 1000 \mu\text{m}^2$ and 6 pads of $2000 \times 2000 \mu\text{m}^2$. All AMCPs of one test structure have the same layer thickness and are etched with an identical channel aperture. The 9 SEM test structures are placed on the wafer as reference points that are taken to measure the channel apertures and the layer thickness. This measurement is destructive as it has to be measured from a cross section using the SEM, in order to see the channel diameter variations in the depth of the layer.

As a next step, the decoupling layer and intermediate electrode are deposited by PECVD, step 3 in figure 4.2. For the following PECVD layers, the wafer is kept at a nominal temperature of 205°C and the depositions are done using a plasma frequency of 70 MHz. After evacuating the deposition chamber to 10^{-7} mbar, the wafer surface is cleaned with a hydrogen plasma for 5 min. An adhesion layer of 70 nm SiO_2 is deposited, with a gas mixture of 98 sccm H_2 , 2 sccm SiH_4 and 4 sccm CO_2 at a pressure of 700 μbar . An a-Si:H layer of $2 \mu\text{m}$ is deposited from 15 sccm H_2 and 40 sccm SiH_4 at 450 μbar . In the device, this layer separates electron multiplication current from the leakage current, for a high signal to noise ratio, see chapter 3.4. Phosphorous-doped $\mu\text{c-Si}$ deposited from 98 sccm of H_2 , 2 sccm of SiH_4 and 10 sccm of PH_3/H_2 (0.1% PH_3) at 450 μbar serves as the intermediate electrode in the AMCP stack. In order to contact this electrode, a 50 nm Cr layer is evaporated on top. A contacting area is protected with P70 resin and subsequently the rest of the Cr layer is etched with Chromium etchant. The resist is removed with a piranha solution. The Cr contact of the intermediate electrode is shown in figure 4.3d.

4.3 Fabrication of the multiplication layer

The most delicate step in the fabrication of AMCPs is the deposition of the thick layer of a-Si:H, the multiplication layer, depicted as step 4 of figure 4.2. During the deposition of a-Si:H the amorphous network is built and for the thickness of up to $100 \mu\text{m}$, mechanical stress in the layer and accumulation of hydrogen become important. The deposition recipe, formerly adjusted to the 4" substrate, needed to be readjusted. Figure 4.4 shows microscope images of a $95 \mu\text{m}$ PECVD layer and a $82 \mu\text{m}$ PECVD layer deposited for the work of this thesis with the same recipe on a 4" wafer (a) and on a 6" wafer (b). For the fabrication of the multiplication layer, another adhesion layer of 50 nm SiO_x was deposited on the intermediate electrode followed by the thick layer of a-Si:H. a-Si:H is deposited via PECVD from a mixture of 15 sccm H_2 and 30 sccm SiH_4 at 650 μbar . During the deposition, the temperature was changed from 205°C to 207°C after 6 h. After 12 h, the deposition was stopped, and the wafer gradually cooled down, while keeping the chamber under a vacuum of about 10^{-6} mbar. Depositions resulted in layers as thick as $83 \mu\text{m}$.

A SEM image of a cross section is shown in figure 4.6. Intrinsic compressive stress in the thick amorphous material creates local delamination of the layer at the interfaces, as the substrate does not bend enough to compensate for that. Deposition on the larger area substrate is more challenging due to a non uniform deposition rate inside the comparatively small PECVD chamber and a more rigid substrate due to its thickness. 6" wafers have a thickness of $500 \mu\text{m}$,

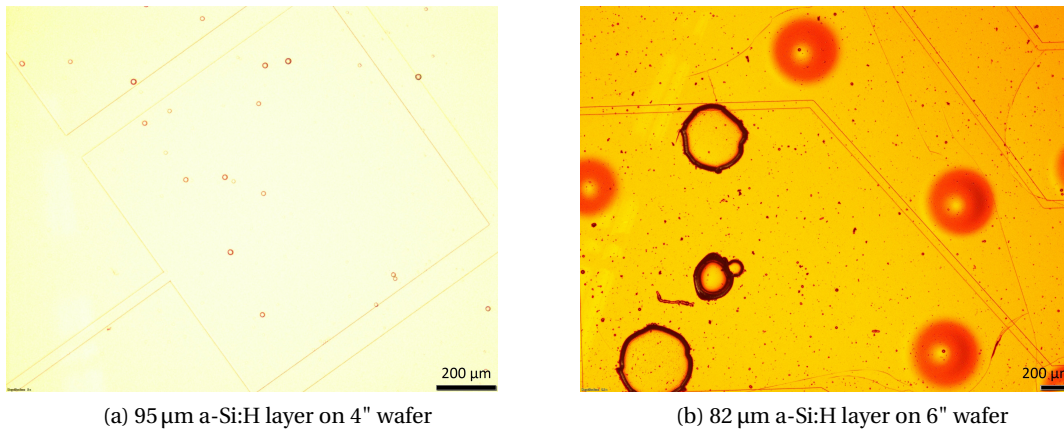


Figure 4.4 – Microscope images of the surface of a 95 μm layer and 82 μm layer of a-Si:H, that were deposited on a 4" (a) and on a 6" (b) wafer respectively, using the same deposition recipe.

compared to the formerly used 4" wafer with a 200 μm thickness. Thus, the substrate was less forgiving for compressive stress in the layer, and additionally the layer deposition was less uniform. As the thicker wafer would bend less, an increased number of defects in the atomic network lead to hydrogen accumulation and stress in the deposited layer and at the interfaces between layers. This creates macroscopic defects and delamination. The delamination can be seen from the top as bubbles and craters in figure 4.4b. The 95 μm thick a-Si:H layer on the 4" wafer does not exhibit large defects. Accumulation points of hydrogen in the layer create much smaller defects, occupying a negligible part of the area.

Intrinsic stress in amorphous silicon layers has been analyzed by [Johlin 2012], where the dependence on silane gas pressure during the deposition was shown to lead to compressive or tensile stress, depending on the gas pressure. For their experimental conditions, Johlin et al. found the ideal gas pressure at the transition point between compressive and tensile stress. Paduscheck et al. [Paduscheck 1983] observed the role of hydrogen content in amorphous silicon for the formation of tensile or compressive stress and the transition between both states. The hydrogen content and thus the mechanical stress in the layer is determined by the process conditions and can be adjusted amongst others by adjusting the process temperature.

SEM images in figure 4.5 show a cross section of the most prominent defects in the a-Si:H layer on the 6" wafer. As the a-Si:H layer seemed to delaminate at the adhesion layer, this layer was improved by increasing its thickness from 70 nm to 85 nm. At the same time the temperature profile of the thick a-Si:H deposition was modified, with a steady increase in temperature during deposition from 205 $^{\circ}\text{C}$ up to 215 $^{\circ}\text{C}$, increasing every 1.5 h, to smoothly counteract defect formation. The effect of temperature on a-Si:H formation will be explained in detail in the next paragraph.

An SEM image in figure 4.6 shows a 80 μm a-Si:H layer deposited on a 6" wafer, after optimization of the deposition temperature and increasing of the adhesion layer thickness. The thickness profile over the whole layer of finished AMCPs was measured by SEM analysis of

4.3. Fabrication of the multiplication layer

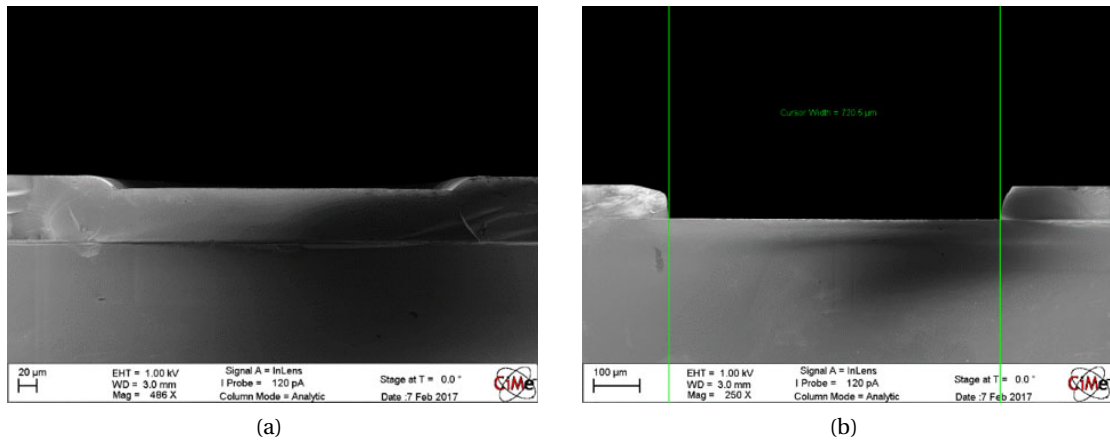


Figure 4.5 – SEM images of defects in 80 µm thick amorphous silicon layers in an AMCP stack on 6" wafers. Defects run through the whole depth of the a-Si:H layer and delaminate at the adhesion layer.

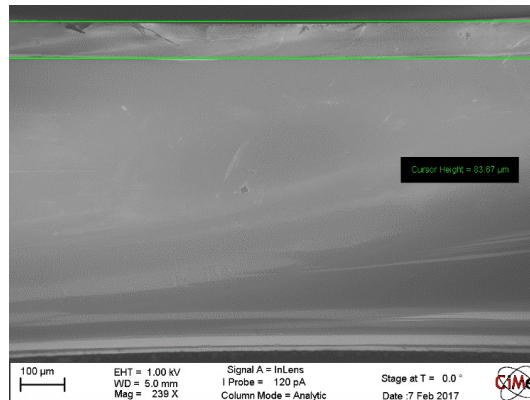
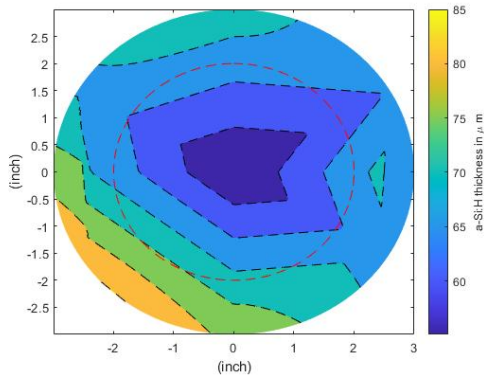
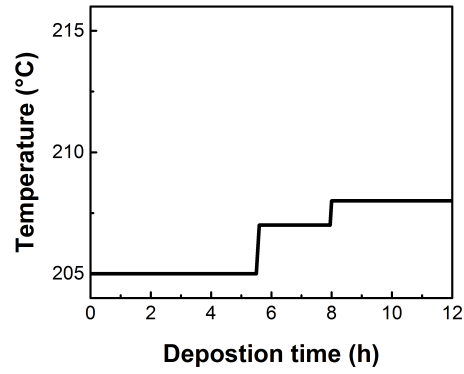


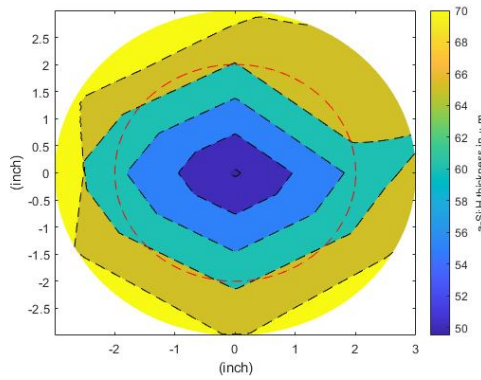
Figure 4.6 – SEM image of about 80 µm of a-Si:H deposited on a 6" wafer, after optimization of the deposition temperature.



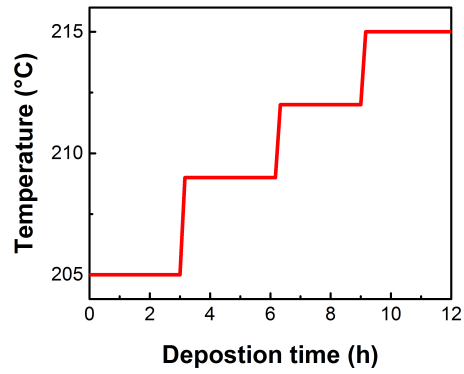
(a) Homogeneity $3.9 \mu\text{m}/\text{cm}$



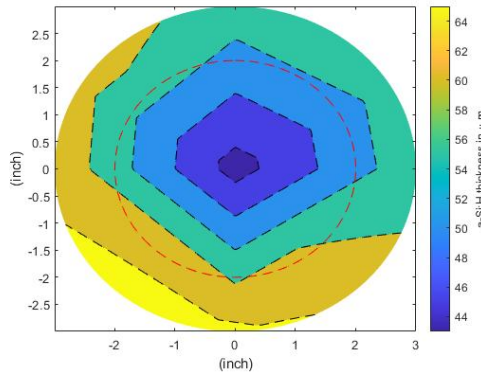
(b)



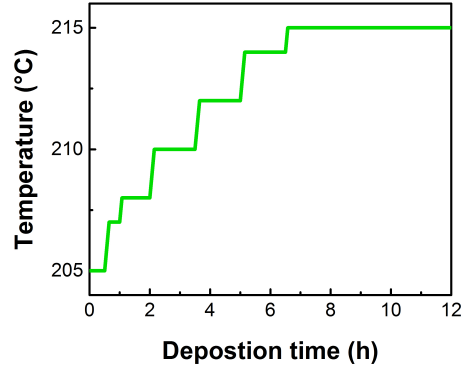
(c) Homogeneity $2.6 \mu\text{m}/\text{cm}$



(d)



(e) Homogeneity $2.9 \mu\text{m}/\text{cm}$



(f)

Figure 4.7 – a-Si:H layer thickness variation (a,c,e) and their respective deposition temperature profile (b,d,f). The thickness was measured from cross sections of SEM1-9, located on the wafer as shown in figure 4.3a. The deposition temperature was optimized to reduce defects in the a-Si:H layer. At the same time, due to higher temperatures, the deposition rate was reduced and the homogeneity improved. The total thickness after optimization varies up to $16 \mu\text{m}$ over the 6" area. The red circle shows a 4" inlet.

cross sections of selected parts distributed evenly over the area of the wafer. Figure 4.3b shows the placement of the SEM structures on the wafer. Figure 4.7 shows the typical thickness variation on a 6" wafer and an improvement in homogeneity from (a) to (c) and (e). The respective temperature profiles during deposition of the layers are shown in figure 4.7 (b) to (f). The quality of the thick amorphous layer is very sensitive to the deposition temperature. The temperature affects the layer uniformity, the formation of stress in the layer and delamination, which should both be prevented. While keeping the deposition temperature low at the start prevents hydrogen accumulation at the bottom of the layer, the higher temperature later on in the deposition process helps to reduce defect formation. A deposition temperature of 210°C at the start of the deposition leads to delamination, while keeping a low temperature leads to the defects seen in 4.4b. While the increase in average temperature from (a) to (e) in figure 4.7 reduced the defects in the layer, the average deposition rate was decreased as well, from 19 Å/s to 15 Å/s. The layer thickness in figure 4.7 (e) was reduced to 80% compared to the thickness in (a), which reduced the inhomogeneity of the thickness at the same rate. The thickness varies with about 30% of the total layer thickness. The homogeneity of a-Si:H layers of the 3rd generation AMCPs that had been deposited on 4" wafers varied between 1.1 µm/cm and 2.4 µm/cm using a deposition recipe with 17 Å/s. A defect free thick amorphous silicon layer with important thickness variations represents a challenge for uniformity of resists in the following lithography step and in the last step of the fabrication process, deep reactive ion etching of the micro channels, as the etch rate of DRIE is constant over the whole area. To ease micro channel fabrication, deposition of a uniform a-Si:H thickness could be improved by using a deposition chamber designed for the comparatively larger substrate.

4.4 Deep reactive ion etching of AMCP microchannels

The last steps in the fabrication of the 4th generation AMCPs are the deposition of the top electrode, the top electrode patterning and etching of the microchannels, depicted in figure 4.2, step 5-9. Microchannels were etched in the active area of the AMCP test structures marked in red in figure 4.3c. Channels of each test structure had identical diameters, while a number of test structures with different diameter and pitch were realized. Channel diameters ranged from 2 µm to 6 µm and three different open area ratios, 0.03, 0.06 and 0.11, were realized.

DRIE process of the channels for AMCPs had been first tested on c-Si wafer and then the etch rate had to be optimized for the a-Si:H later, as a function of the present aspect ratios. The AMCP layer structure was coated with a 25 nm Cr layer via evaporation, while tests on the c-Si wafer had been done with a more homogeneous layer using sputtering. The wafer has been dried at 200°C for 30 min, then 2 µm of AZ1518 photoresist have been coated on the surface. The wafer has been exposed, and then developed with a 16.67% AZ351B aqueous solution. After a hard baking time of 30 min at 85°C, the Cr was dry etched. The photoresist mask was left on the Cr mask during the DRIE, for a better masking effect.

The DRIE system used here was a new generation of etching system, the SPTS Rapier™. The DRIE process is more homogeneous, than the one used for the 3rd generation of AMCPs.

Chapter 4. AMCPs with high aspect ratio

Switching of gases in the new system happens faster, which allows for a better verticality of the etched structures. The electrostatic clamping with ceramics used now allows for a better placement of the wafer than the polymer chucks used in the former system. Additionally, the cooling was improved. Results of the DRIE in c-Si can be seen in figure 4.8. Straight and vertical channels have been realized with diameters of $5.6\text{ }\mu\text{m}$ and depth of $57\text{ }\mu\text{m}$. On the same wafer, channels with diameters as small as $2.7\text{ }\mu\text{m}$ have been etched. The etch rate in these narrow channels is only about 13% slower than the rate in the $5.6\text{ }\mu\text{m}$ channels. In AMCPs the Cr bottom layer works as an etch stop. This makes it possible to etch different diameter structures, and therefore different aspect ratios, at the same time. This is a very promising result, which allows etching of high aspect-ratio structures in silicon with apertures down to $2\text{-}3\text{ }\mu\text{m}$.

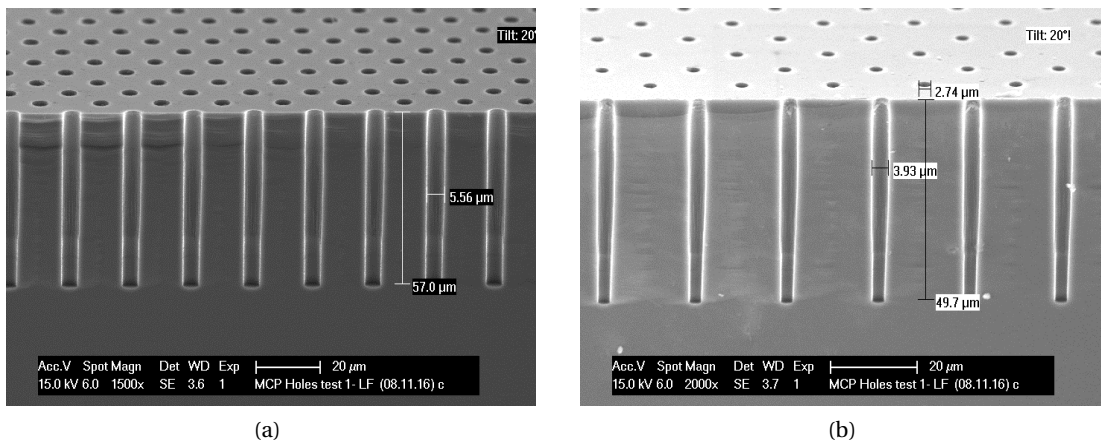


Figure 4.8 – (a) SEM cross section of DRIE etched super straight micro channels in a Si wafer with $5.6\text{ }\mu\text{m}$ diameter and excellent verticality. (b) On the same wafer, channels with diameters down to $2\text{-}3\text{ }\mu\text{m}$ have been etched.

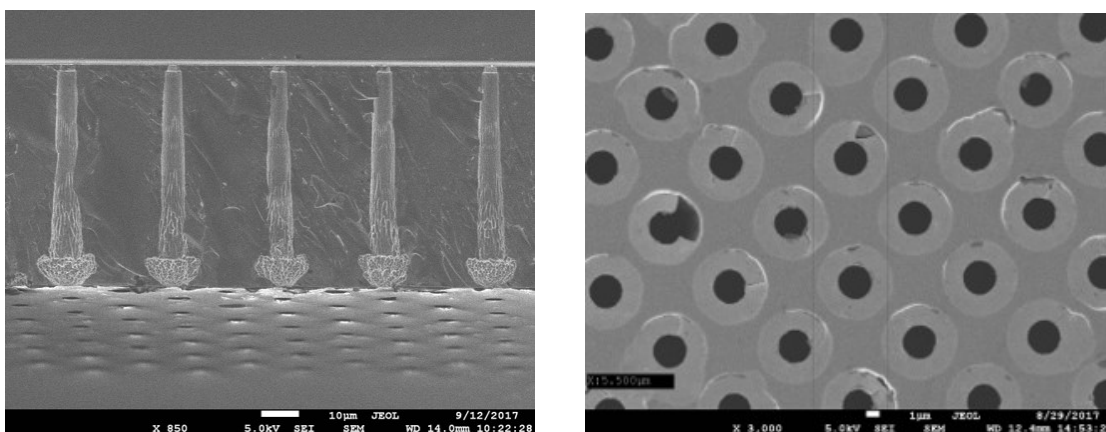


Figure 4.9 – (a) SEM image of AMCP channels cross section showing typical etching difficulties during DRIE due to wafer bending, thickness variation and channel diameter variation. (b) Top view of overetched channels.

4.4. Deep reactive ion etching of AMCP microchannels

Several challenges were encountered when DRIE etching the channels in AMCPs. As a basic design, we chose to have AMCP structures with different channel diameters distributed on the whole area of the wafer. As the etch rate depends on the opening, channels with different diameters were etched at different speeds, as can be seen in figure 4.8. Additionally to a varying etch rate the needed etch depth varied with the layer thickness. Wafer bending due to compressive stress in the a-Si:H layer poses an additional difficulty for clamping of the wafer for DRIE, and also for a high resolution lithography. Typical defects encountered from DRIE, due to these non-uniformities, are shown in figure 4.9. Here, the Cr layer is underetched. DRIE on a more uniform wafer, that did not exhibit considerable compressive stress, is shown in figure 4.10 (a). Channels with diameters of only $2.6\mu\text{m}$ were etched here, although not fully until the bottom of the a-Si:H layer. On a more centered part of the wafer, with a lower thickness, channels with $2\mu\text{m}$ diameter were fully etched. Figure 4.10 (b) shows the bottom of such a channel and the fine structure of the inner wall surface after DRIE. The usually observed scalloping from DRIE cannot be observed here, however, the channel surface shows a very rough surface. This surface rugosity could have an effect on the electron emission secondary yield of the AMCP channel.

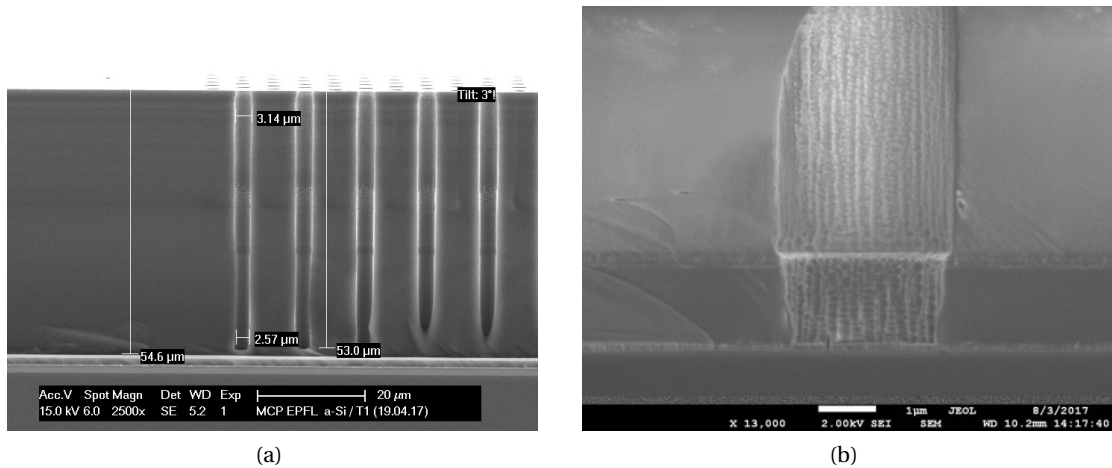


Figure 4.10 – (a) Cross section showing the etch depth of narrow channels, that are not completely etched to the bottom electrode of the AMCP due to the thickness variations of the a-Si:H layer. (b) SEM image of the channel bottom of a completely etched narrow channel, showing the reduced diameter at greater etch depth. A rough surface structure of the channel is visible, which might have an effect on the secondary yield.

Figure 4.11 shows the etch depth compared to the layer thickness at different locations on the wafer. While the channels with diameters below $6\mu\text{m}$ are not fully etched on the outer parts of the wafer (SEM 1-9), shown in (a), channels with all diameters are fully etched in the middle of the wafer (SEM 5), shown in (b). After improving the homogeneity of the 20 nm Cr top layer evaporation, AMCPs with straight and high aspect ratio channels were etched. SEM images of channels with about $5\mu\text{m}$ and with about $2.7\mu\text{m}$ diameters in a $60\mu\text{m}$ layer are shown in figure 4.12.

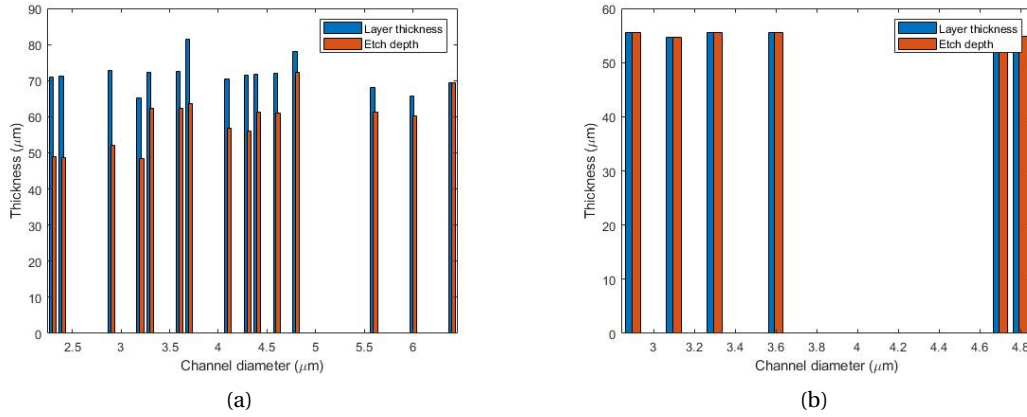


Figure 4.11 – Etch depth of microchannels where (a) at the outer parts of the wafer (SEM1-9) thin channels are not completely etched and (b) in the middle of the wafer (SEM5) with an average thickness of about 55 μm channels with diameters down to 2.9 μm have been etched completely

Another SEM image of a narrow channel is shown in figure 4.13 (a) with a very porous surface structure. In figure 4.13 (b) an image of a 1.5 μm circle is shown, made using the photolithography tools used for the AMCPs in this thesis. The resolution of our photolithography process should allow us to go down to these very narrow channel diameters. If the circularity of the channels does not play a major role, we could imagine having microchannels with diameters down to the 500 nm range. It remains open to see how well channels in this diameter range can be etched by DRIE and how well they would perform as AMCPs. The phenomenon of a very rough structure inside the channel was mostly seen for narrow channels. It remains to see if etching even narrower channels would increase this phenomenon and would benefit the performance of AMCPs.

In chapter 6 we compare the surface roughness of DRIE channels with the a-Si:H layer surface deposited with the same recipe as AMCPs, and with a flat a-Si:H layer, deposited by PECVD with a recipe optimized for a high surface homogeneity.

As a summary, we found that at this stage, the channel diameter is not a limiting factor for the fabrication of AMCPs. The crucial part of AMCP fabrication is the deposition of the thick homogeneous a-Si:H multiplication layer, and adjusting the deposition recipe to avoid defect formation and wafer bending due to compressive stress in the layer. Layer deposition must be homogeneous on the used area of the substrate, which was not the case in the PECVD system used here. For this system, the deposition area should be decreased in order to fabricate a homogeneous layer for ideal DRIE conditions. Additionally, etching of similar diameters on one wafer would be beneficial to further optimize DRIE.

4.4. Deep reactive ion etching of AMCP microchannels

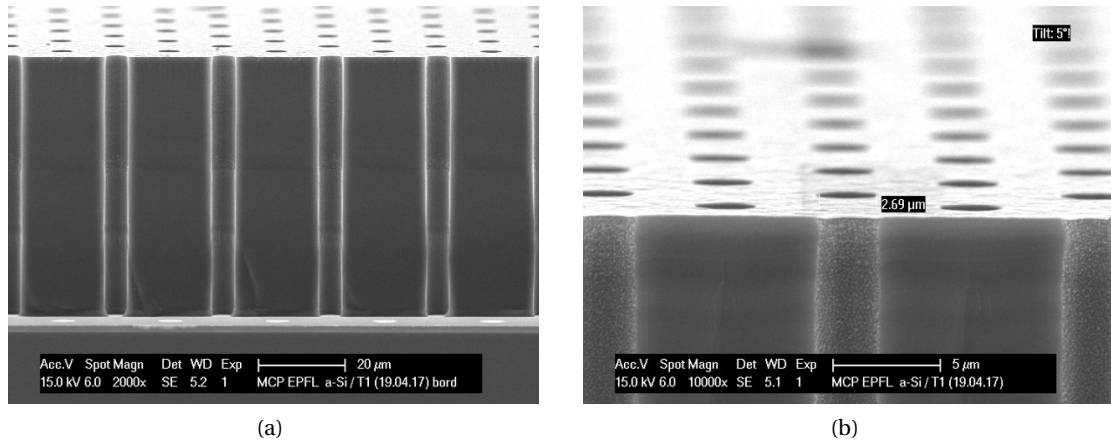


Figure 4.12 – SEM images of AMCPs with channels etched in about 60 μm a-Si:H layers. The minimal channel diameter was 2.7 μm.

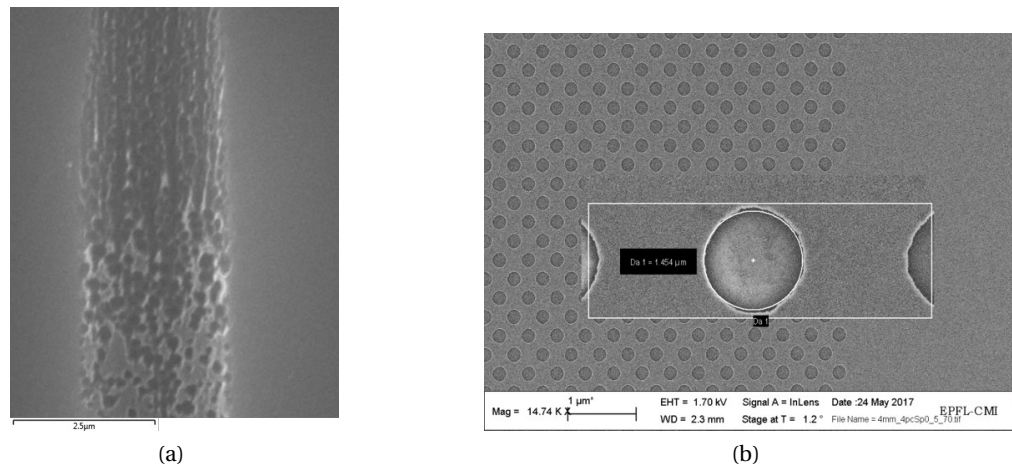


Figure 4.13 – (a) SEM of a rough channel structure and channel diameter of about 2.5 μm. (b) SEM image of the spatial resolution of tens of nm of the photolithography systems used. For a roughly circular geometry channel diameters down to 500 nm could potentially be fabricated using this lithography process.

4.5 AMCP channel surface roughness

In this section, we study the surface of AMCP channels due to their fabrication method by DRIE. The surface roughness is of great importance for secondary emission, which is the driving force of electron multiplication in AMCPs. Surface curvature has been shown to increase the collected secondary yield, whereas, on the other hand, shading effects can occur in rough surfaces. The angular dependence of secondary emission also depends on the surface roughness. The effects of surface roughness on the secondary emission process will be further addressed in chapter 5, where we describe the electron emission process in detail.

The present section serves as a general overview of the channel roughness in AMCPs. For a more detailed analysis the influence of different etching processes, diameters and the location inside the channel, would need to be taken into account. The roughness has been reconstructed from two SEM images at different angles using the stereoscopic reconstruction tool of MountainsLab®.

In figure 4.14 we show two SEM images taken at the end of an AMCP channel with a diameter of $6\mu\text{m}$ at 0° and 5° tilt. The surface is reconstructed from an area of $2.1 \times 2.1\mu\text{m}^2$, shown with a yellow frame in figure 4.14. The reconstructed surface was flattened to remove the channel curvature and the resulting rugosity is shown in figure 4.14c. We measured an average roughness of $R_a = 10.5\text{ nm}$ and a kurtosis of 3.3. The kurtosis is a measure of the sharpness of a roughness profile. A value of 3 corresponds to a normal height distribution and higher values to a more spiked distribution. More roughness values are shown in figure 4.15.

In figure 4.16 we show the two SEM images taken at the top of an AMCP channel with a diameter of about $4\mu\text{m}$ at 2° and 10° tilt. The surface is reconstructed from an area of about $2.1 \times 2.1\mu\text{m}^2$ here as well. The reconstructed part of the channel is shown with a yellow frame in figure 4.16 (a) and (b). The reconstructed surface was flattened for this channel as well and the resulting rugosity is shown in figure 4.16c. The overall height distribution has its peak at about 90 nm. The peaks appear more densely spaced here than for the previous wider channel. We measured an average roughness of $R_a = 13.3\text{ nm}$ and a kurtosis of 3.3. An overview of roughness values and the directionality of this surface are shown in figure 4.17.

With an average roughness of slightly more than 10 nm in both cases (wide and narrower channels) and an average height distribution about 90 nm in the second case, the current roughness is still negligible compared to diameters in the μm range. Scalloping from DRIE is seen at the top of the channel in figure 4.16. At the bottom of the channel, in figure 4.14, we do not see this surface waviness. This does not affect the measured roughness. When moving towards the fabrication of smaller channel diameters for AMCPs with diameters in the sub micrometer range the surface roughness might need to be taken into account. The roughness and surface orientation determines the secondary emission. For tightly spaced peaks we would expect shading of emitted electrons, which would reduce the AMCP gain. Surface curvature, on the other hand, has been shown to increase the secondary yield and thus, would increase the AMCP gain. We discuss the effect of surface roughness and surface orientation on the secondary emission in detail in chapter 6.

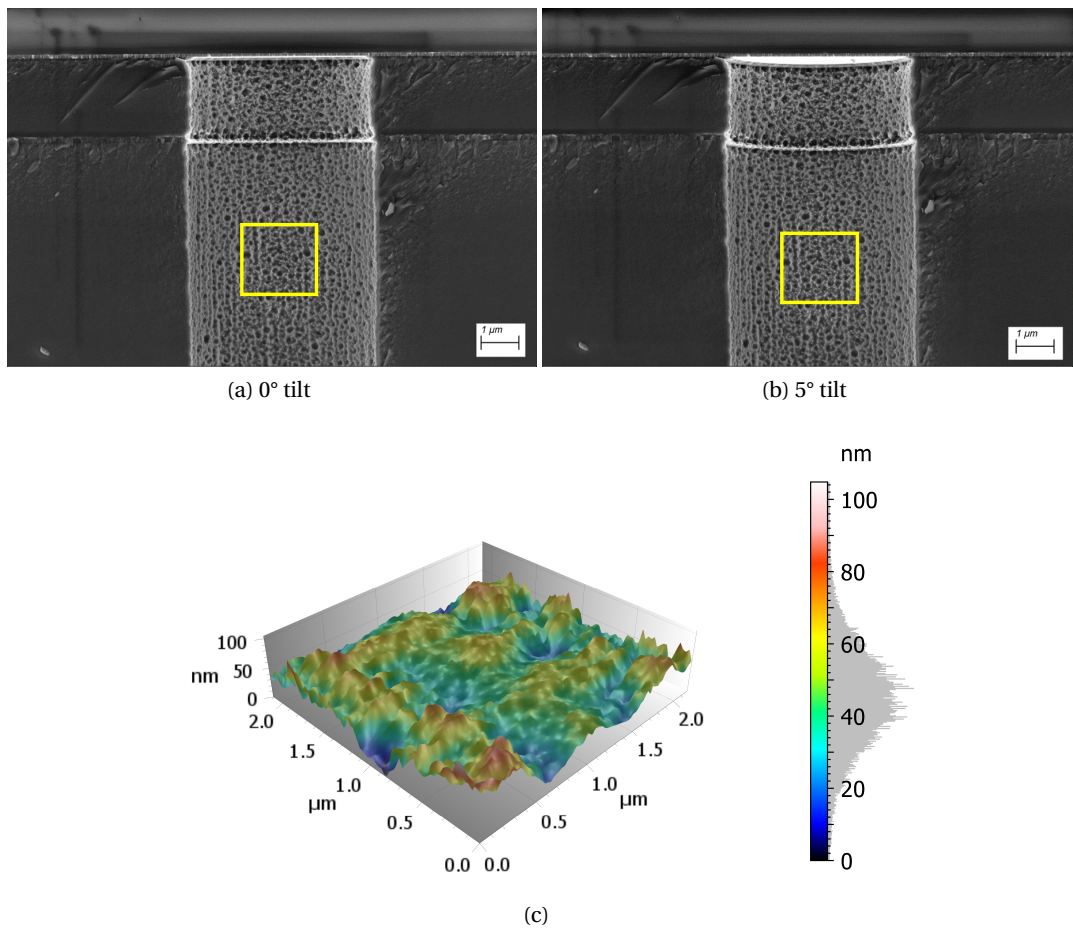


Figure 4.14 – Reconstructed 3D surface of a of a 3rd generation AMCP microchannel.

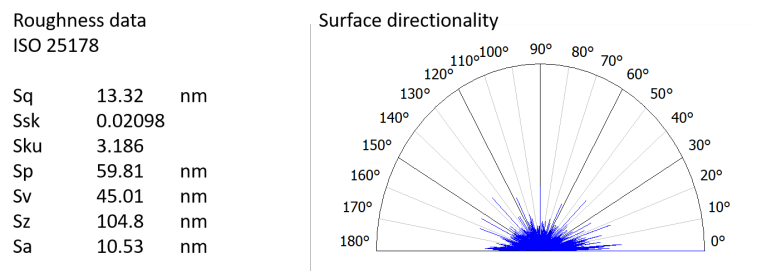


Figure 4.15 – Roughness values of the channel surface shown in 4.14

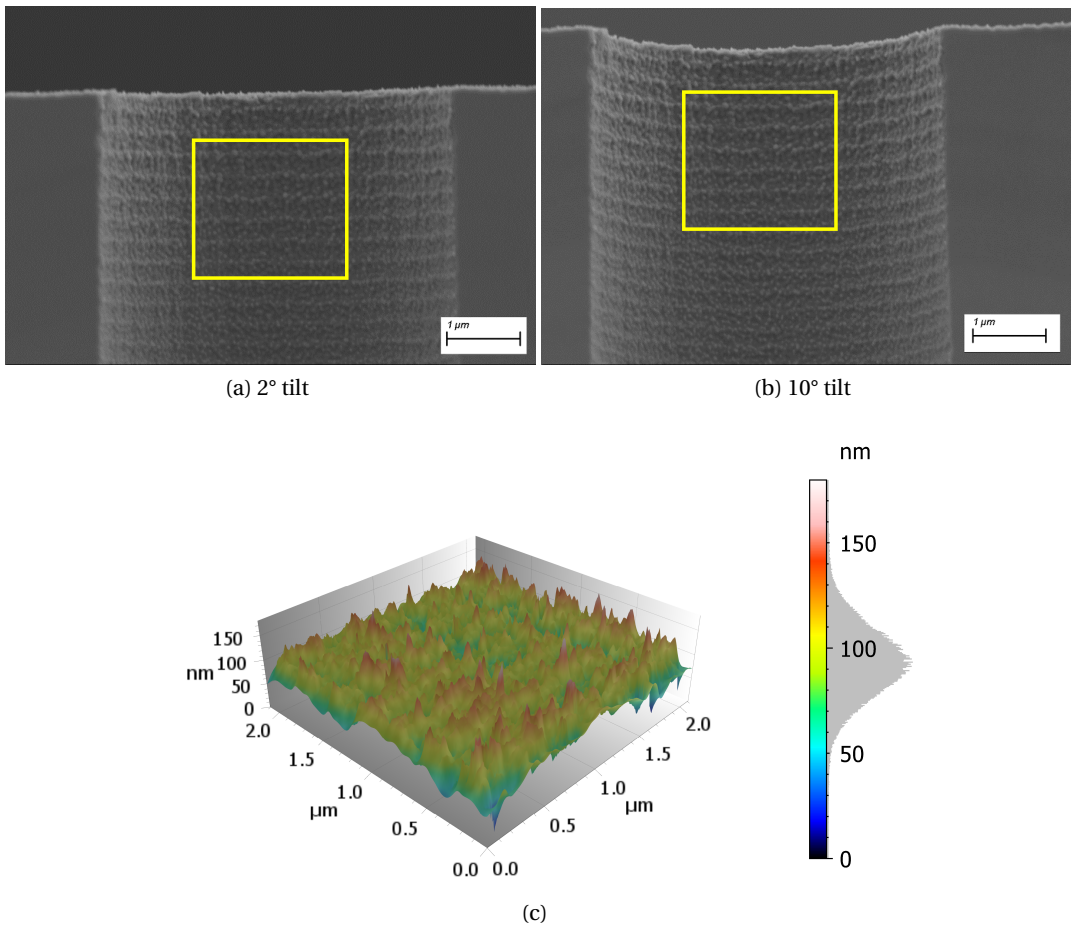


Figure 4.16 – Reconstructed 3D surface of a of a 5th generation AMCP microchannel.

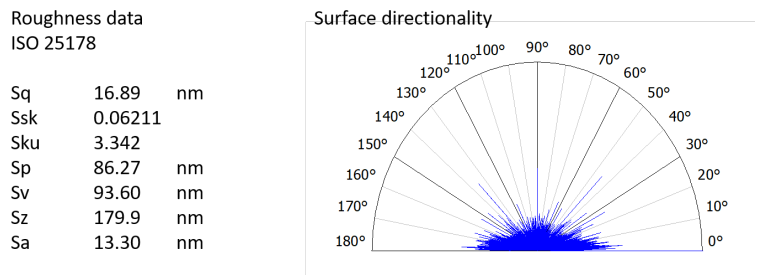


Figure 4.17 – Roughness values of the channel surface shown in 4.16

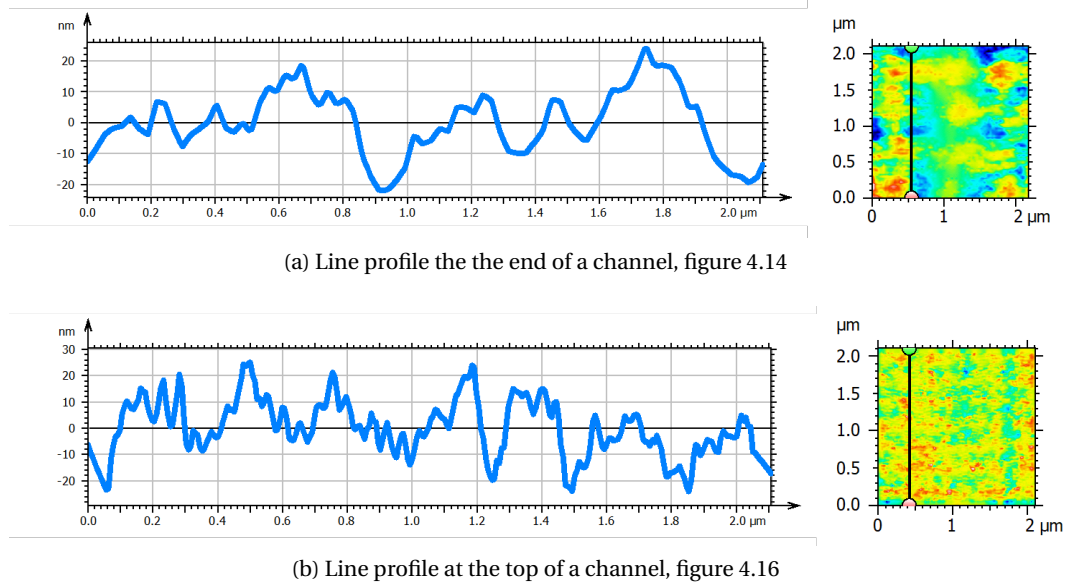


Figure 4.18 – Line profiles of the characterized surfaces. A periodicity in surface rugosity can be seen at the top of the channel in (b) and disappears at the end of the channel in (a). See the color scale of the respective images for height values of the colored areas.

Line profiles of the two AMCP channels are shown in figure 4.18. The line profile at the top of the channel, shown in (b) has a finer roughness structure and waviness that can be associated with scalloping due to the DRIE process, than the line profile at the bottom of the channel, shown in (a). Although the overall roughness is very similar, the surface rugosity of the characterized channels differs. Secondary emission not only depends on an average surface roughness, but on the surface rugosity.

In summary, we found a similar average roughness R_a of 10-13 nm for two different AMCP channel diameters, that were characterized. As a tendency, the top of the channel seems to be more affected by scalloping due to DRIE and has a finer surface structure. The AMCP gain is determined by many factors, the surface roughness being one of them. Although these measurements do not let us draw concrete conclusions on the effect of the surface roughness on the AMCP gain, we give an overview of the expected roughness in the channels. From this analysis, together with the secondary emission theory in in chapter 6, we conclude that secondary emission parameters of AMCPs might need to be calibrated according to experimental results, as the surface rugosity varies inside the AMCP channels, depending on the fabrication process, even along the length of each channel.

4.6 Characterization

In this section we present a modified characterization setup for AMCPs. First measurements of AMCPs under 1 kHz irradiation at low photon flux have been realized. We explain how all components of the setup were further improved for high frequency measurements, after the

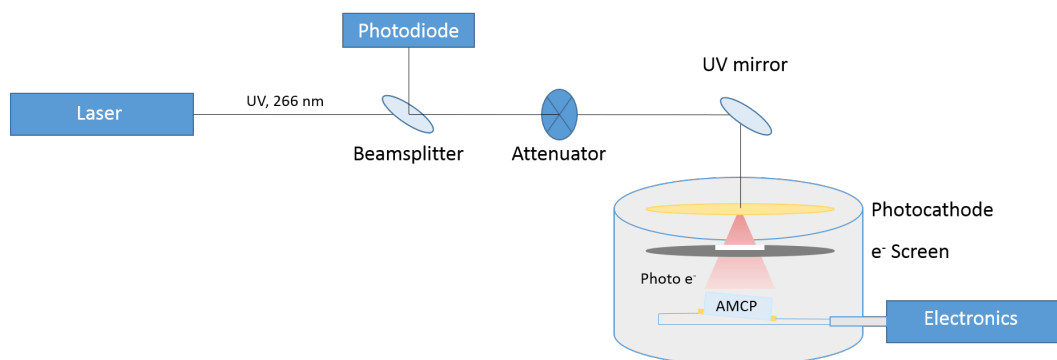


Figure 4.19 – Setup for transient characterization of AMCPs. The UV laser pulse with 7 ns FWHM and tunable frequency between 1 kHz and 4.7 kHz is guided through a filter into the vacuum chamber. Inside the chamber, UV photons are hitting a photocathode and release photoelectrons. The photoelectrons are impinging on the AMCP through an electron screen.

first tests.

The characterization setup for AMCPs was revised, in order to test 4th generation AMCPs under transient photon flux conditions. To this end we used a 266 nm (UV) laser source with a tunable repetition rate between 1 kHz and 12 kHz. As in the test setup for 3rd generation AMCP, UV light is guided into a vacuum chamber. Inside the vacuum chamber the UV pulse hits a photoelectrode, where photoelectrons are released. A scheme of the setup is shown in figure 4.19. The expected incoming charge from the photoelectrons has been calculated, in order to fit the electronic readout to the expected signal.

The solid state 266 nm laser has a peak power of 486 W and a Gaussian shaped pulse of about 7 ns at FWHM. This corresponds to a number of $4.55 \cdot 10^{12}$ photons per pulse with a photon energy of $7.47 \cdot 10^{-19}$ J. The beam is split, in order to synchronize the timing with a photo diode. Half of the original intensity arrives at the photocathode inside the vacuum chamber through a quartz window. An attenuator can be used optionally to further reduce the intensity arriving at the vacuum vessel. A 16 nm thin gold film deposited on quartz glass serves as a photocathode. The photocathode has a transmissivity of 40% and a maximum quantum efficiency of 0.01% has been measured at 266 nm [Chevallay 1994]. Note that photocathode efficiency values greatly depend on the exact surface composition. An efficiency up to 0.05% has been measured after a surface treatment described in [Srinivasan-Rao 1991]. Srinivasan-Rao et al. observed a linear increase in efficiency with the electric field strength for electric fields above $5 \cdot 10^7$ V/m. In our case, a maximum of $9.12 \cdot 10^8$ photoelectrons might be emitted upon an incident laser pulse. Although the work function of gold has been measured to be about 4.9 eV [De Boer 2005] and 5.1 eV [Rangarajan 1980], which is more than the photon energy of 4.66 eV at 266 nm, photoemission of gold layers has been reported at this wavelength. This might be due to multi photon excitations of the electronic states. The electric field applied at the photocathode could also lead to a lowering of the workfunction and thus lead to more photoemission. Certainly, at photon energies of 4.66 eV the induced photoemission in a gold photocathode is limited.

Gold was chosen because of its robustness. In this characterization setup chamber, the vacuum is broken in order to exchange samples. Therefore, no air sensitive photocathode can be used. Most highly efficient photocathodes conventionally used with MCPs are highly hygroscopic and their efficiency vanishes upon contact with air, e.g. CsI. Alternative photocathodes, that are robust and can easily be fabricated, come with a lower efficiency. Metallic photocathodes are most suitable for our application as they have the longest lifetime. Cu photocathodes have shown an efficiency of 0.001-0.01% at 266 nm and are among the most robust ones. Mg has an efficiency of 0.06% at 266 nm and a lifetime of years or more. Mg-Ba has a photon conversion efficiency of up to 0.1% at 266 nm, although a low lifetime. Non-metallic photocathodes are divided into those with a positive electron affinity (PEA) and a negative electron affinity (NEA). The photo conversion of a PEA photocathode made of CsI and Ge for example shows an efficiency of 0.13% at 262 nm. There are also differences in the response time of photocathodes. Cs₂Te has a ps response time and efficiencies between 8-12% at 253 nm. Its lifetime is measured in hours and does not extend 1 month. GaN is a robust NEA photoelectrode that can be doped with Mg to further increase its efficiency. 150 nm GaN with an Mg doping of 10^{18} cm^{-3} have been proven to be most efficient. A very comprehensive overview of photocathodes that have been measured at 266 nm is given by the Photoemission Laboratory of CERN at [CERN - Photoemission laboratory].

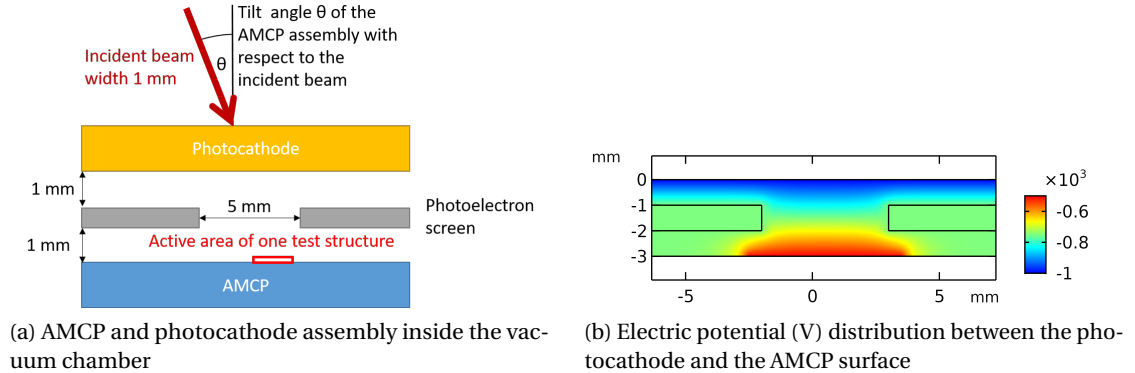


Figure 4.20 – (a) Schematic drawing of the geometrical arrangement of photocathode and the AMCP test structure. (b) Electric potential (V) between the photocathode and the AMCP.

Although photoelectrons are emitted isotropically, their initial energy is very low. We assume they are emitted at rest or with sufficiently low energy that their initial energy does not affect their trajectory, which is then solely governed by the electric field between the photocathode and the AMCP surface, shown in figure 4.20b. In a first approximation the photoelectrons are emitted from the same area as the incident laser spot, an area with a width of about 1 mm. The distance between the photocathode and the AMCP test structure is about 3 mm, see figure 4.20, and the electric field strength is about $2.5 \cdot 10^5 \text{ V/m}$. A photoelectron screen has historically been placed between the photocathode and the AMCP surface to avoid photoelectrons from directly shining on the readout pads when using a UV lamp as a photon source. Although the incident beam width can be increased by a beam expander from its original size of about 1 mm, the photoelectrons induced by the laser beam should not reach the bottom electrode

readout pads when the laser is adjusted onto the active AMCP area and the photoelectron screen might be redundant when using the laser as a photon source. This screen might be removed in order to not influence the electric field and prevent electrons from being guided onto the screen. Additional mirrors in the beam path are used to adjust the beam onto the test structure.

We show the calculated electric potential distribution between the photocathode and the AMCP top electrode in figure 4.20b. If the laser spot of 1 mm is well adjusted despite the tilt of the AMCP-photocathode assembly with respect to the incident beam, and if the beam is not widened when passing through the quartz window of the vacuum chamber and through the quartz substrate of the photocathode, the biggest part of the electrons should reach the active area. According to our calculations, changes in the beam position of hundreds of micrometers can lead to a reduction of 50% of the signal. If the laser beam is well adjusted onto the active area of an AMCP test structure (maximum size $1.8 \times 1.8 \text{ mm}^2$), and taking into account the active area of about 0.1, a maximum number of about $9 \cdot 10^7$ electrons arrive in the AMCP channels. This corresponds to a charge signal of a few pC.

A picture of an AMCP with 23 test structures, mounted on a PCB is shown in figure 4.21a. The

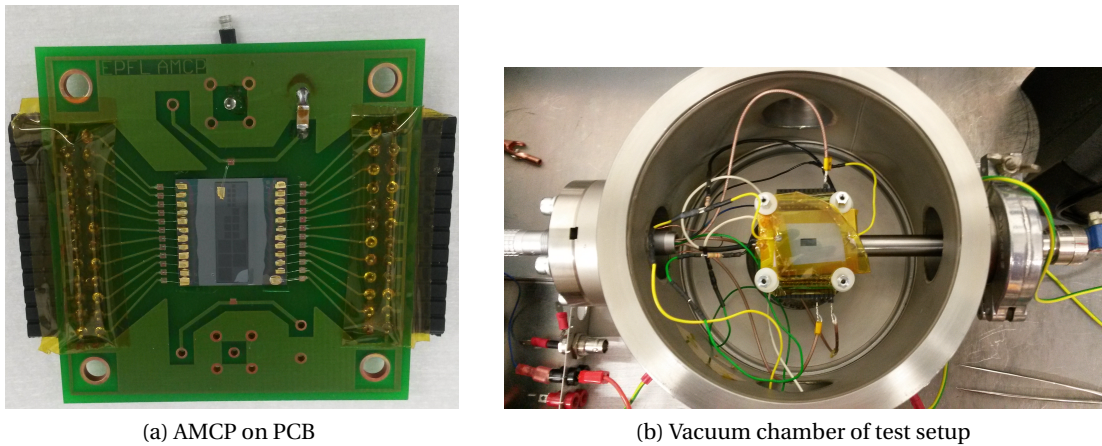
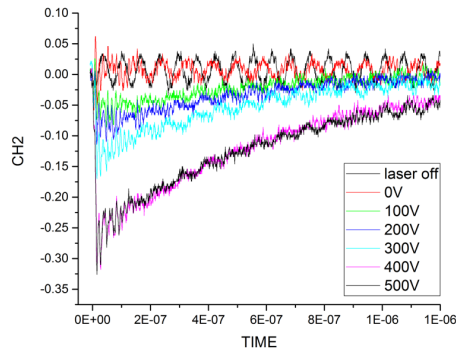


Figure 4.21 – (a) Picture of an AMCP mounted on the PCB. For all the contacts, gold pads are glued on the electrodes using a silver glue and then the pads are wire bonded to the PCB. (b) Vacuum chamber after a first revision with shielded cables.

electrodes are connected to the PCB using gold pads that have been glued on the Cr pads with a silver glue. The gold pads were then wire bonded to the PCB. The top electrode is connected via the single connector on top. The bottom electrodes of all test structures are connected on either side of the PCB, using single pins for the signal and ground. The intermediate electrode is also connected through a single pin on the bottom right of the PCB. Soldered connectors are covered with Kapton tape to prevent electric arcs inside the chamber. Figure 4.21b shows the vacuum chamber from the top. The AMCP-photocathode assembly, in the middle of the chamber, is mounted on a tilting rod. The shielded cables are used to measure the AMCP signal. Other cables inside the chamber are used to apply the photocathode bias, the electron screen bias and the bias of the AMCP top electrode and to ground the intermediate electrode

of the AMCP.

As multiplication factors of about 40 have been measured for the 3rd generation AMCPs, the output signal has to be amplified with a charge sensitive preamplifier. After a first attempt of measurements, shown in figure 4.22, we were not able to detect a reference signal and to calculate an AMCP gain. This might be due to the low signal. Figure 4.22a shows the oscilloscope output of the amplified AMCP signal of one test structure with an area of $1.8 \times 1.8 \text{ mm}^2$. The signal fall time is much slower than the laser signal, because of the amplifier capacitance. The maximum charge measured were 375 fC at an AMCP bias of -500 V, shown in figure 4.22b. In order to measure such low signals at high frequency, electrical shielding is crucial. As a consequence, we upgraded all electrical connections in the setup to shielded cables and connectors. The AMCP test structures were redesigned as a 5th generation to incorporate a guard ring around each bottom anode and with an increased conductivity of all electrodes. To further increase the signal collection efficiency, we chose the CR-110 preamplifier from Cremat Inc to be integrated into the vacuum vessel, directly on the PCB. The PCB was re-designed to implement the preamplifier and all connections were shielded and kept as short as possible. The newly designed PCB is shown in figure 4.24. (a) shows the top of the PCB with all connections and where the AMCP is mounted in the middle, and (b) shows the bottom, where the 8-pin preamplifier is mounted along with all the electronics and the option to read out the signal without going through the preamplifier. Measurements of the 5th generation AMCPs with the use of this setup are the work of another thesis, made in the framework of a collaborative project to use AMCPs for time-of-flight positron emission tomography.



(a)

AMCP bias	Current	Charge
-100	0.0625 mA	63 fC
-200	0.1125 mA	113 fC
-300	0.1875 mA	188 fC
-500	0.375 mA	375 fC

(b)

Figure 4.22 – (a) Oscilloscope output showing an AMCP response to a 266 nm laser pulse, using the setup described figure 4.19. The AMCP area was 3.6 mm^2 and the aspect ratio was 13.6. The AMCP signal was triggered on the photo diode output. We used an external amplifier that was connected to the AMCP output outside the vacuum chamber. (b) Current and charge calculated from the signal in (a). No reference signal could be measured due to the very low incident number of electrons. As a conclusion, a further system upgrade was decided to improve transient measurements.

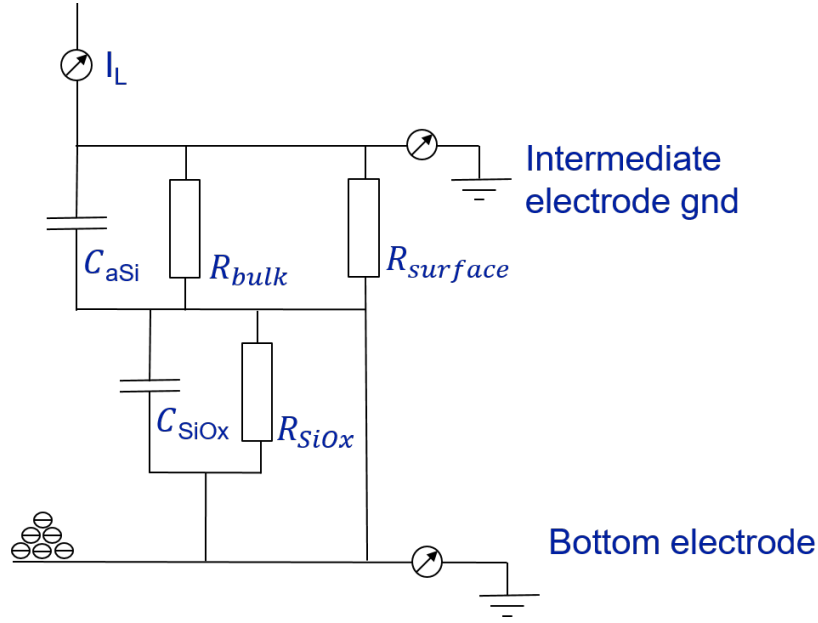
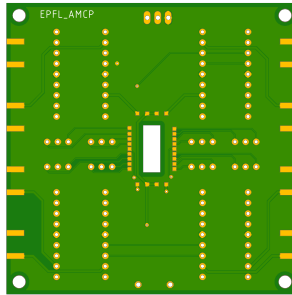
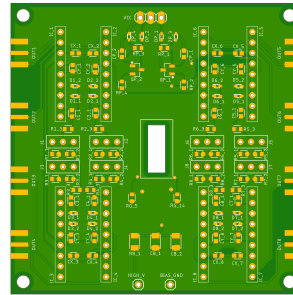


Figure 4.23 – Electrical circuit between the intermediate electrode and the bottom pad. We calculate the RC constant to evaluate potential leakage currents towards the intermediate electrode in transient mode. C_{SiOx} and R_{SiOx} are the capacitance and resistance of the SiO_x layer, C_{aSi} and R_{bulk} are the capacitance and resistance of the a-Si:H decoupling layer and $R_{surface}$ is the resistance of the channel surface.



(a) PCB top



(b) PCB bottom

Figure 4.24 – (a) Top and (b) bottom side of the newly designed PCB for transient measurements with an integrated charge sensitive amplifier, CR-110, that can be mounted from the bottom side of the PCB along with all the electronics parts. The AMCP is mounted on top and wire bonded to the gold pads around the open space in the middle.

For transient measurements the detector capacitance becomes important, as the design of readout electronics needs to be adjusted to the input capacitance. We measured the capacitance between the intermediate electrode and the bottom pads for the three different sizes of AMCP test structures using an impedance meter. We measured a capacitance between 1.5 pF and 10 pF and a resistance between 700 Ω and 7 k Ω for the structures of all three sizes. We did not find a correlation of these values with the pad size. Furthermore we calculated the expected RC constant between the intermediate electrode and the bottom pad for an AMCP area of 1x1 μm^2 . We show the circuit between the bottom pad and the intermediate electrode in figure 4.23. C_{SiO_x} and R_{SiO_x} are the capacitance and resistance of the SiO_x layer, C_{aSi} and R_{bulk} are the capacitance and resistance of the a-Si:H decoupling layer and R_{surface} is the resistance of the channel surface. A resistance of 10 k Ω has been measured for $R = 1 / (1/R_{\text{surface}} + 1/R_{\text{bulk}})$ on 1x1 mm^2 [Franco 2014a]. We calculated a capacitance of 50 μF and a resulting time constant of 0.6 s.

As a conclusion from the first round of transient measurements with a revised setup, the gold photocathode appears to be less effective than expected at the laser wavelength. Alternatively, adjustment effects and eventual deflection or scattering effects of the laser beam at the glass interfaces and inside the glass layers that were not taken into account here, could be more important than we assume and might be part of the reason for a reduced signal by about 3 orders of magnitude. As a consequence, the setup should be modified further with a Mg photocathode, and potentially with a Mg doped GaN photocathode, which should both be able to increase the incident photoelectron charge to more than a few fC.

In this chapter, we presented the fabrication of high aspect ratio AMCPs with an aspect ratio of up to 23 and uncovered the potential of state-of-art DRIE to produce AMCPs aspect ratios of up to 30 easily, if not more by reducing the diameter further. The bottleneck of the fabrication remains the deposition of a high quality thick a-Si:H layer. By reducing the diameter, AMCP performance can be increased even with moderate a-Si:H layer thicknesses of about 50-6 μm , which can be fabricated more easily. Also switching back to 4" substrates is an important step to ease fabrication in order to focus on increasing the aspect ratio, before considering fabrication of larger area AMCPs. We then characterized the surface roughness of AMCP channels due to deep reactive ion etching. A surface roughness R_a of about 10-13 nm was measured for two different AMCP channels with diameters of 5 μm and 6 μm . Secondary emission, and thus the AMCP gain depends on the surface rugosity. The surface rugosity depends on the detailed fabrication process of the AMCP and also varies within the length of the channel, as the top of the channel is more exposed to the etching gases during the whole process of channel etching. Furthermore, we measured a first transient AMCP signal. In the framework of another thesis the setup has been fully rebuilt for high frequency and transient measurements and first samples of generation 5 should be characterized shortly.

In the following second half of this thesis, we analyze the AMCP operation principle in detail and develop a Monte-Carlo model in order to predict the gain and timing we expect for high aspect ratio AMCPs. The model also serves as a basis to assess the limits of increasing the gain via reducing the AMCP diameter. We also incorporate the Monte Carlo model within a finite element method tool, in order to determine the effect of different geometries, which allow for

Chapter 4. AMCPs with high aspect ratio

example for high collection efficiency, on the performance of AMCPs. In the next chapter we lay the theoretical foundation for AMCP modeling.

5 (A)MCP operating principle

The operating principle of AMCPs and MCPs is electron multiplication by secondary electron emission. In this chapter we explore the signal formation within the channels, the theoretical background and the possibilities to describe it. First we explain secondary electron emission in the low energy range and then the available simulation tools. Next, we report on a probabilistic model for electron emission that is best suited to describe the formation of the electron cloud in MCPs. Then we explain the typical behavior and theoretical descriptions for the most important multiplication parameter, the secondary yield. Finally we give an overview of MCP models.

5.1 Secondary electron emission at low energies

Secondary electron emission (SEE) occurs with a certain probability in all materials when an electron or particle impinges on their surface. The emission happens in three steps. First, the arriving electron creates internal secondary electrons on its way through the material. Then these electrons travel to the surface and eventually they can escape over the vacuum barrier if their energy is higher than the electron affinity of the surface. The efficiency of secondary emission depends thus on many parameters like energy and incident angle of the incoming particle, the energy losses of the secondary electrons on their way to the surface and the potential barrier at the vacuum interface. For materials with a wide band-gap the escape depth is generally higher, as electron-electron interactions are less likely.

Figure 5.1 shows the different possible interactions of an incident electron with a material. When the electron reaches the interface, it can either be scattered elastically (figure 5.1a), or it can scatter inelastically (figure 5.1b) or be absorbed by the material. In the two latter cases, the electron impact can lead to emission of secondary electrons (figure 5.1c). Inside the material, the electron path can be described with Monte Carlo simulations, where the electron travels an average mean free path, according to the elastic scattering cross section, before it either scatters elastically, or inelastically. Inelastic scattering includes a variety of physical processes that occur when the electron travels through the material. In the low energy range these are mainly interactions with loosely bound valence electrons with binding energies of a

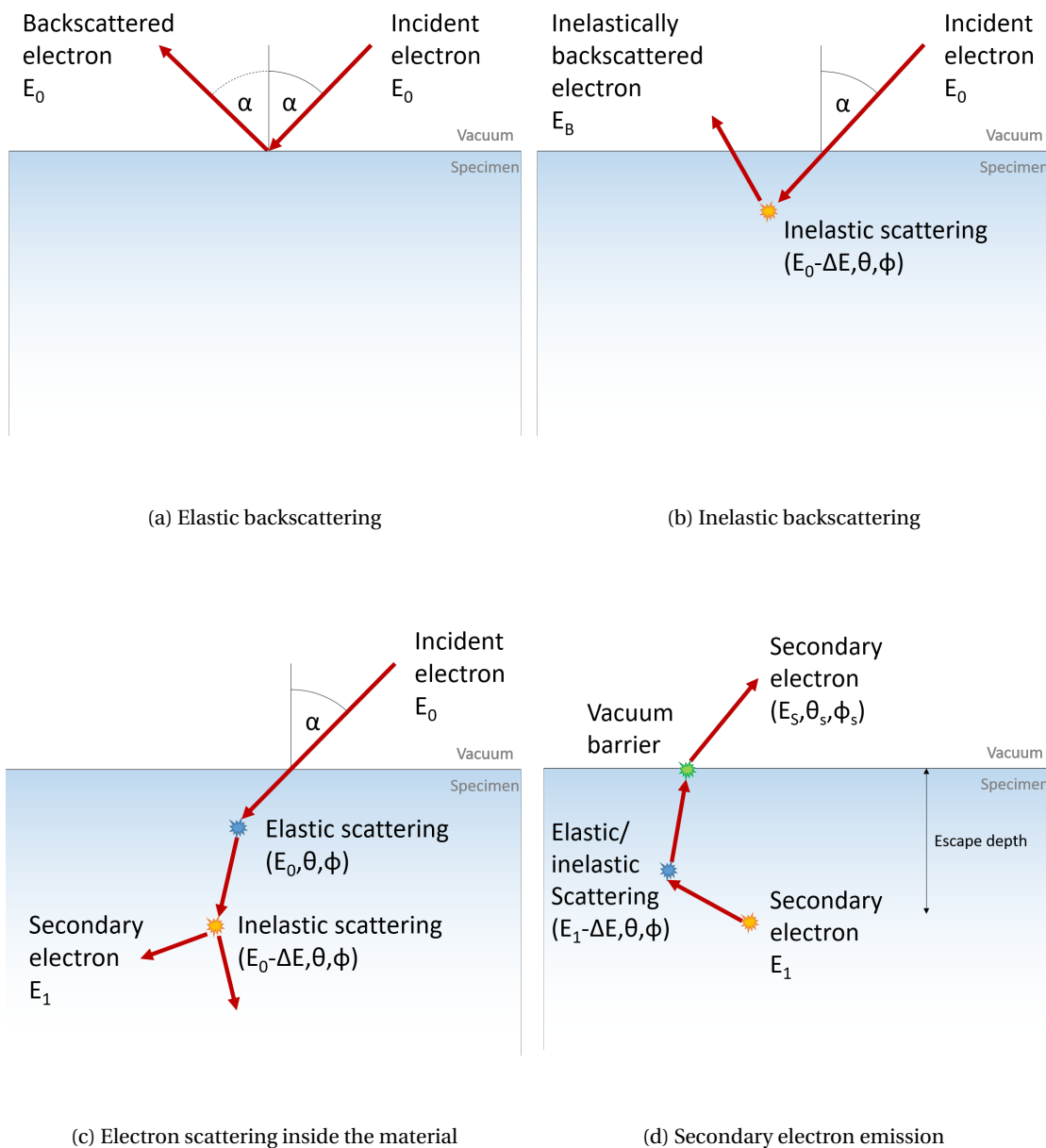


Figure 5.1 – (a) Elastic backscattering of an incident electron. (b) Inelastic backscattering of an incident electron (c) Scattering of an incident electron inside the material and secondary electron creation. (d) Secondary electron scattering inside the material and emission to the vacuum.

few eV, that can be ejected as secondary electrons, generation of plasmons (for metals) and generation of phonons (heating of the material). Generated secondary electrons need to travel to the interface and overcome the vacuum barrier to be ejected (figure 5.1d). The secondary electron emission coefficient of a material depends on the incident electron energy and angle, and on the surface morphology.

For an incident electron the number of emitted secondary electrons is defined as the secondary electron yield δ . The number of backscattered electrons is expressed by the backscattering yield η and the total electron yield σ is the sum of both

$$\sigma = \delta + \eta. \quad (5.1)$$

Secondary electrons are emitted with very low energies, the most probable secondary electron energy being a few eV. For SEM purposes, where incident energies are usually well above 50 eV, the maximum energy of secondary electrons has been defined as 50 eV [Redhead 1968]. At lower incident energies, this definition becomes arbitrary. According to this definition, and at incident energies starting from 100 eV, the SEE yield δ has been measured for a wide range of materials [Joy 1995], alkali compounds exhibiting the highest yields. In 1997 Shih et al. [Shih 1997] explained a high SEE yield with a study on hydrogenated diamond which can be generalized to other materials. They identified the last step, where the electron has to overcome the vacuum barrier, to be as important as the secondary electron's escape depth. Consequently, materials with a wide band-gap and low electron affinity yield the highest secondary electron emission. More recent studies found that the shape of the surface plays a role as well, and a higher curvature is shown to be beneficial for a high SEE yield [Dzhanoev 2015]. This effect is most pronounced for surface structures in the nanometer to micrometer range. For a more accurate description of granular surfaces shading effects also have to be taken into account. In extremely porous structures shading can reduce the SEE significantly [Swanson 2016].

Secondary electron emission in amorphous Si is comparable to that in crystalline Si, although a little higher. The largest SEE coefficient reported in literature is $\delta = 1.42$ for an incident electron energy of 500 eV, while for c-Si the maximum yield has been measured for electron energies between 250-300 eV [Seiler 1983]. Comparing the two morphologies to the earlier mentioned study [Shih 1997] on hydrogen terminated diamond, the difference between c-Si and a-Si:H can be explained by the hydrogenation of amorphous silicon. At the surface of a-Si:H present hydrogen bonds decrease the electron affinity, lowering the vacuum barrier for electrons at the interface. At the same time, its higher band gap may lead to a higher escape depth, even though the presence of defects has to be considered for the scattering cross section of free electrons. Due to the relatively low value for the SEE yield, the a-Si:H surface has to be additionally coated with a high SEE coefficient material in order to reach a high electron multiplication.

Secondary electron emission has been extensively studied for scanning electron microscopy applications, where incident electron energies start at about 1 keV. Inside the MCP, the electron energies are far below this mark. With the MCP model of Eberhardt [Eberhardt 1981] an average potential difference of 38.2 ± 3.9 V between impacts has been calculated. Similar values

can be calculated for AMCPs using Eberhardt's model [Franco 2014b], although the validity of the model for very low aspect ratios and gains is not clear and we might overestimate the potential difference in this case. Also, the number of collisions is assumed to be independent of the applied bias voltage, although the electron energy in between collisions depends on the bias voltage. Between the number of collisions of about 7 and a number of collision of 2 for aspect ratios of 13.6 and 6 respectively, and an applied voltage of 500 V in both cases, this would lead to an estimation of potential differences between 70 V and 250 V. To verify the electron energy range, the energy of electrons exiting AMCP channels has been measured, and resulted in a maximum energy of 40 eV [Frey 2019]. This fits very well to the MCP data. Electron energies inside the AMCP channels are thus assumed to be in the very low energy range, below 50 eV.

Measurement techniques to accurately measure the secondary yield at low energies have been developed recently. For pure conductive samples measurements of different facilities and Monte Carlo calculations fit well [Pierron 2017], while the measurement of dielectric samples is more challenging due to charging effects of the samples under electron irradiation. As secondary electrons are emitted a positive charge, an accumulation of holes, forms in the emitting material. The charging effect can be avoided by measuring the samples with a short pulsed electron beam and a reference probe [Belhaj 2009]. Charging effects are more pronounced in samples with high yield, which are usually insulators. The charge balance can be expressed as

$$I_{in} = I_{in}(\delta + \eta) + \frac{\partial Q}{\partial t} + I_{ev}, \quad (5.2)$$

with the incident current I_{in} , charge Q and time t , and the evacuation current I_{ev} . A study of the charge balance in insulators concludes that the effects of chemical composition is much larger than charging effects [Cazaux 2006]. Surface treatments influence the secondary electron escape probability and the structural disorder has a profound effect on the transport of secondary electrons prior to their emission. Furthermore, the secondary yield is also influenced by the specimen temperature [Belhaj 2010]. The study found that an increase in temperature increases the thermally activated conductivity, and thus the evacuation current I_{ev} inside the material, which counteracts charging.

5.2 Electron scattering simulators

Monte Carlo simulators for electron scattering are either based on stopping power relations or on dielectric function theory to describe inelastic scattering of electrons inside the material. The open source code CASINO developed by Sheerbroke University [Hovington 1997] and MONSEL developed by NIST [Villarrubia 2007] are based on the stopping power relations and are used for SEM applications. CASINO includes stopping power models for incident electron energies down to 50 eV. Below 1 keV, the models are based on experimental measurements of the energy loss function [Joy 1996]. An example for Al_2O_3 is given in [Insepov 2011]. Here, two material parameters determine the MC model: the energy spent per creation of a secondary

electron ε , typically in the range of a tens of eV, and the secondary electron escape depth λ , typically in the range of tens of Å.

Elastic scattering for electrons with energies above 200 eV is well described by Mott scattering used in the CASINO code. In Mott scattering the incoming electron is described as a plane wave. The wave is scattered when crossing the atom, resulting in a scattered wave. It comes as no surprise that this model fails at low electron energies as an energy of 200 eV corresponds to a Dirac wavelength of 62 Å. The lower the electron energy, the more atoms are involved in its scattering. Finally, this can be described as phonon scattering for energies below 100 eV. To take into account phonon scattering at low energies FEI [Kieft 2008] developed a low energy extension for CERN's particle simulator GEANT4 [Agostinelli 2003] module MuElec [?]. The low energy extension is based on dielectric function theory. One of the first electron scattering simulation tools based on the dielectric function has been developed in [Kuhr 1999]. OSMOSEE, a Monte Carlo material specific model for aluminum based on dielectric function theory has been developed at ONERA Space Institute by [Roupie 2013] taking into account interactions at low energies down to 10 eV.

As none of the above models is suited to simulate electron scattering at low energies for a wide range of materials, a Monte-Carlo electron-specimen interaction simulator has been developed by TU Delft [Verduin 2017] to describe electron scattering at low energies and for rough geometries. We use their code to simulate electron yield curves in this thesis. The code is based on dielectric function theory and is using the same physics as the low energy extension developed by Kieft. Contrary to the extension, the simulator is completely independent from GEANT4. It has been built from scratch in order to process a large number of low energy electron interactions in complex geometries by using the combined power of GPUs and CPUs [Verduin 2016].

The simulator calculates electron interactions based on the mean free path (MFP). The MFP describes electron movement in media until their next event. The interaction events of low energy electrons can be the following: Elastic scattering, inelastic scattering and boundary scattering. The MFP determines the trajectory of electrons in media, the interaction volume and the number of secondary electrons. Each scattering event has a certain probability to be elastic or inelastic and to create secondary electrons. For energies below 100 eV, the acoustic deformation potential of the material needs to be known, which is not well documented in literature. Other material parameters, like the speed of sound, density and the lattice constants are also needed. In between 100 eV and 200 eV the mean free path is interpolated from the phonon scattering curve and the Mott scattering curve. Electrons loose part of their energy through inelastic scattering events. This is described by the dielectric function of the material. For high energies this corresponds to the Bethe Bloch stopping power.

For an accurate description of electron specimen interaction of low energy electrons, with energies below 50 eV, even the low energy extension electron scattering code is not suitable. There is a lot of improvement in that area, mostly for SEM analysis, but the lack of experimental data in the low energy range means that the theory is an extrapolation of higher energy interactions. Also the effect of surface morphology is just starting to be taken into account. It is a novelty in simulation methods for SEM images to calculate edge effects [Van Kessel 2020].

Chapter 5. (A)MCP operating principle

The simulator can be used to calculate electron scattering of a rough surfaces, using the power spectral density of the surface and the method of Thorsos [Thorsos 1988], explained in [Mack 2013] to reconstruct the surface.

Novel theoretical models are being developed at very low energies of a few eV that fit well to experimental data of the investigated materials [De Vera 2019] [Astašauskas 2020], even below 10 eV [Cazaux 2012]. Models for electron scattering in compound materials are being developed as well [Hussain 2020]. A general description for the inelastic mean free path for the measurable elements and compounds still has to be elucidated at low energies to then be implemented in Monte Carlo codes for electron scattering.

In summary, there is no existing model that is suitable to directly simulate interactions within an MCP, since there are still unanswered questions about the physics of very low energy electron scattering. As a consequence, we use a probabilistic model to describe the electron multiplication process inside the MCP.

5.3 Probabilistic model for electron emission

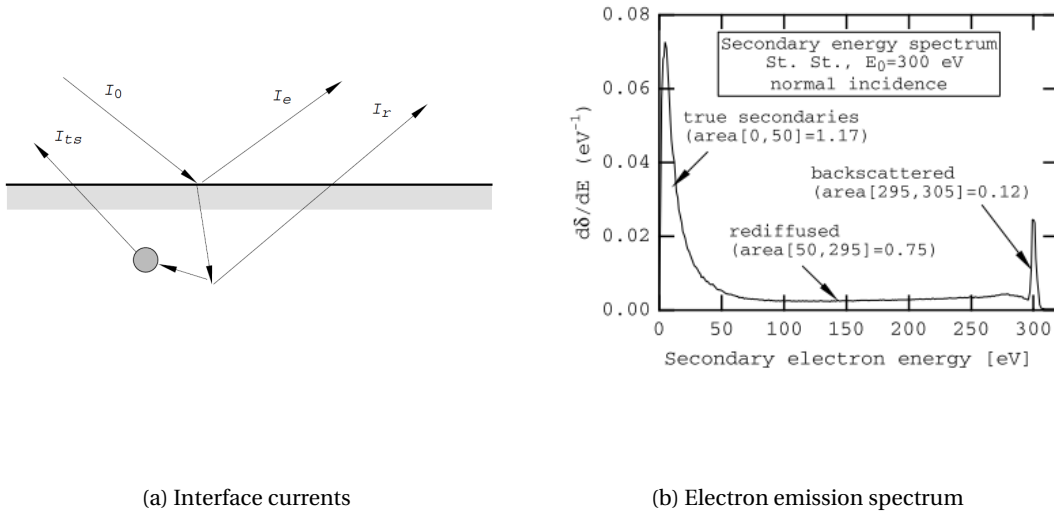


Figure 5.2 – (a) Interface currents. A probabilistic model for electron emission is developed based on measurements of the interface currents, which are the incident current I_0 , the elastically reflected electron current I_e , rediffused electron current I_r and the secondary electron current I_{ts} . (b) Electron emission energy spectrum. According to their respective energies, the electron peaks are attributed to the nature of emission. The peak at low energies are secondary electrons, and the peak around the incident energy are backscattered electrons. Electrons with energies in between are inelastically backscattered. Images taken from [Furman 2002].

A probabilistic model for electron emission, including elastic and inelastic backscattering, has been developed by [Furman 2002]. The model is based on total emission yield $\sigma(E_{in}, \theta_{in})$

measurements and measurements of the electron emission energy spectrum $\frac{d\sigma}{dE}$ for an incident energy E_{in} and incident angle θ_{in} . Alternatively the emission energy spectrum can be calculated using Monte-Carlo methods. The spectrum consists of three distinct parts, see figure 5.2b, from which the relative probability of the three types of events, secondary emission P_{SE} , elastic P_{BS} and inelastic backscattering P_{IBS} , can be calculated. Secondary electrons have very low energies and make up the first part of the spectrum. The area of the peak corresponds to the secondary electron part δ of the total yield σ . Elastically backscattered electrons are all electrons with energies around the incident electron energy. The area of the peak at this energy corresponds to the amount of backscattering η . The remaining area can be associated with inelastically backscattered electrons, also called rediffused electrons. The total electron yield function σ is the sum of the three distinct yield functions:

$$\sigma = \eta_e + \eta_{ie} + \delta = \frac{I_e + I_{ie} + I_{ts}}{I_0} \quad (5.3)$$

with the incident current I_0 , the elastically backscattered current I_e , the inelastically backscattered current I_{ie} and the secondary electron current I_{ts} . Note that the sum of the emitted currents can be greater than one, due to the emission of secondary electrons.

The yields η_e and η_{ie} correspond to the probability of elastic and inelastic backscattering. On an event basis, these two events can either yield 1 or 0 emitted electrons. The yields are calculated from their relative probabilities P_{BS} and P_{IBS} drawn from the emission spectrum and from the total emission yield as

$$\eta_e = P_{BS} \cdot \sigma \text{ and } \eta_{ie} = P_{IBS} \cdot \sigma. \quad (5.4)$$

Elastic backscattering and secondary emission are mutually exclusive, while the yields are calculated from an experimental setting where they happen at the same time for distinct incident electrons. To correct for this discrepancy, the probability of secondary emission should be calculated using a modified secondary yield for mutually exclusivity. The corrected secondary yield is calculated from the total emission yield σ and the backscattering yields η_e and η_{ie} derived from the electron emission energy spectrum as

$$\delta = \frac{\sigma - \eta_e - \eta_{ie}}{1 - \eta_e}. \quad (5.5)$$

This correction is especially important at low energies, where backscattering is the main emission mechanism, and, without using this correction, the secondary emission would be underestimated. The number n of emitted electrons for a given secondary yield δ can then be calculated using the Poisson distribution

$$P(n, \delta) = \frac{\delta^n \cdot e^{-\delta}}{n!}, 0 \leq n < \infty \quad (5.6)$$

with the average number of emitted secondary electrons $\langle n \rangle = \delta$. $P(n, \delta)$ is the probability of emitting a number of n secondary electrons for a secondary yield δ .

Additionally to the number n of secondary electrons, the emission angles θ_{SE} , φ_{SE} and emission energy E_{SE} for each secondary electron are also drawn from probability distributions. The secondary electron emission angle is known to follow a cosine distribution according to Lambert's law

$$P(\theta_{SE}) = \frac{1}{\pi} (1 + \cos(2\theta_{SE})) \quad (5.7)$$

where θ_{SE} is the emission angle relative to the surface normal, between 0 and $\pi/2$. The azimuthal angle φ_{SE} is independent of this distribution and can take all values between 0 and 2π

$$P(\varphi_{SE}) = \frac{1}{2\pi}. \quad (5.8)$$

The angular emission distribution function differs from Lambert's law as a function of the emission energy spectrum. Lambert's law would hold true for a most probable emission energy (MPE) of 1 eV. From calculations at high incident energies where the incident energy $E_{in} >$ the energy with maximum yield E_m an isotropic distribution of secondary electrons inside the material can be assumed. The transmission probability is calculated according to the law of refraction at the interface

$$\sqrt{E_s} \sin \theta_i = \sqrt{E_k} \sin \theta_{SE} \quad (5.9)$$

with the secondary electron energy E_s and angle θ_i inside the material and the secondary electron emission energy E_k and angle θ_{SE} . The angular distribution has been calculated for Si with different electron affinities resulting in different MPEs and consequently in different angular distributions [Cazaux 2010b]. No time dependent variation of the angular distribution of secondary emission has been found according to simulations of [Li 2019].

The secondary electron energy distribution is given by the emission energy spectrum. In general, the emission energy of secondary electrons is well below 50 eV and, at low incident energies, depends on the incident energy. The emission energy spectra can be measured and calibrated as shown in [Villemant 2017]. For higher incident energies, calculated emission energy spectra tend to be used as measurements are time intensive and electron emission spectra need to be measured for several energies E_{in} and angles θ_{in} . Especially at higher incident energies, Monte-Carlo calculations of the spectra are quite accurate and the emission energy spectrum of secondary electrons can be modeled. The angular and energetic distribution of secondary electrons vary depending on the work function [Cazaux 2010b]. In figure 5.3a we show the angular spread due to a variation of the most probable emission energy. The secondary electron energy distribution $\partial\delta/\partial E_s$ of semiconductors is modeled as

$$\partial\delta/\partial E_s = C \cdot E_s / (E_s + \chi - E_G)^2 (E_s + \chi)^{5/2}, \quad (5.10)$$

with the secondary electron emission energy E_s , a normalization factor c , the electron affinity χ and the band gap E_G . For silicon $\chi = 3.2$ eV and $E_G = 1.12$ eV. The most probable emission

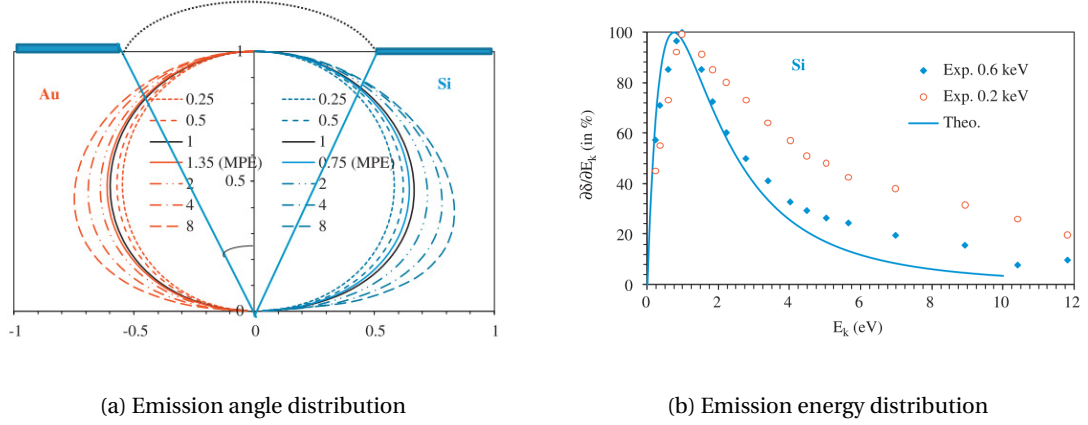


Figure 5.3 – (a) Secondary electron emission angle θ_{SE} distribution calculated for Au and Si for normalized angles from -1 to 1, corresponding to -90° to 90° . For high incident electron energies, the angular distribution inside the material can be assumed to be isotropic. From the most probably emission energy (MPE), the angular distribution of emission can be calculated using the law of refraction at the interface. The emission angle distribution varies with the MPE. (b) Emission energy spectrum of Si. Both taken from [Cazaux 2010b]

energy for Si is at 0.75 eV. The equation is modified for insulators as follows

$$\partial\delta/\partial E_s = C \cdot E_s / (E_s + \chi)^3. \quad (5.11)$$

This distribution has its MPE at about $\chi/2$, typically at a value below 0.5 eV. No dependence of the incident energy is assumed. The equations were developed according to data collected at high incident energies. They seem to fit less at low energies as shown in figure 5.3b for silicon. The energy distribution of secondary electrons will clearly be different for very low incident energies below 50 eV.

5.4 Secondary electron emission yield modeling

Semi-empirical theories have been developed by [Kanaya 1978] [Seiler 1983] [Lin 2005] and others, to describe the secondary yield δ , its dependence on the incident energy and the incident angle. The secondary yield is defined as

$$\delta = \int n(x, E) P_s(x) dx, \quad (5.12)$$

where E is the incident electron energy, n is the number of secondary electrons created inside the material at depth x and $P_s(x)$ the surface escape probability. n is defined as proportional to the average incident electron's energy loss $\frac{dE}{dx}$ with

$$n(x, E) = -\frac{1}{\varepsilon} \frac{dE}{dx} \quad (5.13)$$

and the energy ε required to create a secondary electron. The secondary yield at normal incidence is defined as

$$\delta(E) = P_s(0) \frac{\lambda \cdot E}{\varepsilon \cdot R_p} \left(1 - \exp \left(-\frac{R_p}{\lambda} \right) \right) \quad (5.14)$$

with the range R_p of the primary electron in the material, the escape depth λ of a secondary electron and the surface escape probability $P_s(0)$. The range of the primary electron in the material is described by the power law with

$$R_p = b \cdot E^n. \quad (5.15)$$

b is a material constant and $1 < n < 2$. The parameter n in the power law is arbitrary and does not have a physical meaning. [Lin 2005] derived the so-called universal law for SEE yield that is independent of the material constants

$$\delta = \delta_m \cdot 1.28 \left(\frac{E}{E_m} \right)^{-0.67} \left(1 - \exp \left(-1.614 \left(\frac{E}{E_m} \right)^{1.67} \right) \right). \quad (5.16)$$

δ_m and E_m are the maximum secondary yield and the energy at which the maximum yield occurs. The author of [Cazaux 2006] questions the assumption that the energy dissipation is constant to the depth of the range R . For a more realistic model, Cazaux proposed an isotropic rather than a linear depth range inside the material. The author describes the primary energy dissipation with a sphere, starting from a center C near the surface. C depends on the material, as this center would be closer to the surface for heavy materials and more in depth for light materials. The location of C in depth x relative to the range R is

$$k = \frac{x_C}{R}. \quad (5.17)$$

The secondary yield is then expressed as a function of k that varies for different materials. He also describes how charging affects the measured secondary yield for insulators.

Figure 5.4a shows the energy range where charging happens in an insulator and figure 5.4b shows how this can potentially reduce the measured secondary yield, depending on the incident fluence $I_0 \tau / S$ where τ is the time interval and S the illuminated area. As mentioned in section 5.1, the main contributor to changes in the secondary yield is the vacuum barrier that the electrons have to overcome. Impurities and oxidation result in a change in the work function (for metals) and the electron affinity respectively (for semiconductors and insulators). An increase in electron affinity increases the effective potential barrier for the electron to be emitted into the vacuum, shown in figure 5.5a taken from [Cazaux 2010a], and therefore decreases the emission probability. The secondary yield of pure KCl in figure 5.5b shows a shift in the SEY, where the SEY of the clean surface decreases dramatically with impurities and oxidation.

Normally, the secondary yield curves follow a pattern of growing yield for higher angles of

5.4. Secondary electron emission yield modeling

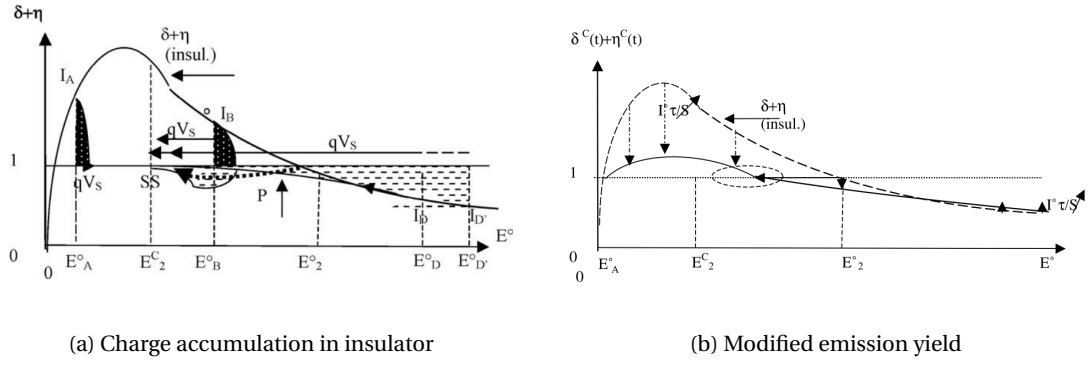
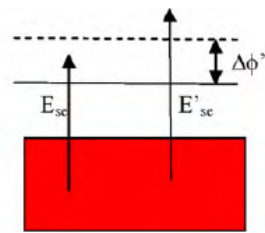
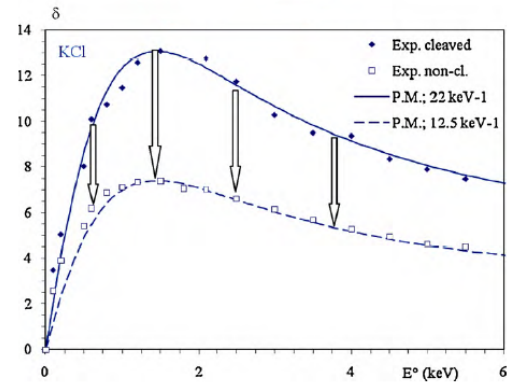


Figure 5.4 – (a) Effect of charging in an insulator on the emission yield spectrum at different energies. Positive charging accumulates in areas where the total emission yield is above 1. Negative charging in areas that have a yield below 1 at high incident electron energies. (b) Modification of total emission yield curve due to charging under an incident electron fluence $I_0 \tau / S$ where τ is the time interval and S the illuminated area. From [Cazaux 2006]



(a) Work function variation



(b) Measured and simulated secondary yield for different work functions

Figure 5.5 – (a) Potential barrier for secondary electrons and (b) its effect on the secondary yield of KCl. Both taken from [Cazaux 2010a]

incidence. Hereby, the incident angle is defined as the angle relative to the surface normal. A growing SEY for higher angles of incidence can be well explained by a lower penetration depth and therefore a higher escape probability for secondary electrons. Especially for high incident energies the incident angle influences the penetration depth significantly. A simple relation for the angular dependence of the secondary yield function $\delta(\theta)$ is given as

$$\delta(\theta) = \delta(0^\circ)(\cos\theta)^{-n}. \quad (5.18)$$

The angular dependence has been improved by [Bundaleski 2015] to fit experimental data and is then calculated according to:

$$\delta(E, \theta) = \frac{0.5 \cdot \lambda}{\varepsilon \cdot b \cdot \cos\theta} \cdot \frac{1 - \exp\left(-\frac{b \cdot E^{n \cdot \cos\theta}}{\lambda}\right)}{E^{n-1}}. \quad (5.19)$$

The model fits well to experimental secondary yield measurements of flat surfaces of selected materials.

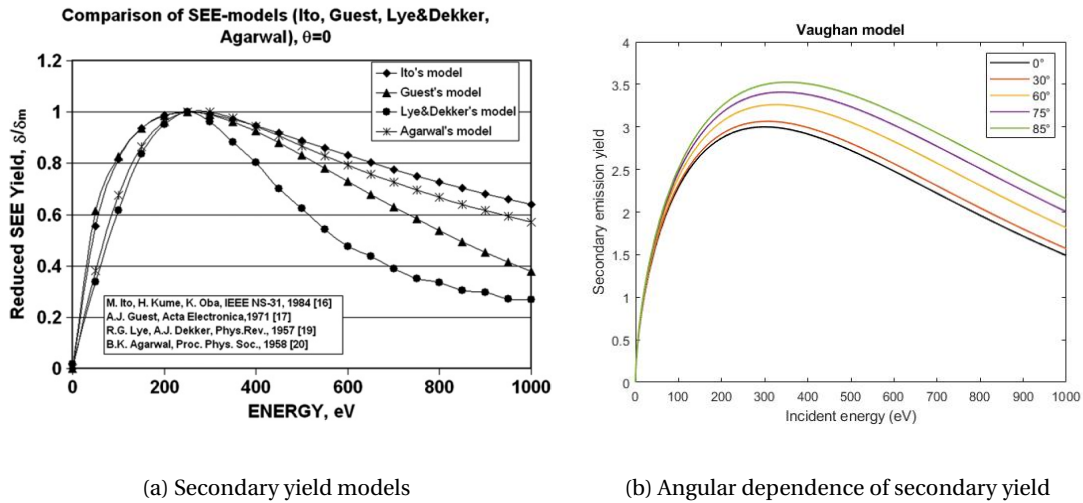


Figure 5.6 – (a) Comparison of different empirical models for the incident electron energy dependence of the secondary yield used for MCP simulations [Insepov 2010]. For comparison the yield is plotted relative to the maximum yield and with the maximum yield at a fixed energy. (b) Angular dependence of secondary electron yield in glass MCPs according to [Kruschwitz 2011]. Experimental results from MCP gain measurements were fitted to the SEY model of [Vaughan 1989].

A variety of empirical models exist that describe the secondary yield dependence on the incident electron energy and angle. An overview of four different approaches for SEY curves at normal incidence is given in [Insepov 2010]. The yield curves are shown in figure 5.6a.

According to the model of [Agarwal 1958] the yield δ is calculated from

$$\delta = \delta_m \cdot \frac{2 \left(\frac{E}{E_m} \right)}{1 + \left(\frac{E}{E_m} \right)^{1.85(2Z/A)}}, \quad (5.20)$$

where Z is the atomic number and A the atomic weight. The formula of [Lye 1957] plotted in figure 5.6a, has been improved by [Vaughan 1989]. The angular dependence of the secondary electron yield δ can then be modeled with:

$$\delta(E, \theta) = \delta_m(\theta) \left(\frac{E}{E_m(\theta)} \exp \left[1 - \frac{E}{E_m(\theta)} \right] \right)^s, \quad (5.21)$$

where E and θ are the incident energy and angle and s is a parameter chosen to best fit the data. E_m and δ_m are defined as

$$E_m(\theta) = E_m(0) \left(1 + k \frac{\theta^2}{2\pi} \right) \quad (5.22)$$

and

$$\delta_m(\theta) = \delta_m(0) \left(1 + k \frac{\theta^2}{2\pi} \right). \quad (5.23)$$

$E_m(0)$ is the energy of maximum secondary yield $\delta_m(0)$ at normal incidence. The parameter k is a constant between 0 and 2 and indicates the surface smoothness. An example for the modeled SEY of MCP glass is shown in figure 5.6b, parameters are taken from [Kruschwitz 2011]. Another model, specifically for the secondary yield of MCPs, has been developed by [Guest 1971], shown in figure 5.6a, where

$$\delta(E, \theta) = \delta_m(0^\circ) \cdot \left(\frac{E}{E_m} \sqrt{\cos \theta} \right)^\beta \cdot \exp \left[\alpha (1 - \cos \theta) + \beta \left(1 - \frac{E}{E_m} \sqrt{\cos \theta} \right) \right]. \quad (5.24)$$

α is a material constant and β a parameter fitted to the yield curve at normal incidence. Another model for the SEY of MCPs shown in figure 5.6a has been developed by [Ito 1984]. Here, the angular dependence of the secondary yield is

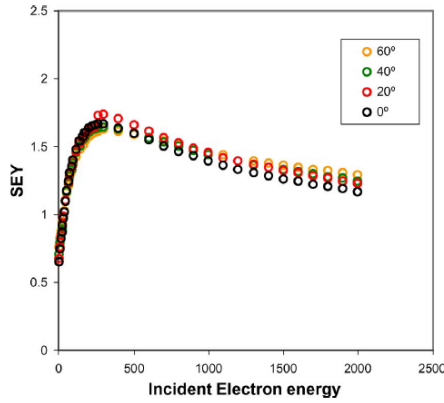
$$\delta(E, \theta) = \frac{4 \cdot E \cdot \delta_m(\theta)}{E_m(\theta) \cdot \left(1 + \frac{E}{E_m(\theta)} \right)^2} \quad (5.25)$$

with

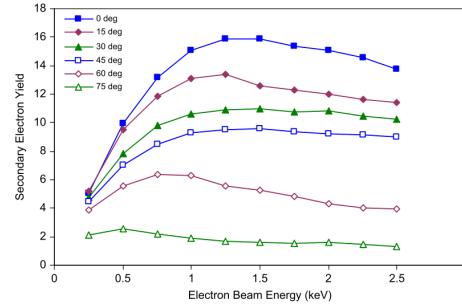
$$\delta_m(\theta) = \delta_m(0^\circ) \exp [\alpha (1 - \cos \theta)] \quad (5.26)$$

and

$$E_m(\theta) = \frac{E_m(0^\circ)}{\sqrt{\cos \theta}}. \quad (5.27)$$



(a) Measured secondary yield of a rough Cr sample



(b) Measured secondary yield of CVD diamond

Figure 5.7 – Exceptional angular dependence of the total electron emission yield measured for (a) a rough Cr sample [Balcon 2012] and measured for (b) a CVD diamond surface [Lapington 2009].

It remains challenging to model the secondary yield curves at low energies as the underlying mechanisms of electron scattering are not yet well enough known. Even at higher energies the real surface morphology, the precise atomic composition and charging effects have a huge impact on electron emission and cannot easily be reproduced by models. Measurements show how the angular dependence of the yield varies with the surface morphology. In [Balcon 2012] the SEY of two Cr samples with different surface morphology shows a distinct behavior. In this case a rough sample does not show any change in SEY when measured at different angles of incidence, as shown in figure 5.7a, while a flat Cr sample shows the typical behavior of growing SEY with growing incident angle. Furthermore, the SEY curves of CVD diamond were measured at a variation of incident angles [Lapington 2009]. The measured secondary yield curves show an opposite trend of decreasing yield for higher angles of incidence, see figure 5.7b. Besides surface roughness effects, that can introduce unexpected behavior of the angular dependence of the yield curves, the surface composition is the main contributor that needs to be known in order to predict secondary yield curves.

5.5 Microchannel plate modeling

A very simple relation between the gain G , the secondary emission coefficient δ and the number of collisions n has already been stated by [Ladislav Wiza 1979] with $G = \delta^n$. The MCP channel is represented as discrete dynodes, see figure 5.8a, which happens to agree quite well with experimental data collected in the early days. The gain is exponentially dependent on the number of collisions. This number grows with larger channel length and smaller channel

apertures, which corresponds to the aspect ratio of the channels. The gain can be further enhanced by tilting the MCP to an optimal grazing angle. A gain model was further developed by Eberhardt around 1980 [Eberhardt 1979], [Eberhardt 1981]. The MCP gain is calculated using the following equation:

$$G = \delta_1 \cdot \delta^{n-1} = \delta_1 \cdot \left(\frac{V}{n \cdot V_c} \right)^{k(n-1)} \quad (5.28)$$

where δ_1 is the SEE coefficient of the first collision. The remaining $n - 1$ collisions have an average SEE coefficient of δ , which is described by the bias voltage V , the first crossover potential V_c , which is the channel voltage at which the gain of each multiplication event is unity and k , a proportionality constant related to the curvature of the secondary emission yield curve. The energy gained by an electron travelling through the axial part z of the channel with the electric field ϵ is related to the bias voltage V . Thus, the secondary emission function $\delta(V_z)$ can be determined as $\delta = \left(\frac{V_z}{V_c} \right)^k$. The model describes the MCP response to an input current that is sufficiently large to neglect statistical variation of single electrons. The model fits experimental data of MCPs in a limited range of conditions. It fits best when the fabrication and thereby the surface morphology and material is unaltered for MCPs with different ARs. Even then, with increasing aspect ratio and for high output charges, the gain dependence of real MCPs is nonlinear, as charging effects increase in these conditions. According to the model, the same number of stages is assumed for different bias voltages, which is unlikely as the impact point of the electrons depends on the acceleration voltage.

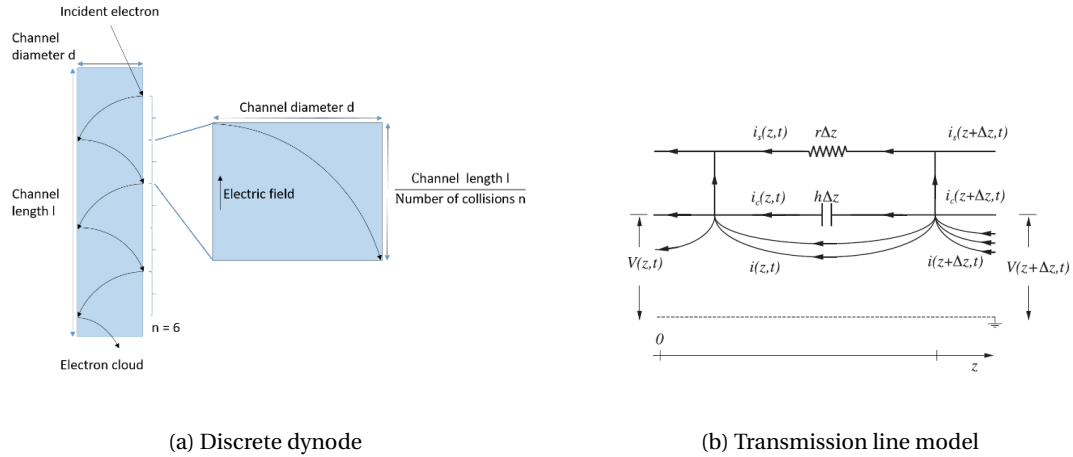


Figure 5.8 – (a) Simple representation of a discrete dynode with a fixed number of stages for electron multiplication. This simplification was used in the first MCP models. (b) Electrical network describing an element between two stages of the MCP channel in the time dependent transmission line model, taken from [Giudicotti 2011].

The idea of a constant number of stages has been further developed in electrical models, the so called transmission line models. Again, this kind of model is valid for MCP response to an input charge current, not for single electrons. A simple model to describe saturation in

MCPs has been derived by [Shikhaliev 1999]. Three different kinds of saturation occur in a microchannel plate. The first two kinds of saturation, space charge saturation and positive wall charge saturation, occur when the MCP is operated in pulsed mode at a frequency, where the gain can be completely recovered between events. Space charge saturation can then occur for MCPs with high gain and wide channels, when the electron cloud leads to a decrease in the electric field of the channel. Wall charge saturation occurs when the electric field is neutralized due to the positive charge in the channel wall. The third kind is current saturation and creates one of the main bottlenecks of MCPs. Current saturation occurs when MCPs are operated above the frequency where the gain can be recovered. Then a significant part of the bias current goes into the creation of the avalanche and the electric field becomes nonuniform. The basis of the model is current conservation. For an input current i_0 , the conduction current I_0 is increased by ΔI and the total current is:

$$I_0 + \Delta I + i_0 = I(0) + i(0) = I(z) + i(z), \quad (5.29)$$

where z is the coordinate along the channel axis. Saturation depends largely on the resistance R along z . The resistance at a point z is $R(z) = R_0 z/L$, where L is the channel length. Equation 5.29 leads to the set of differential equations

$$\frac{di}{dz} = \frac{1}{L} i F(L \frac{dV}{dz}) \quad (5.30)$$

$$\frac{L}{R} \frac{dV}{dz} + i = I_0 + \Delta I + i_0. \quad (5.31)$$

V is the bias voltage of the channel and the initial conditions of the equations are $V(0) = 0$, $V(L) = V_0$, $i(0) = i_0$, and $i(L) = i_0 G$ with the gain G and the function $F(V_0) = \ln G$. The gain is then calculated for an ideal and non ideal detector. The gain function F is assumed to be linear in an ideal detector model and approximated by a hyperbolic function in a non ideal detector model. Consequently, the authors suggest a nonlinear resistance distribution along the MCP channel to extend the dynamic range of the detectors.

An up to date transmission line model incorporates the charging effects leading to saturation, and can describe the time dependent behavior of MCPs [Giudicotti 2011]. One element of the channel, between two multiplication stages is shown in figure 5.8b. Here $r = R/L$ is the resistance per unit length with the resistance R and the channel length L . The inverse capacitance per element is $h = \frac{1}{C \cdot L}$, where C is the capacitance of the channel. The time dependent current that forms the signal $i(z, t)$ is calculated along the axis. The multiplication of the signal is described by the gain equation of a continuous multiplier:

$$\frac{1}{i(z, t)} \frac{\partial i(z, t)}{\partial z} = k \cdot \ln \left(\frac{L}{V_c} \frac{\partial V(z, t)}{\partial z} \right). \quad (5.32)$$

The possibility to model real conditions like saturation is introduced by the term for the time

dependent strip current i_S

$$i_S(z, t) = I_S + I(z, t) \quad (5.33)$$

and the voltage

$$V(z, t) = \frac{V_S}{L} z + \Phi(z, t) \quad (5.34)$$

where V_S is the constant external bias voltage and $I_S = \frac{V_S}{R}$ the constant strip current. $I(z, t)$ and $\Phi(z, t)$ are the excess strip current and voltage respectively due to an input signal that is not vanishingly small. A new gain equation is formulated that incorporates the perturbations:

$$\frac{1}{i(x, t)} \frac{\partial i(x, t)}{\partial x} = G + \ln \left(1 + \frac{1}{v_s} \frac{\partial \Phi(x, t)}{\partial x} \right) \quad (5.35)$$

with $x = k \cdot z$, $G = \ln \left(\frac{V_S}{V_m} \right)$ and $v_s = \frac{V_S}{k \cdot L}$. The term $\frac{1}{v_s} \frac{\partial \Phi(x, t)}{\partial x}$ is the ratio between the perturbed $E(x, t)$ and the unperturbed electric field E_S in the channel and expressed as

$$\psi(x, t) = \frac{1}{v_s} \frac{\partial \Phi(x, t)}{\partial x} = \frac{E(x, t)}{E_S} = e^{-t/RC} \left[\psi(x, 0) + \frac{1}{Q_S} \int_0^t e^{-t'/RC} i_W(x, t') dt' \right], \quad (5.36)$$

where RC is the channel multiplier time constant, $i_W(x, t')$ the excess wall current and Q_S is the total charge initially stored in the channel. Using the time dependent TLM model allows to deduce saturation parameters using the measured output current of MCPs. For this the dependence of the electric field perturbation on the wall charge $Q_{W0}(t)$, the initial charge $Q_0(t)$ and the signal charge $Q(x, t)$ is defined as

$$\psi(x, t) = \psi(x, 0) + \frac{Q_{W0}(t) + Q_0(t) - Q(x, t)}{Q_S}, \quad (5.37)$$

Finally, the time dependent gain at each point of the channel is

$$g(x, t) = \exp \left[Gx + \int_0^x \ln \left(1 + \psi(x', 0) + \frac{Q_{W0}(t) + Q_0(t) - Q(x', t)}{Q_S} \right) dx' \right] \quad (5.38)$$

These equations and the solutions found using perturbation theory can describe the saturation behaviour of the MCP gain $g(z, t)$, the recovery time and the output current to be expected from consecutive events when the channel is not yet fully restored.

MCP response to single electron or single photon incidence has to be modeled following the trajectories of each single electron, using a probabilistic description of electron emission. This kind of models are taking into account the varying secondary emission coefficient depending on the incident energy and the incident angle. While the existing models all use their respective secondary yield models and electron emission energy dependencies, the models share the same basis of probability functions for electron emission embedded in their geometry. Probabilistic modeling of electron emission has been described in section 5.1. The actual number of secondary electrons n per event is calculated from a Poisson distribution, using

equation 5.6, with the calculated secondary yield δ as the mean value. The secondary electron emission angles are chosen according to the cosine law, equations 5.7 and 5.8.

A first 2D Monte Carlo model for MCPs simulating the charge cloud in a channel, including electron energies and angles, is described in [Price 2001]. For this model secondary emission curves have been fitted to the experimental data. The semi-empirical law for the incident energy dependence of the secondary yield at normal incidence, equation 5.14, was used. Here, the angular dependence of the secondary yield is defined as

$$\delta(E_{in}, \theta) = \delta(E_{in}, \theta = \pi/2) \exp(P(E_{in}) \cdot (1 - \sin \theta)) \quad (5.39)$$

with a function $P(E_{in}) = 0.7664 - 1.533 \exp(-3.598E_{in})$, the electron energy E_{in} in keV and the incident angle θ contrary to the common definition, here defined as the angle of incidence relative to the surface. The electron emission energy distribution was assumed to be independent of the incident electron energy. The probability distribution for the secondary electron emission energy E_s was formulated as

$$f(E_s) = C \left(\frac{E_s}{E_{av}} \right)^\beta \exp\left(\frac{-\gamma E_s}{E_{av}} \right), \quad (5.40)$$

where C is a normalization factor, E_{av} is the average emission energy, and β and γ are fit parameters for lead silicate glass. Backscattering of electrons was not taken into account. Endspoilage of the MCP channel happens when the electrode coating reaches into the channel and a part of the channel wall is coated with a metal at the MCP channel exit. The 2 dimensional electric field including the effect of a variable length of metallic endspoilage was calculated. Furthermore, the effect of wall charging was taken into account using a static relation for the electric field dependence on the wall current and the changing conductivity of the wall material with the accumulation of charges along the depth of the channel. The change of the relative electric field E_r along the channel axis x was expressed as

$$\frac{dE_r}{dx} = -\frac{4E_s}{E_0 E_R D^2} \frac{(1 - E_r)(\delta - 1)}{\left(1 + 2AqE_0^2 E_R \frac{(1 - E_r)}{(1 + AqE_0^2 E_R^2)}\right)}. \quad (5.41)$$

with the unperturbed electric field E_0 at the entrance of the channel, the channel diameter D and $A = 1/W$ where W is the electron-hole pair creation energy. So, additionally to the electron energies and angles, gain values for the operation of MCP in current saturation was calculated. Identical assumptions were used in a 3D Monte Carlo model for MCPs [Tremsin 2008]. The static axisymmetric E-field of the channel was calculated in 3D and the aforementioned electron emission parametrization were used to calculate the MCP output charge for a variation of saturation modes and endspoilage parameters.

In [Kruschwitz 2011] a time dependent Monte Carlo model has been developed to calculate the response of MCPs to sub-nanosecond bias voltage pulses. Contrary to the earlier models, this model takes into account backscattering and energy conservation of the secondary electrons. Like earlier models, this is a one channel model. Thus, cross talk or pore bleaching effects,

where the avalanche in one channel affects the electric field in adjacent channels were not taken into account. The electron emission energy E_s is drawn from a probability distribution, which is similar to the one of the presented 2D models:

$$f(E_s) = C \exp\left(-\frac{[\ln(E_s/E_{MP})]^2}{2\sigma^2}\right). \quad (5.42)$$

The most probably energy is $E_{MP} = 2.3\text{eV}$, $\sigma = 0.65$ and C is again a normalization factor. Here as well, the secondary electron energy distribution does not depend on the incident electron energy E_i . Energy conservation is implemented by sampling the energies of secondary electrons for one incident electron until the condition $\Sigma E_s \leq E_i$ was met. The secondary yield is parameterized according to the empirical SEY model of [Vaughan 1989], equations 5.21-5.23, and shown in figure 5.6b. Secondary emission only happens, when the electron is not backscattered. The probability for elastic backscattering η_{el} is calculated from

$$\eta_{el}(E_i) = \frac{(\sqrt{E_i + E_0} - \sqrt{E_i})^2}{(\sqrt{E_i + E_0} + \sqrt{E_i})^2}. \quad (5.43)$$

E_0 is an unknown parameter, fitted to their data with E_0 about 170 eV. Electrons that are backscattered continue along the channel keeping their incident energy, while the radial component of the velocity is reversed. Saturation in the channel is taken into account by calculating the effect of the charge cloud in the channel on 1) the radial field, and thereby the time of flight of the electrons and 2) the axial field and thereby the electric field strength. The effect of wall charges are not taken into account as, with its timescale of ms, it is irrelevant for the application of this model, which is aimed to describe single photons and a sub nanosecond time dependent bias voltage pulse. Gain saturation, and the gain as a function of time, called the gate profile, for MCPs with diameters down to $2\mu\text{m}$ were calculated. The time lag of secondary electrons in the range of hundreds of attoseconds is negligible, even for time dependent models, as it is much shorter than the transit time. It is assumed in the model that secondary electrons are generated instantaneously. With these assumptions the signal transit time is calculated and seems to fit well to the handful of existing experimental data.

MCP Monte Carlo models have been further developed to take into account parallel channels for an accurate description of noise in MCPs. This is done by calculating parallel and serial amplification stages [Shymanska 2015b]. The mean and variance of the entire multiplication process can then be calculated by the mean and variance of the separate sequential and parallel stages. For k sequential stages and n parallel stages, $p_k(v)$ describes the probability distribution of the number of electrons at the k -th stage, produced by one electron at its input. The generating function of the probability distribution function (PDF) of the k -th stage $p_k(v)$ is

$$q_k(u) = \sum_{v=0}^{\infty} u^v p_k(v), u \leq 1. \quad (5.44)$$

Chapter 5. (A)MCP operating principle

The generation function for the PDF of the N -th stage is

$$Q_N(u) = q_0(q_1(q_2(\dots(q_N(u))\dots))). \quad (5.45)$$

Using the substitution $v = \ln u$ the generation function becomes

$$h_k(v) = \ln \sum_{v=0}^{\infty} e^{\nu v} p_k(v) \quad (5.46)$$

for the k -th stage and

$$H_n(v) = \ln \sum_{v=0}^{\infty} e^{\nu v} P(v) \quad (5.47)$$

for the N -th stage. Using the properties of the logarithmic function, the derivative of $H_n(v)$ with respect to v and setting $v = 0$, the mean value of the probability function at the N -th stage $P_N(v)$ can be calculated as

$$M = m_0 m_1 \dots m_k \dots m_N = \prod_{k=0}^N m_k. \quad (5.48)$$

The second derivative can be used to calculate the variance. The electron can be multiplied by one of n parallel paths with the probability ρ_k of choosing the k -th path. Each path gives an average of g_k particles at the output with a variance of v_k . The probability distribution of the number of particles v at the output of the k -th path would be $\varphi_k(v)$. The gain of the entire system is then calculated from the probability distribution $\Phi(v) = \sum_{k=1}^n \rho_k \varphi_k(v)$

$$G = \sum_{v=0}^{\infty} \Phi(v) v = \sum_{k=1}^n \rho_k \sum_{v=0}^{\infty} \varphi_k(v) v = \sum_{k=1}^n \rho_k g_k. \quad (5.49)$$

The variance of the entire system can be calculated according to

$$V = \sum_{k=1}^n \rho_k v_k + \sum_{k=1}^n \rho_k g_k^2 - G^2. \quad (5.50)$$

The sums here are replaced by integrals for the continuous systems of MCP channels. This kind of model has been used to investigate the effect of high emissive layers on noise of MCPs [Shymanska 2015a], as the jitter due to low secondary yield inside the MCPs channels is known to be a noise factor. The secondary yield model of [Guest 1971] shown in figure 5.6a and the energy distribution function of [Yakobson 1966] with

$$P(E) = 2.1 \cdot E_{av}^{-1.5} \cdot \sqrt{E} \exp\left(-1.5 \frac{E}{E_{av}}\right) \quad (5.51)$$

were used here.

This summarizes the most important MCP models. All of them are tailored to their specific application and experimental conditions. There is no universal model that can describe the

behavior of MCPs under all kinds of irradiation and biasing conditions, with different coatings, geometries and surface morphologies.

For the work of this thesis we use the probabilistic description of electron emission and incorporate it into a Monte Carlo model. This allows us to describe electron trajectories and the formation of the electron cloud in AMCPs. Similar to the approach of [Kruschwitz 2011] we incorporate backscattering and energy conservation into our model. While the secondary yield, secondary emission spectra and backscattering dependencies were fitted to MCP gain measurements in their case, we deduce all of these parameters from electron emission measurements of the materials used in AMCPs: amorphous silicon, AlO_x and MgO . This is shown in the following chapter. The goal of this approach is to develop an AMCP model that incorporates the angular dependence of all parameters, so that the model can be used for AMCP geometries that differ from the cylindrical channels of MCP.

6 Electron emission in AMCPs

In this chapter we present the electron emission characteristics of AMCP materials, which have been measured and simulated in order to generate the input values for a complete Monte Carlo model of electron trajectories in AMCPs. The electron emission measurements were done using a setup dedicated to secondary emission measurements [Belhaj 2009] located at the ONERA Space Institute in Toulouse. The emission spectra, as well as the total emission yield were measured on layers of a-Si:H and on atomic layer deposited AlO_x and MgO at incident angles ranging from normal incidence to 70° incidence. Additionally, the total emission yield was calculated using a Monte Carlo model for electron-specimen interaction, low energies included, developed for SEM image analysis. The theoretical foundations of the model are those presented in chapter 5.2 and the code has been developed by TU Delft. According to our measured and simulated values, compared with those from the literature, we derive the parameterization for the AMCP single channel model and the AMCP model for non cylindrical shaped channels, which are both presented in the following chapters.

In order to model electron trajectories, the electron emission energy needs to be known. As we have limited measurements of the emission energy distribution dependence on the incident energy, we separate the electron emission spectrum into backscattered electrons and secondary electrons. For elastically backscattered electrons, we know that the incident energy is kept and the electron is reflected at the channel wall. By separating backscattered electrons, we only need to know the probability of backscattering at a certain energy. We separate the electron emission yield further into an inelastically backscattered and secondary electrons. This enables us to compare our secondary electron emission spectra with the emission spectra from literature, as secondary electrons are conventionally defined as electrons with an emission energy below 50 eV. According to the same definition, backscattered electrons are conventionally defined as electrons the electrons with emission energies above 50 eV. According to this, seemingly arbitrary definition, we define inelastically backscattered electrons as the electrons with energies above 50 eV and below 2 eV of the incident electron energy. This allows us in a first place to deduce the emission energy distribution for any incident energy, by using only four measured spectra and, in a second place, to compare our measurements to literature values.

6.1 Experimental setup to characterize electron emission

The aim of the samples produced for the measurements was to simulate the real surface of the AMCPs as well as possible. Therefore the emission energy spectra of a 12 nm a-Si:H layer and of a 12 nm a-Si:H layer coated with 5 nm of ALD deposited alumina were measured. The thin a-Si:H layer was deposited on a single side polished conductive Si substrate by PECVD using the recipe used for the multiplication layer of AMCPs. For the alumina sample, the AlO_x layer was deposited consecutively by ALD. The average roughness of the samples was about 7 nm; an atomic force microscope (AFM) scan is shown in figure 6.1a. The total emission yield of the layers was measured as well. Additionally, the total emission yield was measured on flat samples of about 12 nm thick a-Si:H layer deposited by PECVD with an average roughness below 2 nm and 5 nm thick AlO_x layer and 5 nm thick MgO layer both deposited by ALD as flat as the substrate with a roughness below 1 nm. An exemplary AFM scan of the a-Si:H layer is shown in figure 6.1b. The ALD layers were deposited directly on single side polished Si substrate without an intermediate a-Si:H layer. The substrate were HF cleaned right before the layer deposition in order to remove the native oxide layer, to improve the conductivity and thus to ensure a maximum charge collection.

The setup of the characterization chamber for electron emission spectra is shown in figure 6.2a. The sample is tilted at an angle of 45° with respect to the incident electron beam. The slit of the hemispherical electron analyser is positioned at angle normal to the surface. Sample characterization with this analysis chamber has been analysed in depth for the purpose of measuring the energy balance of electron emission [Villemant 2017]. We use the procedure presented by the author to correct the measured emission spectra.

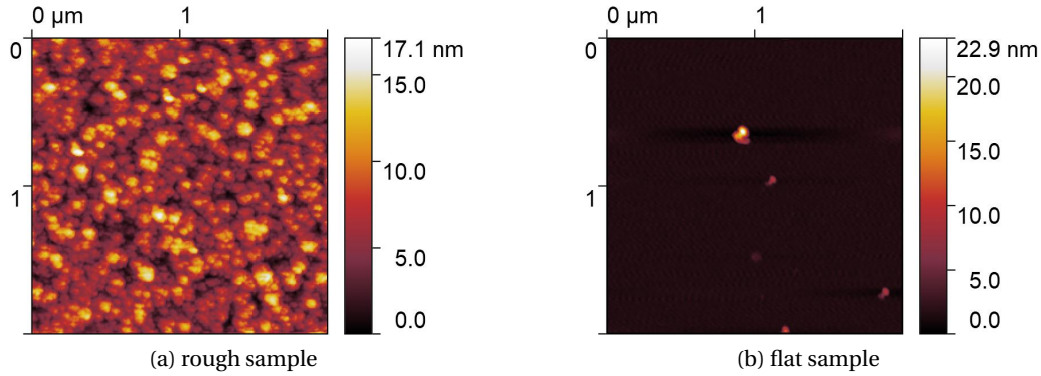


Figure 6.1 – AFM images of sample surfaces used for the measurements. (a) Surface of a rough sample used for measuring the electron emission spectrum. Samples with this kind of roughness were used to measured the emission spectra of a-Si:H and AlO_x . The total emission yield was measured as well. (b) As the electron emission yield varies greatly with the incident angle, samples with a flat surface have been used for complementary electron yield measurements at a various incident angles.

The total emission yield σ of the samples is measured using a Kelvin probe based approach. The analysis chamber elements used for the measurement are shown in figure 6.2b. The

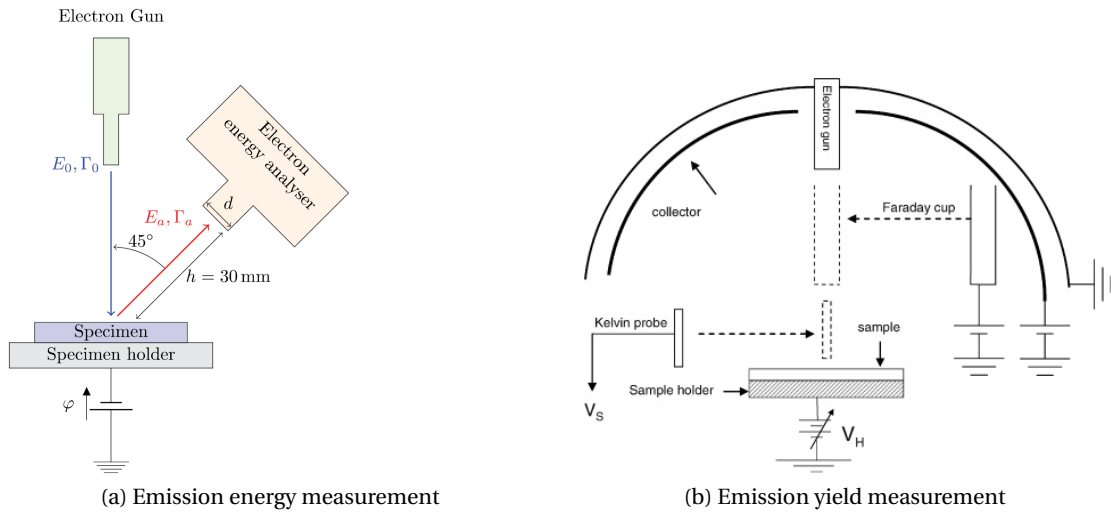


Figure 6.2 – (a) Setup for energy emission spectra measurements. An incident monochromatic electron beam creates electron emission at various emission energies E_a , that are analysed using a hemispherical electron energy analyser, positioned at an angle of 45° relative to the incident electron beam. Image taken from [Villemant 2017]. (b) Kelvin probe based setup for total electron yield measurements developed for measurements of thin insulating layers. The emission yield is measured indirectly, by measuring the charge induced by electron emission inside the sample. Image taken from [Belhaj 2009]

electron beam charge is collected with a Faraday cup. The emission yield is measured as accumulated charge inside the sample using a capacitively coupled charge detector. Emitted electrons are evacuated towards the collector and reabsorption of emitted electrons is prevented by the sample bias. The Kelvin probe bias V_s is characteristic to the sample capacitance and adjusted accordingly. When electrons are emitted from the sample upon electron radiation, the induced charge is measured. For an electron yield below 1 this charge is negative, for yield values above 1 the charge induced in the sample is positive.

6.2 Energy distribution of emitted electrons

Electron emission spectra are used to deduce the energy distribution of secondary electrons and the relative probability of inelastic and elastic backscattering, depending on the incident electron energy. A 12 nm thick a-Si:H layer and a 12 nm thick a-Si:H layer coated with 5 nm thick AlO_x , both with a roughness of about 6 nm, as shown in figure 6.1a have been measured using the setup shown in figure 6.2a. The raw spectra of a-Si:H and AlO_x are shown in figure 6.3 (a) and (b) respectively. a-Si:H has been measured at electron beam energies of 25 eV, 55 eV, 105 eV and 205 eV. The actual energies of the arriving electrons are reduced by the sample bias ϕ . AlO_x has been measured at incident electron beam energies of 15 eV, 25 eV, 55 eV, 105 eV and 205 eV.

The first peak at low energies are secondary electrons. We use the convention of SEM analysis

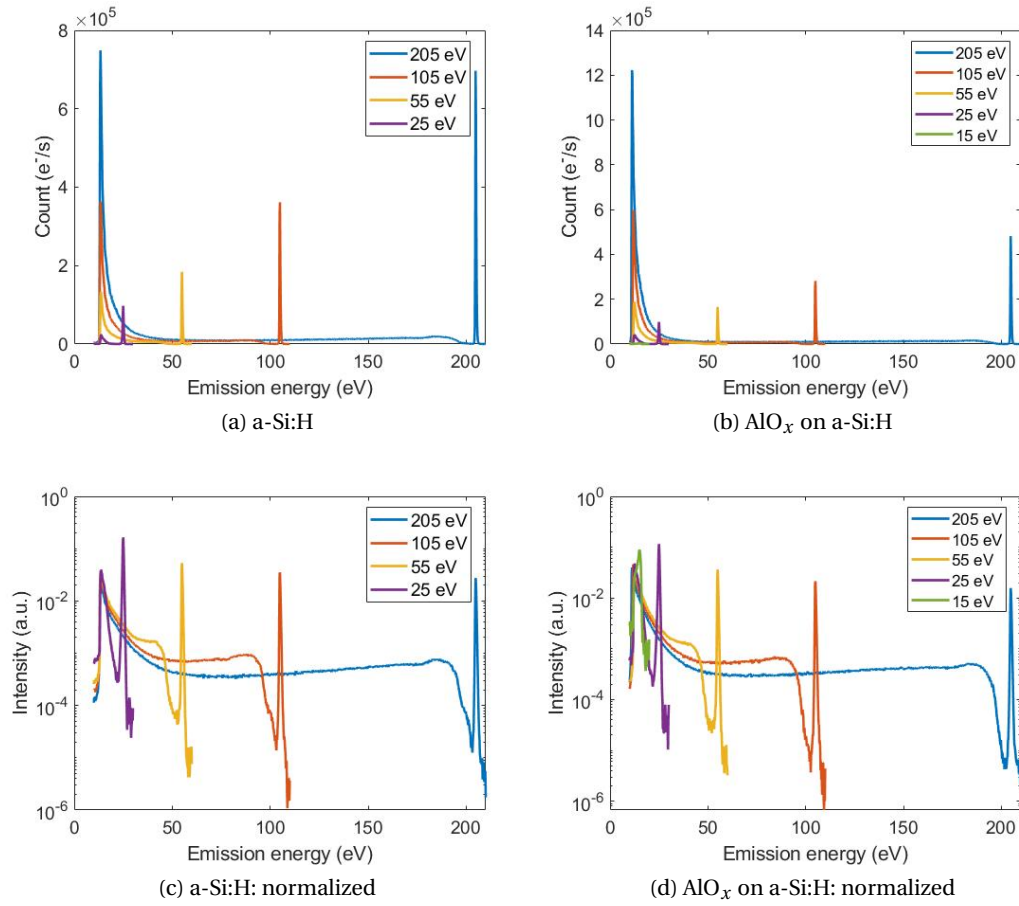


Figure 6.3 – Electron emission energy spectra measured using the setup shown in figure 6.2a with the hemispherical electron analyzer. The energy spectrum in (a) has been measured for the rough a-Si:H layer of 12 nm without an additional coating. The normalized data are shown in (c). The emission spectrum of the rough a-Si:H layer of 12 nm with an ALD coating of 5 nm AlO_x is shown in (b) and the normalized data are shown in (d).

[Redhead 1968] to divide inelastically backscattered and secondary electrons, and define the secondary electron energies as those below 50 eV. The peak around the incident energy are elastically backscattered electrons. Emitted electrons with energies above 50 eV and more than 2 eV below the incident energy are inelastically backscattered electrons. The division between secondary electrons and inelastically backscattered is arbitrary at these low energies. We use these definitions to be able to compare the measured secondary yield to literature values, where the yield of secondary electrons and of backscattered electrons is conventionally separated this way.

We found that it was important for our purpose to take into account inelastically backscattered electrons as well, even if they are rare events as their energy is comparably high. As a consequence, they should either be considered separately, as we did, or the energy distribution of secondary electrons should be considered between 0 eV up to the backscattering peak. The spectra of a-Si:H and AlO_x , normalized with respect to the total incident charge before correction are shown in figure 6.3 (c) and (d).

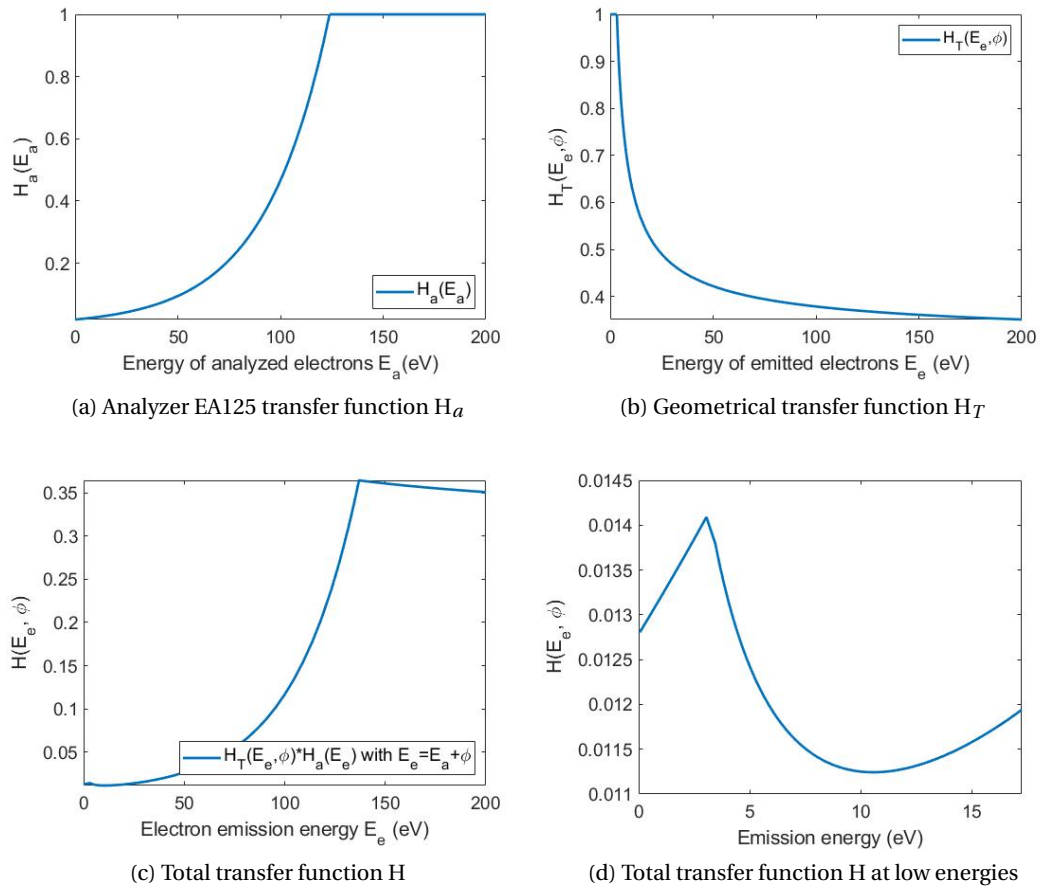


Figure 6.4 – Transfer function to correct the measured emission energy data according to [Villemant 2017]

Villemant et al. [Villemant 2017] suggested to use a correction, as discussed below, for spectra

	Si	a-Si:H	AlO _x
E_G	1.12 eV	1.8 eV	
χ	3.2 eV	3.92 eV	1.35 eV
Normalization factor C	331	513	12.3
MPE	0.75 eV	0.8 eV	0.7 eV
E_{av}	3.3 eV	3.7 eV	5.8 eV

Table 6.1 – Material constants and normalization factor used to calculate the secondary electron emission energy spectra in figure 6.6 and the resulting most probable emission energy (MPE) of the distribution.

measured at low energies with the setup that was used for our measurements. There are two characteristics of the electron emission analyzer setup that need to be taken into account in the correction. First, the analyser is calibrated for energies above 300 eV, our measurements are done below that. Second, low energy electrons tend to follow the electric field more than electrons with higher energies. To correct for both these effects, we use the transfer function of Villemant. The analyzer transfer function $H_a(E_a)$ of the analyzed electron energy E_a is shown in figure 6.4a.

$$H_a(E_a) = \begin{cases} A \cdot \exp(\alpha \cdot E_a) & \text{for } 0 \leq E_a < 124 \text{ eV} \\ 1 & \text{for } E_a \geq 124 \text{ eV}, \end{cases} \quad (6.1)$$

with $A = 0.0192$ and $\alpha = 0.0319$. This transfer function is used to take into account the varying sensitivity of the analyzer EA125 for low incident energies. Although the analyzer is calibrated for energies above 300 eV, this correction needs to be made at low energies, as the analyzer is less sensitive to low incident electron energies. Without this correction the proportion of emitted electrons with higher energies would be overestimated. Additionally, the geometrical losses in the analysis chamber are corrected by the transfer function $H_T(E_e, \phi)$ of the emitted energy E_e and the sample bias ϕ .

$$H_T(E_e, \phi) = \begin{cases} 1 & \text{for } 0 \leq E_e \leq 3.25 \text{ eV} \\ \frac{\arctan(\frac{d}{2h})}{\arctan(\sqrt{\frac{E_e}{|\phi|}})} & \text{for } E_e > 3.25 \text{ eV}, \end{cases} \quad (6.2)$$

with $d = 0.03 \text{ m}$ and $h = 0.03 \text{ m}$. The geometrical losses depend on the sample bias and the emitted electron energies, as electrons with higher energies are more likely to keep their original trajectories, thus not being collected by the analyser. The complete transfer function is the product of both, shown in figure 6.4c. The emitted electron energy is detected at the analyser as $E_e = E_a + \phi$. The sample bias ϕ is a negative voltage to avoid recapture of emitted electrons and was in the range of -11 to -13 V for the measurements. The transfer function at very low energies is shown in figure 6.4d.

The corrected spectra of a-Si:H and AlO_x are shown in figure 6.5. Especially at higher incident energies above 50 eV, secondary emission at low energies below 50 eV is the main emission

6.2. Energy distribution of emitted electrons

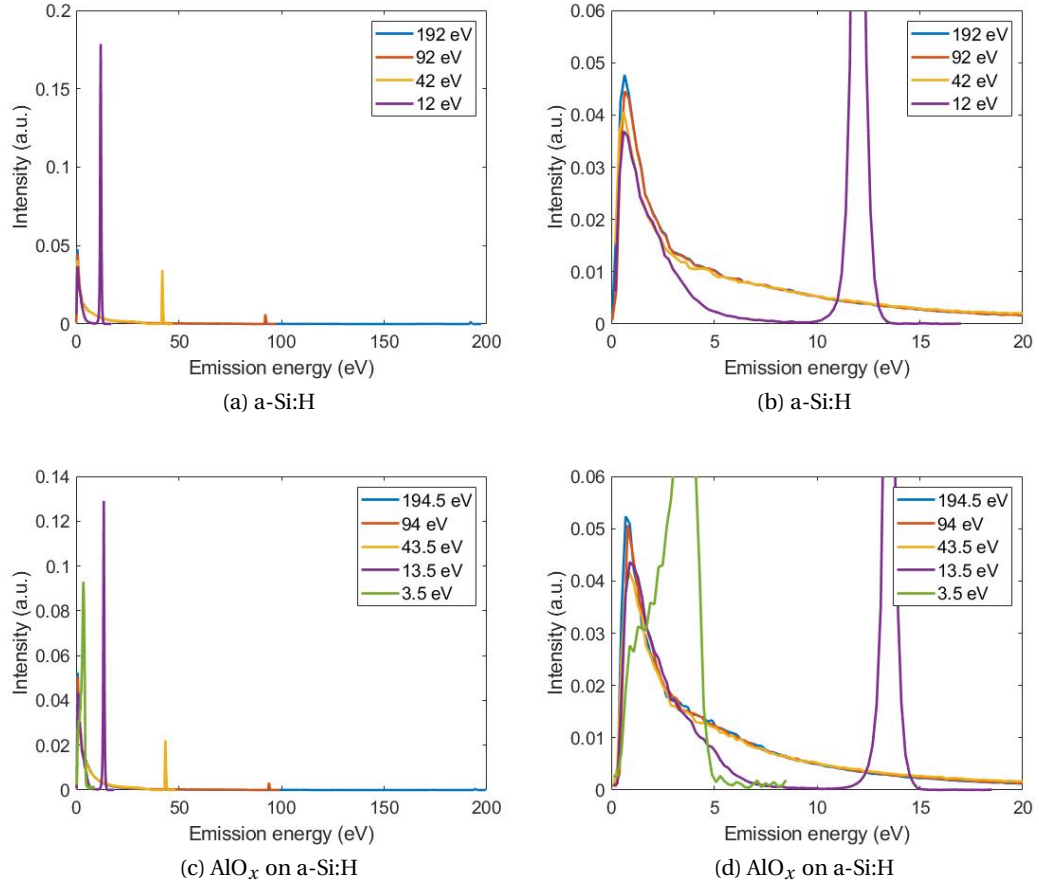


Figure 6.5 – Emission energy spectra after correction. (a) Emission spectra of a-Si:H for the corrected incident energies. (b) The low energy spectra, with the secondary electron emission peak overlapping for the different incident energies. (c) Emission spectra of AlO_x for the corrected incident energies and (d) low energy part of the AlO_x emission spectra, where the secondary electron energy distribution overlaps for incident energies of 13.5 eV and above.

a-Si:H			AlO _x		
E_{in}	MPE	E_{av}	E_{in}	MPE	E_{av}
12 eV	0.6 eV	2.0 eV	13.5 eV	0.9 eV	2.5 eV
42 eV	0.6 eV	8.0 eV	43.5 eV	0.9 eV	7.3 eV
92 eV	0.65 eV	8.8 eV	94 eV	0.8 eV	7.5 eV
192 eV	0.65 eV	8.0 eV	194.5 eV	0.7 eV	6.8 eV

Table 6.2 – Most probable emission energy of secondary electrons and the average energy of secondary electrons for the measured a-Si:H and AlO_x surfaces

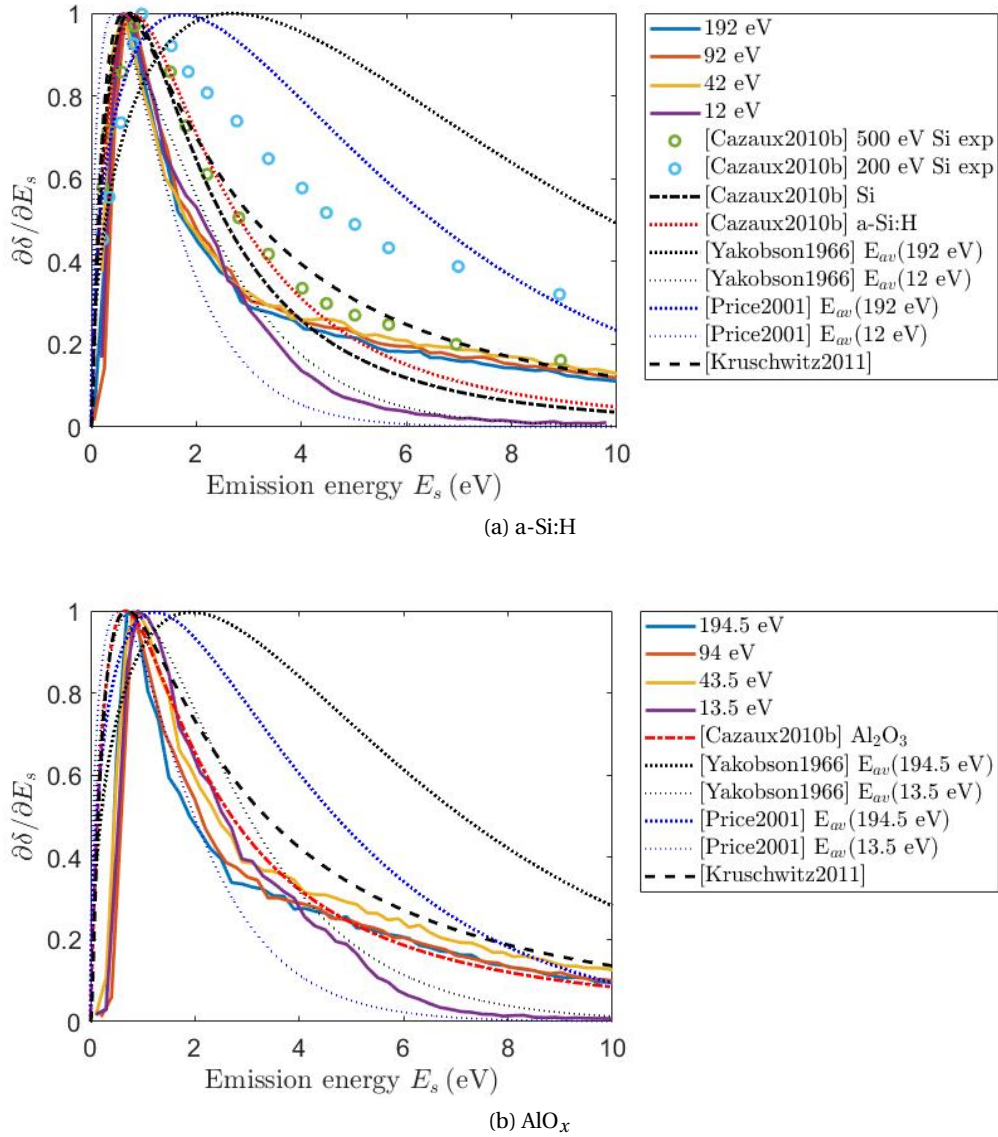


Figure 6.6 – Secondary electron emission energy distribution after correction shown for 0 to 10 eV. (a) a-Si:H spectra compared to measured literature values of Si from [Cazaux 2010b] and the calculated curve for Si and a-Si:H and the general curve fits of equation 5.51 [Yakobson 1966], equation 5.40 [Price 2001], and equation 5.42 [Kruschwitz 2011]. The literature values of table 6.1 and the average emission energy values of table 6.2 have been used to calculate the curves. (b) The AlO_x spectrum fits well to the calculated curve of Al_2O_3 using the theoretical formula of [Cazaux 2010b] and the values of table 6.1

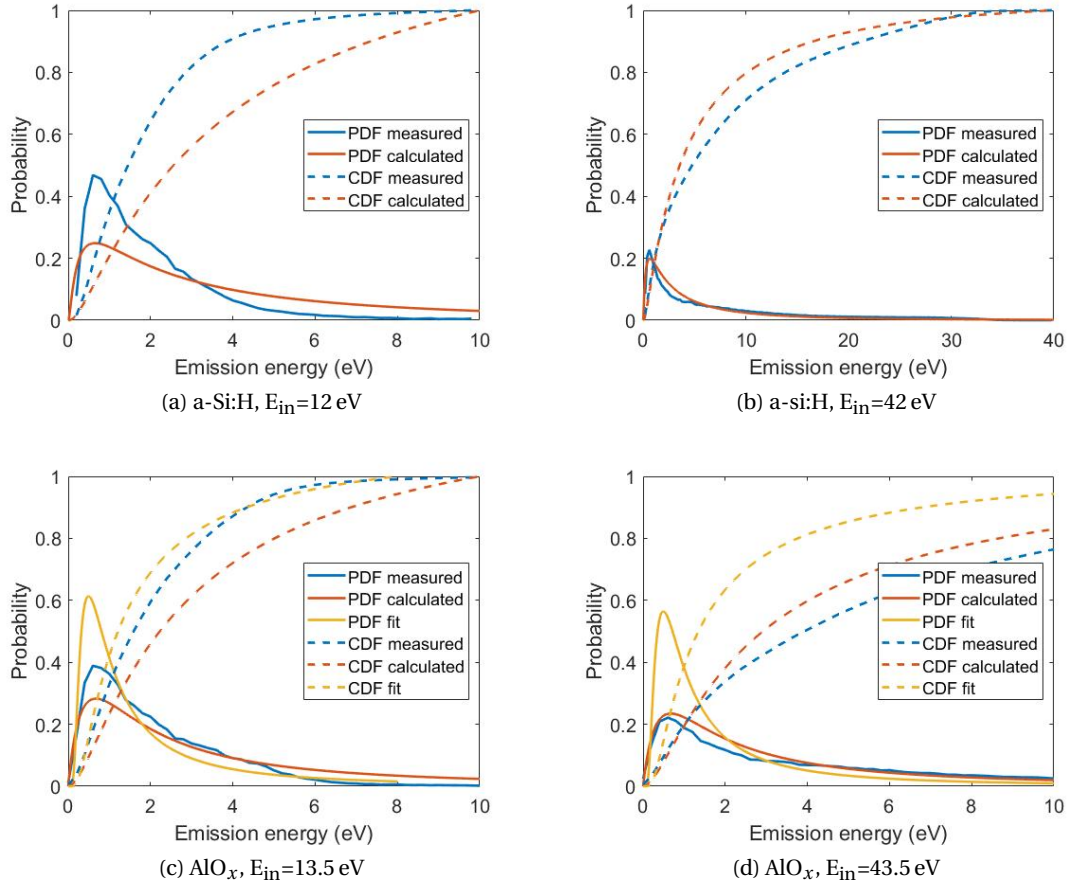


Figure 6.7 – Secondary electron emission spectra probability density function (PDF) and resulting cumulative distribution function (CDF). For a-Si:H the measured curves are compared to the fit of [Kruschwitz 2011]. (a) In the low energy range the measured curve cannot be represented by the model, thus we use a fit for incident energies below 25 eV. (b) For higher energies the modeled curve fits well. For AlO_x we use the model of Cazaux [Cazaux 2010a]. (c) As for a-Si:H, in the low energy range, data are better represented by a fit. (d) For energies above 25 eV the model fits well to the measurement.

process, while at low incident energies backscattering is predominant. The most probable energy (MPE) of secondary emission was about 0.6 eV for a-Si:H and about was 0.8 eV for AlO_x . The MPEs and average emission energies of a-Si:H depending on the incident energy are listed in table 6.2. For an insulator, the theoretical MPE is about $\chi/2$, which fits well in the case of AlO_x , especially at high incident energy.

We can now compare the secondary emission parts of the energy spectra to the theoretical emission energy curve described in chapter 5.3 in figure 6.6. Equation 5.10 was used to calculate the secondary emission energy distribution of Si and a-Si:H, figure 6.6 (a). The parameters used for Si and a-Si:H and the expected MPEs are listed in table 6.1. The shape of the modeled a-Si:H emission energy curve does not fit the shape of the data. The reason could be a potential difference in the work function of the detector relative to the sample [Cazaux 2010b]. Another reason could be a different electron affinity value of the a-Si:H sample due to the chemical composition at the surface or that the model is no more valid at low incident energies where the secondary electrons might not have isotropic directions when arriving at the vacuum boundary.

Additionally, we compare the curves to the measurements of Si of [Cazaux 2010b]. The measurement of Si at 200 eV has a much broader energy spectrum than the spectrum we measured for a-Si:H at 192 eV. We also compared the curve to the fit equations used in MCP models, presented in chapter 5.5. We used equation 5.51 of [Yakobson 1966] and equation 5.40 of [Price 2001] with the average energies E_{av} of 12 eV and 192 eV incidence. We also fitted our curves to the model of [Kruschwitz 2011], equation 5.42, using an MPE of 0.6 eV for a-Si:H. This curve fits best to our measurements and is used to model the energy emission distribution at incident energies above 30 eV.

In figure 6.6 (b) we show the low energy part of the emission spectrum of AlO_x . The theoretical curve was calculated from equation 5.11 using the parameters of table 6.1. The curve fits well to the measured data for incident energies above 50 eV. Below 50 eV the curve clearly depends on the incident energy. For simulations of electron multiplication in the AMCP channels we use a fit of the measured curves to deduce the emission energy spectra at incident energies below 50 eV.

As none of the theoretical curves can represent the change of the emission spectrum for low incident energies, we were constrained to use a fit of our measured energy spectra for simulations of electron emission energies in AMCPs at low incident energies. Figure 6.7 shows the secondary electron emission spectra probability density function (PDF) and the resulting cumulative distribution function (CDF) for a-Si:H and AlO_x at two incident energies. For a-Si:H the measured curves are compared to the calculated probability using equation 5.42 with the following normalization:

$$\partial\delta/\partial E_s = \exp\left(-\frac{\ln[E_s/\text{MPE(a-Si:H)}]^2}{2 \cdot 1.33^2}\right). \quad (6.3)$$

Figure 6.7a shows the low energy range, where the measured curve cannot be represented by the model. Here we use a fit for incident energies below 25 eV. Figure 6.7b shows the probability distribution for a higher energy, at 42 eV. Here, the modeled curve fits well.

For AlO_x we use equation 5.11 with the following normalization:

$$\partial\delta/\partial E_s = 12.3 \cdot E_s / (E_s + \chi_{\text{AlO}_x})^3. \quad (6.4)$$

As for a-Si:H, in the low energy range, data are better represented by a fit. In figure 6.7c we show the calculated curve, the measured curve and the fit of the measured curve. At higher incident energies above 25 eV the model fits well to the measurement, as shown in 6.7d.

The fit function used for incident energies below 25 eV for both a-Si:H and AlO_x depends on the incident energy E_{in} :

$$\partial\delta/\partial E_s(E_{in}) = \frac{\Gamma((P_1 + P_2)/2) \cdot (P_1/P_2)^{P_1/P_2} \cdot E_s^{P_1/P_2-1}}{\Gamma(P_1/2) \cdot \Gamma(P_2/2) \cdot (1 + P_1/P_2 \cdot E_s)^{(P_1+P_2)/2}} \quad (6.5)$$

with $P_1 = 39 \cdot \exp(-E_{in}/68) + 111$ and $P_2 = 2$.

After having determined the energy distribution of the emitted electrons, we now move on to separate the contributions of backscattered and secondary electrons to the emission spectrum.

6.3 Backscattering probability

The probability of elastic and inelastic backscattering are calculated from the areas of the respective energy region. Figure 6.8 shows all of the collected spectra of a-Si:H at the corrected incident energies of 12 eV, 42 eV, 92 eV and 192 eV. Electron energies corresponding to secondary emission (SE) are colored in red, energies corresponding to backscattered electrons (BS) are colored in blue, and those that are inelastically backscattered (IBS) at incident energies above 50 eV are colored in green.

Figure 6.8 (e) and (f) shows the IBS and BS electrons at the respective incident energies of 92 eV and 192 eV. Compared to secondary emission at these incident energies shown in (c) and (d), the proportion of backscattering is very low.

The emission spectra of AlO_x for the corrected incident energies of 3.5 eV, 13.5 eV, 43.5 eV, 94 eV and 194.5 eV are shown in figure 6.9. The relative probability of secondary emission relative to backscattering increases with increasing incident electron energy. The lowest energy spectrum has been recorded for an incident energy of 3.5 eV, where the backscattering peak has been fitted with a Gaussian distribution. At this energy, there is no separation between a backscattering peak and secondary emission. The greater part of the electrons are backscattered and the remaining part of the signal are lower energy electrons.

We used the spectra of figures 6.8 and 6.9 to calculate the relative probability function $P_{BS}(E_{in})$ of backscattering for both materials in figure 6.10. The relative probability of elastic backscattering is

$$P_{BS}(E_{in}) = a_{BS} \cdot \exp(b_{BS} \cdot E_{in}) + c_{BS}, \quad (6.6)$$

with the constraint that $P_{BS}(0) = 1$. The relative probability of inelastic backscattering for

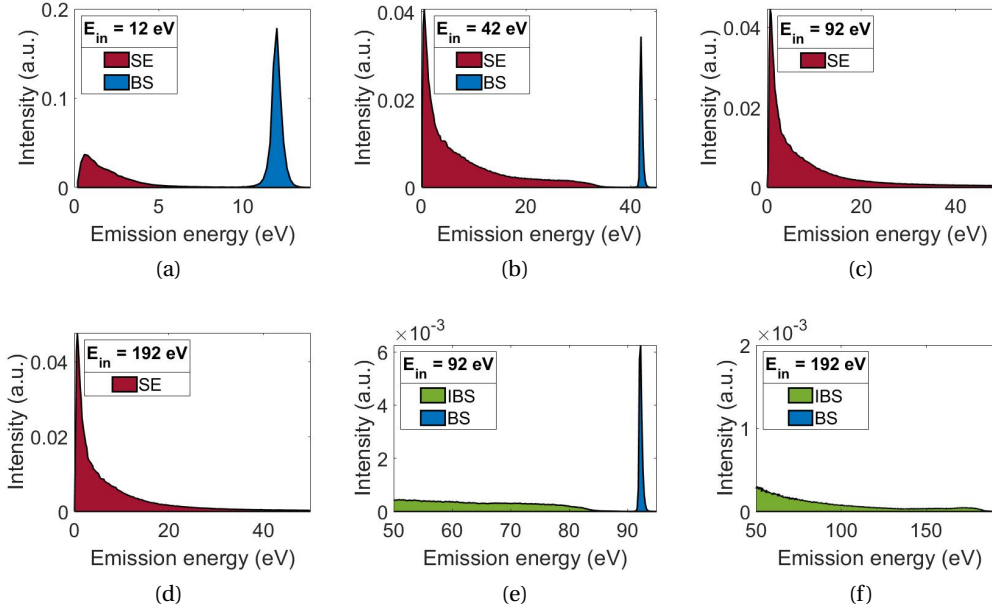


Figure 6.8 – a-Si:H emission energy spectra after correction. The blue part of the total area corresponds to the elastic backscattering probability (BS), the green part to inelastic scattering (IBS) and the red part to the secondary emission probability (SE). In this low energy range, the relative probability of backscattering decreases for increasing incident energies.

energies above 50 eV is

$$P_{IBS}(E_{in}) = a_{IBS} \cdot E_{in} + b_{IBS}. \quad (6.7)$$

The fit parameters for a-Si:H and the alumina surface we deduced are shown in table 6.3. In the following section, we use this set of equations for the backscattering probability to calculate the elastic and inelastic backscattering yield η_e and η_{ie} , and the secondary yield δ from measurements of the total electron emission yield σ .

In figure 6.11 we compare the relative backscattering probability of both Si and a-Si:H that we deduced with literature values and Monte-Carlo simulations, using the yield data of the

Fit parameter		a-Si:H	AlO _x
P_{BS}	a_{BS}	0.9901	0.9948
	b_{BS}	-0.0481 [1/eV]	-0.0623 [1/eV]
	c_{BS}	0.0099	0.0052
P_{IBS}	a_{IBS}	$3.75 \cdot 10^{-5}$ [1/eV]	$2.37 \cdot 10^{-5}$ [1/eV]
	b_{IBS}	0.05	0.03

Table 6.3 – Derived fit constants for the relative elastic (BS) and inelastic (IBS) backscattering probabilities of a-Si:H and AlO_x.

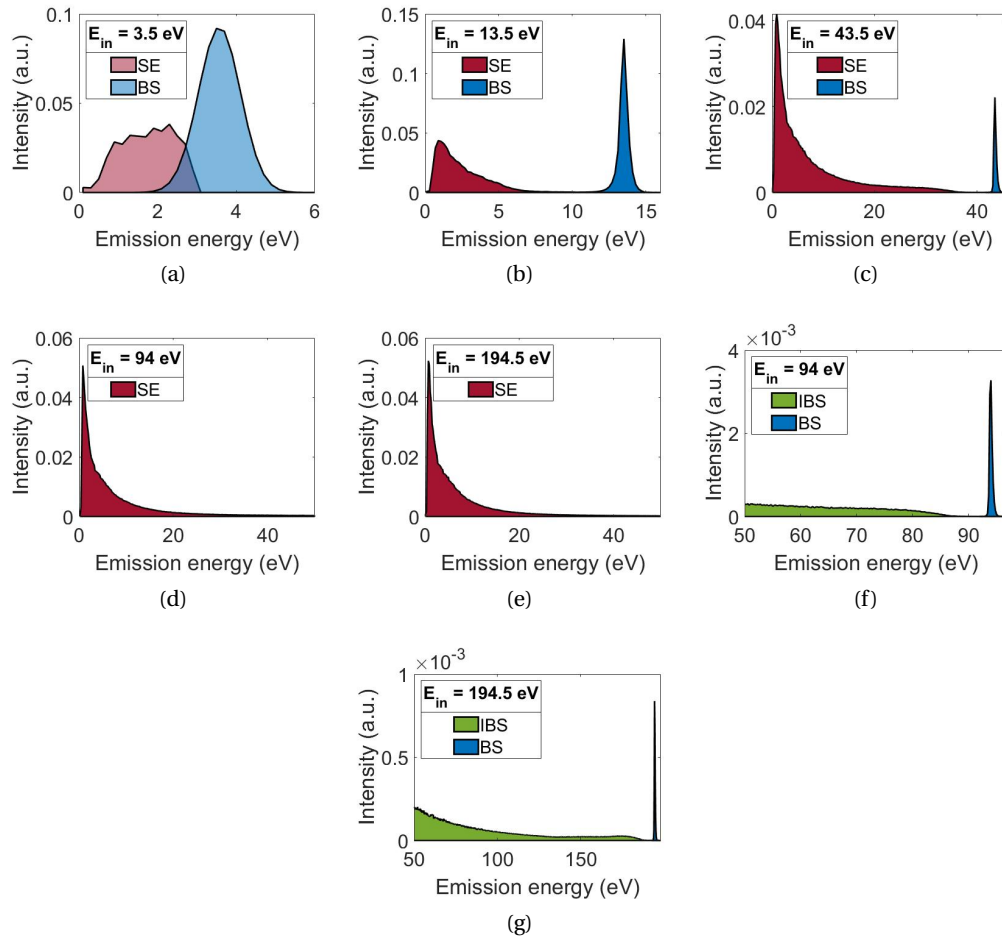


Figure 6.9 – AlO_x emission energy spectra after correction. The blue part of the total area corresponds to the backscattering probability (BS), the green part to inelastically backscattered electrons (IBS) and the red part to the secondary emission probability (SE). As for a-Si:H the relative proportion of backscattering decreases and the proportion of secondary emission increases with increasing incident energy.

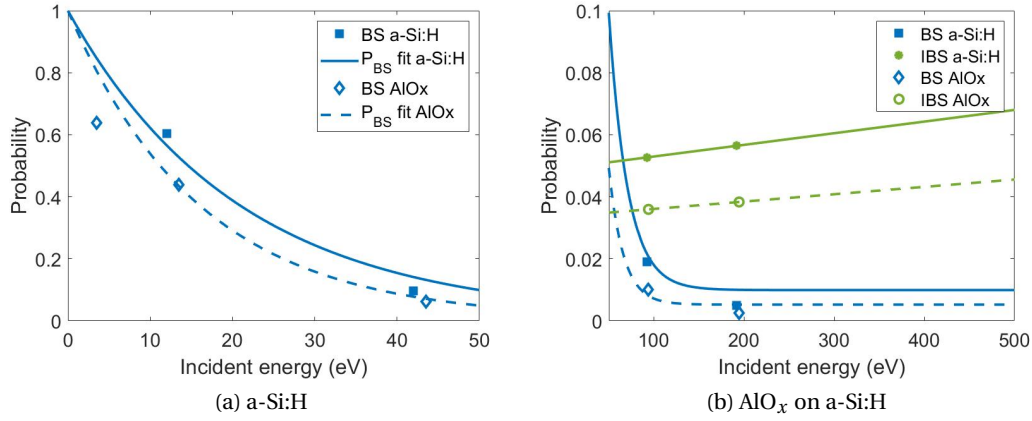


Figure 6.10 – (a) Relative probability for elastic backscattering (BS) fits for a-Si:H and AlO_x. The data point at 3.5 eV for AlO_x has been ignored for the fit, as there is no equivalent point for a-Si:H. (b) Probability for electrons to be inelastically backscattered (IBS) and linear fits for a-Si:H and AlO_x on two IBS measurement points. Inelastic backscattering was extracted from the measured spectra at two points above 50 eV. In this energy range it is the major backscattering mechanism. The fits together with total yield curves are used to quantify elastic and inelastic backscattering events for AMCP calculations.

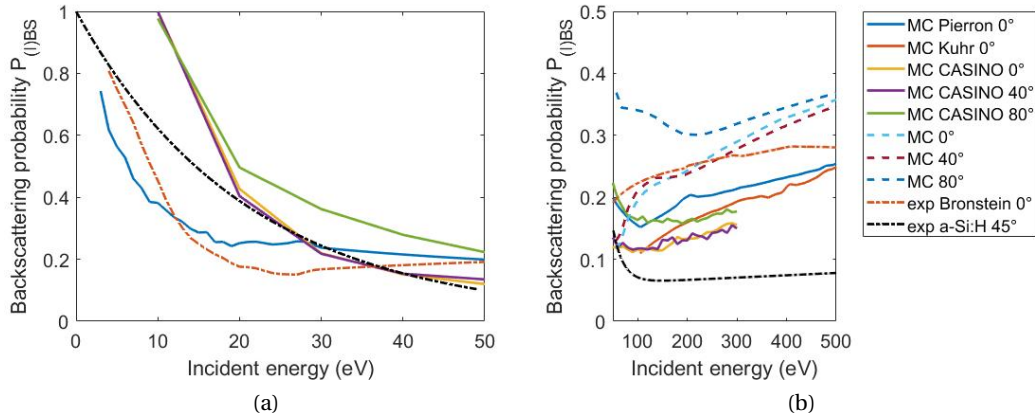


Figure 6.11 – Backscattering probability $P_{BS} + P_{IBS}$ calculated from literature values and MC models for Si and our experimental data for a-Si:H. (a) At energies below 50 eV we see that the our calculated backscattering probability fits very well to literature values. Only the simulations done with CASINO differ. (b) At energies above 50 eV: The backscattering probability lies in a wide interval between 0.07 according to our measurements up to about 0.4 according to our MC simulations. Literature values are in between these values.

literature to calculate $P_{BS}(E_{in}) = (\eta_e + \eta_{ie})/\sigma$. In some cases backscattered electrons are defined as emitted electrons with an energy higher than 50 eV, in some cases, as in our case, they are defined only as elastically backscattered electrons, and in some cases they are the sum of elastically and inelastically backscattered electrons. Knowing that the majority of the backscattered electrons at low energies are elastically backscattered, and that the majority is inelastically backscattered at higher energies we are still able to compare the observed tendencies.

First, we discuss the low energy behavior of the backscattering probability, shown in figure 6.11a. For all of the calculations and measurements, the low energy limit $P_{BS}(0) = 1$ is observed. Given the difficulties to measure and theoretically describe these low energies, our experimental curve (exp a-Si:H 45°), the experimental curve of [Bronstein] (exp Bronstein 0°) and the Monte-Carlo calculation of [Pierron 2017] (MC Pierron 0°) agree very well. The calculations we did using CASINO for angles between 0° and 80° might overestimate backscattering at very low energies.

At high energies above 50 eV, displayed in figure 6.11b, the backscattering probability varies a lot. We see the biggest discrepancy between our Monte-Carlo simulations (MC 00° to MC 80°) and our experimental measurements (exp a-Si:H 45°). The Monte-Carlo simulations of Pierron [Pierron 2017] and Kuhr [Kuhr 1999] (MC Pierron 0° and MC Kuhr 0°) agree very well. As we observe this important variation in the backscattering probability, we deduce that the proportion of backscattering is a parameter that needs to be further adjusted within AMCP simulations.

In figure 6.12 we show the relative backscattering probability P_{BS} of AlO_x . At low energies,

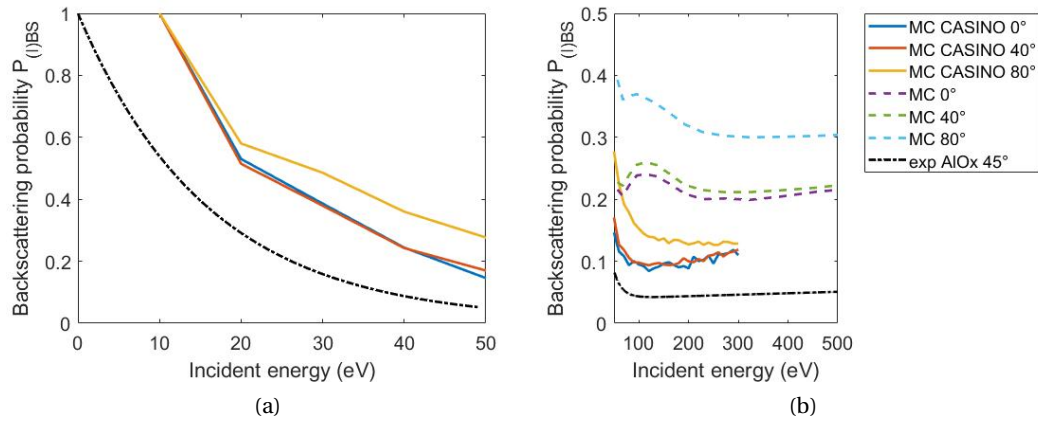


Figure 6.12 – Backscattering probability, $P_{IBS} + P_{BS}$ of Al_2O_3 from simulations and measurements. (a) At low energies we can only compare our measurements to the curves calculated with CASINO. (b) At high energies: As for Si, the backscattering probability lies in a wide interval between 0.05 according to our measurements up to about 0.4 according to our MC simulations. We assume this is mostly due to inelastic backscattering.

figure 6.12a, as seen for a-Si:H, the backscattering probability we deduced using Monte-Carlo simulations with CASINO (MC CASINO 0° to 80°) might be overestimating backscattering. At

energies above 50 eV, figure 6.12b, calculations suggest a higher backscattering yield than the one we deduced from the experiment. As for a-Si:H, the backscattering probability is one of the parameters that can be adjusted within the AMCP simulation.

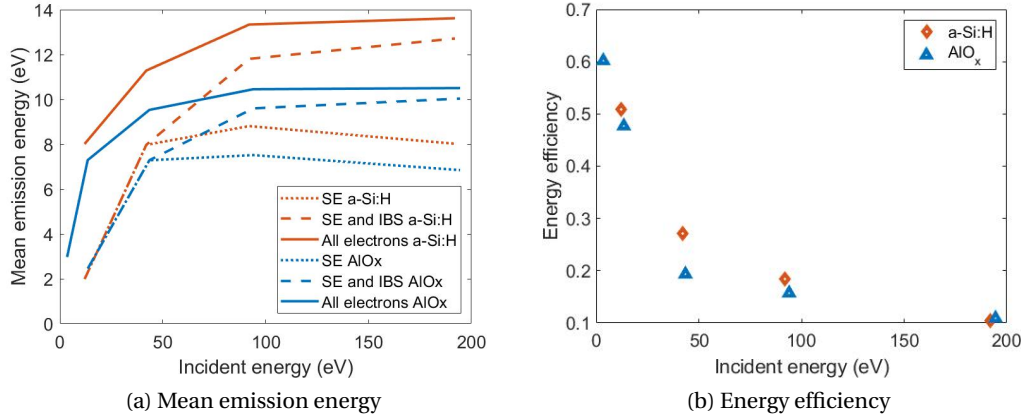


Figure 6.13 – (a) The mean emission energy of emitted electrons depending on the incident energy. The emission energies are generally higher in a-Si:H, while the emission yield of a-Si:H is lower. Inelastically backscattered electrons should be taken into account for AMCP simulations, as their energetic contribution is very high. (b) The energy efficiency has been calculated from the total emission yield and the emission spectra. The efficiency is similar for the two materials and generally higher at low energies where a bigger part of the electrons are backscattered.

Finally, we used the spectra of figure 6.8 and figure 6.9 to calculate the mean emission energy of a-Si:H and AlO_x and show them in figure 6.13a. It becomes clear that backscattered electrons need to be taken into account for calculations of electron multiplication in AMCPs. The average emission energy of secondary electrons is about 7 eV for AlO_x and about 8 eV for a-Si:H whereas the average emission energy of all emitted electrons is about 10.5 eV for AlO_x and close to 14 eV for a-Si:H. While the emission energies of AlO_x are below those of a-Si:H, the emission yield of AlO_x is greater than that of a-Si:H. Taking into account the total yield and the average emission energy, we compared the energy efficiency of both materials in figure 6.13b. Overall the energy efficiency of the two materials is similar. Emission from a-Si:H surfaces yields a lower number of electrons with comparatively high emission energies whereas emission from AlO_x surfaces yields a higher number of electrons with lower emission energies. The higher emission yield of AlO_x is beneficial to increase the overall gain of AMCPs.

6.4 Electron emission yield

In the previous section we have considered the relative probabilities of backscattering compared to the secondary emission. We now present measurements of the electron yield and,

using the relative probabilities from the previous section, separate the yield into its respective contributions of secondary electrons, inelastically and elastically backscattered electrons.

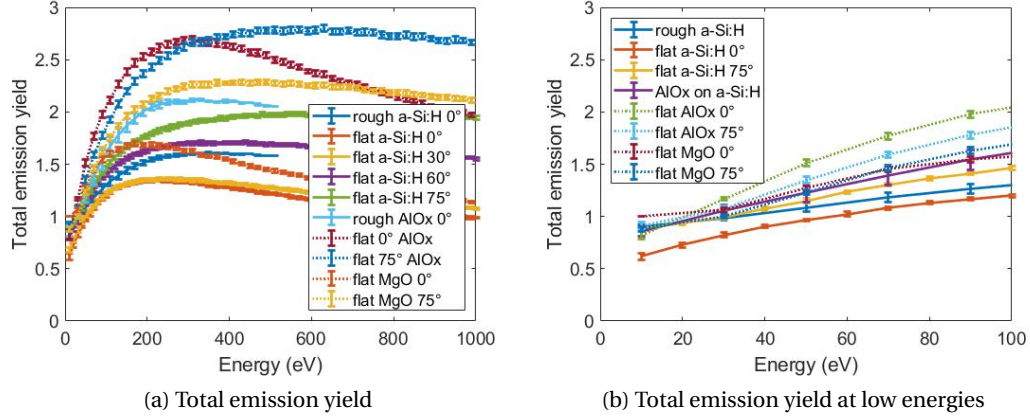


Figure 6.14 – (a) Total emission yield (TEY) measurements of rough and flat a-Si:H, AlO_x on rough a-Si:H, and flat ALD deposited AlO_x and MgO measured at various degrees of incidence in the energy range between 0 and 1000 eV. (b) TEY of the low energy region from 0 to 100 eV.

The total emission yield σ was measured using the setup shown in figure 6.2b. The yield was measured for a rough sample of a-Si:H of about 12 nm, a flat sample of about 12 nm, an ALD deposited AlO_x layer of 5 nm on a rough layer of about 12 nm a-Si:H and an ALD deposited AlO_x layer of 5 nm. An ALD deposited 1 nm MgO layer has been measured as well. All of the flat and ALD deposited single layers were deposited on a freshly HF cleaned polished Si substrate. The total emission yield of the layers is shown in figure 6.14. The total yield of a-Si:H was measured for the rough sample at normal incidence between 0 and 500 eV and for the flat sample at 0°, 30°, 60° and 75° incidence between 0 and 1000 eV. The yield grows with incident angle and the yield of the rough sample corresponds to the yield of a flat sample at about 45° incidence, see figure 6.15a.

As expected, the total emission yield with an AlO_x coating is higher than the yield of a-Si:H. Although the measurement of AlO_x on a-Si:H is limited by charging, the AlO_x coated a-Si:H shows an increase in the yield. This limitation is clear, when we compare the maximum yield of 2.1, measured here, with the literature values of an AlO_x layer of 5 nm, where a maximum yield of 2.5 or more is expected. Charging of the sample is expected in this case as the total layer thickness of 17 nm are fairly isolating layers. The real yield of AlO_x , without charging limitations was measured on the ALD deposited AlO_x layer at incident angles of 0° and 75°. No significant difference in the yield was observed between AlO_x deposited at 200°C and at 300°C. AlO_x can thus be deposited at 200°C on AMCPs, which is not affecting the electronics. The yield was compared to yield measurements of [Jokela 2012] and [van der Graaf 2017] and fits very well to the expected yield of 5 nm AlO_x . The quality of the MgO layer deposited by ALD still needs to be improved, as can be seen in figure 6.15d. So far, we deposited a layer below 1 nm. The deposition recipe still needs to be optimized to deposit a 4-5 nm MgO layer. For calculations of AMCPs with MgO layers, we use the total yield from the literature values of

[Jokela 2012] of 5 nm thick MgO.

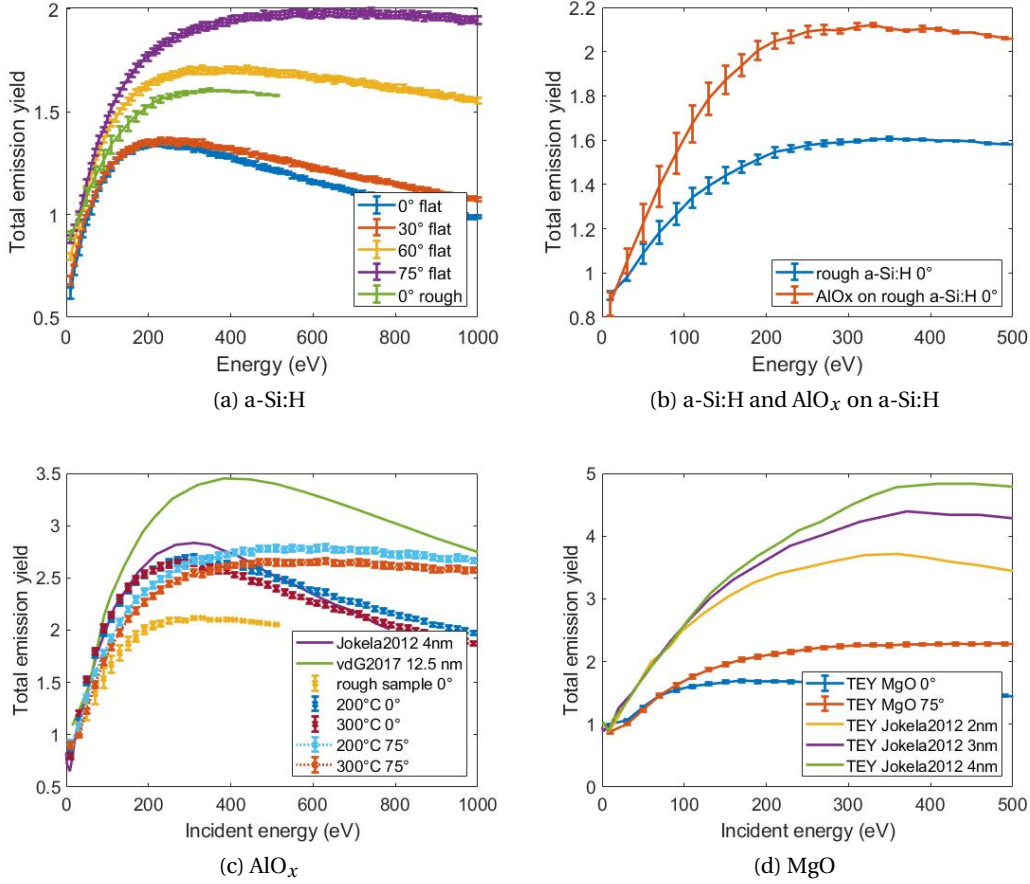


Figure 6.15 – (a) Total emission yield measurements of a flat a-Si:H layer at 0° to 75° incidence and a rough a-Si:H layer at 0° incidence. The yield of the rough sample behaves like a mixture of the yields of the flat sample at different angles. (b) TEY enhancement through AlO_x layer on a-Si:H. (c) TEY measurements of ALD deposited AlO_x layers. The yield is comparable to literature values of [Jokela 2012] and [van der Graaf 2017], taking into account the thickness of 5 nm. (d) TEY of ALD deposited MgO coating and comparison to [Jokela 2012]. The MgO coating needs to be improved.

Because total yield measurements are time extensive and as they had to be done at an external facility, we additionally calculated the total yield using the available Monte-Carlo simulation tools. In case of finding a good agreement between the measurements and the calculations, we could have used the calculations much more easily to derive the yield at a wide range of incident angles.

We calculated the total emission yield of Si and Al₂O₃ using the Monte Carlo code for electron-specimen interaction developed by TU Delft. We simulated a flat layer of Si and Al₂O₃ with the incident electron beam at angles from 0° to 80°. The simulated Si curve was compared to simulations and measurements of [Pierron 2017], [Kuhr 1999] and [Bronshtein] of pure silicon. The

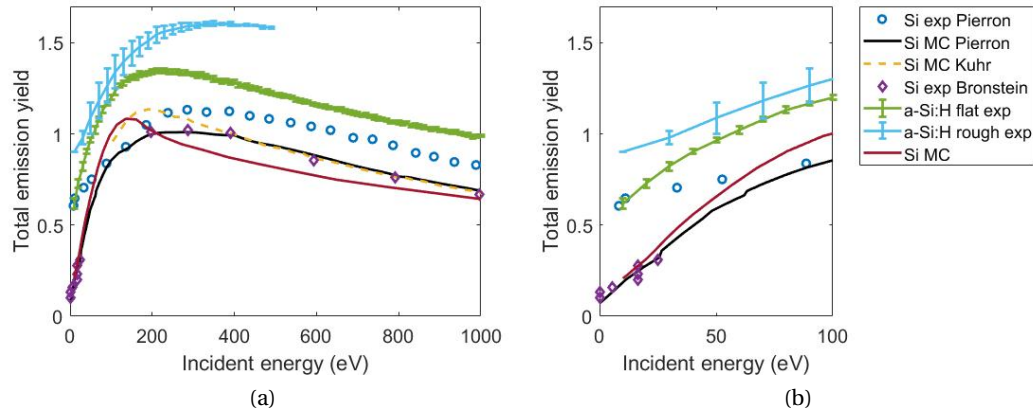


Figure 6.16 – Total emission yield of Si at normal incidence from simulations and measurements compared to measurements of a-Si:H, of a flat and a rough surface and Monte-Carlo simulations of the total yield of Si using the electron scattering code of TU Delft.

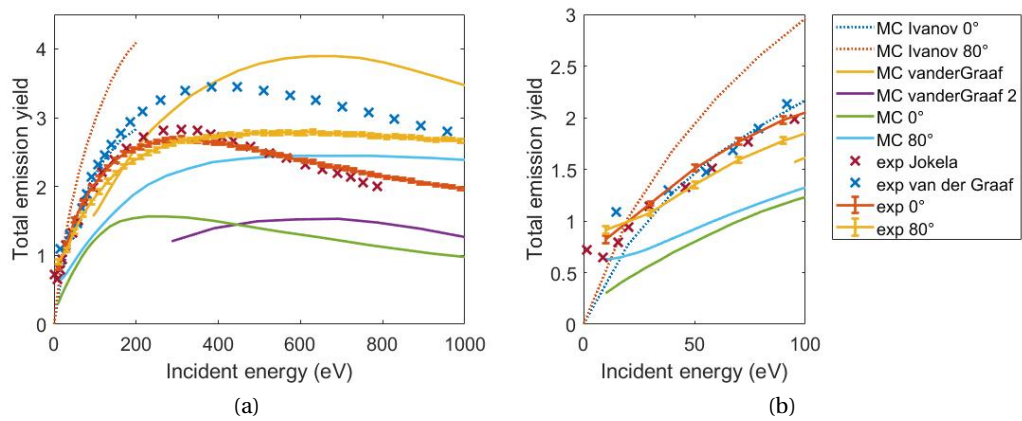


Figure 6.17 – Total emission yield of Al_2O_3 at normal incidence and a high incident angle of 80° from simulations and of 75° from measurements compared to literature values. Measurements of different authors agree well with our measurements. The simulated curves are very different for Al_2O_3 . This may be because electron scattering simulations are mostly used and developed for Si and metals.

simulated AlO_x curve was compared to simulations and measurements of [van der Graaf 2017], [Jokela 2012] and [Ivanov 2018]. Pierron and van der Graaf used the low energy extension of GEANT4 for their simulations. Ivanov used CASINO to simulate the emission yield of Al_2O_3 . For silicon our simulated curves fit very well to the GEANT4 simulation, to measurements of Si and Monte-Carlo simulations of the cited authors, see figure 6.22. As expected and explained in chapter 5.1, the yield of amorphous silicon is higher than the yield of silicon. The rough amorphous silicon sample shows an even higher yield.

For AlO_x the simulated total yield curves vary a lot, see figure 6.17, while the measurements agree very well, especially taking into account the different layer thickness that is known to increase the yield. The discrepancy in the calculations might be due to the different approaches used, with Ivanov using CASINO based on the stopping power and the dielectric function approach used by van der Graaf and us. The two curves calculated by van der Graaf are calculated for constant irradiation (MC van der Graaf 2) on a 20 nm thick layer and for single electron incidence on a 10 nm thick layer (MC van der Graaf). The second reason for the discrepancies in the calculated curves could be different assumptions in irradiation. The experimental yield curves are in very good agreement taking into account the difference in thickness, as shown in figure 6.15c.

As a consequence of the discrepancies between the different simulation methods and measurements and the higher yield of a-Si:H compared to Si, we did not use simulations of the emission yield. Instead, we exclusively based the parametrization of the yield on the total yield measurements.

6.5 Backscattering and secondary yield parametrizations

In this section, we separate the total emission yield into the respective contributions: the secondary yield, and the inelastic and elastic backscattering yield. We then parameterize the respective yield curves in order to use them in AMCP simulations. The yields are used in the simulations in order to calculate the probability of backscattering and the average number of secondary electrons with respect to the incident energy and angle.

Using the measured curves for the total yield σ at the various angles shown in the former section and the relative backscattering probabilities $P_{BS/IBS}(E_{in})$, calculated in section 6.2 for a-Si:H and AlO_x , we now calculate the elastic and inelastic backscattering yield for all measured angles for the respective materials.

In this chapter, the notations of TEY and σ are both used for the total emission yield, BSY and η_i , as well as backscattering probability are used interchangeably for the elastic backscattering yield and IBSY along with η_{ie} are used for the inelastic backscattering yield.

The yields are calculated according to

$$\eta_{(i)e}(E_{in}) = \sigma(E_{in}) \cdot P_{(I)BS}(E_{in}). \quad (6.8)$$

and

$$\delta(E_{in}) = \sigma(E_{in}) - \eta_e(E_{in}) - \eta_{ie}(E_{in}). \quad (6.9)$$

As measured in [Jokela 2012] for Al_2O_3 , in [Cimino 2004] for Cu, and theoretically derived by Cazaux in [Cazaux 2012], the backscattering yield goes towards 1 for incident energies towards 0 eV. The total yield has a minimum usually around 5-10 eV. Below that, even though the secondary yield goes towards 0, backscattering is predominant and the total yield $\sigma(0) = 1$. Taking this into account, we add the point for $\sigma(0 \text{ eV}) = 1$ with $\eta_e(0 \text{ eV}) = 1$ and $\delta(0 \text{ eV}) = 0$. As we measured the relative backscattering probabilities at an incident angle of 45° , we first derive the TEY at 45° from our measurements using the cosine dependence of the emission yield. We calculated the TEY at 45° of a-Si:H from the TEY at 30° and 60° and the TEY at 45° of AlO_x from the TEY at 0° and 75° . The resulting total yield is shown in figure 6.18.

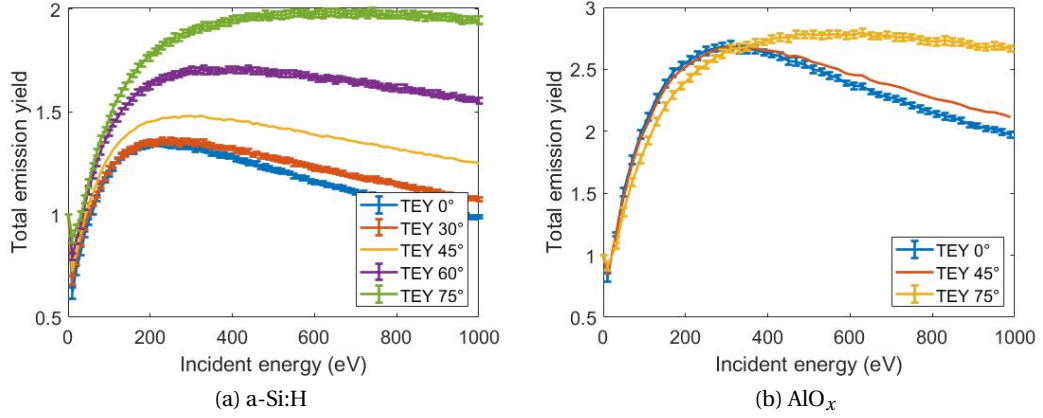


Figure 6.18 – Total emission yield of (a) a-Si:H and (b) AlO_x after adding $\text{TEY}(0 \text{ eV})=1$ and deriving the TEY at 45° .

Next, we look at the elastic backscattering yield and compare our values to two backscattering models, the one derived by [Cazaux 2012], where the angular dependence of backscattering is calculated and the one used in [Kruschwitz 2011], equation 5.43. Their equation for backscattering is derived from quantum mechanics [Cimino 2004]. The equation does not incorporate any angular dependence of backscattering. The angular dependent formula for backscattering according to Cazaux is

$$\eta_e(E_{in}, \theta) = \frac{\left(1 - \sqrt{1 + (\chi / (E_{in} \cdot \cos^2 \theta))}\right)^2}{\left(1 + \sqrt{1 + (\chi / (E_{in} \cdot \cos^2 \theta))}\right)^2}. \quad (6.10)$$

The electron affinity χ of the relevant materials is given in table 6.1.

The elastic backscattering yield η_e for a-Si:H at the measured incident angles calculated

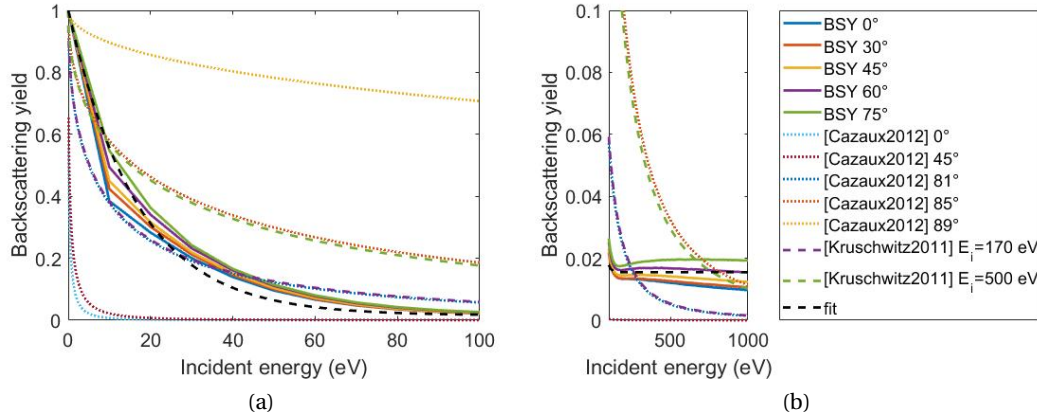


Figure 6.19 – Backscattering yield of a-Si:H, for incident energies between 0 and 100 eV in (a), shown for higher incident energies in (b). The yield is calculated using the relative probability P_{BS} and the TEY. The backscattering yield does not vary much with the incident angle, as we calculated P_{BS} only for 45°. The fit curve of [Kruschwitz 2011], equation 5.43 and the formula of [Cazaux 2012] can both be used to describe the yield.

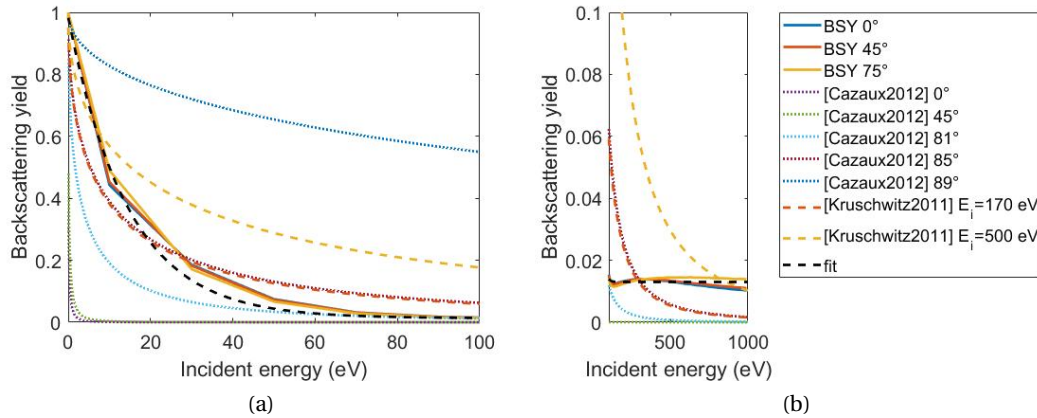


Figure 6.20 – Backscattering yield of AlO_x , for incident energies between 0 and 100 eV in (a) and for energies between 100 eV and 1000 eV in (b). The backscattering yield does not vary much with the incident angle for AlO_x either. The fit curve of [Kruschwitz 2011], equation 5.43 and the formula of [Cazaux 2012] can both be used to describe the yield.

according to equation 6.8 is shown in figure 6.19. The backscattering yield we derived is very similar for all angles that were considered. This could be due to the fact that we only measured the relative backscattering probability P_{BS} at 45° and used the same relative backscattering probability for all angles.

The backscattering yield and the fit curves are shown in figure 6.19 (a) for low energies from 0 to 100 eV, where the the description of [Kruschwitz 2011] with $E_i = 170$ eV represents well the yield we derived from our measurements. The theoretical expression for the backscattering yield from [Cazaux 2012] show the important yield dependence on the incident angle from 0° up to 89° . Our measurements for all angles are comparable to the theoretical curve of Cazaux at 85° . Thus, the theoretical curves cannot be use the calculate the BSY below this angle, but they present a solution to parameterize the BSY at very high incident angles above 85° , where we do not have experimental data.

We fitted the elastic backscattering yield with

$$\eta_e(E_{in}) = a \cdot \exp(-b \cdot E_{in}) + c \quad (6.11)$$

Figure 6.19 (b) shows the fits for energies from 100 eV to 1000 eV. At high energies, although the measured BSY varies, the fit represents the yield better than any of the models. As a consequence, we use the BSY fit for all incident angles up to 85° . For higher incident angles, we use the theoretical model of Cazaux.

Figure 6.20 shows the backscattering yield of AlO_x . Here, we can draw the same conclusions as for a-Si:H and also use a fit of the BSY for all incident angles up to 85° and the model of Cazaux for higher incident angles.

At the end of this chapter in table 6.4, we list the values of the fit constants of $\eta_e(E_{in})$ for both materials, along with the fit constants for the secondary yield.

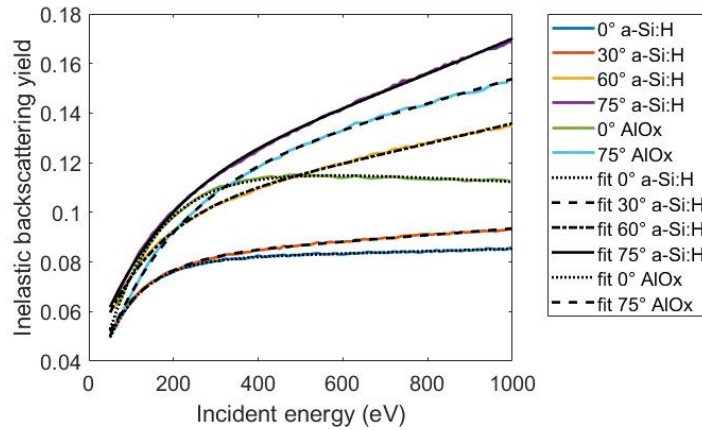


Figure 6.21 – Inelastic backscattering yield curves and fits with $a(\theta) \cdot \exp(b(\theta) \cdot E_{in}) + c(\theta) \cdot \exp(d(\theta) \cdot E_{in})$. Inelastic backscattering is the main backscattering mechanism at high incident energies, whereas at low energies elastic backscattering is predominant.

Inelastic backscattering yield curves were derived from the measurements using equation 6.8

and fitted with

$$\eta_{ie}(E_{in}) = a(\theta) \cdot \exp(b(\theta) \cdot E_{in}) + c(\theta) \cdot \exp(d(\theta) \cdot E_{in}). \quad (6.12)$$

No clear dependence on θ has been found for inelastic backscattering. The inelastic backscattering yield and the fits are shown in figure ?? . As the backscattering yield varies a lot for different experiments and simulations, for a-Si:H as well as for AlO_x , we do not use an exact fit for the inelastic backscattering yield in our AMCP simulations. Instead we use a rough estimation of an average inelastic backscattering yield of about 0.2.

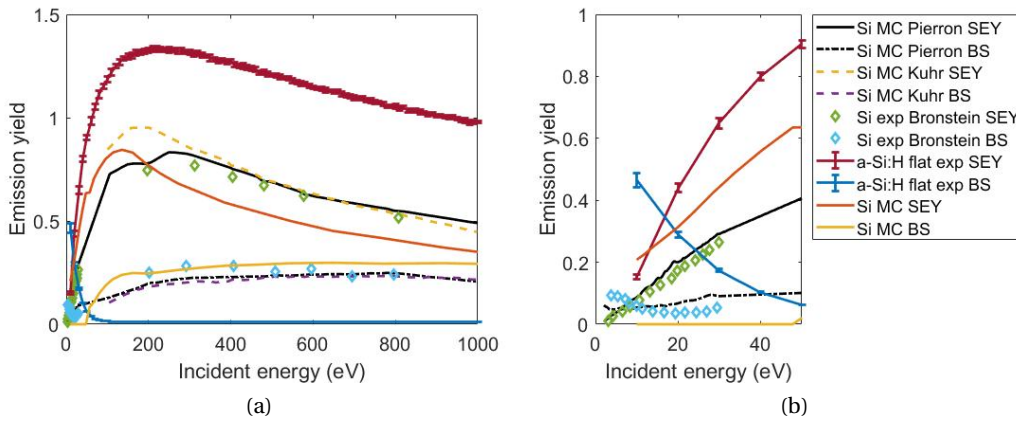


Figure 6.22 – Secondary yield and backscattering yield of Si from literature values compared to our MC calculations and the yields calculated from our experimental TEY curve of a-Si:H

In a first place we calculated the 'real' (= not corrected for backscattering) secondary emission yield according to equation 6.9 to compare the SEY curve to literature values. Figure 6.22 shows the secondary yield (SEY) and backscattering yield (BS) at 0° . The measured secondary yield δ of a-Si:H (a-Si:H flat exp SEY) is higher than the secondary yield curves of Si, as expected. Looking at high energies in figure 6.22a, the backscattering yield we deduced is much lower than measured and calculated from the other authors. Only at low energies, below 50 eV, shown in figure 6.22b, the backscattering yield we deduced (a-Si:H flat exp BS) is higher than the measured and calculated literature values.

On an event basis, elastic backscattering and secondary emission are mutually exclusive whereas an inelastically backscattered electron can create secondary emission. The secondary yield δ for an incident electron with energy E_{in} is corrected for backscattering as in equation 5.5 and defined for $E_{in} > 0$:

$$\delta_{corr}(E_{in}) = (\sigma(E_{in}) - \eta_e(E_{in}) - \eta_{ie}(E_{in})) \cdot \frac{1}{1 - \eta_e(E_{in})}. \quad (6.13)$$

The second term is a correction for mutual exclusivity of secondary emission and backscat-

6.5. Backscattering and secondary yield parametrizations

tering, as the total yield has been collected from the sum of both events. The effect of the correction term is predominant at low incident energies, as shown in figure 6.23. The secondary yield would be underestimated without using the correction.

For the AMCP model, we do not subtract the inelastic backscattering yield, so that both, the secondary yield and the inelastically backscattered yield, can be adjusted independently without affecting the total yield. We use a modified yield $\delta_{mod}(E_{in})$, which is a sum of inelastic backscattering and secondary emission:

$$\delta_{mod}(E_{in}) = \delta(E_{in}) + \eta_{ie}(E_{in}) = (\sigma(E_{in}) - \eta_e(E_{in})) \cdot \frac{1}{1 - \eta_e(E_{in})}. \quad (6.14)$$

We use the yield $\delta_{mod}(E_{in})$ calculated here in the AMCP model as the expected value of the Poisson distribution, to calculate the actual sum of the possibly inelastically backscattered electron and secondary electrons per event. The parameter values of $\delta_{mod}(E_{in})$ for a-Si:H, AlO_x and MgO are given in table 6.4.

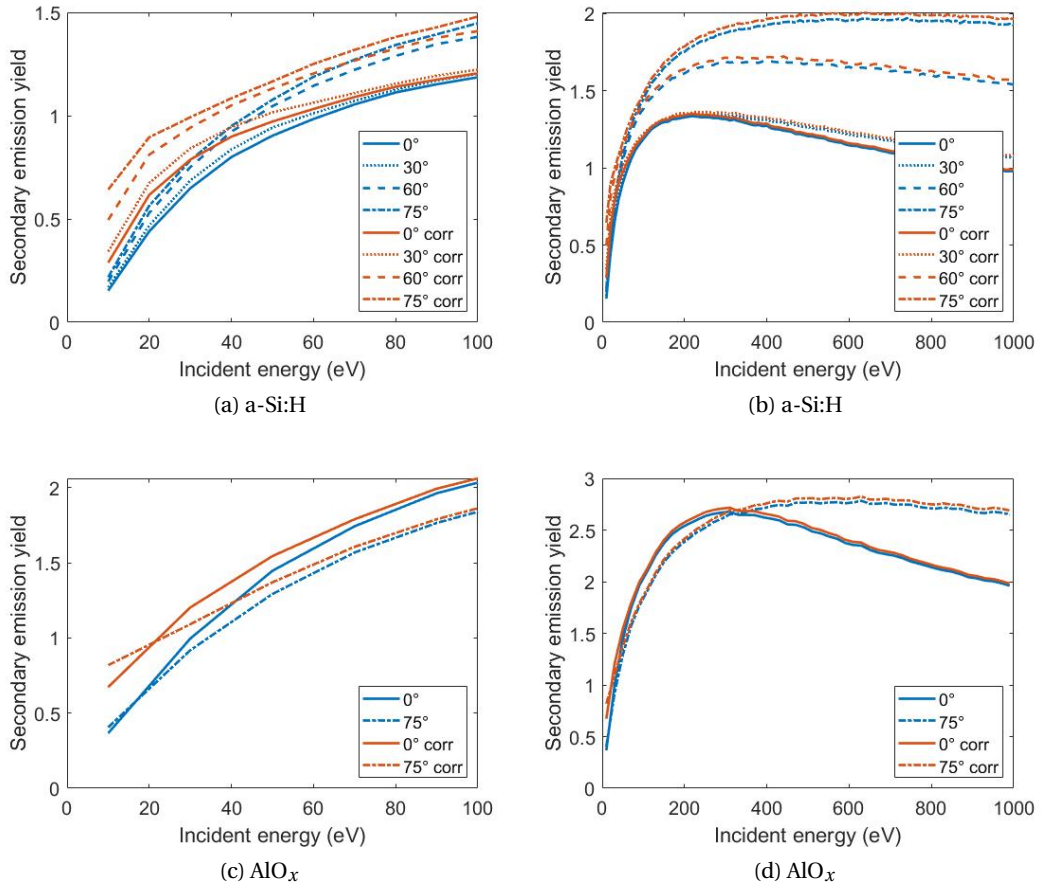


Figure 6.23 – Secondary yield of a-Si:H and AlO_x without (blue) and with (red) correction term for mutual exclusivity of elastic backscattering and secondary emission in Monte Carlo simulations. This correction is most important at energies below 50 eV.

The uncorrected secondary emission yield has been fitted to the secondary yield curve of [Bundaleski 2015]. We show the fit for a-Si:H in figure 6.24a. The angular dependence, expressed in the model by a factor $1/\cos\theta$ might be overestimated when using this factor. We found a better agreement with the measurements when using an exponent of $1/4$ on this cosine dependence. The yield at higher angles is then calculated from the yield at 0° using a factor of $1/\cos\theta^{1/4}$. In figure 6.24b we show the low energy dependence of the same fit. We also fitted the uncorrected secondary yield of AlO_x and of MgO to the model of Bundaleski. The material constants we used and the fit parameters are shown in table 6.4.

As the Bundaleski model cannot be used to fit the corrected secondary yield curve, we use the SEY parametrization of [Vaughan 1989] to that end. The corrected secondary yield of a-Si:H is shown in figure 6.24c for energies between 0 eV and 1000 eV and the low energy part is shown in figure 6.24d. With the AMCP single channel model introduced in the next chapter, we fitted the Vaughan model to the experimental gain and adjusted the parameter δ_m for a-Si:H and AlO_x . Overall, the fit constants vary a lot, not only depending on the material, but also depending on the MCP fabrication and on the Monte-Carlo model used. For conventional MCPs, the fit values of SiO_2 were reported to vary between $\delta_m = 3 - 4$ at $E_m = 350$ eV [Kruschwitz 2011] and $\delta_m = 5.63$ at $E_m = 350$ eV [Ivanov 2018]. The values we use to model AMCPs are comparatively modest, even with the high emissive emitter AlO_x . As our calculations are based on the measurements of a limited number of AMCPs, we might underestimate the gain when calculating novel AMCP geometries, based on these values. The fit parameters for a-Si:H and for AlO_x and MgO are shown in the overview table, table 6.4, at the end of this chapter.

6.6 Summary and parameter lookup table

In this chapter, we have presented measurements of the electron emission characteristics of a-Si:H and AlO_x and the emission yield of MgO . We compared the measurements to simulations, theoretical models and, where available, to literature values.

The emission energy distribution of secondary electrons can be well described by a theoretical model (equations 5.42 and 5.11) for incident energies above 25 eV. For lower incident energies we use a fit function for the emission energy distribution $\partial\delta/\partial E$ (equation 6.5).

The total yield measurements fit well to the literature values, taking into account the layer thickness, roughness and elemental composition. There is an important variation in backscattering probabilities from calculations and in the available literature, this might partly be due to differences in the definition, where some authors do not distinguish between inelastic and elastic backscattering.

We separated the total yield in the respective parts, secondary yield, inelastic and elastic backscattering yield using the relative probability for backscattering measured at an incident angle of 45° . As a consequence, there might be more important variations in the yield with respect to the incident angle, that we are not taking into account.

While other authors of MCP Monte-Carlo models fitted these functions and parameters to their experimental data, we chose to derive the values from a detailed analysis of the layers for two

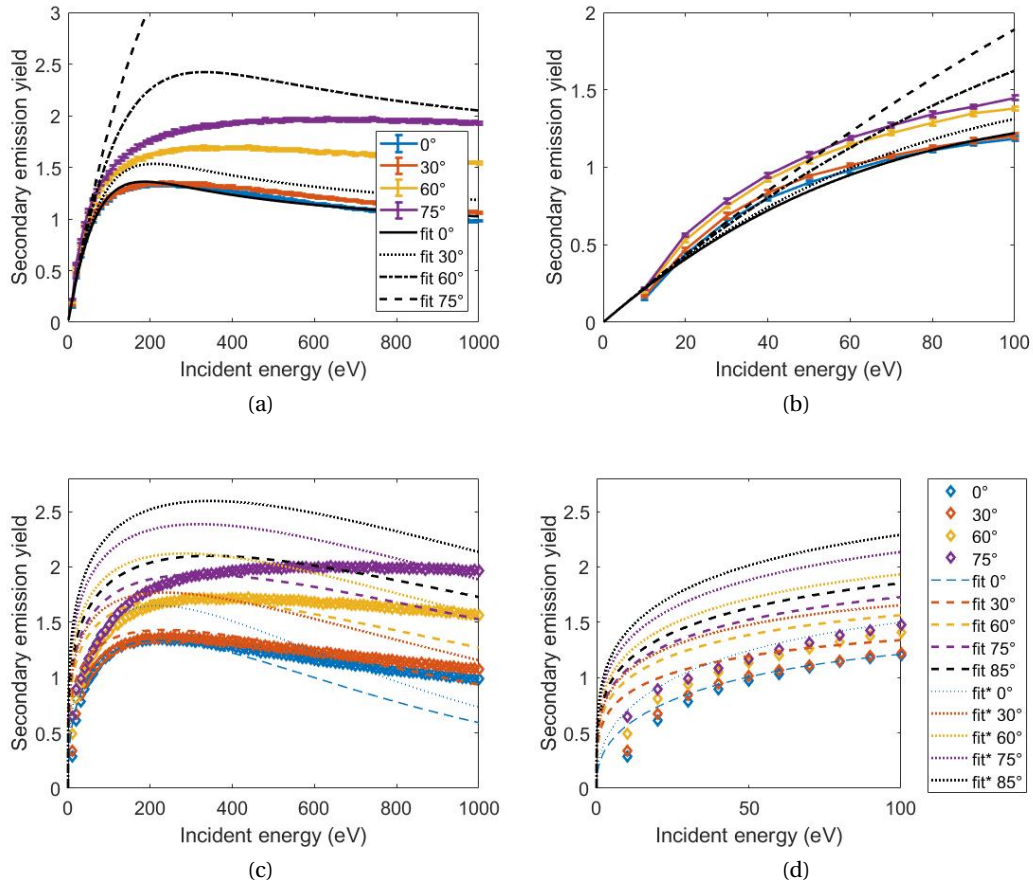


Figure 6.24 – Secondary yield of a-Si:H fitted to the curve of [Bundaleski 2015] in (a) and (b) and fitted to the curve of [Vaughan 1989] in (c) and (d). The Vaughan fit is used for AMCP simulations and the fit* curves were fitted to the experimental gain of AMCPs.

reasons. First, we do not have measurements on a wide range of AMCP geometries available at the moment. As MCPs have been used since the 1980s, they are much better characterized. Second, contrary to MCP models, for the AMCP model, we want to be able to describe shapes that differ from the conventional cylindrical shape. Consequently, dependencies of all the parameters on the incident angle are more important in this case.

As a result we now have a set of functions and parameters for the emission energy distribution and the emission yield, which we can use for AMCP modeling. In the following summary table 6.4 we list all the functions and parameters that were derived in this chapter and that are used in the following two chapters for AMCP modeling. As a comparison, we also show the secondary emission parameters used for MCP models, where the material is SiO_2 . There is an important variation in these literature values, even for MCP models.

Despite our efforts, these are not the absolute values and merely give an approximate idea of the respective functions. Additionally, in a real device, charging effects may play an important role. These are not taken into account yet in our models. We adjusted two of the parameters to the measurements of AMCPs, the inelastic backscattering yield and the maximum secondary yield, using the Monte Carlo model for AMCPs. These adjustments are described in the next chapter, after introducing the model. Along with new measurements of AMCPs (e.g. larger aspect ratio AMCPs), these and other parameters, like the secondary yield shaping parameters s and k , might need to be further adjusted.

6.6. Summary and parameter lookup table

Fit eq. 6.11 for angles $\theta \leq 85^\circ$

Material	Fit parameters		
	a	b	c
a-Si:H	0.9845	0.06005	0.0155
Al ₂ O ₃	0.987	0.069	0.013
MgO	was not calculated, we use the parameters of Al ₂ O ₃		

Theoretical model of [Cazaux 2012] eq. 6.10 for angles $\theta > 85^\circ$

(a) Elastic backscattering yield η_e

Semi-empirical model of [Bundaleski 2015] for $\delta(E_{in})$

Material	Material constants		Fit constants	
	ε (eV)	λ (Å)	b	n
a-Si:H	23 (fitted)	30 (λ/b fitted)	0.15	1.21
Al ₂ O ₃	20 [Joy 1987]	60 [Insepov 2011]	0.08	1.33
MgO	20 [Kanaya 1978]	120 [Kanaya 1978]		

Empirical model [Vaughan 1989] for $\delta_{mod}(E_{in})$

Material	Fit constants			
	δ_m	E_m (eV)	k	s
a-Si:H	1.33 - 1.65*	220	1.63	0.23
Al ₂ O ₃	2.5* - 2.68	310	0.45	0.45
MgO	4.8	514	1.67	0.69
SiO ₂	3-4** - 5.63***	300** - 350***	0.5-1**	0.62**

(b) Secondary emission yield δ

Table 6.4 – Fit parameter values for the elastic backscattering yield and the secondary emission yield of a-Si:H, AlO_x and MgO. The inelastic backscattering yield was approximated to be 0.2 for incident energies above 50 eV. Fit* values were fitted to the experimental AMCP gain. The values for MgO were fitted to the secondary yield measured by [Jokela 2012] and the angular dependence simulated by [Ivanov 2018]. For conventional MCPs the values ** were derived by [Kruschwitz 2011] and those marked *** were derived by [Ivanov 2018].

7 Single channel model for AMCPs

In this chapter, we introduce the cinematic Monte-Carlo model used to calculate electron trajectories inside cylindrical AMCP channels. We use two kind of models for AMCP simulations in this thesis: a cinematic model which has been developed for secondary yield calibration and a finite element method based model that will be presented in the next chapter. The cinematic single channel model serves as a basis for modeling more advanced AMCP geometries with a finite element method model in the next chapter and to predict the timing and gain of cylindrical high aspect ratio AMCPs that have not been measured yet. As a basis for all our AMCP models we use the probabilistic description introduced in chapter 5.3 with the phenomenological probability functions derived in chapter 6. The secondary yield parametrization is calibrated by adjusting the calculated gain to the gain that has been measured on existing AMCPs. We also present a simplified approach to calculate the limits of increasing the aspect ratio in order to raise the gain.

As a result and in agreement with MCP literature we calculated a very short signal rise time of about 7 ps and an average FWHM of about 10 ps for the AMCP channels that are currently fabricated. The timing depends on the channel geometry, but does not vary significantly with the secondary yield. The expected gain using a-Si:H without an additional coating is an average of about 2000 for an aspect ratio of 30. This value can be further increased by coatings with AlO_x or MgO . As secondary electron emission at each collision is Poisson distributed, we observe a considerable AMCP gain variation as a response to the impact of a single electron entering the channel.

7.1 General setup of the Monte-Carlo model for a single channel

In the single channel model electron movement is calculated starting from their first impact inside the channel wall. The first impact inside the channel is at a random height between the top of the channel with length l and a height $l - \tan(\theta)/d$, depending on the incident angle θ and the diameter d , see figure 7.1.

At the first impact the electron can either be elastically backscattered according to $\eta_e(E_{in}, \theta)$ (equation 6.11) or the electron can enter the material. In case the electron is backscattered,

the radial part of its velocity is reversed while the electron continues to travel along the electric field of the channel with unchanged energy $E_{BS} = E_{in}$. In case an electron enters the material, it can be inelastically backscattered according to $\eta_{ie}(E_{in}, \theta)$ (equation 6.12) and it can lead to the emission of secondary electrons.

The number of secondary electrons is chosen according to the secondary emission yield $\delta(E_{in}, \theta)$. An interpolation of the corrected secondary yield of figure 6.23 is used in the first place. Then, the secondary yield parameterization and the inelastic backscattering yield are adjusted to fit the gain measurements of AMCPs. For the latter $\delta_{mod}(E_{in}, \theta)$ parametrization we use the secondary yield model of Vaughan (equation 5.21). The actual number of emitted secondary electrons N is sampled from the Poisson distribution in equation 5.6, with the expected value $\delta_{mod}(E_{in}, \theta)$.

The electron emission angle for inelastically backscattered electrons and for secondary electrons is chosen from the PDFs in equations 5.7 and 5.8. In the case of inelastic backscattering, the electron's energy E_{IBS} is randomly chosen between $E_{in} - 2$ eV and 50 eV and the number of secondary electrons N_{SE} emitted at this impact is reduced by one, $N_{SE} = N - 1$. In case the incident electron is not inelastically backscattered, $N_{SE} = N$ secondary electrons are emitted. The secondary electron emission energy is sampled from the PDF of the measured secondary electron energy distribution $\partial\delta/\partial E(E_{in})$, see figure 6.6. The secondary emission energy is sampled until the condition of energy conservation

$$\sum_1^{N_{SE}} E_{SE} \leq E_{in} - E_{IBS} \quad (7.1)$$

is met.

Each electron created by or backscattered from the first impact is accelerated by the electric field and every impact in the channel wall leads to further backscattering and secondary emission events according to the same mechanisms. The time of each electron moving through the electric field of the channel is calculated. Electron emission and backscattering is assumed to be instantaneous. The time and energy of the electrons arriving at the bottom of the channel are recorded.

Electron-electron interactions and charging effects are not taken into account in the models.

7.2 3D cinematic model

Electron movement within the channel is calculated using cinematic equations between the wall interactions. The electron has an initial energy and angle when emitted as a secondary electron or after being backscattered. The electron is then accelerated by the electric field until its next encounter with the channel wall.

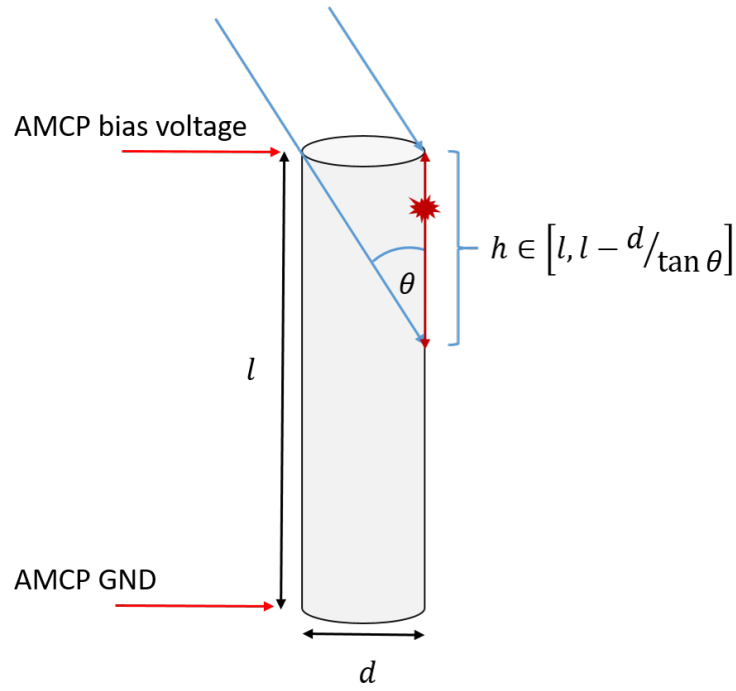


Figure 7.1 – Schematic drawing of the 3D channel geometry used for the simulations shown in this chapter. The channel length is l and its diameter is d . The electron is assumed to hit the channel at a random height in the upper part between l and a height $l - \tan(\theta)/d$, depending on the incident angle θ of the beam. The AMCP bias voltage is always negative with respect to the ground (GND), even when not explicitly mentioned in the text.

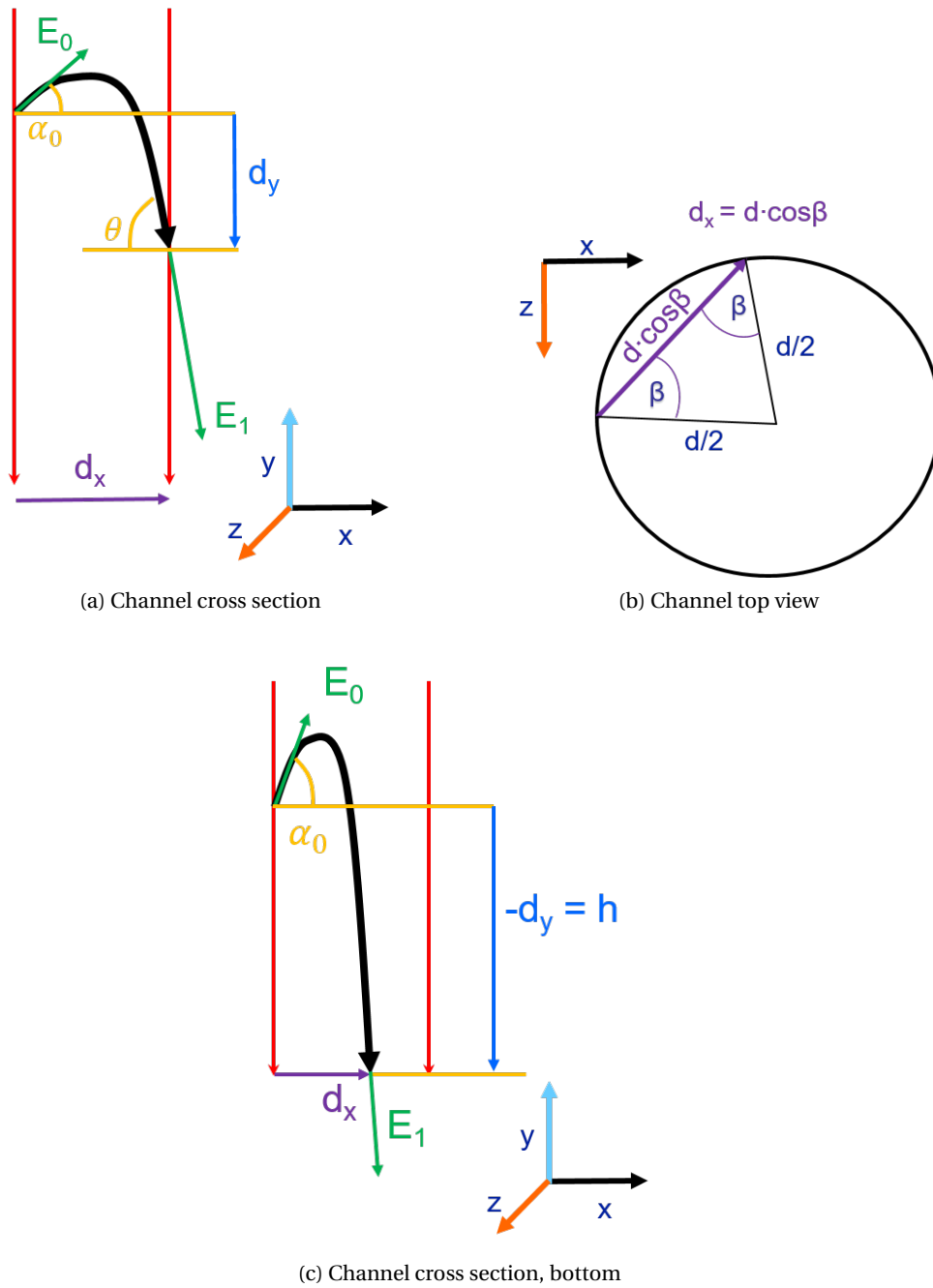


Figure 7.2 – Definition of angles and distances in the cinematic AMCP model and its coordinate system.

7.2.1 Model setup

We defined the coordinate system relative to the channel according to the schematic in figure 7.2. The channel length is defined along the y-direction, thus the electric field is applied uniformly in y direction. The electron travels from a height with positive value $y = l$ until it reaches the bottom of the channel where $y = 0$. The electron emission angle is described by its radial part β in the x-z plane and the angle α_0 relative to the y-axis. The electron travels the distance $d_x = d \cdot \cos \beta$ until it hits the channel wall. The travel time t depends on the angle α_0 and the emission energy E_0 :

$$d_x = d \cdot \cos(\beta) = v_{0x} \cdot t = \sqrt{\frac{2E_0}{m_e}} \cdot \cos \alpha_0 \cdot t, \quad (7.2)$$

with the initial velocity in the xz-plane v_{0x} and the electron mass m_e . The travel time is

$$t = \frac{d \cdot \cos \beta}{\cos \alpha_0} \cdot \sqrt{\frac{m_e}{2E_0}}. \quad (7.3)$$

During this time the electron travels the y-distance d_y

$$d_y = \frac{1}{2} a_y t^2 + v_{0y} \cdot t = \frac{qE}{2m_e} \cdot t^2 + \sqrt{\frac{2E_0}{m_e}} \cdot \sin \alpha_0 \cdot t, \quad (7.4)$$

with the initial acceleration a_y and velocity v_{0y} in y-direction, the elementary charge $q = -1.602 \cdot 10^{-19}$ C and the electric field strength $E = V/l$. The distance traveled is then

$$d_y = d \cdot \cos \beta \left(\frac{qEd \cos \beta}{4E_0 \cos^2 \alpha_0} + \tan \alpha_0 \right). \quad (7.5)$$

The incident energy E_1 of the electron is calculated depending on d_y

$$E_1 = E_0 + qEd_y. \quad (7.6)$$

The second term becomes negative when the electron hits the channel at a higher point than its starting point. The incident angle is calculated from the partial incident velocities in the following way:

$$\theta = \arctan \frac{\sqrt{v_{1z}^2 + v_{1y}^2}}{v_{1x}} \quad (7.7)$$

with the partial velocities at impact v_{1x} , v_{1y} and v_{1z} in x, y, and z-direction respectively. v_{1x} and v_{1z} are equal to the initial velocities, while the velocity in y-direction is calculated from the acceleration through the electric field E . The incident velocities are:

$$v_{1x} = v_{0x} = \sqrt{\frac{2E_0}{m_e}} \cdot \sin \beta \cdot \cos \alpha_0, \quad (7.8)$$

$$v_{1z} = v_{0z} = \sqrt{\frac{2E_0}{m_e}} \cdot \cos \beta \cdot \cos \alpha_0, \quad (7.9)$$

$$v_{1y} = v_{0y} + a_y \cdot t = \sqrt{\frac{2E_0}{m_e}} \cdot \sin \alpha_0 + \frac{qE}{m_e} \cdot t = \sqrt{\frac{2E_0}{m_e}} \cdot \left(\sin \alpha_0 + \frac{qEd \cos \beta}{2E_0 \cos \alpha_0} \right). \quad (7.10)$$

Once an electron arrives to the bottom of the channel and the next hit would be at a value below $y = 0$, its arrival time $t_{end}(y = 0)$ and energy $E_{1,end}(y = 0)$ are calculated. The energy is calculated as

$$E_{1,end}(y = 0) = E_0 - qEh. \quad (7.11)$$

E_0 is the electron's emission energy at the last wall interaction and h the y -distance between the last interaction point and $y = 0$. The arrival time is calculated from the time intervals $t(i)$ of all N wall interactions and the time between the last wall interaction and hitting the bottom t_{last}

$$t_{end}(y = 0) = \sum_1^N t(i) + t_{last}. \quad (7.12)$$

The last time step is calculated using the equation

$$\frac{1}{2} a_y t_{last}^2 + v_{0y} t_{last} + h = 0. \quad (7.13)$$

After simplification, the last time step is

$$t_{last} = \frac{\sqrt{2m_e E_0}}{qE} \left(-\sin \alpha_0 - \sqrt{\left(\sin^2 \alpha_0 - \frac{hqE}{E_0} \right)} \right). \quad (7.14)$$

7.2.2 Calibration of the secondary yield curves with AMCP measurement data

The models were calibrated using experimental gain measurements of all AMCP samples that have been measured so far, published in [Franco 2014a] and [Frey 2019]. We use measurements that have been done at low incident flux of $\Phi = 1.5 \cdot 10^{10}$ electrons/cm²/s and below. AMCP gain has been shown to increase when the incident flux is decreased. AMCPs response to fluxes lower than $6.9 \cdot 10^9$ e⁻/cm²/s have not been measured yet. For AMCP channels with 6 μ m diameter this corresponds to an average number of 2070 electrons impinging per second in each channel. An amplification scheme with a charge sensitive amplifier has been set in place for future measurements of AMCPs in the low flux regime, see chapter 4.6.

Here, we use the gain measurements of AMCPs listed in table 7.1 as the calibration for the secondary yield curve of a-Si:H and AlO_x. The measured gain of all AMCPs is shown in figure

Channel length (μm)	Diameter (μm)	Aspect ratio (AR)	Flux Φ ($\text{e}^-/\text{cm}^2/\text{s}$)	
90	6.6	13.6	$6.9 \cdot 10^9$	[Frey 2019]
90	7.6	11.7	$6.9 \cdot 10^9$	[Frey 2019]
76	6.1	12.5	$9 \cdot 10^9$	[Franco 2014b]
76	7.4	10.3	$9 \cdot 10^9$	[Franco 2014b]
74	6.1	12*	$1.5 \cdot 10^{10}$	[Franco 2014a]
49	6.1	8	$9 \cdot 10^9$	[Franco 2014b]

Table 7.1 – Dimensions of all measured AMCPs and the flux used for gain measurements.
* Samples of these dimensions have been fabricated with an AlO_x coating as well and measured with the same flux.

7.3 as a function of the applied bias voltage and in figure 7.4 as a function of the applied electric field. In a first place, we used the secondary yield equation of a-Si:H derived in chapter 6.2 from measurements of a flat layer and calculated the simulated gain with the cinematic model. We then adjusted the maximum gain parameter δ_m of δ_{mod} (see table 6.4) to fit the maximum gain measurement. In the following, we use the adjusted parameters.

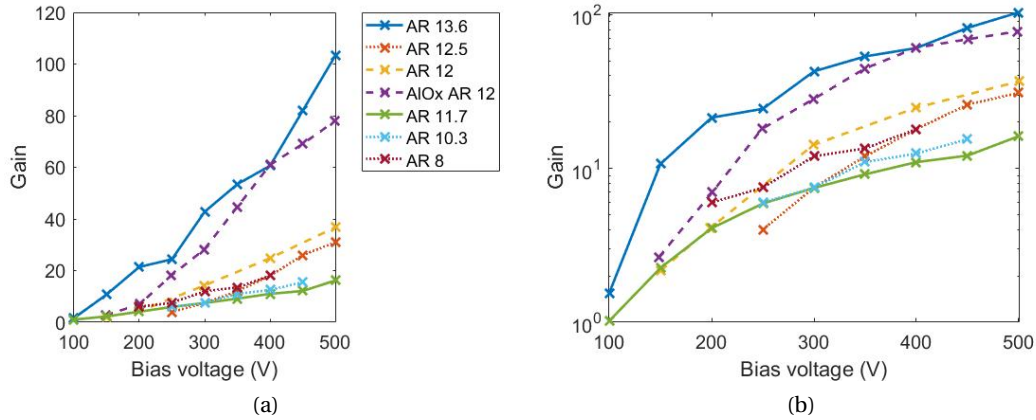


Figure 7.3 – AMCP gain measurements that are used to calibrate the secondary yield parameter δ_m of a-Si:H and AlO_x for AMCP modeling. Measurements done with the same flux (see table 7.1) are illustrated with the same line style. The gain data are displayed in logarithmic scale in (b).

We analyzed the effect of the secondary fit parameters on the calculated gain and timing for an AMCP with an expected gain of 100 at a bias voltage of 500 V and aspect ratio of 13.6. The dimensions of the channel are given in table 7.1. The results of this sensitivity analysis are shown in figure 7.6. We varied the fit parameters s and k of equation 5.21 between 0.1 and 1, and between 0.1 and 2 respectively. The two parameters are shaping parameters of the secondary emission yield curve. Low values of s lead to a rapid increase in secondary yield for very low energies. The lower the parameter s , the faster the critical yield of 1, below which more electrons are absorbed than generated, is passed. the shaping parameter k determines

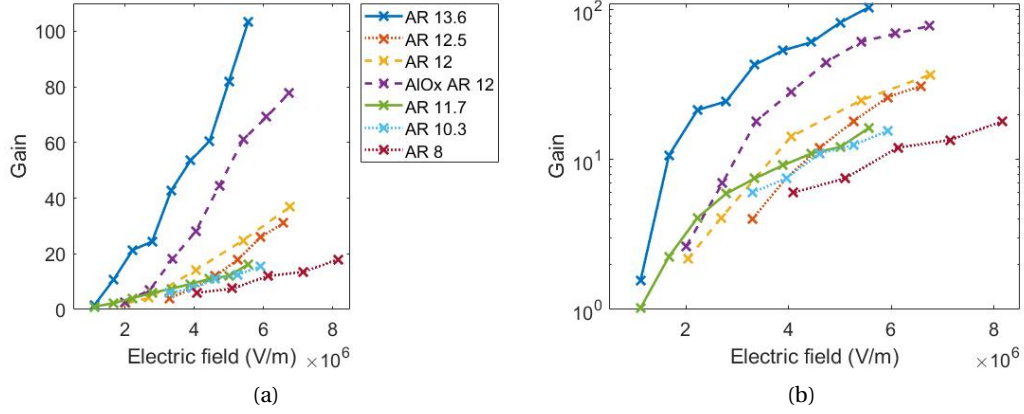


Figure 7.4 – AMCP gain dependence on the applied electric field (a), displayed with logarithmic scale in (b)

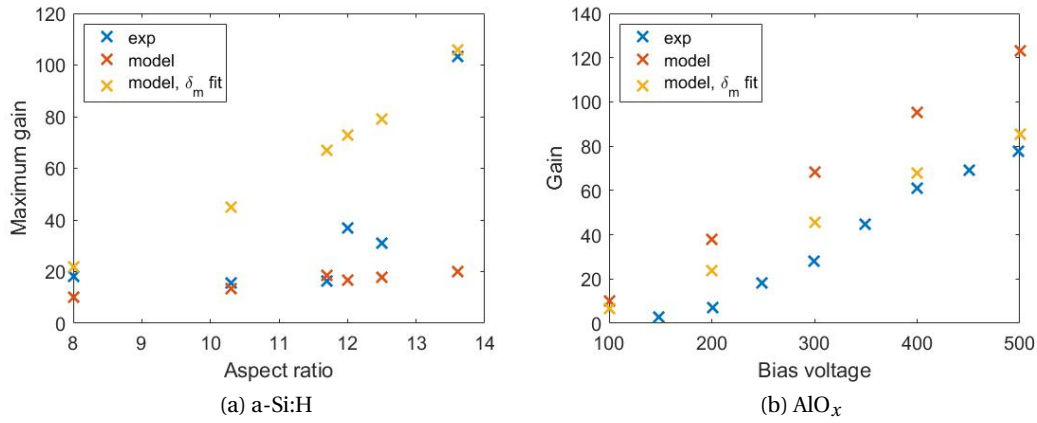


Figure 7.5 – (a) Gain calculated with the AMCP single channel model before and after calibration of the maximum secondary yield at normal incidence δ_m of a-Si:H for all measured aspect ratios at the maximum electric field they were measured respectively. (b) Gain depending on the bias voltage calculated for AlO_x before and after calibration and compared to the experimental values.

the rate of increase in yield with the incident angle. For higher k values higher incident angles lead to a comparatively higher yield. As expected, the gain is highest for a low value of s and a high value of k . We fitted the result of the experimental AMCP gain to $s=0.23$ and $k=1.67$. For higher values of s than 0.4, the calculated gain is below 50, even for high values of k . The average rise time is about 10 ps for low values of s and about 8 ps for higher values of s . The definition of the rise time is introduced in the next section. Here we are particularly interested in the relative change in timing caused by the fitting parameter, and chose to use the rise time as the timing parameter.

We also varied the maximum yield parameter δ_m and the value we added to the inelastic backscattering yield, in order to calibrate the model. The effect of the variation of both parameters is shown in figure 7.6 (c) and (d). As expected, a higher AMCP gain is reached with higher secondary yield δ_m . The gain increases slightly with the inelastic backscattering parameter as well. There is no clear influence of both parameters on the average rise time.

7.2.3 Results

With the cinematic model we calculated the gain and timing for the AMCPs being fabricated at the moment with a channel length of 60 μm and a diameter of 2 μm , thus an aspect ratio AR of 30. We first show the results of calculations using the calibrated parameterization of a-Si:H, an incident angle of 30° and a bias voltage of 500 V, corresponding to an electric field of $8.3 \cdot 10^6 \text{ V/m}$. The average gain we calculated for this geometry is about 2000.

In figure 7.7 we show a summary of the results for 1000 initial electrons. Each of the electrons at the input creates one of the electron clouds arriving at bottom. The arrival time and the number of generated electrons from each initial electron is plotted in figure 7.7a. While the number of electrons created per initial electron is distributed over a broad range from about 10^2 to 10^4 , the arrival time of the electron clouds is similar for all initial electrons, independent of the gain.

The average electron arrival time from all 1000 input electrons was plotted in figure 7.7b. The distribution of the electron arrival time in the range of 30 ps is very narrow, as expected for a narrow channel diameter of 2 μm . The average timing can be fitted with a normal distribution with a mean value of 31.8 ps and a full width half maximum (FWHM) of 11.8 ps. This is the transit time spread of the signal created by the total number of initial electrons.

The possible events upon electron impact at the channel wall were categorized into the following categories: elastic backscattering (BSE), inelastic backscattering (IBSE), elastic backscattering and secondary emission (IBSE), secondary emission (SEE), absorption (Absorbed), arriving at the bottom (Bottom) and escaping at the top (Top). For the calculated channel geometry the overall event proportion is shown in 7.7c. 32% of the generated electrons arrive at the bottom and under 1% escape at the top for the incident angle of 30°. 35% of the electron impacts lead to secondary emission, 3% lead to secondary emission and backscattering, 10% are absorbed and 23% are backscattered, thereof 19% elastically. Although the backscattering yield is only significantly high for electrons with energies below 50 eV (see figure 6.19) backscattering

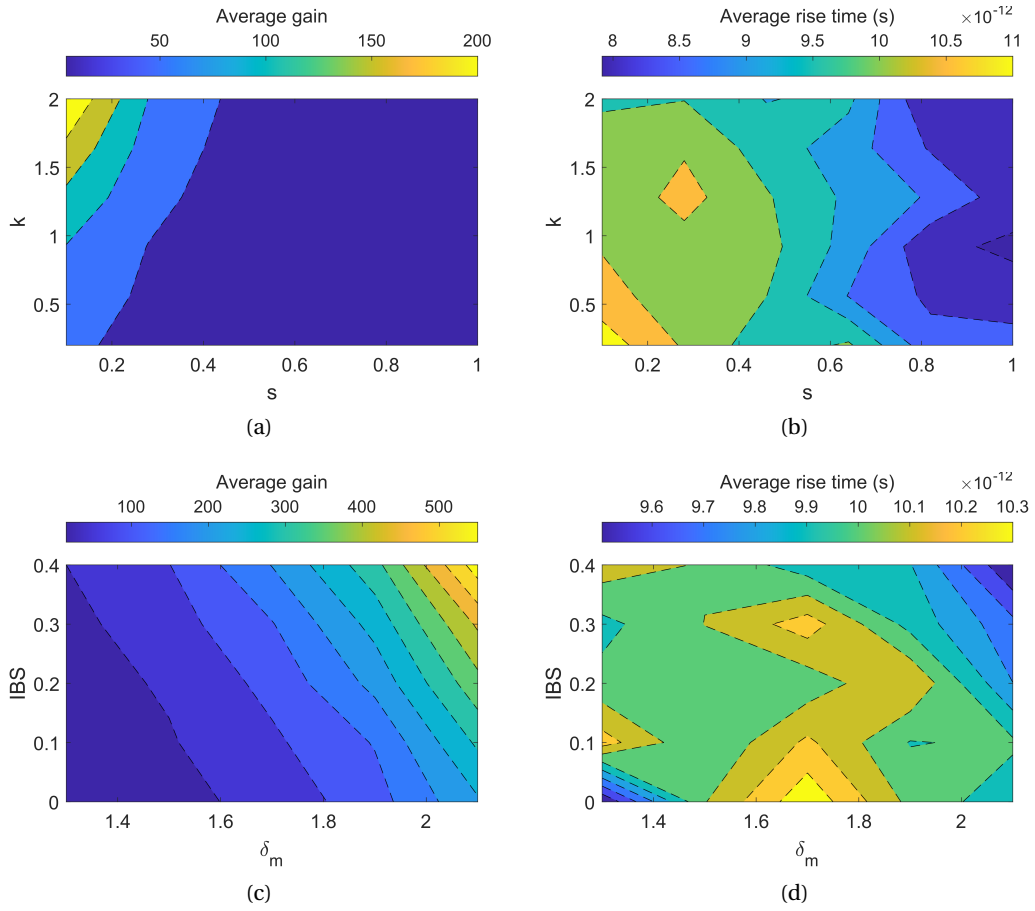


Figure 7.6 – Sensitivity of AMCP gain and rise time for an AMCP sample with aspect ratio 13.6 and expected gain of about 100 on the secondary yield curve shaping parameters s and k shown in (a) and (b), and on the maximum secondary yield δ_m and the additional inelastic backscattering probability IBS shown in (c) and (d).

makes up an important part of the interactions with over 20%.

The gain distribution is shown in the histogram of figure 7.7d with a bin size of 200. As seen in figure 7.7a, the gain generated from one electron has a broad distribution. The reason is that the actual electron emission is Poisson distributed, which introduces a notable variation in the number of emitted electrons per impact. For each of the initial electrons the overall number of electrons arriving at the bottom of the channel then varies significantly. This variation does not play a role when the AMCP is used to detect an incident photon flux, as the average signal is measured in that case, as in our measurements. In the case of single photon detection though this variation needs to be taken into account.

Figure 7.7e shows the number of wall interactions, which grows along the channel depth. This is an important way to see if the AMCP is working in its optimal multiplication mode, when the diameter is still wide enough with respect to the applied electric field to generate in average more electrons than are absorbed.

Finally, in figure 7.7f we show the energy distribution of the electrons that arrive to the bottom of the channels. We see that most electron energies are below 50 eV with an exponential decrease towards higher energies. A maximum electron energy of about 40 eV has been measured experimentally in AMCPs [Frey 2019]. The simulation results agree with the measurement.

Furthermore, we calculated the current generated by each initial electron. The number of generated electrons is multiplied by their charge of $-1.602 \cdot 10^{-19}$ C and the current is then calculated from the incremental charge per time interval $\Delta Q / \Delta t$.

In figure 7.8 we show the current and the distribution of its rise time t_r and amplitude I_{max} . The rise time t_r is defined as the time interval between the times when 10% and 90% of the maximum current I_{max} are reached respectively, $t_r = t(0.9 \cdot I_{max}) - t(0.1 \cdot I_{max})$. The average rise time is 7.2 ps with a standard deviation of 1.7 ps. The average amplitude is 41 μ A. The standard deviation of the amplitude was calculated as 33 μ A, although additionally to this value the asymmetric distribution of the amplitude needs to be taken into account, where low amplitude values are more likely than the rare very high amplitude values in the hundred μ A range. The transit time spread of AMCPs, which is equivalent to the timing jitter in electronics, is defined as the FWHM of the threshold time distribution. Here, we set the threshold to a value of 80% of the average current amplitude $0.8 \cdot I_{av}$, and then plot the time when each of the generated current pulses reaches this threshold values. The time distribution is shown in figure 7.8e. We calculated a timing jitter of about 6 ps for the given channel dimensions. The definition of the timing jitter depends on the electronics used to detect the electron cloud generated by the AMCP. A constant fraction discriminator can be used to decrease the time spread further. In figure 7.8f, we show the time distribution of the calculated current pulses, when they reach a fraction of 80% of their respective maximum amplitude. With this approach, the intrinsic timing jitter of one channel is decreased to 2.7 ps. Compared to the lowest intrinsic single photon timing resolution of 7 ps that has been reported for SPADs [Nolet 2018], AMCPs could be used to drastically improve the current single photon detection timing limits.

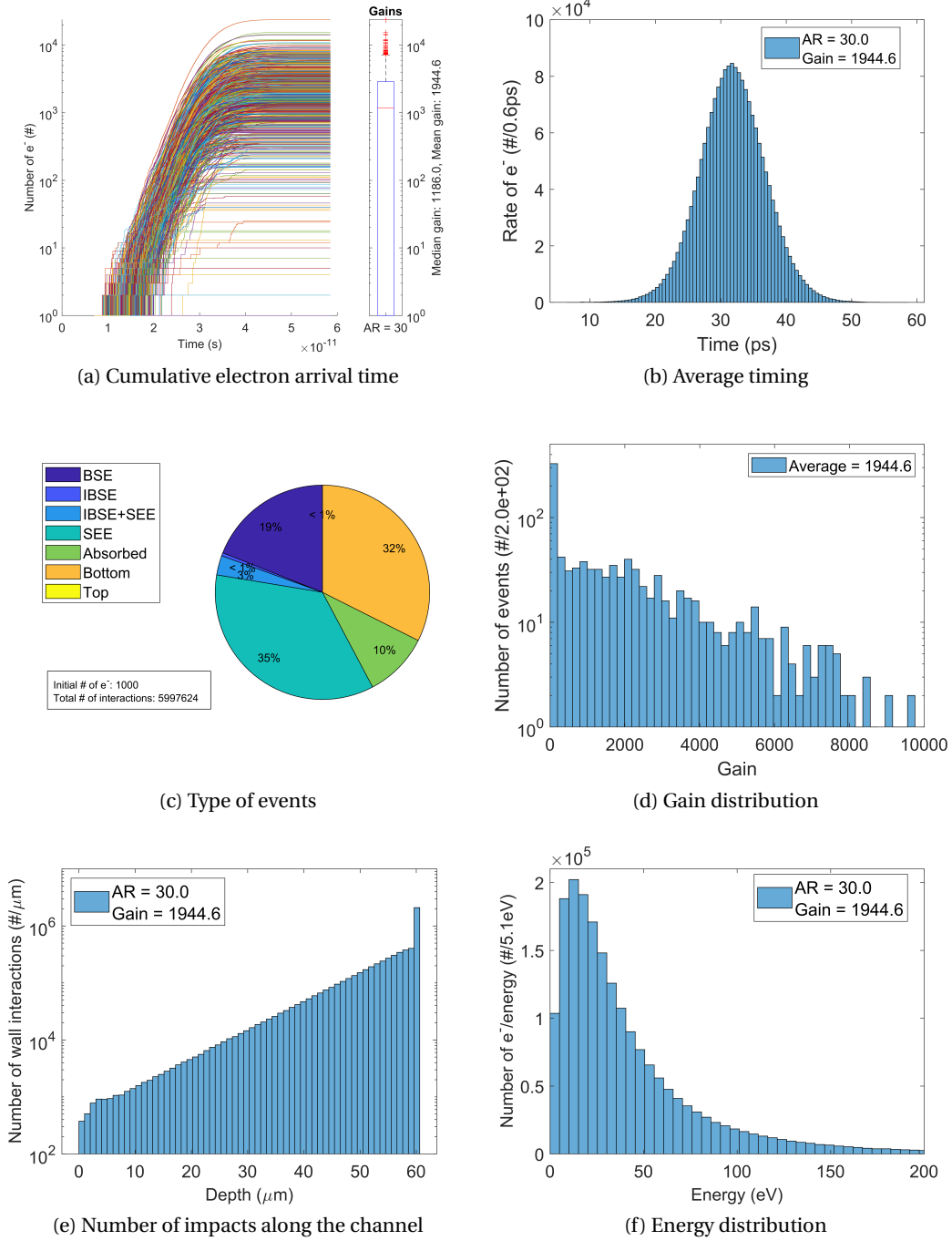


Figure 7.7 – Results for an AMCP with aspect ratio 30 and without an additional coating.

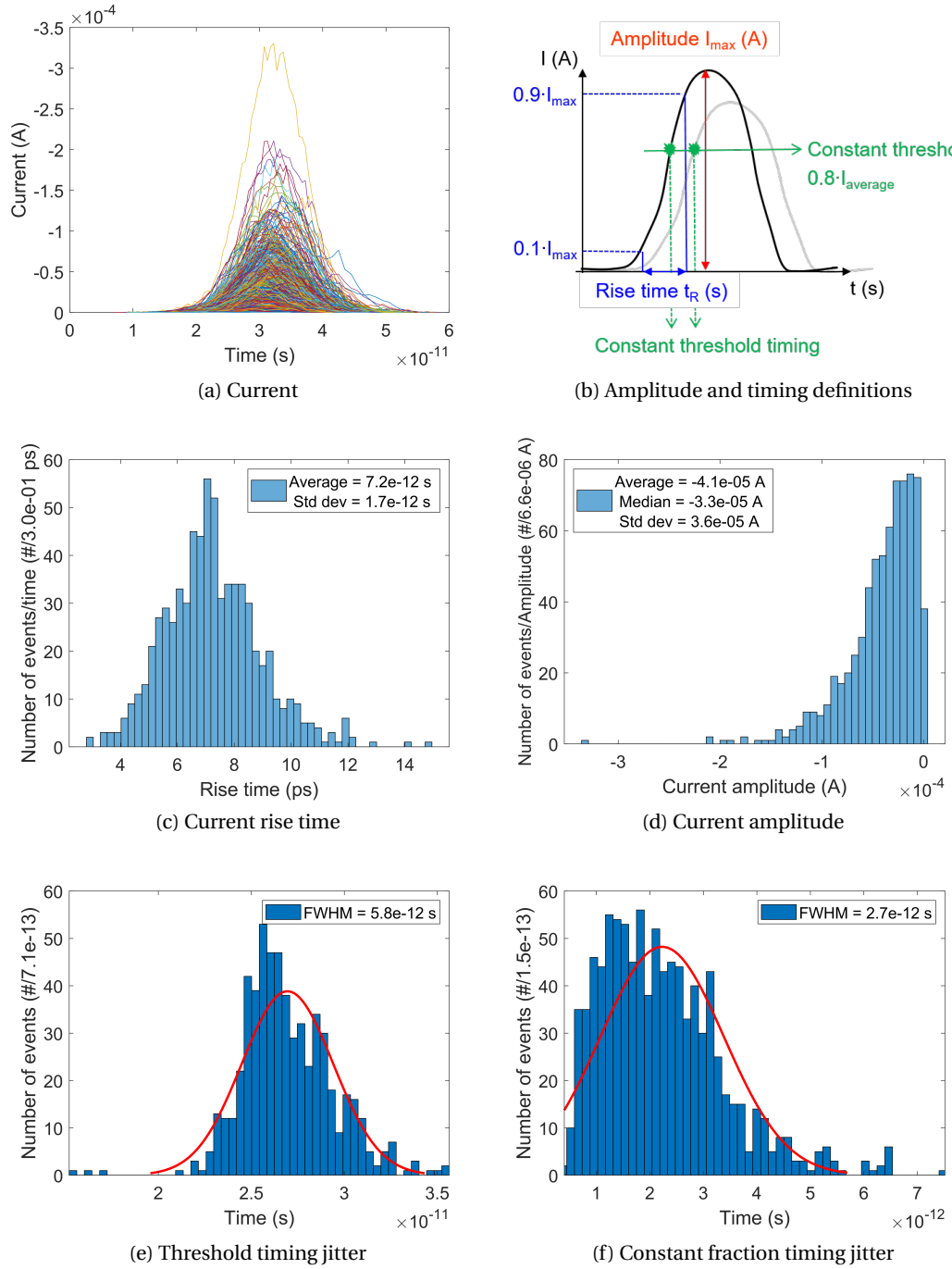


Figure 7.8 – a) Current signals for an AMCP with aspect ratio 30 and without an additional coating calculated for 1000 events. One event is one incident electron at the top of the channel according to the incident angle of 30° , see figure 7.1. b) Definition of the current rise time, amplitude and threshold timing for each current pulse. c) Distribution of the current rise times. d) Current amplitude distribution. e) Timing distribution for a constant threshold. The timing jitter is 5.8 ps. f) The timing jitter is reduced to 2.7 ps, when a constant fraction discriminator is used.

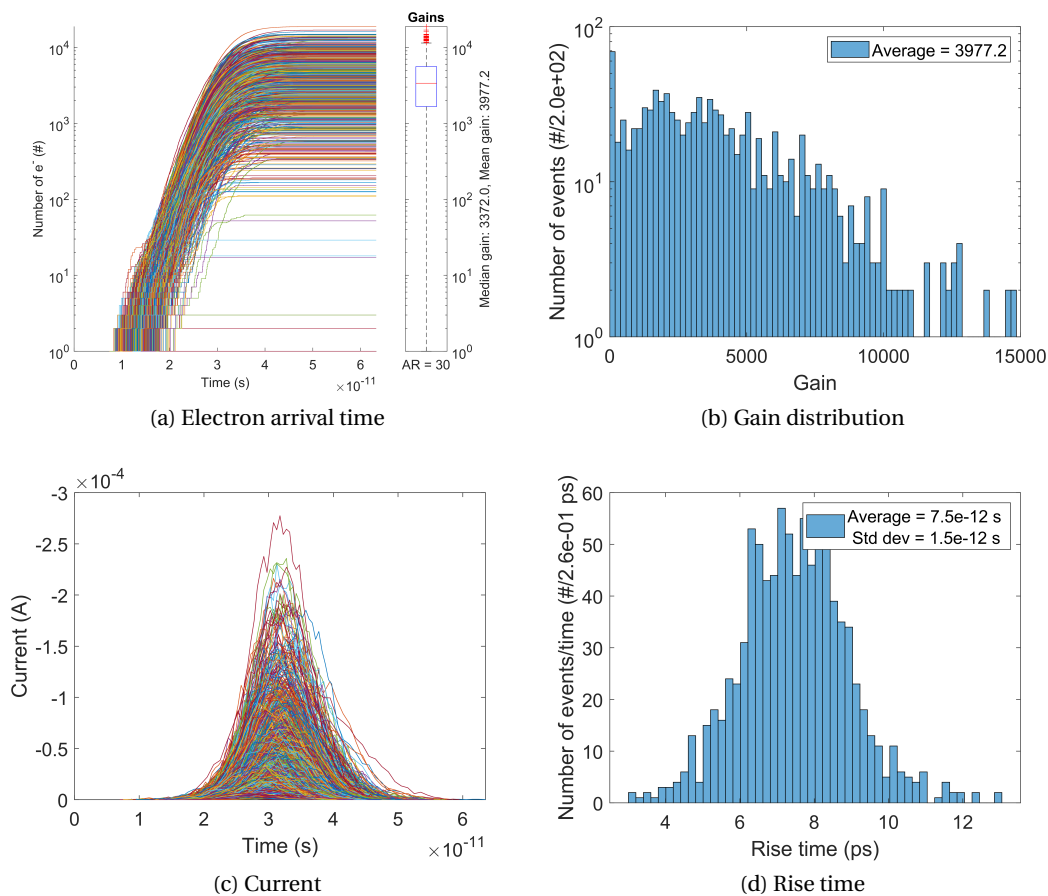


Figure 7.9 – Results for an AMCP with aspect ratio 30 with no additional coating inside the channel and a coating on top of the channel with an average SEY of 5.

In figure 7.9 we show the results for a high emissive layer on top of the channel, for the first impact, where the secondary yield is assumed to be 5, compared to the yield of 2 for the calculations of an a-Si:H channel without coating. The average gain in that case is about 4000 and the average arrival time is 31.9 ps with a standard deviation of 5.1 ps. The arrival time is therefore not affected by the secondary yield at the first impact.

The gain and timing characteristics for AMCPs with an AlO_x coating and with an MgO coating were calculated. For AlO_x , all the parameters used were presented in chapter 6. For MgO we showed the secondary yield parameters in table 6.4 and we use the secondary electron emission energy distribution of [Cazaux 2010a], equation 5.11 with the electron affinity $\chi = 1.4$ eV [Thomas 1980] of MgO.

With the parametrizations used, we calculated a gain of about 1400 for AlO_x and about 2000 for MgO, while the timing characteristics remain unchanged. The gains are lower than expected, compared to the gain calculated for a-Si:H. Although, when using the parameters s and k from the fit to experimental gain measurements of AMCPs, we calculate a gain of more than $3.9 \cdot 10^6$ for AlO_x . As the expected gain of MgO is even higher, we did not pursue these calculations. These gains can only be reached with an ideal charge replenishment, and as we do not take into account such effects at this stage, such high gains cannot be verified.

Surely, the gain of AMCPs will increase with high emissive coatings, probably by one or several orders of magnitude. Quantitatively this increase cannot be predicted on the basis of the present experimental data. More AMCPs with MgO and AlO_x coatings need to be measured in order to improve the secondary yield model for both materials.

We calculated the expected gain and timing for incident electrons at different impact heights in the channels. We varied the impact height according to the angle of an incident beam (see figure 7.1), where small angles lead to electrons impinging along the whole length of the channel or even on the bottom of the channel without generating an electron cloud and for steeper angles, electrons are more likely to impinge at the entrance of the channel. In a real AMCP, electrons reaching the bottom without interacting with the wall is unlikely, even at very low incident angles or with an incident direction parallel to the channel wall. A real AMCP has a roughness, is not completely straight, and the electric field might not be perfectly perpendicular to the top electrode.

We varied the incident angle between 1° and 45° for channel diameters of $2\text{ }\mu\text{m}$, $3\text{ }\mu\text{m}$ and $4\text{ }\mu\text{m}$. The channel length was $60\text{ }\mu\text{m}$ and the bias voltage was 500 V. The average gain and rise time and their standard deviation are shown in figure 7.10. The gain varies with the incident position of the electron. For low angles, the electron can arrive close to the bottom of the channels, whereas for higher incident angles, the electron's first impact height is close to the top of the channel. For example for a $2\text{ }\mu\text{m}$ channel diameter, an incident angle of 45° corresponds to an initial impact height between $60\text{ }\mu\text{m}$ and $58\text{ }\mu\text{m}$, and for an incident angle of 1° almost 50% of the electrons arrive directly at the bottom, while the remaining electrons impact at a point along the whole length of the channel. The average gain varies significantly with the incident angle, for one aspect ratio and bias voltage, between 400 and 1800 for a $2\text{ }\mu\text{m}$ channel diameter. The average gain and its standard deviation, figure 7.10a and c, vary in a

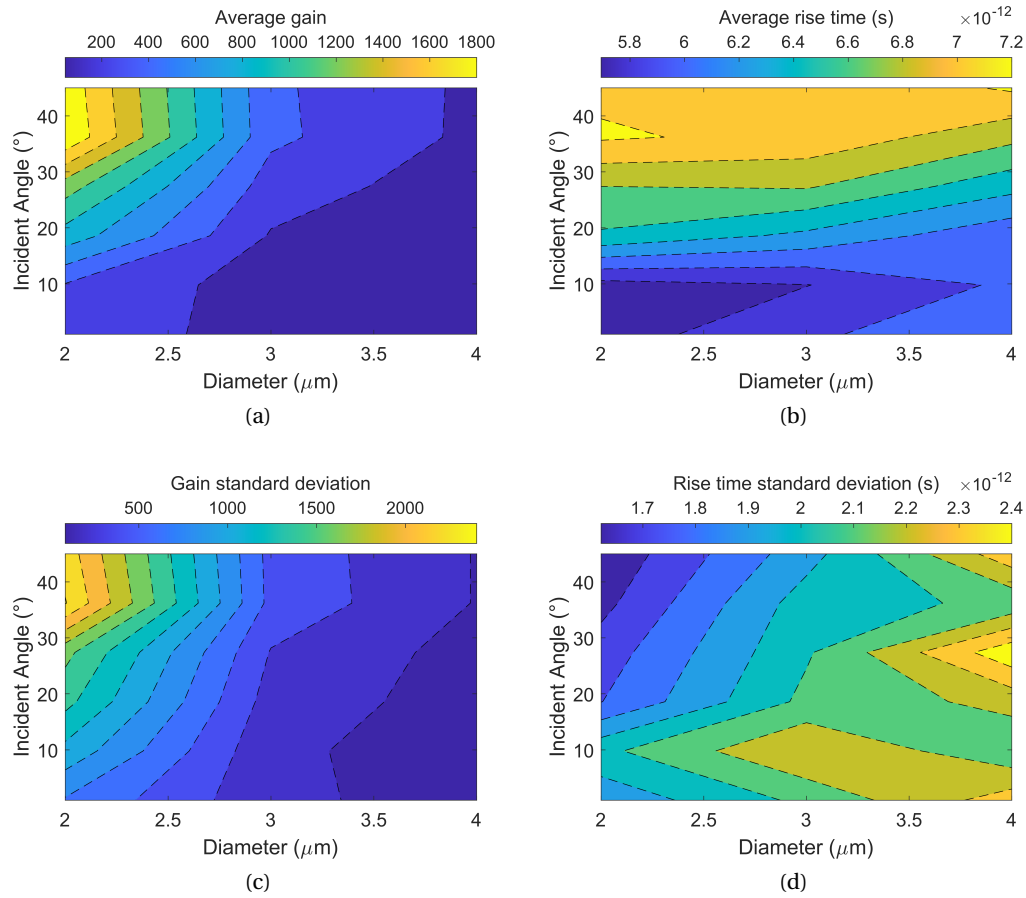


Figure 7.10 – Variation of the average gain and rise time with the incident angle of the first electron and thereby the range of the impact height (see figure 7.1) for AMCP channels with a length of $60\mu\text{m}$ and diameters between $2\mu\text{m}$ and $4\mu\text{m}$. The standard variation of the gain varies in the same manner as the gain. Variations in the gain are not due to the incident angle, but due to the Poisson distribution of the secondary electron emission. The rise time decreases for lower incident angles, as electrons travel a smaller part of the channel.

similar manner depending on the incident angle. The important variation in the calculated gain is due to the Poisson distribution of the secondary yield at each impact. Additionally, the average gain varies with the incident angle. This variation does not increase the relative variance of the gain.

The variation of the rise time and the standard variation of the rise time is shown in figure 7.10b and c. We notice a slight increase in rise time from 5.8 ps to 7.2 ps for higher incident angles, when electrons impact at a higher point in the channel. This variation correlates to the longer travel time of the electrons. The standard deviation additionally depends on the channel diameter, although the change in the standard deviation of the rise time is below 1 ps.

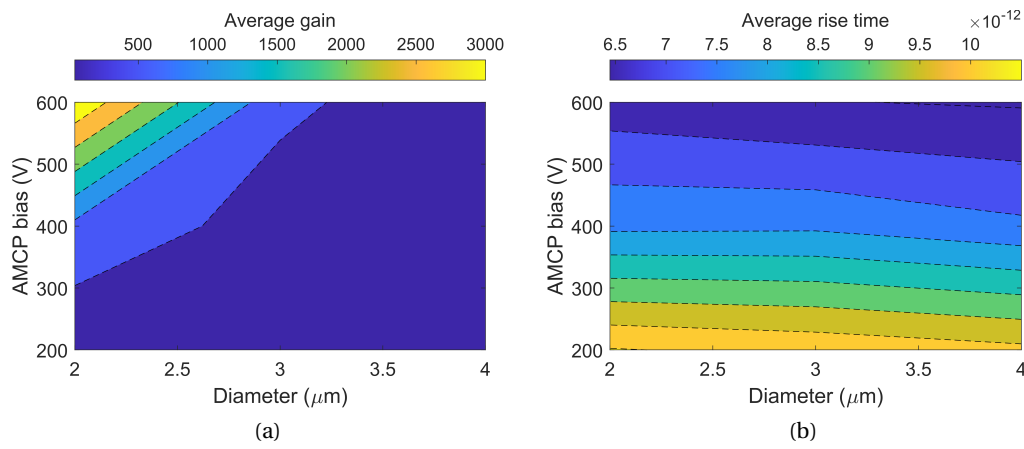


Figure 7.11 – Overview of expected gain and rise time for AMCPs with a channel length of $60\text{ }\mu\text{m}$ for different channel diameters and a bias voltage between 200 V and 600 V. 600 V correspond to half of the maximum electric field a-Si:H can sustain.

We calculated the expected gain and timing for AMCPs with a length of $60\text{ }\mu\text{m}$ and incident angle of 30° for different diameters and a bias voltage between 200 V and 600 V. The analysis was done for a-Si:H, where the secondary emission parameters are best known. An overview of the gain dependence on these parameters is shown in figure 7.11. The gain increases rapidly with the electric field and with a decrease in the channel diameter. The maximum bias voltage shown here corresponds to half of the maximum field amorphous silicon can sustain. Using higher bias voltages can increase the gain dramatically, as can be seen for the smallest channel diameter of $2\text{ }\mu\text{m}$. The rise time decreases with the applied bias voltage, as is expected from the higher acceleration of electron in a higher electric field.

Considering the fabrication possibilities, one could imagine to fabricate AMCPs with very high aspect ratios and even smaller diameters by reducing their thickness further. In figure 7.12, we show the expected gain for a-Si:H with very small geometries, channel lengths between $10\text{ }\mu\text{m}$ and $30\text{ }\mu\text{m}$ and diameters between $0.5\text{ }\mu\text{m}$ and $1\text{ }\mu\text{m}$, for the maximum electric field of $2 \cdot 10^7\text{ V/m}$. The gain of a channel with a length of $30\text{ }\mu\text{m}$ and a diameter of $0.5\text{ }\mu\text{m}$ was not calculated as the number of electrons generated per event surpasses 10^7 . The gain of AMCPs

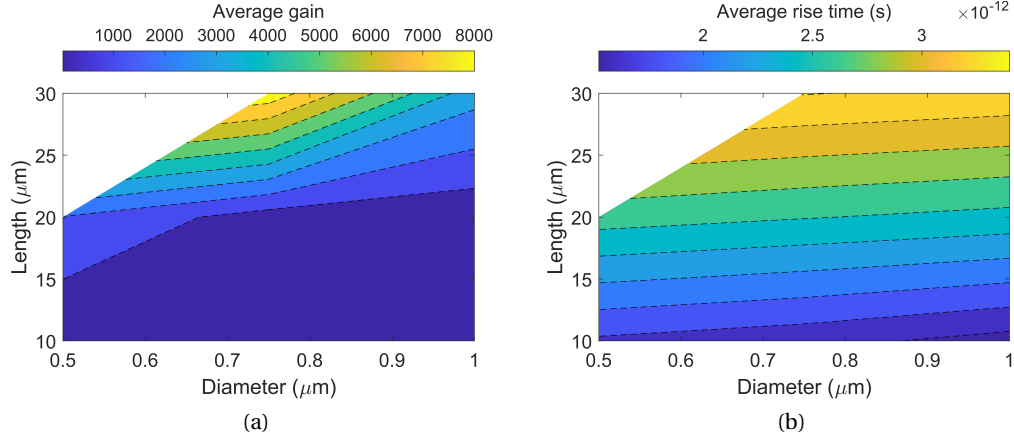


Figure 7.12 – Expected gain and rise time when miniaturizing AMCPs. The results are shown for the maximum electric field of $2 \cdot 10^7$ V/m. The channel length was varied between 10 μm - 30 μm and the diameter was varied between 0.5 μm - 1 μm .

with a channel length of 20 and less is not sufficient, whereas an AMCP with 30 μm could still produce an adequate gain, for an aspect ratio above 40. The average rise time in these channels is very short with about 3 ps for a diameter of 0.75 μm and a length of 30 μm , where a gain of up to 8000 can be reached. Of course, longer channels would be recommended in order to apply a larger potential difference and increase that number further. Here, we explore the limits and the maximum performance of AMCPs when going towards smaller structures. When reducing the diameter further for a constant channel length, we would expect an increase of the gain. Theoretically, does the gain keep increasing when going towards much lower diameters in the hundreds or tens of nanometer range? We answer this question in the next section, using a simplified gain model.

7.3 Simplified gain model evaluated for high aspect ratio

We use the gain equation of MCPs derived by [Ladislav Wiza 1979] as a basis for a simplified analytic description of the AMCP gain as a function of diameter. Our goal is to analyze the limits of high aspect ratios by the mean of reducing the diameter. For a given electric field strength, reducing the aspect ratio by reducing the diameter leads to more collisions and lower energy electrons inside the channels, as their average energy uptake between wall impacts is reduced. The secondary yield function in the low energy region below 50 eV can be assumed to be linear. In this case, backscattered electrons are not taken into account. We use the gain equation:

$$G = \delta^n = (a \cdot E_{in} + b)^n. \quad (7.15)$$

7.3. Simplified gain model evaluated for high aspect ratio

The number of average impacts inside the channel can be derived from an average emission angle normal to the channel wall, an average emission energy E_0 and the channel length l and diameter d

$$n = \frac{l}{d_y} = \frac{l}{\frac{qVd^2}{4E_0l}}. \quad (7.16)$$

V is the bias voltage and q the elementary charge. The average incident energy is

$$E_{in} = E_0 + \frac{1}{4E_0} \left(\frac{qVd}{l} \right)^2. \quad (7.17)$$

The maximum bias voltage that can be applied depends on the electric field strength the material can sustain. The maximum field strength for amorphous silicon is $E_{max} = 2 \cdot 10^7$ V/m. The maximum bias voltage is then $V_{max} = E_{max} \cdot l$. The maximum gain can then be calculated as

$$G = \left(a \cdot \left(E_0 + \frac{q^2 E_{max}^2 d^2}{4E_0} \right) + b \right)^{\frac{4E_0l}{qE_{max}d^2}}. \quad (7.18)$$

In the case of a-Si:H, the average secondary yield at the first impact is 2, and equation 7.18 becomes

$$G = 2 \cdot \left(a \cdot \left(E_0 + \frac{q^2 E_{max}^2 d^2}{4E_0} \right) + b \right)^{\frac{4E_0l}{qE_{max}d^2} - 1}. \quad (7.19)$$

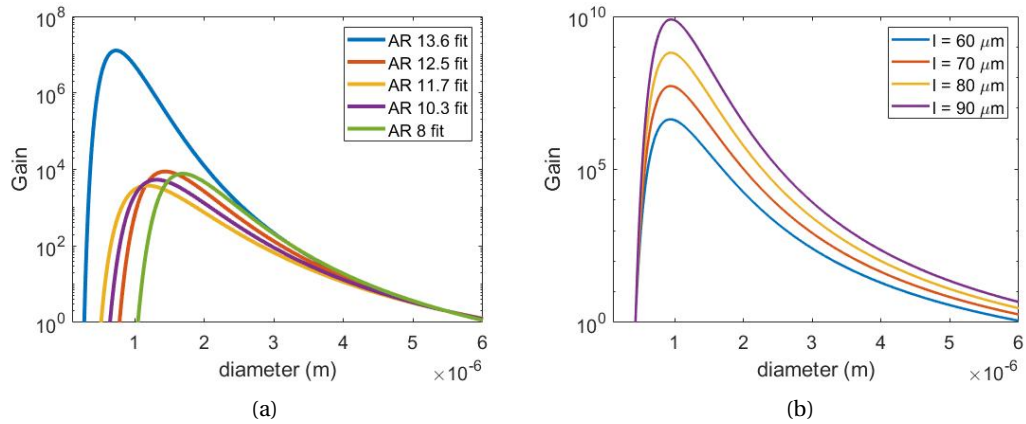


Figure 7.13 – Limits of reducing the diameter for high gain in AMCPs. (a) Linear secondary yield fitted to AMCP gain measurements with different aspect ratios (ARs) result in slightly different curves. Overall, diameters below $1 \mu\text{m}$ result in a rapid decrease in gain. (b) Assuming an upper limit for the electric field, an increase in channel length leads to an increase of the expected gain without changing the ideal diameter.

We used the linear secondary yield parameters a and b fitted to gain measurements of AMCPs

with aspect ratios between 8 and 13.6, listed in table 7.1, to determine the ideal diameter for a channel length of $60\text{ }\mu\text{m}$ and to calculate the expected gain for a channel length between $60\text{ }\mu\text{m}$ and $100\text{ }\mu\text{m}$. The secondary yield curves are fitted to AMCPs without an additional coating. Thus the gain calculated here is constrained by the limited secondary yield of a-Si:H. Figure 7.13 shows the expected gain behavior when the diameter is reduced. The gain decreases rapidly for diameters below about $1\text{ }\mu\text{m}$. A variation in channel length does not affect the lower limit for the diameter.

We conclude that increasing the aspect ratio of AMCPs by reducing the diameter is limited by the electric field the material can sustain. As backscattering is the dominant process at low energies, this very approximate model might not be realistic. When low energy electrons are backscattered, they can continue along the electric field of the channel and pick up more energy, and at the next impact might have enough energy to produce an emission yield > 1 , increasing the gain. The importance of considering backscattering in the simulation of electron cloud formation from low energy electrons with energies below 20 eV , has been shown in [Cimino 2004]. Cimino et al. show an increase in electron density of more than 6 orders of magnitude when backscattering is considered in simulations compared to simulations where only the secondary emission is considered.

To answer the question, if the gain can be raised even further when going towards nanometer structures, our model points towards the fact that there could be an ideal diameter, below which we expect the gain to decrease. Considering backscattering could significantly change this conclusion.

7.4 Summary

In this chapter, we introduced Monte-Carlo simulations of electron trajectories in a cinematic single channel model. The model can be used to calculate the expected AMCP timing and the gain of high aspect ratio AMCPs and AMCPs with highly emissive coatings. We calculated an expected gain of about 2000 for the AMCP channels that are realized at the moment with a channel length of $60\text{ }\mu\text{m}$ and a $2\text{ }\mu\text{m}$ diameter and with no additional coating. We also showed a signal rise time of about 7-9 ps. This agrees with the literature for MCPs. As in MCPs the timescale of the signal formation in AMCPs is very fast. We determined a maximum timing jitter of about 12 ps for this geometry. Furthermore we did not observe a dependence of the timing on the gains. The timing is governed by the geometry of the channels. Wider channels result in a wider time spread, while the narrow channels we presented result in a narrow time spread below 2 ps according to the standard deviation of the calculated signal rise time.

In the next chapter, we use the finite element method to calculate electron trajectories within an electric field. For cylindrical shapes, the results from both approaches are comparable and using the cinematic model is more time effective. The way the cinematic model is set up, it cannot be easily extended to other geometries. As a consequence, in the next chapter, we will introduce the FEM model, which can be used to simulate AMCPs with arbitrary channel shapes.

8 Simulations of AMCPs with non-cylindrical channel shapes

After calculating the response of cylindrical AMCPs to an incident electron and calibrating the secondary yield parameters with experimental data in the former chapter, we now use this parametrization to calculate the response of other AMCP geometries. Funnel shapes are useful to increase the collection efficiency of AMCPs. These calculations give a first estimation on how these shapes would affect the AMCP gain and timing.

Electron trajectories in the AMCP channel are modeled using the finite element method. We use this model to simulate cylindrical AMCP channels, to verify our simulation results with experimental data and the results from the cinematic model. The FEM single channel model serves then as a basis for AMCP modeling with geometries that differ from the cylindrical MCP channel shape.

8.1 General model setup

We set up the model within the electrostatics and particle tracing modules of COMSOL Multiphysics® 5.5. At all instances where values need to be chosen according to a probability density function (PDF), we use the LiveLink™ for MATLAB® with our own code in the form of MATLAB® functions to calculate the PDF and to choose the value accordingly. As for the cinematic model we use at least 1000 runs to calculate one scenario, because of the randomness in the AMCP electron multiplication. One event corresponds to one photoelectron arriving at the AMCP wall, at a random position between the channel entrance and the height defined by the beam tilt, see figure 7.1.

The geometry of the single channel is shown in figure 8.1. The top of the channel is set to $z=0$ and the channel length shown here is $60\text{ }\mu\text{m}$. The volume where electrons can move freely, according to the electric field, is marked blue in figure 8.1a. The bias voltage is set at the layers marked blue in figure 8.1b. From top to bottom the layers correspond to the photocathode, the AMCP top electrode and the grounded AMCP bottom electrode. Here, the photocathode is modeled with a distance d_{PC} of only $20\text{ }\mu\text{m}$ to save computation time. For a realistic electric field at the channel entrance the photocathode bias V_{PC} is set as $V_{PC} = V_{PCexp} \cdot d_{PC} / d_{PCexp}$,

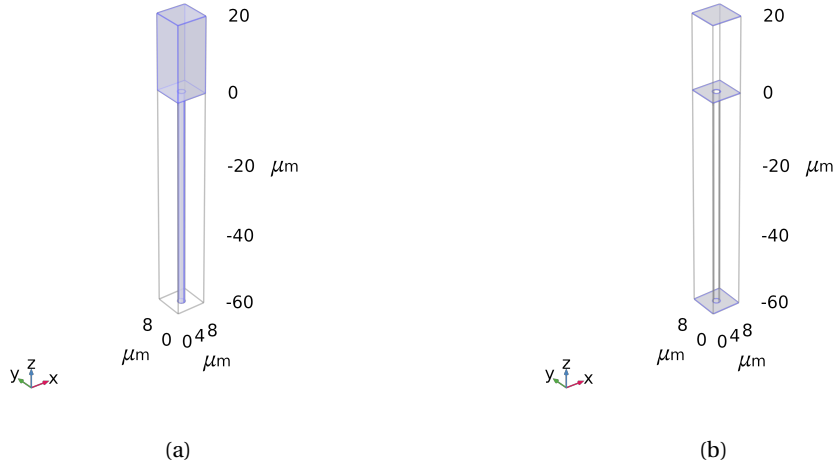


Figure 8.1 – Single channel model geometry with the cylindrical channel and a photocathode above the channel entrance. (a) The blue parts represent air (vacuum). (b) Bias voltage is set at the blue layers. From top to bottom the layers represent the photocathode, the AMCP top electrode and the AMCP bottom electrode.

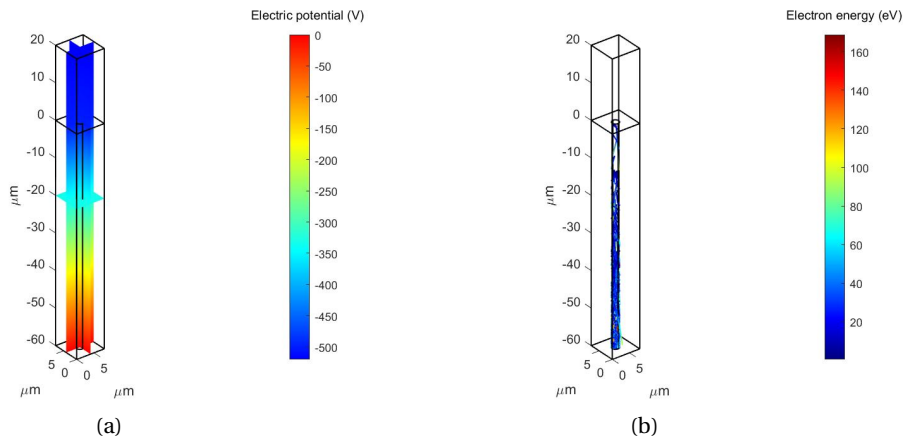


Figure 8.2 – The electric field distribution is shown for an AMCP channel bias of -500 V and a photocathode bias of -520 V, to take into account the reduced distance here with respect to the experiments.

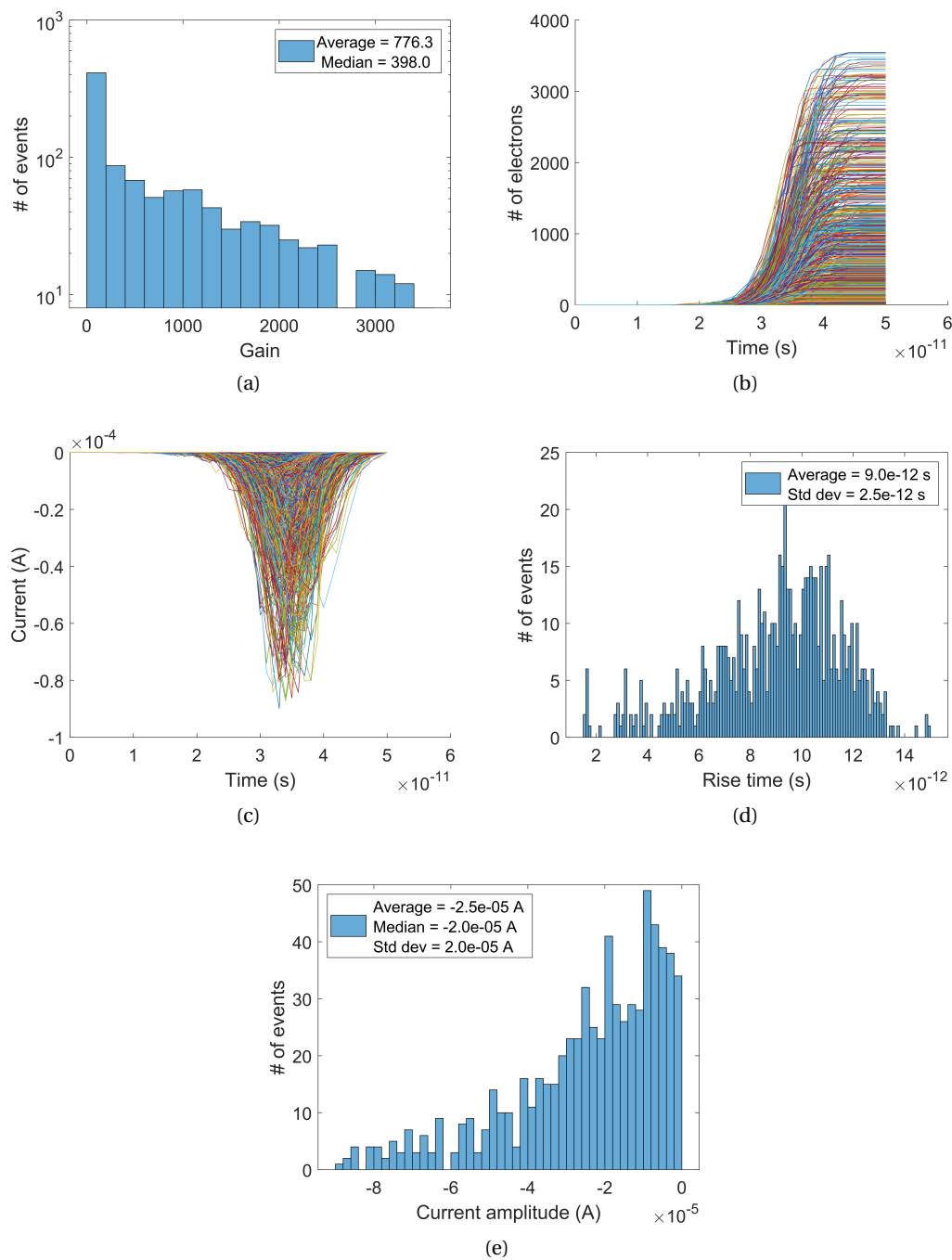


Figure 8.3 – Results of the single channel FEM model.

with the experimental photocathode bias V_{PCexp} of -1000 V and the photocathode distance d_{PCexp} of 1 mm.

For the simulation of electron trajectories in a single channel, we solved the model for time steps of 2 ps between 0 ps and 16 ps, followed by 1 ps steps up to 40 ps and 2 ps steps up to 50 ps. We chose a physics-controlled mesh with a minimum element size of 200 nm and a maximum size of 4 μm . The time steps were chosen after a few test runs that determined the expected timing and the mesh was chosen with the elements as tall as possible, as long as the interaction point inside the channel could still be allocated by the model, to reduce the computation time for 1000 runs.

At first we show the electric field distribution and the electron trajectories in a channel in figure 8.2. The electric field distribution is shown in (a) for an AMCP top electrode bias of -500 V and a photocathode bias of -520 V. The resulting electron trajectories from one incident electron are shown in 8.2b. The maximum electron energy collected inside the channel is about 170 eV. As we only show one trajectory, this is only the energy distribution from one event. This agrees with the electron energy distribution where the most probable energies are very low, as seen in the former section.

Next, we show results, where we use an AMCP channel bias of -500 V, a photocathode bias of -1000 V and a photocathode distance of 20 μm . The results we show here, are simulation results where inelastic backscattering was not taken into account and where elastic backscattering had been parameterized with lower values. Contrary to the cinematic model, we could not yet implement energy conservation in an adequate way here.

An overview of the results for the simulation of one channel is shown in figure 8.3. As a consequence from the lower backscattering probabilities used, we observe a lower average gain and a gain distribution, where low gains are more probable. The median gain is only 398, whereas the average gain is 776. The expected current pulse has an average rise time of 9 ps compared to 7 ps calculated with the cinematic model. This agrees quite well despite the differences in the implementation of the backscattering mechanism.

The implementation of backscattering and energy conservation can be further improved for the results to agree more with the results of the cinematic model and to lay a better foundation for modeling AMCPs with other geometries.

8.2 Funnel shaped channels

The electric field distribution in funnel shaped channel openings has been calculated using the electrostatics tool of COMSOL. We simulated different funnel shapes, width and distances. The distance parameters that were varied are shown in figure 8.4.

For a fixed diameter and a fixed distance between channels, it is clearly beneficial to increase the funnel width to a maximum in order to increase the collection efficiency. We show a simulation of the electric field lines (red) and the electric potential lines (blue) for different parameters in figure 8.5. The width is varied between the figure 8.5 (a) and (c), while all other parameters are constant. From the simulations we see that a great funnel width allows the

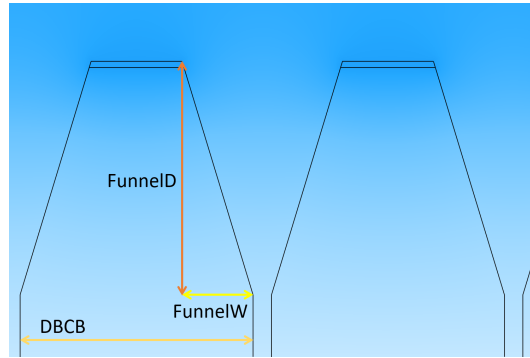


Figure 8.4 – Distance parameters of funnels that were varied in this study of the electric field distribution.

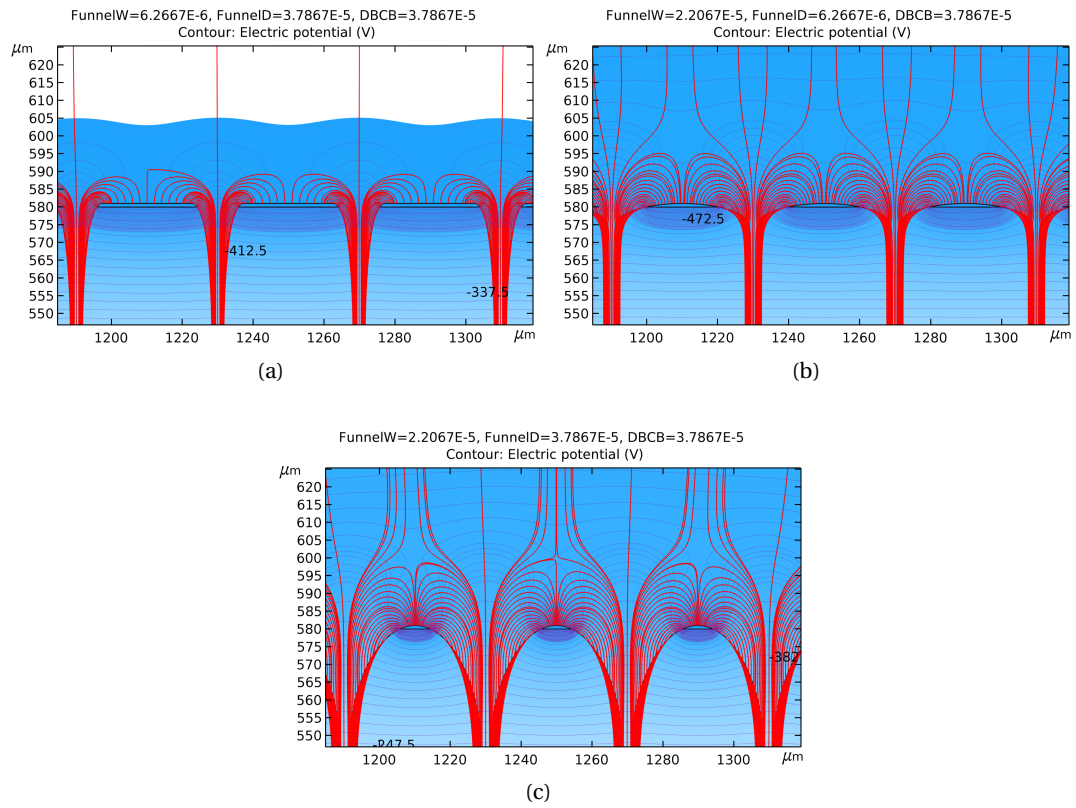


Figure 8.5 – Electric field lines (red) and electric potential lines (blue) simulated in 2D for AMCP channels with different funnel widths in (a) and (c), and different funnel depths in (b) and (c), while all other parameters are constant.

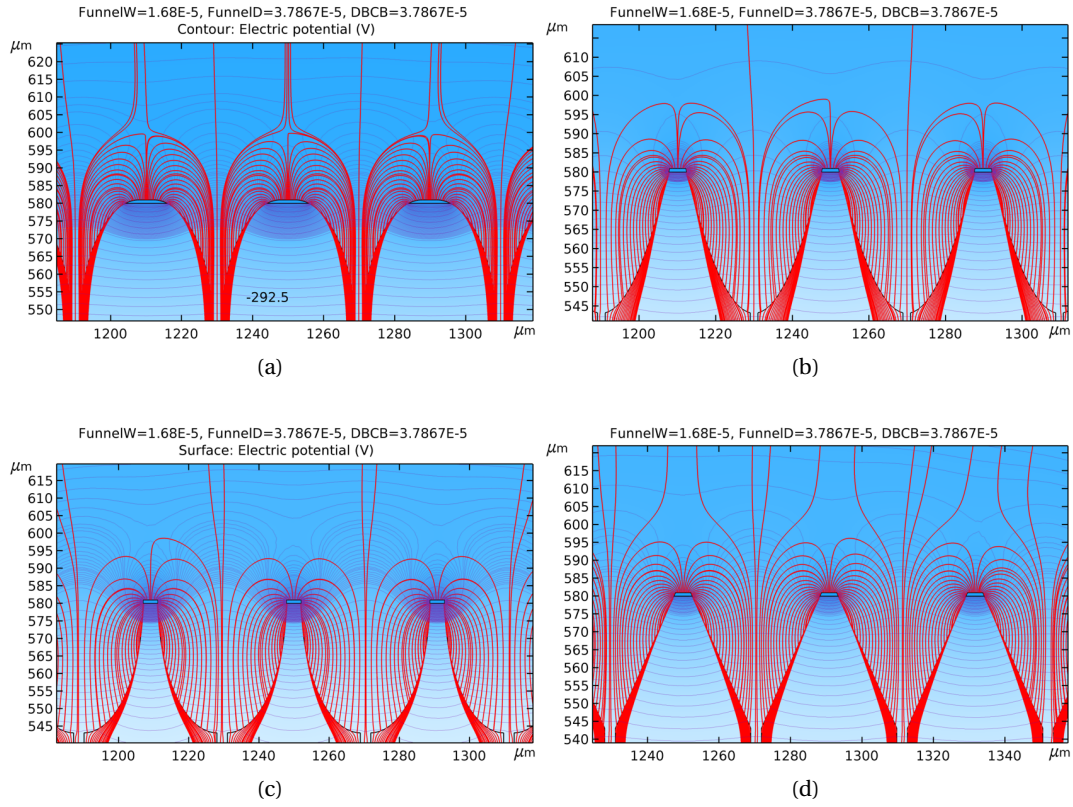


Figure 8.6 – Electric field lines (red) and electric potential lines (blue) simulated in 2D for AMCP channels with funnel opening. From (a) to (d) we show different funnel shapes, keeping the same funnel depth and funnel opening for all examples

8.3. 3D electron trajectories in funnel shaped channels

electric field lines to enter the channels. As low energy secondary electrons follow the field lines, this might be effective to guide electrons inside the channel, even when a large funnel width is used. In figure 8.5 (b) and (c) we compare two funnel depths while the remaining geometry is constant. The funnel depth needs to be adjusted according to the width, to not generate a flat channel entrance, which might not be beneficial for electron multiplication due an electric field that is almost perpendicular to the surface.

Furthermore, we compared the effect of the funnel shape on the electric field distribution, shown in figure 8.6. Here, all parameters, like the funnel depth and distance are constant for the different shapes. The electric field lines are shown in red and the equipotential lines of the electric potential are shown in blue. We see in figure 8.6, the shape of the funnel affects the density of the electric field lines and thus the strength of the electric field. For the shape figure 8.6a, we would expect electron collection to be most efficient. In the case of figure 8.6c, the field lines are perpendicular to the surface, which does not promote electron movement towards the channel opening. The other two cases are in between the two. From this electrostatics analysis, the electric field of funnel shapes appear to be dependent of the exact funnel shape. As a next step potential shapes can be identified experimentally, and consequently the effective gain and timing of AMCPs with these shapes can be simulated. After drawing general conclusions from this simple analysis of the electric field distribution in funnels with different shapes, we now move on to the simulation of electron multiplication in a complete 3D AMCP funnel model.

8.3 3D electron trajectories in funnel shaped channels

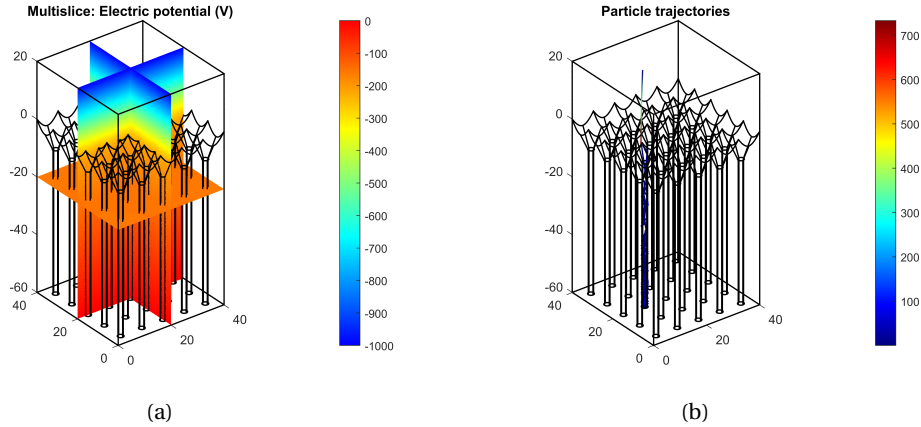


Figure 8.7 – (a) Electric field distribution in the AMCP assembly with a photocathode bias of -1000 V and a channel bias of -500 V. (b) Particle trajectories upon one event, the emission of one electron from the photocathode. The unit of the colorbar is eV.

We simulated an assembly of funnel shaped channels instead of one channel, in order to take into account eventual backscattering events between channels, which is possible depending on the funnel opening. In figure 8.7, we show the distribution of the electric field in (a) and

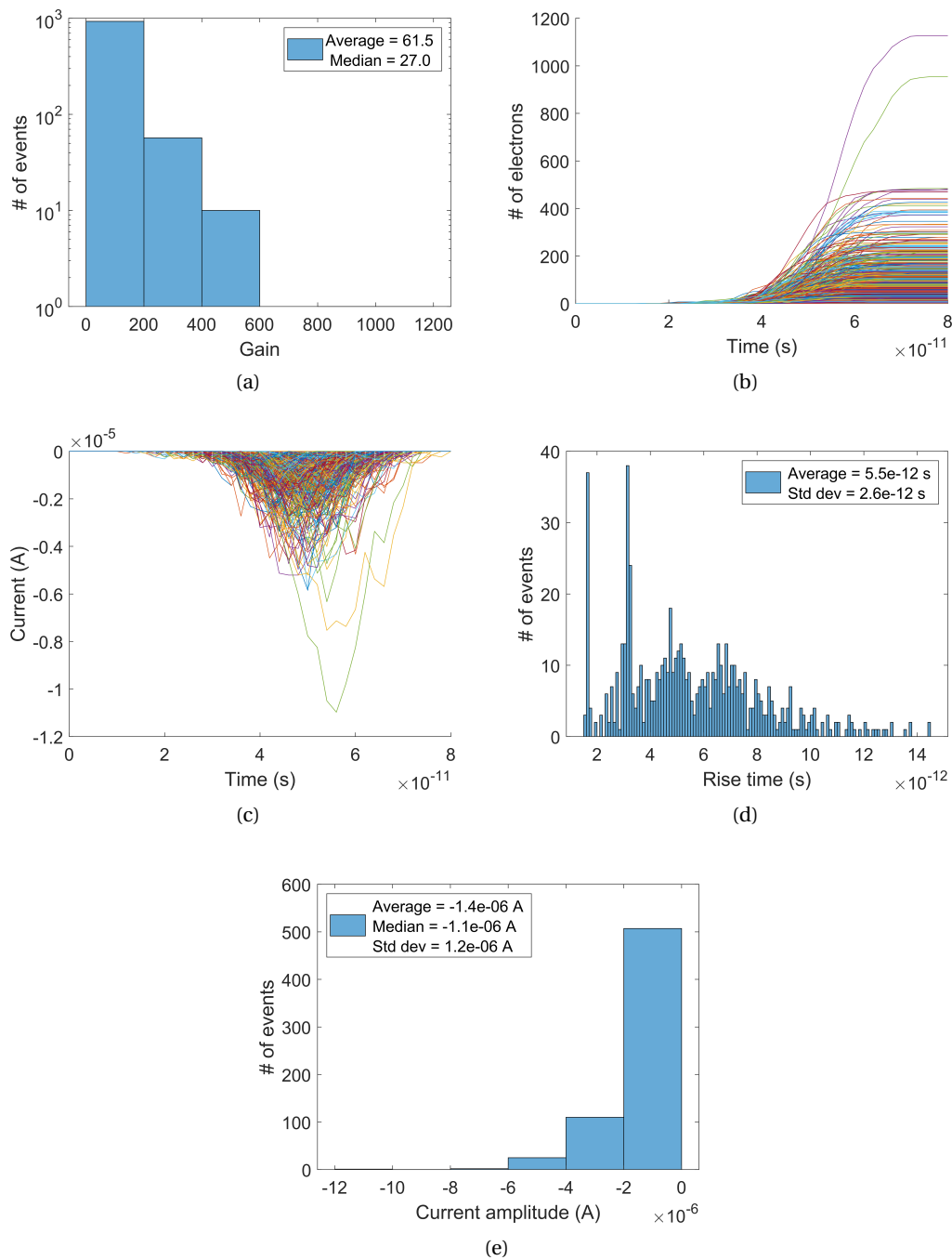


Figure 8.8 – Results of the FEM model for funnel shaped channels.

the electron trajectories from one photoelectron starting at the photoelectrode in (b). For one event, one photoelectron is emitted at a fixed point on the the top surface. We assume the emitted electron to have a very low energy of 0.1 eV and choose the emission angle from a random distribution inside an isotropic hemisphere. The model is solved for time steps of 2 ps between 0 ps and 80 ps and the minimum element size is 0.8 μm .

The model is set up with a photocathode distance of 20 μm and a photocathode bias of 1000 V. Although the electric field distribution in this case does not correspond to the experimental electric field distribution. While experimentally the photocathode was at a distance of 1 mm, this setup was here chosen to minimize computation time, while assuring the incident electron energies to be 500 eV. The color scale in figure 8.7b shows the electron energies. Here the electron energies range up to 700 eV.

We show the results of the funnel shaped channel model in figure 8.8. As for the single channel FEM model, the implementation of backscattering still needs to be improved, as inelastic backscattering and energy conservation have not yet been implemented. As a trend, the gain seems to decrease when using the funnel shapes. With the chosen funnel depth of 10 μm , the signal rise time seems not to be affected. The average rise time was calculated as 5.5 ps, see figure 8.8d. It is promising that funnel shaped channels show this fast timing, even considering the moderate funnel opening. On the other hand, the calculated gains are low (much lower than the values obtained with the cinematic model). The reasons for these low values seem to be linked with the fact that secondary electron trajectories of electrons emitted from the funnel and accelerated by the electric field, are almost parallel to the channel wall. Thus, the electrons arrive at a very low angle with respect to the channel wall and might only initiate a multiplication in the lower part of the channel. The effect of the incident angle on the gain of an AMCP channel has been shown in figure 7.10. For future simulations, the funnel geometry can be improved to increase multiplication, according to funnel geometries that can be realized experimentally. Additionally, the low gain we see in the simulations might not be representative for a real AMCP channel assembly, see discussion below.

In this chapter, we presented non-cylindrical geometries that have been calculated with the finite element method and a simulation of multiplication in these shapes with the Monte-Carlo FEM model is shown. From a simple analysis of the electric field distribution, we conclude that the electric field distribution depends on the funnel shape, and that the funnel opening needs to be adjusted to the depth of the funnel to favor electron collection. The actual effect of the electric field distribution on multiplication can be further investigated with the AMCP 3D model that includes multiplication once possible funnel geometries were determined experimentally. From simulations of an assembly of funnel shaped channels with the AMCP 3D model we calculated a negligible effect of the moderate funnel opening of twice the diameter on AMCP timing. We calculated an average signal rise time of about 6 ps, which is comparable to the timing calculated with the single channel model. The gain we calculated is one order of magnitude below the expected gain. This could be explained by the geometry we chose. In the former chapter, when modeling a single channel, we started at the first impact inside the channel. Here, electrons might not impact the channel at a suitable height. Electrons might directly hit the bottom electrode in our simulations. As mentioned in the former chapter for

incident electrons parallel to the channel wall, it is a challenge to represent real processes in this case, as in a real device the channel wall might not be perfectly parallel, the electric field not perfectly perpendicular and with the additional channel roughness this might modify electron trajectories in favor of a higher impact probability than what we calculate with the model and thus a higher gain. In case this is a real issue for AMCPs at some stage, this might be a reason to tweak the electric field at the entrance of the channels in a way that the electrons are guided onto the channel entrance, instead of being accelerated all the way through.

9 Conclusion and optimization path for single photon detection

In this thesis, we investigated the potential of amorphous silicon based microchannel plates using a state-of-the-art DRIE system. AMCPs with narrow channels were fabricated, which resulted in aspect ratios of up to 23 that had been limited to 13 before. We developed a model for the multiplication process in AMCPs that can be applied to any geometries. We now put together the key results and then show the implications of the results for potential applications, like single photon detection and give a direction how to continue the developments.

9.1 Summary of the key results

Since their introduction a few years ago, AMCPs now offer a great flexibility of fabrication thanks to a lot of improvements in microfabrication. With aspect ratios of up to 50 achieved with DRIE processes in Si, we can directly implement that for AMCPs. Even though for the work of this thesis, we stayed close to the conventional cylindrical shape of AMCPs and considerably lower aspect ratio values, the new possibilities are exciting.

We fabricated AMCPs with channel diameters of $2.7\text{ }\mu\text{m}$ for a channel length of $60\text{ }\mu\text{m}$. The AMCP diameter had been limited to $6\text{ }\mu\text{m}$ before. This fabrication result opened up the possibility to fabricate AMCPs with high aspect ratios without having to further increase the thickness of the amorphous silicon layer. The fabrication of AMCPs with gains that are high enough for the application in a detector system is not limited is no longer limited technologically.

The former bottleneck of the fabrication of AMCPs with high aspect ratios was the deposition of a thick amorphous silicon layer. Using a PECVD system with homogeneous deposition over the size of the substrate would greatly improve the results. Because of the thickness, the deposition time of the thick layer extends to several days. Increasing the deposition speed is thus of importance and the fabrication optimum lies in the sweet spot between layer homogeneity and deposition speed. Thick amorphous silicon layers with $90\text{ }\mu\text{m}$ and a good layer quality had been fabricated on 4" wafers [Franco 2014a]. We extended the deposition to 6" wafers and fabricated $60\text{ }\mu\text{m}$ thick layers with a good material quality on those substrates. First characterization results of AMCPs in transient conditions were obtained. However, a

reference signal could not be measured due to the low signal intensity. Consequently, the measurement setup has been improved to be suitable for high-frequency measurements with shielded cables and connectors. A new scheme for AMCP samples has been deduced from the first tests as well. For high frequency measurements the AMCP bottom pads should incorporate electrically insulating guard rings, smaller areas for a lower capacitance and much shorter connection lengths before reaching a charge amplifier. To that end a charge sensitive amplifier has been chosen to be integrated directly on the PCB. The PCB has been redesigned for this purpose. The solutions we found to high frequency measurements of AMCPs will be implemented and tested, together with redesigned AMCPs, within the framework of another thesis.

Through a detailed characterization of the electron emission properties of the AMCP channel surface, we set up a Monte-Carlo model to simulate the formation of the electron cloud inside the AMCP channel. The model was calibrated with experimental gain measurements and allows to calculate the gain and timing parameters for AMCPs with a cylindrical shape and any dimensions. We calculated an average gain of about 2000 for AMCPs with a channel length of 60 μm and a diameter of 2 μm . The variation of the gain upon incidence of a single electron is higher than the gain, as some rare events can create much higher gains. The signal rise time of this geometry is 7 ± 2 ps with a spectacular single photon timing jitter below 3 ps for a very moderate channel bias of 500 V. The channel bias corresponds to less than half of the maximum field that can be applied to the amorphous silicon layer. For higher electric fields, the gain will increase tremendously and the signal will be formed on an even shorter timescale. The model allowed us to conclude that a further miniaturization of AMCPs is possible, as long as the channel length of AMCPs is not reduced beyond 30 μm . To expect a useful gain at this channel length the AMCP need to work at the maximum electric field of $2 \cdot 10^7 \text{ V/m}$ and the aspect ratio needs to be at least 40. Keeping the AMCP channel length in the range of 50-60 μm would be ideal, as this allows for a higher potential difference, and the gain can be increased much further.

Furthermore, we implemented the AMCP model into a finite element tool that can take into account various shapes that can be produced with clean room technology. The highest collection efficiency can be reached with funnel shaped AMCPs. The highest aspect ratio of 50 realized for Si trenches can be used for AMCPs with high gain. Even with the fabrication results of this thesis, with a AR of up to 30, a considerable AMCP gain improvement is expected. The simulation tool can be used to quickly rule out shapes of AMCPs, or to find an optimal geometry once the experimental constraints and the application goal are given.

9.2 Perspectives

9.2.1 Future developments

AMCPs should now be characterized in a transient flux regime. This will help to understand how the properties of amorphous silicon can be beneficial for a fast charge replenishment. With a faster charge replenishment time than conventional MCPs, AMCPs could be used for

high frequency measurements under higher photon flux.

The high secondary emissive layers AlO_x and MgO , which have been characterized for this thesis will further increase the gain of high aspect ratio AMCPs.

The AMCP layer structure can be directly deposited on a readout chip, for an even better integrated amplification scheme at low incident flux and for single photon detection.

Funnel shaped channels can be etched in order to increase the collection efficiency of AMCPs up to 100%. Other shapes could be imagined as well, for example a combination of transmission dynodes with AMCP channels, or rectangular channels, if these shapes are demonstrated to increase the gain without affecting the timing. For such an analysis, our AMCP model can be used to predict the expected gain and timing.

The AMCP model parametrization should be adapted when high aspect ratio AMCPs with and without high emissive coatings have been measured. AMCP channel assemblies with wider funnel openings can be simulated, which might lead to less low gain events, as more electrons will hit the channel at a higher impact point (closer to the entrance of the channel) and thus be able to create a higher signal. As a down side, wider funnels might lead to a slower timing and more jitter. The tool we developed during this thesis will be ideal to gain more insight into the effects of geometry on the timing and to determine a good compromise between AMCP gain and timing.

9.2.2 AMCP applications

AMCPs can be used for a wide range of applications, where MCPs are used nowadays and beyond. The applications range from astronomy and space science, to single molecule fluorescence in biology, ultrafast spectroscopy in chemistry, single photon detection in medical scanners to high-energy physics.

After this first step towards 100% collection efficiency, AMCPs could be imagined in applications where the detection of each single photon is important like in clinical PET systems. Additionally, like SiPMs which have a lower spatial resolution, the bulk material of AMCPs is insensitive to magnetic fields and AMCPs could potentially be used in combined TOF-PET-MRI systems. How the magnetic field impacts electron trajectories in the AMCP channels and if it can even be used to improve the gain will need to be investigated. The combination of PET and MRI is more efficient and more comfortable for patients and helps to increase the accuracy of diagnoses and treatment plans. Present medical applications of PET-MRI scanners range from cardiology to oncology, paediatrics and neurology [Cabello 2018]. Measuring the time-of-flight would additionally increase the accuracy of the scanners.

The radiation hardness of amorphous silicon makes AMCPs an ideal choice where the radiation dose is important, outside the earth's atmosphere and in high energy physics experiments. Plasma sensors are used on spacecrafts for in-flight measurements of electron and ion distributions to study fundamental processes in the earth's magnetosphere [McFadden 2008].

AMCPs could replace scintillators for neutron detection, as the high hydrogen content of AMCPs promotes neutron-proton interactions. Conventional MCPs, where ^{10}B and Gd are efficient neutron converters, have already been shown to have a considerably higher detection

efficiency than scintillators [Pinto 2017].

For the detection of hard X-rays in astronomy, MCPs with square channels were used [Price 2002]. AMCPs with square channels can easily be fabricated, and in applications like this, the shape can be fitted to the experimental requirements.

With modern electronics MCPs are now used with increased count rates for applications ranging from photon counting to ion and electron time-of-flight measurements [Tremis 2020a] [Cremer 2019]. A fast charge replenishment time of AMCPs would additionally open up a new range of high frequency applications where at the same time a high incident flux needs to be detected.

Bibliography

- [Agarwal 1958] Bipin Kumar Agarwal. *Variation of secondary emission with primary electron energy*. Proceedings of the Physical Society, vol. 71, no. 5, pages 851–852, 1958.
- [Agostinelli 2003] S. Agostinelli, J. Allison, K. Amako, J. Apostolakis, H. Araujo, P. Arce, M. Asai, D. Axen, S. Banerjee, G. Barrand, F. Behner, L. Bellagamba, J. Boudreau, L. Broglia, A. Brunengo, H. Burkhardt, S. Chauvie, J. Chuma, R. Chytrcek, G. Cooperman, G. Cosmo, P. Degtyarenko, A. Dell’Acqua, G. Depaola, D. Dietrich, R. Enami, A. Feliciello, C. Ferguson, H. Fesefeldt, G. Folger, F. Foppiano, A. Forti, S. Garelli, S. Giani, R. Giannitrapani, D. Gibin, J. J. Gomez Cadenas, I. Gonzalez, G. Gracia Abril, G. Greeniaus, W. Greiner, V. Grichine, A. Grossheim, S. Guatelli, P. Gumplinger, R. Hamatsu, K. Hashimoto, H. Hasui, A. Heikkinen, A. Howard, V. Ivanchenko, A. Johnson, F. W. Jones, J. Kallenbach, N. Kanaya, M. Kawabata, Y. Kawabata, M. Kawaguti, S. Kelner, P. Kent, A. Kimura, T. Kodama, R. Kokoulin, M. Kossov, H. Kurashige, E. Lamanna, T. Lampen, V. Lara, V. Lefebvre, F. Lei, M. Liendl, W. Lockman, F. Longo, S. Magni, M. Maire, E. Medernach, K. Minamimoto, P. Mora de Freitas, Y. Morita, K. Murakami, M. Nagamatsu, R. Nartallo, P. Nieminen, T. Nishimura, K. Ohtsubo, M. Okamura, S. O’Neale, Y. Oohata, K. Paech, J. Perl, A. Pfeiffer, M. G. Pia, F. Ranjard, A. Rybin, S. Sadilov, E. di Salvo, G. Santin, T. Sasaki, N. Savvas, Y. Sawada, S. Scherer, S. Sei, V. Sirotenko, D. Smith, N. Starkov, H. Stoecker, J. Sulkimo, M. Takahata, S. Tanaka, E. Tcherniaev, E. Safai Tehrani, M. Tropeano, P. Truscott, H. Uno, L. Urban, P. Urban, M. Verderi, A. Walkden, W. Wander, H. Weber, J. P. Wellisch, T. Wenaus, D. C. Williams, D. Wright, T. Yamada, H. Yoshida and D. Zschesche. *GEANT4 - A simulation toolkit*. Nuclear Instruments and Methods in Physics Research, Section A: Accelerators, Spectrometers, Detectors and Associated Equipment, vol. 506, no. 3, pages 250–303, 2003.
- [Anacker 1991] D. C. Anacker and J. L. Erskine. *Analysis of microchannel plate response in relation to pulsed laser time-of-flight photoemission spectroscopy*. Review of Scientific Instruments, vol. 62, no. 5, pages 1246–1255, 1991.
- [Anelli 2004] G. Anelli, S. C. Commichau, M. Despeisse, G. Dissertori, P. Jarron, C. Miazza, D. Moraes, A. Shah, G. M. Viertel and N. Wyrsh. *A new concept of monolithic silicon pixel detectors: Hydrogenated amorphous silicon on ASIC*. Nuclear Instruments and

- Methods in Physics Research, Section A: Accelerators, Spectrometers, Detectors and Associated Equipment, vol. 518, no. 1-2, pages 366–372, 2004.
- [Arrell 2014] C. A. Arrell, J. Ojeda, M. Sabbar, W. A. Okell, T. Witting, T. Siegel, Z. Diveki, S. Hutchinson, L. Gallmann, U. Keller, F. Van Mourik, R. T. Chapman, C. Cacho, N. Rodrigues, I. C E Turcu, J. W G Tisch, E. Springate, J. P. Marangos and M. Chergui. *A simple electron time-of-flight spectrometer for ultrafast vacuum ultraviolet photoelectron spectroscopy of liquid solutions*. Review of Scientific Instruments, vol. 85, no. 10, 2014.
- [Astašauskas 2020] Vytautas Astašauskas, Alessandra Bellissimo, Pavel Kuksa, Christian Tomastik, Henryk Kalbe and Wolfgang S.M. Werner. *Optical and electronic properties of amorphous silicon dioxide by single and double electron spectroscopy*. Journal of Electron Spectroscopy and Related Phenomena, vol. 241, no. October 2018, pages 4–10, 2020.
- [Balcon 2012] N. Balcon, D. Payan, M. Belhaj, T. Tondu and V. Inguibert. *Secondary electron emission on space materials: Evaluation of the total secondary electron yield from surface potential measurements*. IEEE Transactions on Plasma Science, vol. 40, no. 2 PART 1, pages 282–290, 2012.
- [Beaulieu 2009] D. R. Beaulieu, D. Gorelikov, P. de Rouffignac, K. Saadatmand, K. Stenton, N. Sullivan and A. S. Tremsin. *Nano-engineered ultra-high-gain microchannel plates*. Nuclear Instruments and Methods in Physics Research, Section A: Accelerators, Spectrometers, Detectors and Associated Equipment, vol. 607, no. 1, pages 81–84, 2009.
- [Beetz 1999] Jr Beetz. *Silicon etching process for making microchannel plates*, 1999.
- [Belhaj 2009] M. Belhaj, T. Tondu, V. Inguibert and J. P. Chardon. *A Kelvin probe based method for measuring the electron emission yield of insulators and insulated conductors subjected to electron irradiation*. Journal of Physics D: Applied Physics, vol. 42, no. 10, 2009.
- [Belhaj 2010] M. Belhaj, T. Tondu, V. Inguibert, Pierre Barroy, François Silva and Alix Gicquel. *The effects of incident electron current density and temperature on the total electron emission yield of polycrystalline CVD diamond*. Journal of Physics D: Applied Physics, vol. 43, no. 13, 2010.
- [Blase 2018] Ryan C Blase, Roland R Benke and Keith S Pickens. *Review of Measured Photon Detection Efficiencies of Microchannel Plates*. IEEE Transactions on Nuclear Science, vol. 65, no. 12, pages 2839–2851, 2018.
- [Bläsi 2016] B. Bläsi, N. Tucher, O. Höhn, V. Kübler, T. Kroyer, Ch. Wellens and H. Hauser. *Large area patterning using interference and nanoimprint lithography*. Spie, vol. 9888, page 98880H, 2016.

- [Braunger 2012] M. L. Braunger, C. A. Escanhoela, I. Fier, L. Walmsley and E. C. Ziemath. *Electrical conductivity of silicate glasses with tetravalent cations substituting Si*. Journal of Non-Crystalline Solids, vol. 358, no. 21, pages 2855–2861, 2012.
- [Brodsky 1970] M. H. Brodsky, R. S. Title, K. Weiser and G. D. Pettit. *Structural, optical, and electrical properties of amorphous silicon films*. Physical Review B, vol. 1, no. 6, pages 2632–2641, 1970.
- [Bronshtein] I M Bronshtein and B S Fraiman. *VTORICHNAYA ELEKTRONNAYA EMISSIYA. (Secondary Electron Emission)*.
- [Bundaleski 2015] N. Bundaleski, M. Belhaj, T. Gineste and O. M.N.D. Teodoro. *Calculation of the angular dependence of the total electron yield*. Vacuum, vol. 122, pages 255–259, 2015.
- [Burri 2014] Samuel Burri, Yuki Maruyama, Xavier Michalet, Francesco Regazzoni, Claudio Bruschini and Edoardo Charbon. *Architecture and applications of a high resolution gated SPAD image sensor*. Optics Express, vol. 22, no. 14, page 17573, 2014.
- [Cabello 2018] Jorge Cabello and Sibylle I. Ziegler. *Nuclear medicine: Physics and instrumentation special feature review article :Advances in pet/mr instrumentation and image reconstruction*. British Journal of Radiology, vol. 91, no. 1081, 2018.
- [Cazaux 2006] J. Cazaux. *E-Induced secondary electron emission yield of insulators and charging effects*. Nuclear Instruments and Methods in Physics Research, Section B: Beam Interactions with Materials and Atoms, vol. 244, no. 2, pages 307–322, 2006.
- [Cazaux 2010a] Jacques Cazaux. *Calculated influence of work function on SE escape probability and Secondary Electron Emission yield*. Applied Surface Science, vol. 257, no. 3, pages 1002–1009, 2010.
- [Cazaux 2010b] Jacques Cazaux. *Material contrast in SEM: Fermi energy and work function effects*. Ultramicroscopy, vol. 110, no. 3, pages 242–253, 2010.
- [Cazaux 2012] Jacques Cazaux. *Reflectivity of very low energy electrons (< 10 eV) from solid surfaces: Physical and instrumental aspects*. Journal of Applied Physics, vol. 111, no. 6, page 064903, mar 2012.
- [CERN - Photoemission laboratory] CERN - Photoemission laboratory. *Photocathodes*.
- [Chevallay 1994] E. Chevallay, J. Durand, S. Hutchins, G. Suberlucq and M. Wurgel. *Photocathodes tested in the dc gun of the CERN photoemission laboratory*. Nuclear Inst. and Methods in Physics Research, A, vol. 340, no. 1, pages 146–156, 1994.
- [Chittik 1969] R C Chittik, J H Alexander and H F Sterling. *The Preparation and Properties of Amorphous Silicon*. J. Electrochem. Soc., vol. 116, no. 1, page 77, 1969.

- [Cimino 2004] R. Cimino, I. R. Collins, M. A. Furman, M. Pivi, F. Ruggiero, G. Rumolo and F. Zimmermann. *Can low-energy electrons affect high-energy physics accelerators?* Physical Review Letters, vol. 93, no. 1, pages 014801–1, 2004.
- [Cremer 2019] Till Cremer, Bernhard W. Adams, Melvin Aviles, Camden Ertley, Michael R. Foley, Alexey V. Lyashenko, Michael J. Minot, Mark A. Popecki, Travis Rivera, Michael E. Stochaj, Anil U. Mane, Jeffrey W. Elam, Max Gebhard and Oswald H. W. Siegmund. *Recent developments on next-generation microchannel plates for particle identification applications*. no. September 2019, page 21, 2019.
- [De Boer 2005] Bert De Boer, Afshin Hadipour, M. Magdalena Mandoc, Teunis Van Woudenberg and Paul W.M. Blom. *Tuning of metal work functions with self-assembled monolayers*. Advanced Materials, vol. 17, no. 5, pages 621–625, 2005.
- [De Vera 2019] Pablo De Vera and Rafael Garcia-Molina. *Electron Inelastic Mean Free Paths in Condensed Matter Down to a Few Electronvolts*. Journal of Physical Chemistry C, vol. 123, no. 4, pages 2075–2083, 2019.
- [Despeisse 2006] Matthieu Despeisse. *Etude et caractérisation d'un capteur en silicium amorphe hydrogéné déposé sur circuit intégré pour la détection de particules et de rayonnements*. PhD thesis, 2006.
- [Dzhanoev 2015] A. R. Dzhanoev, F. Spahn, V. Yaroshenko, H. Lühr and J. Schmidt. *Secondary electron emission from surfaces with small structure*. Physical Review B - Condensed Matter and Materials Physics, vol. 92, no. 12, pages 1–5, 2015.
- [Eberhardt 1979] E H Eberhardt. *Gain model for microchannel plates*. Applied optics, vol. 18, no. 9, pages 1418–1423, 1979.
- [Eberhardt 1981] E. H. Eberhardt. *An Operational Model for Microchannel Plate Devices*. IEEE Transactions on Nuclear Science, vol. 28, no. 1, pages 712–717, 1981.
- [Ertley 2017] C. D. Ertley, O. H.W. Siegmund, J. Hull, A. Tremsin, A. O'Mahony, C. A. Craven and M. J. Minot. *Microchannel Plate Imaging Detectors for High Dynamic Range Applications*. IEEE Transactions on Nuclear Science, vol. 64, no. 7, pages 1774–1780, 2017.
- [Franco 2012] Andrea Franco, Yannick Riesen, Nicolas Wyrsh, Sylvain Dunand, François Powolny, Pierre Jarron and Christophe Ballif. *Amorphous silicon-based microchannel plates*. Nuclear Instruments and Methods in Physics Research, Section A: Accelerators, Spectrometers, Detectors and Associated Equipment, vol. 695, pages 74–77, 2012.
- [Franco 2014a] Andrea Franco. *Monolithic Particle Detectors based on Hydrogenated Amorphous Silicon*. PhD thesis, EPFL, 2014.
- [Franco 2014b] Andrea Franco, Jonas Geissbühler, Nicolas Wyrsh and Christophe Ballif. *Fabrication and characterization of monolithically integrated microchannel plates based on amorphous silicon*. Scientific Reports, vol. 4, no. August 2015, pages 1–7, 2014.

- [Fraser 2001] G. W. Fraser. *Imaging in astrophysics (and elsewhere)*. Nuclear Instruments and Methods in Physics Research, Section A: Accelerators, Spectrometers, Detectors and Associated Equipment, vol. 471, no. 1-2, pages 170–173, 2001.
- [Frey 2019] S. Frey, J. Löffler, C. Ballif and N. Wyrsh. *Characterization of Amorphous Silicon Based Microchannel Plates with High Aspect Ratio*. In 2019 IEEE Nuclear Science Symposium and Medical Imaging Conference, NSS/MIC 2019. Institute of Electrical and Electronics Engineers Inc., oct 2019.
- [Furman 2002] M. A. Furman and M. T.F. Pivi. *Probabilistic model for the simulation of secondary electron emission*. Physical Review Special Topics - Accelerators and Beams, vol. 5, no. 12, pages 82–99, 2002.
- [Gao 2014] Feng Gao, Sami Ylinen, Markku Kainlahti and Markku Kapulainen. *Smooth silicon sidewall etching for waveguide structures using a modified Bosch process*. J. Micro-/Nanolith. MEMS MOEMS, vol. 13(1), pages 9–14, 2014.
- [Gershman 2018] Daniel J. Gershman, Levon A. Avanov, Dennis J. Chornay, Amy C. Rager, Craig J. Pollock, Guy Grubbs, David A. Mackler, Corey J. Tucker and Nikolaos P. Paschalidis. *Extending the dynamic range of microchannel plate detectors using charge-integration-based counting*. Review of Scientific Instruments, vol. 89, no. 7, 2018.
- [Ghiringhelli 1999] G. Ghiringhelli, K. Larsson and N. B. Brookes. *High-efficiency spin-resolved and spin-integrated electron detection: Parallel mounting on a hemispherical analyzer*. Review of Scientific Instruments, vol. 70, no. 11, page 4225, 1999.
- [Giudicotti 2011] L. Giudicotti. *Time dependent model of gain saturation in microchannel plates and channel electron multipliers*. Nuclear Instruments and Methods in Physics Research, Section A: Accelerators, Spectrometers, Detectors and Associated Equipment, vol. 659, no. 1, pages 336–347, 2011.
- [Gol'tsman 2001] G. N. Gol'tsman, O. Okunev, G. Chulkova, A. Lipatov, A. Semenov, K. Smirnov, B. Voronov, A. Dzardanov, C. Williams and Roman Sobolewski. *Picosecond superconducting single-photon optical detector*. Applied Physics Letters, vol. 79, no. 6, pages 705–707, 2001.
- [Guest 1971] A.J. Guest. *A computer model of channel multiplier plate performance*. Acta Electronica, vol. 14, no. 1, pages 79–97, 1971.
- [Gys 2015] T. Gys. *Micro-channel plates and vacuum detectors*. Nuclear Instruments and Methods in Physics Research, Section A: Accelerators, Spectrometers, Detectors and Associated Equipment, vol. 787, pages 254–260, 2015.
- [Hovington 1997] Pierre Hovington, Dominique Drouin and Raynald Gauvin. *CASINO: A new monte carlo code in C language for electron beam interaction -part I: Description of the program*. Scanning, vol. 19, no. 1, pages 1–14, dec 1997.

Bibliography

- [Hussain 2020] A. Hussain, L. H. Yang, Y. B. Zou, S. F. Mao, B. Da, H. M. Li and Z. J. Ding. *Monte Carlo simulation study of electron yields from compound semiconductor materials*. Journal of Applied Physics, vol. 128, no. 1, page 015305, jul 2020.
- [Iagaru 2015] A Iagaru, R Minamimoto, C Levin, A Barkhodari, M Jamali and D Holley. *The potential of TOF PET-MRI for reducing artifacts in PET images*. EJNMMI Phys., vol. 2, 2015.
- [Insepov 2010] Z. Insepov, V. Ivanov and H. Frisch. *Comparison of candidate secondary electron emission materials*. Nuclear Instruments and Methods in Physics Research, Section B: Beam Interactions with Materials and Atoms, vol. 268, no. 20, pages 3315–3320, 2010.
- [Insepov 2011] Z. Insepov, V. Ivanov, S. J. Jokela, I. Veryovkin, A. Zinovev and H. Frisch. *Comparison of secondary electron emission simulation to experiment*. Nuclear Instruments and Methods in Physics Research, Section A: Accelerators, Spectrometers, Detectors and Associated Equipment, vol. 639, no. 1, pages 155–157, 2011.
- [Ito 1984] M. Ito, H. Kume and K. Oba. *Computer Analysis of the Timing Properties in Micro Channel Plate Photomultiplier Tubes*. IEEE Transactions on Nuclear Science, vol. 31, no. 1, pages 408–412, 1984.
- [Ivanov 2018] V. Ivanov, A. Barnyakov and M. Barnyakov. *Calibration procedure in microchannel amplifiers design*. Nuclear Instruments and Methods in Physics Research, Section A: Accelerators, Spectrometers, Detectors and Associated Equipment, vol. 903, no. June, pages 170–174, 2018.
- [Jarron 2014] P. Jarron and N. Wyrsh. *Microchannel plate and its manufacturing method*, 2014.
- [Johlin 2012] Eric Johlin, Nouar Tabet, Sebastián Castro-Galnares, Amir Abdallah, Mariana I. Bertoni, Tesleem Asafa, Jeffrey C. Grossman, Syed Said and Tonio Buonassisi. *Structural origins of intrinsic stress in amorphous silicon thin films*. Physical Review B - Condensed Matter and Materials Physics, vol. 85, no. 7, 2012.
- [Jokela 2012] Slade J. Jokela, Igor V. Veryovkin, Alexander V. Zinovev, Jeffrey W. Elam, Anil U. Mane, Qing Peng and Z. Insepov. *Secondary Electron Yield of Emissive Materials for Large-Area Micro-Channel Plate Detectors: Surface Composition and Film Thickness Dependencies*. Physics Procedia, vol. 37, pages 740–747, 2012.
- [Joy 1987] David C. Joy. *A model for calculating secondary and backscattered electron yields*. Journal of Microscopy, vol. 147, no. 1, pages 51–64, 1987.
- [Joy 1995] David C. Joy. *A database on electron-solid interactions*. Scanning, vol. 17, no. 5, pages 270–275, dec 1995.
- [Joy 1996] DC Joy, Luo Suichu, R Gauvin, P Hovington and N Evans. *Experimental measurements of electron stopping power at low energies*. Scanning microscopy, vol. 10, no. 3, pages 653–666, 1996.

- [Kanaya 1978] K Kanaya, S Ono and F Ishigaki. *Secondary electron emission from insulators*. Journal of Physics D: Applied Physics, vol. 11, no. 17, pages 2425–2437, dec 1978.
- [Kieft 2008] Erik Kieft and Eric Bosch. *Refinement of Monte Carlo simulations of electron-specimen interaction in low-voltage SEM*. Journal of Physics D: Applied Physics, vol. 41, no. 21, 2008.
- [Kruschwitz 2011] Craig A. Kruschwitz, Ming Wu and Greg A. Rochau. *Monte Carlo simulations of microchannel plate detectors. II. Pulsed voltage results*. Review of Scientific Instruments, vol. 82, no. 2, 2011.
- [Kuhr 1999] J. Ch Kuhr and H. J. Fitting. *Monte Carlo simulation of electron emission from solids*. Journal of Electron Spectroscopy and Related Phenomena, vol. 105, no. 2-3, pages 257–273, 1999.
- [Ladislav Wiza 1979] Joseph Ladislav Wiza. *Microchannel plate detectors*. Nuclear Instruments and Methods, vol. 162, no. 1-3, pages 587–601, jun 1979.
- [Laermer 1996] Franz Laermer and Andrea Schilp. *Method of anisotropically etching silicon*, 1996.
- [Laermer 2010] Franz Laermer, Sami Franssila, Lauri Sainiemi and Kai Kolari. *Deep Reactive Ion Etching*. Elsevier Inc, 2010.
- [Lapington 2009] J. S. Lapington, D. P. Thompson, P. W. May, N. A. Fox, J. Howorth, J. Milnes and V. Taillandier. *Investigation of the secondary emission characteristics of CVD diamond films for electron amplification*. Nuclear Instruments and Methods in Physics Research, Section A: Accelerators, Spectrometers, Detectors and Associated Equipment, vol. 610, no. 1, pages 253–257, 2009.
- [Lehmann 2017] A. Lehmann, A. Britting, W. Eyrich, M. Pfaffinger, F. Uhlig, A. Belias, R. Dzhygadlo, A. Gerhardt, K. Götzen, G. Kalicy, M. Krebs, D. Lehmann, F. Nerling, M. Patsyuk, K. Peters, G. Schepers, L. Schmitt, C. Schwarz, J. Schwiening, M. Traxler, M. Zühlsdorf, M. Düren, E. Etzelmüller, K. Föhl, A. Hayrapetyan, B. Kröck, O. Merle, J. Rieke, M. Schmidt, E. Cowie, T. Keri, P. Achenbach, M. Cardinali, M. Hoek, W. Lauth, S. Schlimme, C. Sfienti and M. Thiel. *Tremendously increased lifetime of MCP-PMTs*. Nuclear Instruments and Methods in Physics Research, Section A: Accelerators, Spectrometers, Detectors and Associated Equipment, vol. 845, pages 570–574, 2017.
- [Li 2019] C. Li, S. F. Mao and Z. J. Ding. *Time-dependent characteristics of secondary electron emission*. Journal of Applied Physics, vol. 125, no. 2, 2019.
- [Lin 2005] Yinghong Lin and David C. Joy. *A new examination of secondary electron yield data*. Surface and Interface Analysis, vol. 37, no. 11, pages 895–900, 2005.
- [Lye 1957] Robert G. Lye and A. J. Dekker. *Theory of Secondary Emission*. Physical Review, vol. 107, no. 4, pages 977–981, aug 1957.

Bibliography

- [Mack 2013] Chris A. Mack. *Generating random rough edges, surfaces, and volumes*. Applied Optics, vol. 52, no. 7, pages 1472–1480, 2013.
- [Mazuritskiy 2019] M. I. Mazuritskiy, A. M. Lerer, S. K. Kulov and D. G. Samkanashvili. *On the Surface Structure of Microchannel Plates and the Excitation of X-Ray Fluorescence in Hollow Microcapillaries*. Journal of Surface Investigation, vol. 13, no. 3, pages 499–507, 2019.
- [McFadden 2008] J. P. McFadden, C. W. Carlson, D. Larson, M. Ludlam, R. Abiad, B. Elliott, P. Turin, M. Marckwordt and V. Angelopoulos. *The THEMIS ESA plasma instrument and in-flight calibration*. Space Science Reviews, vol. 141, no. 1-4, pages 277–302, 2008.
- [Michalet 2011] X. Michalet, R. A. Colyer, G. Scalia, S. Weiss, O. H. W. Siegmund, Anton S. Tremsin, John V. Vallerga, F. Villa, F. Guerrieri, I. Rech, A. Gulinatti, S. Tisa, F. Zappa, M. Ghioni and S. Cova. *New photon-counting detectors for single-molecule fluorescence spectroscopy and imaging*. page 803316, may 2011.
- [Nolet 2018] Frédéric Nolet, Samuel Parent, Nicolas Roy, Marc-Olivier Mercier, Serge Charlebois, Réjean Fontaine and Jean-Francois Pratte. *Quenching Circuit and SPAD Integrated in CMOS 65 nm with 7.8 ps FWHM Single Photon Timing Resolution*. Instruments, vol. 2, no. 4, page 19, 2018.
- [O’Mahony 2016] Aileen O’Mahony, Christopher A. Craven, Michael J. Minot, Mark A. Popecki, Joseph M. Renaud, Daniel C. Bennis, Justin L. Bond, Michael E. Stochaj, Michael R. Foley, Bernhard W. Adams, Anil U. Mane, Jeffrey W. Elam, Camden Ertley and Oswald H. W. Siegmund. *Atomic layer deposition of alternative glass microchannel plates*. Journal of Vacuum Science & Technology A: Vacuum, Surfaces, and Films, vol. 34, no. 1, page 01A128, 2016.
- [Paduschek 1983] P Paduschek, C H Hopfl and H Mitlehner. *Hydrogen-related mechanical stress in amorphous Si and plasma-deposited Si nitride*. Thin Solid Films, vol. 110, pages 291–304, 1983.
- [Pierron 2017] J. Pierron, C. Inguibert, M. Belhaj, T. Gineste, J. Puech and M. Raine. *Electron emission yield for low energy electrons: Monte Carlo simulation and experimental comparison for Al, Ag, and Si*. Journal of Applied Physics, vol. 121, no. 21, 2017.
- [Pinto 2017] S. Duarte Pinto, R. Ortega, S. Ritzau, D. Pasquale, B. Laprade, S. Mrotek, S. Gardell, Z. Zhou, J. Plomp, L. Van Eijck, H. Bilheux and I. Dhiman. *Neutron imaging and tomography with MCPS*. Journal of Instrumentation, vol. 12, no. 12, 2017.
- [Popecki 2016] M. A. Popecki, B. Adams, C. A. Craven, T. Cremer, M. R. Foley, A. Lyashenko, A. O’Mahony, M. J. Minot, M. Aviles, J. L. Bond, M. E. Stochaj, W. Worstell, J. W. Elam, A. U. Mane, O. H. W. Siegmund, C. Ertley, L. M. Kistler and M. S. Granoff. *Microchannel plate fabrication using glass capillary arrays with Atomic Layer Deposition films for resistance and gain*. Journal of Geophysical Research: Space Physics, vol. 121, no. 8, pages 7449–7460, aug 2016.

- [Price 2001] G. J. Price and G. W. Fraser. *Calculation of the output charge cloud from a microchannel plate*. Nuclear Instruments and Methods in Physics Research, Section A: Accelerators, Spectrometers, Detectors and Associated Equipment, vol. 474, no. 2, pages 188–196, 2001.
- [Price 2002] G.J. Price, a.N. Brunton, G.W. Fraser, M. Bavdaz, M.W. Beijersbergen, J.-P. Boutot, R. Fairbend, S.-O. Flyckt, a. Peacock and E. Tomaselli. *Hard X-ray imaging with microchannel plate optics*. Nuclear Instruments and Methods in Physics Research Section A: Accelerators, Spectrometers, Detectors and Associated Equipment, vol. 490, no. 1-2, pages 290–298, 2002.
- [Rangarajan 1980] LM Rangarajan and GK Bhide. *15. Photoemission energy distribution studies of gold thin films under uv excitation by a photoelectron spectroscopic method*. Vacuum, vol. 30, no. 11-12, pages 515–522, 1980.
- [Redhead 1968] P. A. Redhead, J. P. Hobson and E.V. Kornelsen. *The Physical Basis of Ultrahigh Vacuum*. Chap. 4, reprinted by the aip in 1993 as part of the american vacuum society classics series édition, 1968.
- [Roupie 2013] J. Roupie, O. Jbara, T. Tondou, M. Belhaj and J. Puech. *The study of electron emission from aluminum in the very low primary energy range using Monte Carlo simulations*. Journal of Physics D: Applied Physics, vol. 46, no. 12, 2013.
- [Schneider 1987] Ulrich Schneider, Bernd Schröder and Friedhelm Finger. *The creation of metastable defects in a-Si:H films by high dose irradiation with keV-electrons*. Journal of Non-Crystalline Solids, vol. 97-98, no. PART 2, pages 795–798, 1987.
- [Schneider 1999] Bernd Schneider, Peter Rieve and Markus Böhm. *Image Sensors in TFA (Thin Film on ASIC) Technology*. In Handbook of Computer Vision and Applications, B. Jahne, volume 1, chapitre 9, pages 262–295. 1999.
- [Scholz 1993] A Scholz, B Schehr and B Schrsder. *Metastability in p- and n-type a-Si:H investigated by keV-electron irradiation*. vol. 85, no. 9, pages 753–757, 1993.
- [Seiler 1983] H. Seiler. *Secondary electron emission in the scanning electron microscope*. Journal of Applied Physics, vol. 54, no. 11, 1983.
- [Shih 1997] A. Shih, J. Yater, C. Hor and R. Abrams. *Secondary electron emission studies*. Applied Surface Science, vol. 111, pages 251–258, 1997.
- [Shikhaliev 1999] P M Shikhaliev. *Saturation model for secondary electron multiplier detectors*. Nuclear Inst. and Methods in Physics Research, A, vol. 420, no. May 1998, pages 202–212, 1999.
- [Shymanska 2015a] A Shymanska. *Effect of high-efficiency emitter on noise characteristics of electron amplifiers*. Journal of Computational Electronics, vol. 14, no. 1, pages 341–351, 2015.

Bibliography

- [Shymanska 2015b] Alla V. Shymanska and Vitali A. Babakov. *Fast Monte Carlo Method in Stochastic Modelling of Charged Particle Multiplication*. International Journal of Applied Physics and Mathematics, vol. 5, no. 3, pages 218–226, 2015.
- [Siegmund 2011] O.H.W. Siegmund, J.B. McPhate, J.V. Vallerger, A.S. Tremsin, S.R. Jelinsky and H.J. Frisch. *Novel large format sealed tube microchannel plate detectors for Cherenkov timing and imaging*. Nuclear Instruments and Methods in Physics Research Section A: Accelerators, Spectrometers, Detectors and Associated Equipment, vol. 639, no. 1, pages 165–168, may 2011.
- [Siegmund 2013] O. H W Siegmund, J. B. McPhate, S. R. Jelinsky, J. V. Vallerger, A. S. Tremsin, R. Hemphill, H. J. Frisch, R. G. Wagner, J. Elam and A. Mane. *Large area microchannel plate imaging event counting detectors with sub-nanosecond timing*. IEEE Transactions on Nuclear Science, vol. 60, no. 2, pages 923–931, 2013.
- [Srinivasan-Rao 1991] T. Srinivasan-Rao, J. Fischer and T. Tsang. *Photoemission studies on metals using picosecond ultraviolet laser pulses*. Journal of Applied Physics, vol. 69, no. 5, pages 3291–3296, 1991.
- [Sterling 1965] H.F. Sterling and C.G. Swann. *Chemical vapour deposition by r.f. discharge*. Solid-State Electronics, vol. 8, pages 653–654, 1965.
- [Street 1991] R. A. Street. Hydrogenated Amorphous Silicon. 1991.
- [Street 2000] R. A. Street. Technology and applications of amorphous silicon. 2000.
- [Swanson 2016] Charles Swanson and Igor D. Kaganovich. *Modeling of reduced effective secondary electron emission yield from a velvet surface*. Journal of Applied Physics, vol. 120, no. 21, 2016.
- [Tanielian 1982] M Tanielian. *Adsorbate effects on the electrical conductance of a-Si: H*. Philosophical Magazine Part B, vol. 45, no. 4, pages 435–462, apr 1982.
- [Thomas 1980] R.E. Thomas, J.W. Gibson and G.A. Haas. *Low energy electron reflection (LEER) and electron affinity of MgO*. Applications of Surface Science, vol. 5, no. 4, pages 398–405, aug 1980.
- [Thorsos 1988] Eric I. Thorsos. *The validity of the Kirchhoff approximation for rough surface scattering using a Gaussian roughness spectrum*. Journal of the Acoustical Society of America, vol. 83, no. 1, pages 78–92, 1988.
- [Tremsin 1996a] A. S. Tremsin, J. F. Pearson, G. W. Fraser, W. B. Feller and P. White. *Microchannel plate operation at high count rates: New results*. Nuclear Instruments and Methods in Physics Research, Section A: Accelerators, Spectrometers, Detectors and Associated Equipment, vol. 379, no. 1, pages 139–151, 1996.

- [Tremsin 1996b] A. S. Tremsin, J. F. Pearson, J. E. Lees and G. W. Fraser. *The Microsphere Plate: A new type of electron multiplier*. Nuclear Instruments and Methods in Physics Research, Section A: Accelerators, Spectrometers, Detectors and Associated Equipment, vol. 368, no. 3, pages 719–730, 1996.
- [Tremsin 2008] Anton S. Tremsin, Harry F. Lockwood, David R. Beaulieu, Neal T. Sullivan, Eric Munro and John Rouse. *3D microscopic model of electron amplification in microchannel amplifiers for maskless lithography*. Physics Procedia, vol. 1, no. 1, pages 565–572, 2008.
- [Tremsin 2020a] A S Tremsin and J V Vallergera. *Unique capabilities and applications of Microchannel Plate (MCP) detectors with Medipix/Timepix readout*, 2020.
- [Tremsin 2020b] A. S. Tremsin, J. V. Vallergera and O. H.W. Siegmund. *Overview of spatial and timing resolution of event counting detectors with Microchannel Plates*. Nuclear Instruments and Methods in Physics Research, Section A: Accelerators, Spectrometers, Detectors and Associated Equipment, vol. 949, no. March 2019, page 162768, 2020.
- [Vacheret 2011] A. Vacheret, G. J. Barker, M. Dziewiecki, P. Guzowski, M. D. Haigh, B. Hartfiel, A. Izmaylov, W. Johnston, M. Khabibullin, A. Khotjantsev, Yu Kudenko, R. Kurjata, T. Kutter, T. Lindner, P. Masliah, J. Marzec, O. Mineev, Yu Musienko, S. Oser, F. Retière, R. O. Salih, A. Shaikhiev, L. F. Thompson, M. A. Ward, R. J. Wilson, N. Yershov, K. Zaremba and M. Ziembicki. *Characterization and simulation of the response of Multi-Pixel Photon Counters to low light levels*. Nuclear Instruments and Methods in Physics Research, Section A: Accelerators, Spectrometers, Detectors and Associated Equipment, vol. 656, no. 1, pages 69–83, 2011.
- [van der Graaf 2017] Harry van der Graaf, Hassan Akhtar, Neil Budko, Hong Wah Chan, Cornelis W. Hagen, Conny C.T. Hansson, Gert Nützel, Serge D. Pinto, Violeta Prodanović, Behrouz Raftari, Pasqualina M. Sarro, John Sinsheimer, John Smedley, Shuxia Tao, Anne M.M.G. Theulings and Kees Vuik. *The Tynode: A new vacuum electron multiplier*. Nuclear Instruments and Methods in Physics Research Section A: Accelerators, Spectrometers, Detectors and Associated Equipment, vol. 847, no. November 2016, pages 148–161, mar 2017.
- [Van Kessel 2020] Luc Van Kessel, Thomas Huisman and Cornelis Hagen. *Understanding the influence of 3D sidewall roughness on observed line-edge roughness in scanning electron microscopy images*. page 28, 2020.
- [Vandenberghe 2016] S Vandenberghe, E Mikhaylova, E D’Hoe, P Mollet and J S Karp. *Recent developments in time-of-flight PET*. EJNMMI Physics, vol. 3, no. 1, page 3, 2016.
- [Vaughan 1989] J. Rodney M. Vaughan. *A New Formula for Secondary Emission Yield*. IEEE Transactions on Electron Devices, vol. 36, no. 9, pages 1963–1967, 1989.
- [Va’vra 2008] J. Va’vra, C. Ertley, D.W.G.S. Leith, B. Ratcliff and J. Schwiening. *A high-resolution TOF detector—A possible way to compete with a RICH detector*. Nuclear Instruments

- and Methods in Physics Research Section A: Accelerators, Spectrometers, Detectors and Associated Equipment, vol. 595, no. 1, pages 270–273, sep 2008.
- [Verduin 2016] T. Verduin, S. R. Lokhorst and C. W. Hagen. *GPU accelerated Monte-Carlo simulation of SEM images for metrology*. Metrology, Inspection, and Process Control for Microlithography XXX, vol. 9778, no. April 2016, page 97780D, 2016.
- [Verduin 2017] T. Verduin. *Quantum Noise Effects in e-Beam Lithography and Metrology*. PhD thesis, Technische Universiteit Delft, 2017.
- [Villarrubia 2007] John S. Villarrubia, Nicholas W. M. Ritchie and Jeremiah R. Lowney. *Monte Carlo modeling of secondary electron imaging in three dimensions*. Metrology, Inspection, and Process Control for Microlithography XXI, vol. 6518, no. April 2007, page 65180K, 2007.
- [Villeman 2017] M. Villeman, P. Sarrailh, M. Belhaj, L. Garrigues and C. Boniface. *Experimental investigation about energy balance of electron emission from materials under electron impacts at low energy: Application to silver, graphite and SiO₂*. Journal of Physics D: Applied Physics, vol. 50, no. 48, page aa91af, 2017.
- [Wyrsh 2005] N. Wyrsh, C. Miazza, C. Ballif, A. Shah, N. Blanc, R. Kaufmann, F. Lustenberger and P. Jarron. *Vertical integration of hydrogenated amorphous silicon devices on CMOS circuits*. MRS Symp., vol. 869, pages 3–14, 2005. IMT-NE Number: 408.
- [Wyrsh 2006] N. Wyrsh, C. Miazza, S. Dunand, C. Ballif, A. Shah, M. Despeisse, D. Moraes, F. Powolny and P. Jarron. *Radiation hardness of amorphous silicon particle sensors*. Journal of Non-Crystalline Solids, vol. 352, no. 9-20 SPEC. ISS., pages 1797–1800, 2006.
- [Yakobson 1966] A. M. Yakobson. *Estimation of the multiplication coefficient of a secondary electron multiplier with a continuous dynode*. Radiotekhnika i Elektronika, vol. 11, pages 1813–1823, 1966.

Acknowledgements

I would like to thank all the people involved in this thesis. The last 4 and a half years I spent at Microcity to pursue this PhD have been amazing, thanks to all of you.

First of all, I would like to thank Prof. Christophe Ballif for admitting me into his laboratory and for supervising this thesis. With his solution-oriented attitude, critical questions and very helpful remarks he helped me look at the big picture of my work and improve my presentation skills. His feedback greatly improved the structure of the thesis. He also creates a wonderful working atmosphere in the lab. I have very fond memories of the PV-lab summer parties and ski trips, and all the people they involved.

I would like to warmly thank Dr. Nicolas Wyrsh for co-directing this thesis, for fruitful discussions, sharing his deep understanding of physics and his passion for solar cells and detectors, and most of all for his kindness and moral support during all times of the thesis - also the most challenging ones. I'm very grateful that he gave me the opportunity to develop myself personally and professionally, that he was always available and at the same time gave me a lot of freedom to develop and explore my own interests in the frame of the thesis project. I'm also grateful that he corrected the entire thesis manuscript, which greatly improved its quality.

I would like to thank the jury members, Prof. Andras Kis, Dr. Anton Tremsin, Dr. Werner Lustermann and Prof. Jean-Michel Sallès for taking the time to evaluate this thesis. I am very grateful for their enthusiasm and very valuable feedback, which further improved my understanding of the impact of the work of this thesis.

I would like to acknowledge the funding of this thesis, the Swiss National Science Foundation project 200021_162525/1.

I would like to heartily thank our small AMCP team - Samira, Jon and Mo. This thesis wouldn't have been possible without either of your support during the last years. Especially, I would like to thank Samira for being a great colleague and friend. I am so grateful to Samira that she arrived and took over all of the fabrication and characterization and made it possible for me to concentrate on the more theoretical aspects of AMCPs. I'm thankful to Jon for sharing his enthusiasm for programming and building up the whole framework of the cinematic AMCP model. I also would like to thank Mo who recently joined our team and greatly helped me during the last few months of the PhD.

The technical team of PV-lab has also been a huge support for me. I'm grateful to Aymeric,

Acknowledgements

who helped me with so many of my technical questions, soldering parts and cables for me, and ordering parts, and mostly for bringing a joyful atmosphere to the lab and Microcity and organizing the only social event of MC, the weekly beer club.

I'd like to thank Sylvain for showing me all the deposition systems I needed for all of the PECVD layers, evaporations and so on, and for being ready to process my last minute samples just before the end of the PhD. I also thank Cédric, Xavier and Lionel and all of the interns of the technical team for their support.

I'd like to thank Dr. Ulf Roeser for his help in building a suitable characterization setup and coming to Neuchâtel as our personal setup counselor. Thank you for brightening up my days, when I wouldn't know how to continue with this setup.

I am very grateful for the great people at CSEM for letting me into their clean room, Pierre-André who is the best DRIE expert, Giovanni Bergonzi for his jokes and help along the whole fabrication process, and Florence Rigoletti for taking care of the alignment of my difficult bent wafers.

I would like to thank Dr. Mohamed Belhaj for the secondary emission measurement he did for me at his institute, ONERA Space Laboratory in Toulouse, for accepting my request for this informal collaboration and taking the time to answer my questions about the secondary emission experiments. At the same time I would like to thank Dr. Nenad Bundaleski, who initiated this contact, recommending ONERA for this type of low energy measurements. I am very grateful that he took the time to answer my first email, for the further exchange on the issues of roughness and charging for secondary yield measurements and for sharing his knowledge.

I am grateful to Luc Van Kessel for showing me everything about the simulation tool for low energy electron scattering. I am very thankful that he took the time to explain the theoretical background as well as going through the whole setup of the tool, from installation to the creation of materials and geometries. I would also like to thank him for his support when I had any questions about the simulations and the interpretation of the results. I would also like to thank Prof Kees Hagen of the electron scattering group at TU Delft for allowing me to use their simulation tool, also Annemarie Theulings and Prof Van der Graaf for creating the link to the electron scattering simulation group at TU Delft and allowing me to get a thorough understanding of the state-of-the-art in modeling of electron scattering.

Thanks to Juan for being an awesome replacement flatmate for a very short time, and his readiness to help with fabrication, discussing new ideas and solutions, and for fabricating all of the ALD layers that have been used for the work of this thesis. I am also very grateful to Laura for fabricating the first ALD layers for me at the start of the thesis. A very big thank you to Philippe as well, for not only being one of the best colleagues, but also for always sharing his expertise and making the ultra clean samples for the secondary emission measurements and for depositing the most homogeneous a-Si layer that were used for the measurements for the work of this thesis. I would also like to thank Matthieu for being a great teacher, taking the time to answer my questions about detectors and introducing me to the topic at the start of the thesis.

I would like to thank the whole PV-lab/PV-center team for the awesome working atmosphere. I would really like to thank ALL of you who shared this time here at PV-lab with me, each and every one. Josua, Gizem, Jan, Ana, Eleonora, Brett, Fabien, Jean, Lionel, Jordan, Andrew, Arttu, Olivier, Andrea, Monica, Franz, Quentin, Angela, Florent, Marina, Mario, Jérémie, Raphaël, Matthieu, Alessandro, Julie, Marion, Laurie-Lou, Frank, Wenjie, Olatz, Alejandro, Sofia, Ezgi and many more! Your presence in the lab made this an exceptionally good time, with great apéros, summer partys, ski camps, good conversations, entertaining lunches, relaxing coffee breaks, slack lining, climbing etc. thanks for being an awesome bunch of friendly and interesting people and good friends.

Especially, I would like to thank Josua, Jan and Camilo for their incredible support during the difficult times and their friendship.

A big thank you to Karine and Mary-Claude for looking out for all of us in the lab, our bills and plannings, and all the little things, like the fridge, the coffee machine, the plants, stuff that people leave in the offices, knowing who to ask about what etc. On that note, I would also like to thank Cathy for taking care of all the administrative things concerning the doctoral school.

I'm grateful to many more people who made Microcity a lively, collaborative and beautiful place to be.

First of all, I'm very grateful to the former optics lab people. Gaël for helping me a lot, from e-beam lithography to photocathode deposition and also being ready to share his microfab knowledge anytime. Babak, for giving me a first intro into Comsol and nice discussions. And I'd like to thank Irène for showing me the whole photolithography process in the very exclusive optics clean room. Thanks to Alexis for trying to help me with my detector measurements. I'd like to thank as well Paolo for helping to measure our capacitance and letting us work in their lab. And I'd like to thank the AQUA people for soldering parties and a nice collaboration during the last 2 years.

I'd like to thank Hassan for the IT support, very interesting discussions and his good mood and kindness. I'd also like to thank the MAD for organizing events for all of Microcity, skiing, card games etc. especially Jean, Luca, Julie and Laurie-Lou.

I am very thankful to the cantine team for being there for us every day, for their good mood, Vicky for her jokes and especially Hassan for his generosity, always putting a mountain of food on the plate.

Thanks to the FLP group, for providing a platform to share our work experiences and the very nice solution oriented discussions. And especially thanks to Lili for setting up this group. I'd also like to thank our mentors Sarah and Lynda and especially Aïcha, also for her role in the lab and always being ready to help with any questions I had.

I also would like to thank the PV running team, Petra, Christophe, Jan... thanks for showing me the forest trails and the running up Chaumont idea. You really got me up to speed for the half marathon.

I'd like to thank all the people who made this time here so enjoyable, Arun, Brett, Vincenzo, Eric, Kevin, Lili, Patrick, Scott, Alexis, Chunmin, Preethi, Peter, Luis, Marianna, Karin, Nicolas, Joanna, Bedirhan, Simone... for everything from simple coffee breaks and barbecues, to boat

Acknowledgements

rides, climbing and paragliding. Thank you LMTS people for half adopting me into your lab, nice beer clubs and pub quizzes. And especially thanks to Djen, for putting up with me as a flatmate during this last year of the thesis, letting me take over the living room as a home office and providing the room and tranquility I needed. Microcity has been a place full of wonderful people and I am grateful for having been a part of this during the last years.

I'd also like to thank the clean room team of CMi, especially Kaspar Suter who helped me a lot when I started to transfer the fabrication to CMi. I'd also like to thank Fabienne Bobard from CIME for her patience with our special requests on how we wanted to use her microscope.

I also would like to thank the people from Comsol support, especially Linus and Magnus who helped me figure out how to get the best out of the Matlab and Comsol world and to implement all the statistics of our model into their platform.

I'm thankful to my friends here in Switzerland who made this such a wonderful time. Ana, Eli, Hyun Jin, Diego, Edgar, Manu, Fede, Cath, Allen, Varun, Vasia, Vijay... I could not imagine this time without all of you and our adventures and travels. Thanks to Malte and Varun for always sharing a nice time when I went back to the EPFL campus. Thanks to Fede for hosting Samira and me, when we had to do our special SEM measurements at the Lausanne campus and had to be there super early. Thanks to Shadi and Regula and also to Gloria for always having a second home for me in Lausanne. I'd like to thank Mathias for being a wonderful friend and also always taking the time to listen to my detector setup problems and helping me from afar. And I'm grateful to Kay, Rolly, Tobi, Manu, Chris and many more who told me to persevere. To Joe and Mahsa for checking in with me during the time I literally isolated to write this thesis and to David for making up certificates for me and keeping me motivated. I'm also grateful to all the dancers and acrobats, Wolf, Serap, Daan, Michael, Anto, Seb, Ricardo, Soraya, Borja, Laura and so many more, from Neuchâtel and all over Europe and the world, for beautiful evenings, dance and acrobatics events, the time that we shared and the places we discovered. I am deeply grateful to my friends and everyone who supported me during the last years for the work of this thesis, there are many more than I could possibly mention.

I would like to thank the rock of this thesis, my flatmate Sam, who was the best friend a girl could have. Thank you for your friendship and going through most part of PhD life together and making it such a wonderful time with tasty menus and artsy evenings.

I would like to deeply thank François. Thank you for your love and support. Thank you for brightening up my days, for your incredible amount of understanding and always being here for me during the last year of this thesis. I feel very lucky to be the one sharing with you this crazy year 2020 that is like no one before, not only because of writing the thesis.

At last, I would like to thank my family. Mama, Papa, Günter, David and Marc, each one of you, thank you for always supporting me, also through the more difficult times. Without your unconditional love none of this adventure would have been possible.

Neuchâtel, October 2020

Janina



JANINA LÖFFLER

EXPERIENCE

ADDRESS

Chemin de Trois-Portes 23

2000 Neuchâtel

Switzerland

PHONE

+41 78 846 82 41

EMAIL

janina-le@posteo.de

Skype: la_janina

- EPFL Neuchâtel, Photovoltaics and Thin Film Electronics Laboratory 03/2016 – 10/2020
Doctoral assistant
Fabrication and electrical characterization of microchannel plates and probabilistic modeling of signal formation process – thesis successfully defended on Nov 25 2020
- EPFL Lausanne, Laboratory for Ultrafast Spectroscopy 01/2015 – 12/2015
Research assistant
Ultrafast and static X-ray and VIS spectroscopy of TiO₂ and perovskites
- Fraunhofer Institute for Solar Energy Systems Freiburg, Germany 12/2008 – 09/2014
Research assistant
Organic/anorganic thin film deposition, ellipsometry, UV-VIS spectrometry, FTIR spectroscopy, modeling multilayer structures, fuel cell charge transport simulations. Diploma thesis entitled 'Photonic Multilayer Structures for Luminescent Solar Concentrators'

LANGUAGES

German – native speaker

French – fluent

English – fluent

Spanish - basics

IT SKILLS

Matlab

Comsol

MS Office

LaTeX

EDUCATION

- Albert-Ludwigs University Freiburg 10/2006 – 04/2013
MSC. DEGREE PHYSICS (Diplom) – very good
- Albert-Ludwigs University Freiburg 10/2005 – 09/2006
Chemistry studies
- Bilingual German-French high school (Deutsch-Französisches Gymnasium), Freiburg, Germany Class of 2005

REFERENCES

- + NICOLAS WYRSCH
TEAM LEADER, PV-LAB, EPFL
Mail: nicolas.wyrsh@epfl.ch
- + CHRISTOPHE BALLIF
PROFESSOR, PV-LAB, EPFL
Mail: christophe.ballif@epfl.ch

OTHER WORK EXPERIENCE

2003 – 2014

Maths, physics and chemistry tutor for high school students and medicine students, staff at conferences/congresses, at a farmers market, service in a student bar, a bakery, kids animator

ACTIVITIES

Dance, Acro Yoga, Running, Hiking, Swimming

PUBLICATIONS

J. Löffler, J. Thomet, L. van Kessel, C. W. Hagen, M. Belhaj, S. Frey, C. Ballif, N. Wyrsh, Monte Carlo Modeling of Electron Multiplication in Amorphous Silicon Based Microchannel Plates, in Proc. IEEE NSS 2019. 1-6. 10.1109/NSS/MIC42101.2019.9059971.

J. Löffler, C. Ballif, N. Wyrsh, Amorphous silicon-based micro-channel plate detectors with high multiplication gain, Nuclear Instruments and Methods in Physics Research Section A: Accelerators, Spectrometers, Detectors and Associated Equipment, 2018.

C. Hofmann, B. Herter, J. Gutmann, J. Löffler, S. Fischer, S. Wolf, R. Piper, N. Ekins-Daukes, N. Treat, J. C. Goldschmidt, Organic upconverters embedded in a Bragg structure, in Proc. SPIE 9140, Photonics for Solar Energy Systems V, p. 91400H, 2014.

J. C. Goldschmidt, S. Fischer, B. Fröhlich, J. Gutmann, B. Herter, C. Hofmann, J. Löffler, Frank C. J. M. van Veggel, S. Wolf, "Photon management with luminescent materials and photonic structures," in Proc. SPIE 9140, Photonics for Solar Energy Systems V, p. 91400G, 2014.

J. Löffler, J. Gutmann, J. C. Goldschmidt, Fabrication of One-Dimensional Photonic Crystals for Luminescent Solar Concentrators, in Proceeding of the OSA Congress Renewable Energy and the Environment Optics and Photonics, Optics for Solar Energy, p. ST2A.5, 2012.

PRESENTATIONS

2019. J. Löffler, J. Thomet, L. van Kessel, C. W. Hagen, M. Belhaj, S. Frey, C. Ballif, N. Wyrsh, Monte Carlo Modeling of Electron Multiplication in Amorphous Silicon Based Microchannel Plates, 2019 IEEE Nuclear Science Symposium and Medical Imaging Conference, Manchester, UK.

2017. J. Löffler, C. Ballif, N. Wyrsh, Amorphous silicon-based micro-channel plate detectors with high multiplication gain, 8th International Conference on New Developments in Photodetectors, Tours, France.

2012. J. Löffler, J. Gutmann, J. C. Goldschmidt, Fabrication of One-Dimensional Photonic Crystals for Luminescent Solar Concentrators, Optics for Solar Energy 2012, Eindhoven, Netherlands.